

Effect of Electrospun Mesh Diameter, Mesh Alignment, and Mechanical Stretch on Bone Marrow Stromal Cells for Ligament Tissue Engineering

Christopher Alan Bashur

Dissertation submitted to the faculty of the Virginia Polytechnic Institute and State University
in partial fulfillment of the requirements for the degree of

Doctor of Philosophy
In
Chemical Engineering

Aaron S. Goldstein, Chairman
Donald G. Baird
Linda A. Dahlgren
Garth L. Wilkes
Joseph W. Freeman

April 21, 2009
Blacksburg, VA

Keywords: Electrospinning, Tissue Engineering, Contact Guidance, Morphology, Bioreactor,
Co-electrospinning

Copyright 2009, Christopher A. Bashur

Effect of Electrospun Mesh Diameter, Mesh Alignment, and Mechanical Stretch on Bone Marrow Stromal Cells for Ligament Tissue Engineering

Christopher Alan Bashur

ABSTRACT

The overall goal of this research project is to develop methods for producing a tissue engineered ligament. The envisioned tissue engineering strategy involves three steps: seeding bone marrow stromal cells (BMSCs) onto electrospun scaffolds, processing them into cords that allow cell infiltration, and conditioning them with uniaxial cyclic stretch. These steps were addressed in three complimentary studies to establish new methods to engineer a tissue with ligament-like cells depositing organized extracellular matrix (ECM). In the first study scaffold topographies were systematically varied to determine topographies that induce cells to orient and differentiate into ligament-like cells in static culture. Scaffolds – electrospun from poly (ester-urethane urea) (PEUUR) with different fiber diameters degrees of fiber alignments – were biocompatible and supported cell growth. Topographic cues guided cell alignment, and cell elongation increased with increasing fiber alignment. Finally, expression of the ligament-like markers collagen type I and decorin were enhanced on the smallest fiber diameters compared to larger diameters. In the second study BMSCs – seeded onto aligned electrospun PEUUR scaffolds – were cyclically stretched to determine the effect of dynamic mechanical stimulation on BMSC alignment and differentiation. BMSCs remained aligned parallel to the direction of fiber alignment and expressed ligament markers (e.g. collagen type I, decorin, scleraxis, and tenomodulin) on electrospun scaffolds after the application of stretch. However, the cyclic stretch regimen was not able to enhance expression of ECM components. In the third study techniques were developed to produce more clinically relevant constructs with improved cell infiltration. Specifically, a co-electrospun scaffold composed of two well integrated components was developed to create larger pores. The scaffold was also embedding in a photo-crosslinkable hydrogel to prevent the fibers from collapsing. These results demonstrate the feasibility of making a tissue engineered ligament by seeding BMSCs on an aligned, co-electrospun scaffold with submicron diameter fibers and then applying cyclic mechanical stretch. Future work will involve combining these three steps to achieve materials suitable for *in vivo* testing.

Author's Acknowledgements

I would like to thank my advisor and committee members for their help and guidance. I would also like to thank my labmates and the undergraduate students that have worked with me, Mike Mills and Dan Cook. Finally, I would like to thank Mike Vaught and Riley Chan for helping me with the machining and electrical work.

Attribution

Several Committee Members and colleagues aided in the writing and research behind several of the chapters of this dissertation. A brief description of their background and their contributions are included below.

Aaron S. Goldstein - Ph.D. (Department of Chemical Engineering/ School of Biomedical Engineering and Sciences, Virginia Tech) is the primary Advisor and Committee Chair. He provided extensive guidance for the research as well as comments and guidance on the writing.

Linda A. Dahlgren - D.V.M, Ph.D. (Department of Large Animal Clinical Sciences, Virginia-Maryland Regional College of Veterinary Medicine) was a Committee Member. She provided guidance and comments on the writing of **Chapters 2, 3, 5, and 6** as well as guidance on clinical aspects of the research and biological assays.

Scott A. Guelcher - Ph.D. (Department of Chemical Engineering, Vanderbilt University) synthesized and donated the PEUUR used in **Chapters 3, 4, 5, and 6** and **Appendix C**.

Chapter 3: Effect of Fiber Diameter and Alignment of Electrospun Polyurethane Meshes on Mesenchymal Progenitor Cells

Robyn D. Shaffer - B.S. (School of Biomedical Engineering and Sciences, Virginia Tech) was a member of the author's lab, and she performed and analyzed the results of the mRNA expression assays and part of the cell density assays. She also contributed to the discussion section.

Chapter 6: Simultaneously Electrospinning Two Components to Improve Cellular Infiltration

Robyn D. Shaffer - B.S. (School of Biomedical Engineering and Sciences, Virginia Tech) was a member of the author's lab, and she sectioned the sample and took the image for Fig. 6.8.

Mariah S. Hahn - Ph.D. (Department of Biomedical Engineering, Texas A&M University) synthesized and donated the hydrogel used in this chapter. She also performed the cell studies and analyzed the results for Fig. 6.11.

Appendix A: Enhanced Polarization of Embryonic Hippocampal Neurons on Micron Scale Electrospun Fibers

Jae Young Lee. (Department of Chemical Engineering, University of Texas at Austin) was the main writer for this chapter and had also performed most of the research.

Natalia Gomez - Ph.D. (Department of Chemical Engineering, University of Texas at Austin, Austin) also contributed to the research conducted for this chapter.

Christine E. Schmidt - Ph.D. (Department of Chemical Engineering/ Department of Biomedical Engineering, University of Texas at Austin) was the primary investigator for this chapter.

Appendix B: Electroconductive Nanofibers for Neural Tissue Applications: Polypyrrole-Coated Electrospun PLGA Nanofibers

Jae Young Lee. (Department of Chemical Engineering, University of Texas at Austin) was the main writer for this chapter and has also performed most of the research.

Christine E. Schmidt - Ph.D. (Department of Chemical Engineering/ Department of Biomedical Engineering, University of Texas at Austin) was the primary investigator for this chapter.

Appendix C: Computational Predictions of the Tensile Properties of Electrospun Fibre Meshes: Effect of Fibre Diameter and Fibre Orientation

Triantafyllos Stylianopoulos - Ph.D. (Department of Chemical Engineering and Materials Science, University of Minnesota) performed the mathematical modeling work for this chapter and was the main writer.

Victor H. Barocas - Ph.D. (Department of Biomedical Engineering, University of Minnesota) was the primary investigator for this chapter.

Table of Contents

	Page
Chapter 1: Introduction	
1.1 <i>Introduction</i>	1
1.2 <i>Surgical Options for Ligament Repair</i>	1
1.3 <i>Native Ligament</i>	2
1.3.1 Ligament Composition	3
1.3.2 Ligament Organization	5
1.3.2.1 Collagen Fibril Formation	5
1.3.2.2 Higher Level Organization	6
1.3.3 Functional Properties	7
1.3.4 Other Considerations	8
1.4 <i>Tissue Engineering</i>	8
1.4.1 Cell Type	8
1.4.2 Growth Factors	9
1.4.3 Stretch Bioreactor	10
1.4.4 Biomaterial Scaffolds	11
1.5 <i>Biomaterial Choice and Scaffold Fabrication</i>	12
1.5.1 Biomaterials	12
1.5.2 Processing Techniques	13
1.5.3 Electrospinning	14
1.6 <i>Cell Differentiation with Stretch</i>	16
1.6.1 Effect of the Scaffold	16
1.6.2 Effect of Stretch Parameters	18
1.7 <i>Interaction between Cells and the Biomaterial</i>	18
1.7.1 Cell Attachment and Spreading	19
1.7.2 Surface Chemistry	20
1.7.3 Surface Compliance	21
1.7.4 Surface Topography	21
1.8 <i>Experimental Plan</i>	23
1.9 <i>Material in Appendices</i>	24
Chapter 2: Effect of Fiber Diameter and Orientation on Fibroblast Morphology and Proliferation on Electrospun Poly (D,L-lactic-co-glycolic acid) Meshes	
2.1 <i>Introduction</i>	26
2.2 <i>Materials and Methods</i>	27
2.2.1 Materials	27
2.2.2 Electrospinning	27
2.2.3 Cell Culture and Cell Seeding	28
2.2.4 Scanning Electron Microscopy (SEM)	28
2.2.5 Cell Morphology	29
2.2.6 Cell Number	30
2.2.7 Statistical Analysis	30
2.3 <i>Results</i>	30
2.3.1 Electrospun Fiber Architecture	30

2.3.1	Cell Morphology on Electrospun Fibers	32
2.3.1	Cell Density on Electrospun Fibers	35
2.4	<i>Discussion</i>	35
2.5	<i>Conclusions</i>	37
2.6	<i>Acknowledgements</i>	37
Chapter 3: Effect of Fiber Diameter and Orientation of Electrospun Polyurethane Meshes on Ligament Progenitor Cells		
3.1	<i>Introduction</i>	39
3.2	<i>Materials and Methods</i>	41
3.2.1	Polyurethane Synthesis	41
3.2.2	Electrospinning	41
3.2.3	Scanning Electron Microscopy (SEM) Analysis	42
3.2.4	Cell Culture and Cell Seeding	43
3.2.5	Cell Morphology	44
3.2.6	Cell Number	44
3.2.7	mRNA Expression	45
3.2.8	Statistical Analysis	46
3.3	<i>Results</i>	46
3.3.1	Electrospun Meshes	46
3.3.2	Cell Orientation and Morphology on Meshes	48
3.3.3	Cell Density on Meshes	50
3.3.4	Ligament Protein Expression	51
3.4	<i>Discussion</i>	54
3.5	<i>Conclusions</i>	57
3.6	<i>Acknowledgements</i>	57
Chapter 4: Characterization of Segmented Poly (ester-urethane urea)s for Ligament Tissue Engineering Applications		
4.1	<i>Introduction</i>	58
4.2	<i>Materials and Methods</i>	59
4.2.1	PEUUR Synthesis	59
4.2.2	Measurement of Polymer Density	60
4.2.3	Polymer Processing	61
4.2.4	Scanning Electron Microscopy (SEM)	61
4.2.5	Mechanical Testing	62
4.2.6	Further Characterization	62
4.3	<i>Results and Discussion</i>	63
4.3.1	Bulk Properties	63
4.3.2	Properties of Electrospun Meshes	66
4.4	<i>Conclusions</i>	68
4.5	<i>Acknowledgements</i>	68
Chapter 5: The Role of Electrospun Polyurethane Fibers and mechanical stretch on Bone Marrow Stromal Cells Orientation and Differentiation		
5.1	<i>Introduction</i>	70

<i>5.2 Materials and Methods</i>	72
5.2.1 Materials	72
5.2.2 Electrospinning	73
5.2.3 Scanning Electron Microscopy (SEM) Analysis	73
5.2.4 Stretch Bioreactor Design	73
5.2.5 Bioreactor Assembly and Sterilization	74
5.2.6 Cell Culture and Cell Seeding	74
5.2.7 Mechanical Stretch	75
5.2.8 Cell Morphology	76
5.2.9 mRNA Expression	76
5.2.10 Statistical Analysis	77
<i>5.3 Results</i>	78
5.3.1 Electrospun Meshes	78
5.3.2 Cell Orientation and Morphology on Meshes	79
5.3.3 ECM Expression	81
<i>5.4 Discussion</i>	81
<i>5.5 Conclusions</i>	84
<i>5.6 Acknowledgements</i>	84

Chapter 6: Simultaneously Electrospinning Two Components to Improve Cellular Infiltration

<i>6.1 Introduction</i>	85
<i>6.2 Materials and Methods</i>	86
6.2.1 Materials	86
6.2.2 Electrospinning One Component	87
6.2.3 Co-electrospinning	88
6.2.4 Characterization of Mesh Morphology	89
6.2.5 Crosslinking Gelatin	89
6.2.6 Production of PEG-LA-DA Hydrogels	90
<i>6.3 Results and Discussion</i>	91
6.3.1 Co-electrospinning	91
6.3.2 Crosslinking Gelatin Fibers	93
6.3.3 Embedding in a Hydrogel	94
6.3.4 Processing Three-dimensional Samples	96
<i>5.5 Conclusions</i>	97
<i>5.6 Acknowledgements</i>	97

Chapter 7: Conclusions and summarized work

<i>7.1 Conclusions</i>	98
<i>7.2 Future Work</i>	100
7.2.1 Enhance Expression of ECM with Cyclic Stretch	100
7.2.2 Increase Cell Infiltration with Co-electrospinning	101
7.2.3 Three-dimensional Processing and the Effect of Embedding in a Hydrogel	103
7.2.4 Conclusions	104

References	105
-------------------	-----

Appendix A: Enhanced Polarization of Embryonic Hippocampal Nuerons on Micron Scale Electrospun Fibers

<i>A.1 Introduction</i>	119
<i>A.2 Materials and Methods</i>	121
A.2.1 Electrospinning	121
A.2.2 Hippocampal Cell Culture	122
A.2.3 SEM	123
A.2.4 Statistics	124
<i>A.3 Results</i>	125
A.3.1 Fabrication of Electrospun PLGA Fibers	125
A.3.2 Effects of Fiber Sizes	125
A.3.3 Effects of Fiber Orientation	127
<i>A.4 Discussion and Conclusions</i>	129
<i>A.5 References</i>	133

Appendix B: Electroconductive Nanofibers for Neural Tissue Applications: Polypyrrole-Coated Electrospun PLGA Nanofibers

<i>B.1 Introduction</i>	136
<i>B.2 Materials and Methods</i>	137
B.2.1 Materials	137
B.2.2 Electrospinning	138
B.2.3 Polypyrrole Coating	138
B.2.4 Fiber Characterization	139
B.2.4.1 Scanning Electron Microscopy (SEM)	139
B.2.4.2 Surface Resistance	139
B.2.4.3 X-ray Photon Spectroscopy (XPS)	139
B.2.5 Cell Culture	140
B.2.5.3 Sample Preparation	140
B.2.5.3 PC12 Cell Culture and Immunostaining	141
B.2.5.3 Hippocampal Neuron Culture and Immunostaining	142
B.2.6 Immunofluorescence and Image Analysis	142
B.2.7 Assessment of Cellular Morphology	143
B.2.7 Statistics	143
<i>B.3 Result and Discussion</i>	144
B.3.1 Electrospinning PLGA Nanofibers	144
B.3.2 Synthesis of PPy-coated PLGA Nanofibers	145
B.3.3 Characterization of PPy-coated PLGA Nanofibers	146
B.3.4 Cell Culture Experiments	148
<i>B.4 Conclusions</i>	153
<i>B.5 Acknowledgement</i>	153
<i>B.5 References</i>	154

Appendix C: Computational Predictions of the Tensile Properties of Electrospun Fiber Meshes: Effect of Fiber Diameter and Fiber Orientation

<i>C.1 Introduction</i>	158
<i>C.2 Methods</i>	159
C.2.1 Materials	159
C.2.2 Polyurethane Synthesis	159
C.2.3 Electrospinning	160
C.2.4 Scanning Electron Microscopy (SEM)	160
C.2.5 Mechanical Testing	161
C.2.6 Formulation of the Model	162
C.2.7 Governing Equations	164
C.2.8 Comparison of the Model to Experimental Measurements	165
C.2.9 Extension to Engineered Blood Vessels	166
<i>C.3 Results</i>	167
C.3.1 Comparison of the Model to Experimental Measurements	167
C.3.1 Extension to Engineered Blood Vessels	170
<i>C.4 Discussion</i>	171
<i>C.4 Acknowledgements</i>	175
<i>C.5 References</i>	176

Appendix D: Computer Macros

<i>D.1 ImagePro Macro to Take Fluorescent Images</i>	180
<i>D.2 ImagePro Macro to Overlay Fluorescent Images</i>	181
<i>D.3 ImagePro Macro to Analyze Fluorescent Images</i>	185
<i>D.4 ImagePro Macro to Calculate Porosity</i>	189

List of Figures

	Page
Chapter 1	
Figure 1.1. Hematoxylin and Eosin image of an equine tendon taken by Dr. Linda Dahlgren with ECM stained pink in the background and nuclei of tendon fibroblasts stained blue (included with permission).	3
Figure 1.2. Illustration of the assembly of collagen fibrils in a “quarter-staggered array.”	5
Figure 1.3. Ligament architecture for the ACL (adapted from the diagrams by Wang et al. and Dorski et al)	6
Figure 1.4. Ligament behavior under tensile load.	7
Figure 1.5. Diagram of an electrospinning system.	14
Figure 1.6. Illustration of cell adhesion through integrin receptors and the resulting focal adhesion plaque (adapted from Goldstein)	20
Chapter 2	
Figure 2.1. SEM images of PLGA fibers electrospun from different solution concentrations: (a) 5 wt, (b) 11 wt%, and (c) 16 wt%.	31
Figure 2.2. SEM images of PLGA fibers electrospun from 11 wt% solutions onto moving target: (a) stationary target, (b) 1010 rpm, and (c) 1450 rpm.	31
Figure 2.3. Normalized histograms of fiber angle for the different rates of rotation: (a) stationary, (b) 580 rpm, (c) 1010 rpm, and (d) 1450 rpm.	32
Figure 2.4. NIH 3T3 morphology on fiber meshes with diameters of (a) $0.14 \pm 0.07 \mu\text{m}$, and (b) $3.6 \pm 0.6 \mu\text{m}$.	33
Figure 2.5. Effect of PLGA fiber diameter on (a) projected cell area, (b) aspect ratio, and (c) length of long axis.	33
Figure 2.6. Effect of PLGA fiber orientation on (a) projected cell area, (b) aspect ratio, and (c) length of long axis.	34
Figure 2.7. Cell number on PLGA fibers as a function of culture duration: (a) effect of fiber diameter, and (b) effect of fiber orientation.	35
Chapter 3	
Figure 3.1. SEM images of PEUUR fibers electrospun from different solution concentrations: a) 8 wt%, b) 12 wt%, and c) 20 wt%.	47

Figure 3.2. SEM images of PEUUR fibers electrospun from 12 wt% solutions onto a) a stationary target, or a rotating target at b) 2.4 m/s, and c) 4.4 m/s.	47
Figure 3.3. BMSC morphology on fiber meshes electrospun onto a) a stationary target and b) a drum rotating at 4.4 m/s.	48
Figure 3.4. Effect of PEUUR fiber diameter on a) projected cell area, b) aspect ratio, and c) length of long axis.	49
Figure 3.5. Effect of PEUUR fiber orientation on a) projected cell area, b) aspect ratio, and c) length of long axis.	49
Figure 3.6. Cell density on PEUUR fibers as a function of culture duration: a) effect of fiber diameter, and b) effect of fiber orientation.	51
Figure 3.7. Effect of fiber diameter on mRNA expression of <i>Colla1</i> , decorin, tenomodulin, and scleraxis after 7 days of culture.	52
Figure 3.8. Effect of fiber orientation on mRNA expression of <i>Colla1</i> , decorin, tenomodulin, and scleraxis after 7 days of culture.	52
Figure 3.9. Effect of fiber diameter on mRNA expression of a) collagen 1 α 1, b) decorin, c) tenomodulin, and d) scleraxis after 7 and 14 days of culture.	53
Figure 3.10. Effect of fiber orientation on mRNA expression of a) collagen 1 α 1, b) decorin, c) tenomodulin, and d) scleraxis after 7 and 14 days of culture.	53
Figure 3.11. Comparison of mRNA expression on spincoated PEUUR films for collagen 1 α 1, decorin, tenomodulin, and scleraxis after 7 days of culture.	54
Chapter 4	
Figure 4.1. Synthesis scheme for forming PEUUR elastomers for a) formation of the HDI.PCL.HDI prepolymer and b) formation of the PEUUR.	60
Figure 4.2. Stress strain curves of both a) the initial linear region and b) the entire curve for cast polymer dogbones tested in PBS at 10 mm/min and 37°C (representative samples).	64
Figure 4.3. DSC results of the PEUURs showing a) heating curves (dashed line for initial heating and solid line for second heating) and b) the cooling curves.	65
Figure 4.4. Mesh moduli for a) different fiber diameters ($n = 3$) and b) different degrees of alignment ($n = 3$) tested cyclically in PBS at 37°C and 0.5 Hz.	66
Figure 4.5. Stress-strain curve showing hysteresis for a representative sample (0.89 μ m diameter electrospun PEUUR1250 meshes with 29.9° angular standard	

deviation tested parallel to the direction of fiber alignment) in PBS at 37°C and 0.5 Hz.	67
Figure 4.6. Profile of maximum stress with the number of cycles for PEUUR1250 meshes for a) 0.47 μm diameter randomly oriented fibers and b) 0.61 μm diameter fibers tested parallel to the direction of alignment (33.4° angular standard deviation).	67
Chapter 5	
Figure 5.1. a) Diagram and b) an image of the stretch bioreactor.	74
Figure 5.2. Representative images of oriented meshes electrospun both a) as-electrospun on aluminum and b) further processed and statically stretched 25%.	78
Figure 5.3. Representative images of BMSCs after 4 days on silicone surfaces with and without stretch (a and b respectively) and on electrospun meshes with and without stretch (c and d respectively).	79
Figure 5.4. Effect of mechanical stretch and type of surface on BMSC a) projected cell area, b) aspect ratio, and c) length of long axis.	80
Figure 5.5. PCR results normalized by the β -actin housekeeping gene for the different surfaces with and without stretch for $n = 6$ substrates.	81
Chapter 6	
Figure 6.1. Chemical structure of the PEG-LA-DA hydrogel prior to photo-crosslinking.	87
Figure 6.2. Diagram of the co-electrospinning system with two syringes on opposite sides of a rotating drum.	88
Figure 6.3. Superimposed fluorescent images of a coelectrospun a) 9 wt% PLGA/ 9 wt% PLGA peeled mesh, b) 9 wt% PLGA/ 10 w/v% gelatin fibers on a coverslip, and c) 9 wt% PEUUR/ 10 w/v% gelatin fibers on a coverslip.	91
Figure 6.4. Superimposed fluorescent images of a coelectrospun PLGA/gelatin fiber mesh imaged along the length of the rotating drum from a) to c).	92
Figure 6.5. Average pixel intensity ratios for fluorescent images of a well integrated PLGA/PLGA composite mesh.	93
Figure 6.6. SEM images of electrospun gelatin a) before and b) after crosslinking.	93
Figure 6.7. SEM images of electrospun PEUUR/gelatin meshes a) before and b) after crosslinking.	94

Figure 6.8. Histological paraffin section of randomly oriented electrospun PEUUR fibers stained with hematoxylin (blue) for cell nuclei and VectaStain ABC kit for collagen type I (brown).	95
Figure 6.9. Sections of a crosslinked PEG hydrogel a) without and b) with an embedded electrospun mesh.	95
Figure 6.10. NIH 3T3 cells in a crosslinked PEG hydrogel stained with a) DAPI and b) calcein-AM after 3 days in culture.	96
Figure 6.11. Image of a) PEUUR1250 mesh embedded in hydrogel and b) cell inside an embedded hydrogel with brightfield and fluorescent images.	96

Appendix A

Figure A.1. Scanning electron micrographs of PLGA fibers electrospun using different concentrations and rotation speeds of a collector: Random fibers of (A) RD_7, (B) RD_10.5, and (C) RD_13 were electrospun using 7%, 10.5%, and 13% polymer solution at a stationary mode, respectively.	122
Figure A.2. Immunostaining of hippocampal neurons on (A) a spin-coated PLGA films and (B) PLGA nanofibers (RD_7).	126
Figure A.3. Effects of fiber diameter on neuron polarization and average axon lengths of polarized hippocampal neurons cultured for 22 h.	126
Figure A.4. Effects of fiber alignment on neuronal polarization and elongation of hippocampal neurons.	128
Figure A.5. Hippocampal neurons cultured on (A) random fibers (RD_10.5) and (B) aligned fibers (HI_10.5).	128
Figure A.6. Normalized histograms of axon angles on various substrates: (A) the spin-coated films (controls), (B) randomly aligned fibers (RD_10.5), (C) intermediately aligned fibers (INT_10.5), and (D) highly aligned fibers (HI_10.5).	129
Figure A.7. SEM images of hippocampal neurons cultured on various PLGA meshes: (A) RD_7, (B) RD_10.5, (C) HI_10.5, and (D) RD_13. Scale bars are 2 μm .	131

Appendix B

Figure B.1. Schematics of assembly of a PPy-PLGA mesh for in vitro cell culture study and electrical stimulation.	141
Figure B.2. Scanning electron micrographs of electrospun PLGA nanofibers, (a) and (b), and their PPy-coated fibers, (c) and (d).	144

Figure B.3. PPy-coated PLGA meshes.	146
Figure B.4. High resolution (a) C _{1s} and (b) N _{1s} XPS spectra of PLGA and PPy-PLGA.	147
Figure B.5. Immunostaining of PC12 cells cultured on (a) RF, (b) AF, (c) PPy-RF, and (d) PPy-AF.	149
Figure B.6. SEM images of PC12 cells cultured on (a) PPy-RF and (b) PPy-AF for 2 days.	149
Figure B.7. Fluorescence images of hippocampal neurons cultured on (a) RF, (b) AF, (c) PPy-RF, and (d) PPy-AF.	151
Figure B.8. Electrical stimulation of PC12 cells through PPy-PLGA (PPy-RF and PPy-AF) fibers at 0 mV/cm and 10 mV/cm.	152
Appendix C	
Figure C.1. SEM images and model representations of electrospun meshes.	163
Figure C.2. Experimental (squares) and computed (curve) stress–strain curve for PEUUR mesh electrospun from 11 wt% solution in HFIP.	168
Figure C.3. Experimental (black bar) and computed (white bar) moduli for PEUUR meshes electrospun from 11 (diameter 0.53 μm) and 13.5 wt% (diameter 0.90 μm) solutions at stationary drum.	169
Figure C.4. Experimental (black bar) and computed (white bar) moduli for PEUUR meshes electrospun from 13.5 wt% solution at rotation rates of 2.0 m/s (41.2°) and 4.4 m/s (29.9°) parallel (Fig. 9(a)) and perpendicular (Fig. 9(b)) to fibre alignment.	169
Figure C.5. Initial and inflated at 150 mmHg luminal pressure configuration of the blood vessel (left).	170
Figure C.6. Pressure vs. inner diameter response for circumferentially orientated meshes for 250 μm (triangles) and 1000 μm (crosses) wall thickness, and for an intracranial artery (solid).	171

List of Tables

	Page
Chapter 2	
Table 2.1. Fiber diameter and angular standard deviation for PLGA electrospun from 5 and 11 wt% solutions at different rotation rates.	32
Table 2.2. Angular standard deviation of cells and cell orientation relative to fibers on electrospun surfaces with different degrees of orientation.	34
Chapter 3	
Table 3.1. Primer sequences for real-time polymerase chain reaction amplification.	46
Table 3.2. Fiber diameter and angular standard deviation for meshes electrospun from PEUUR solutions of different concentrations and at different rotation rates.	47
Table 3.3. Cell alignment and orientation on aligned meshes.	50
Chapter 5	
Table 5.1. Primers for PCR.	77
Table 5.2. Cell alignment on meshes and PDMS control surfaces.	80
Appendix A	
Table A.1. PLGA fibers synthesized and tested for embryonic hippocampal neuron culture.	121
Appendix B	
Table B.1. Elemental compositions and doping levels of PLGA and PPy-coated PLGA (PPy-RF) using XPS analysis.	147
Appendix C	
Table C.1. Measured fiber diameter, angular standard deviation and elastic modulus for PEUUR meshes electrospun from 11 and 13.5 wt% solutions onto a stationary target.	167
Table C.2. Measured fiber diameter, angular standard deviation and elastic modulus for PEUUR meshes electrospun from 13.5 wt% solution at different rotation rates.	167
Table C.3. β -values predicted by the model and measured for different materials.	172

List of Equations

	Page
Chapter 2	
Equation 2.1. Wrapped normal distribution	29
Equation 2.2. Mean resultant length	29
Equation 2.3. Mean angle	29
Equation 2.4. Angular standard deviation	29
Chapter 3	
Equation 3.1. Mean angle	43
Equation 3.2. Mean resultant length	43
Equation 3.3. Angular standard deviation	43
Appendix B	
Equation B.1. Surface resistance	139
Appendix C	
Equation C.1. Constitutive equation	164
Equation C.2. Cauchy stress tensor	164
Equation C.3. Derivation with Kronecker delta	164
Equation C.4. Boundary crosslinks	165
Equation C.5. Derivation using Leibnitz theory	165
Equation C.6. Stiffness parameter	166

Chapter 1: Introduction

1.1 Introduction

The overall goal of this research project was to develop methods to produce a tissue engineered ligament that can serve as an alternative to an autologous graft and other current surgical techniques. A tissue engineering approach incorporates both a biocompatible scaffold and cells to induce tissue generation through the deposition and organization of extracellular matrix (ECM) [1, 2]. Specific strategies for ligament tissue engineering should be developed with an understanding of the structure of native ligament tissue, the requirements of ligaments in the body (i.e. *in vivo*), the scaffolds that can meet these requirements, and the biological phenomena that can induce specific cell behavior. The ligament tissue engineering strategy used in this research project involves seeding mesenchymal progenitor cells on electrospun scaffolds and mechanically stimulating the cells with a cyclic stretch bioreactor. While other groups (e.g. David Kaplan, Cato Laurencin, James Wang, Jung-Woog Shin, and David Butler [1, 3-6]) have helped to develop particular components of this strategy for ligament applications, the contribution of this research project is in the unique combination of the components to address ligament tissue engineering challenges. These challenges and the motivation for the particular studies performed in this research project are described throughout this section, and the resulting experimental plan is described in Section 1.8.

1.2 Surgical Options for Ligament Repair

An estimated 150,000 reconstructive ACL surgeries are performed annually in the United States to repair tears and ruptures [7]. ACL injuries occur frequently in athletes and often are career ending injuries. Multiple treatment options exist for tears, but for ruptures, surgery is the primary option [8]. The challenge with ligaments like the ACL – that are within a joint – is that ruptures do not heal *in vivo* because of limited vascularization and poor clotting ability [8-10]. In contrast, ligaments outside of a joint, such as the medial collateral ligament (MCL) can normally heal naturally [9]. The limited healing potential of the ACL was demonstrated in a study by Feagin et al. [8]. Both ends of ruptured ACLs were sutured together, but the ends did not effectively fuse after 5 years and 94% of the patients had knee instability [8]. Therefore, the

ACL is currently removed in surgery and replaced with a graft that is fixed to the bone on both ends [11, 12].

Three options for ACL grafting materials include autologous, allogeneic, and synthetic grafts. Each has unique drawbacks. Autologous graft from a patient is currently the “gold standard” for ACL replacement. This graft is most frequently obtained from the patellar tendon or multiple strands of the hamstring tendon bundled together [13, 14]. The high strength of this graft is attractive, but problems include donor site morbidity and a limited amount of donor tissue [15, 16]. Donor site morbidity can cause pain, muscle atrophy, and tendonitis [15, 16]. A second option is allogeneic graft – typically from cadaver – which does not have the problems of donor site morbidity and has a more abundant tissue supply [16], but other drawbacks include risk of disease transmission and immune responses [17]. An immune response can occur because of any active foreign proteins or cell in an allogeneic graft that triggers rejection of the tissue [18]. For both autologous and allogeneic grafts, the strength does not match the strength of native ACL tissue [19]. The third option is synthetic grafts, such as Dacron ®, Gore-Tex ®, and the polypropylene based Kennedy Ligament-Augmentation Device that have been used in the past [16]. These grafts are non-biodegradable and will not repair over time. They are currently not approved for ACL replacement because of success rates between 30 and 60% and with very few prostheses lasting more than 6 years [20]. These low success rates are due to fatigue and creep of the graft that occurs with daily knee movement *in vivo*.

Tissue engineering is a potential fourth option. A tissue engineering approach incorporates both a biodegradable scaffold and an autologous cellular component to induce tissue generation through the deposition of ECM [1, 2]. Tissue engineering avoids the problems of donor site morbidity, limited donor tissue supply, and disease transmission. In addition, in tissue engineering, the cells can repair the ligament graft and prevent fatigue through active remodeling of the ECM, unlike synthetic grafts.

1.3 Native Ligament

An understanding of the structure of native ligament can aid in designing a tissue engineered construct, as the structure of a biological tissue is correlated to its function. Biological tissues are very complex with different components that assemble to create a hierarchical structure that serves multiple functions from maintaining mechanical integrity to the

transport of nutrients and oxygen. Due to the complexity of native tissue, the exact replication of its chemistry and structure in a tissue engineered construct is not feasible, but important functional properties and *in vivo* stimuli can still be mimicked in a tissue engineering strategy. Important considerations for ligament tissue engineering include the tensile properties of the scaffold that are required to maintain mechanical integrity and the stimuli that induce ligament-like cell behavior (e.g. phenotype and ECM deposition).

1.3.1 Ligament Composition

Ligaments are composed of cells, proteins, and proteoglycans that are arranged in a complex hierarchical structure. Fibroblasts, the primary cell in ligaments, are responsible for synthesizing ECM proteins and remodeling the ECM during healing [21, 22]. Mature fibroblasts are sparsely distributed throughout the ligament and have low mitotic activity, but they are responsible for the normal maintenance of the tissue and the deposition of the proteins, proteoglycans, and glycoproteins that primarily comprise the ligament ECM [19]. Mature fibroblasts in ligament have both highly elongated nuclei and cytoplasm [21], although not as elongated as in tendon tissue (**Figure 1.1**) [23]. Further, some fibroblasts in healthy human ACLs have contractile function, as determined by the presence of significant amounts of the marker α -smooth muscle actin [24]. These fibroblasts with contractile function have also been shown to stretch and orient ECM in other types of tissue during wound healing [21, 25].

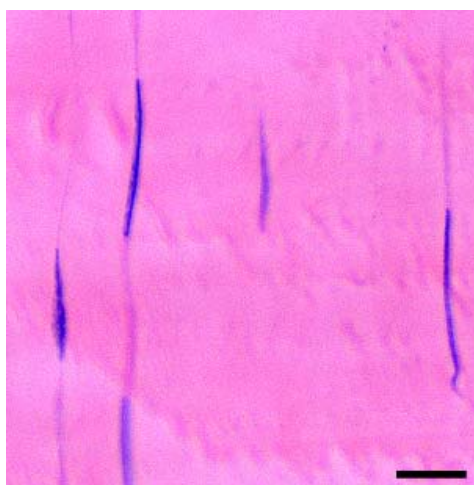


Fig. 1.1. Hematoxylin and Eosin image of an equine tendon taken by Dr. Linda Dahlgren with ECM stained pink in the background and nuclei of tendon fibroblasts stained blue (included with permission). The scale bar is 25 μ m.

The non-cellular components of ligament include water, proteins, proteoglycans, and glycoproteins. The primary protein in ligament ECM is collagen type I (composed of two $\alpha 1$ chains and one $\alpha 2$ chain [26]) that self assembles into fibrils [19, 22]. Other components include collagen type III [22], collagen type V [19], elastin [22], and other types of collagen that are found in limited amounts [22]. The fibrillar collagens (i.e. type I and III) and elastin are the structural components of ligament ECM [21], while globular collagens (e.g. type V) are thought to affect the packing of the collagen type I fibrils [22]. A typical cruciate ligament has a collagen type I: type III ratio of approximately 8:1 [16]. Tendon has very similar composition to ligament tissue, but a typical collagen type I: type III ratio for tendons (i.e. patellar and achilles) is greater than 19:1 [16]. Proteoglycans in ligament include decorin [22], biglycan [19], aggrecan [22], and fibromodulin [19, 27]. Proteoglycans also aid in the packing and organization of the collagen fibrils [28]. Decorin – the most abundant proteoglycan in tendon/ligament – is thought to inhibit the formation of large collagen fibrils [19]. Cartilage oligomeric matrix protein (COMP) is another proteoglycans that has been found to increase the rate of collagen fibril formation in tendon; however, it is generally not found in mature fibrils [29]. Glycoproteins include tenascin-C and fibronectin [22]. Fibronectin provides several specific peptide sequences that aid in cell attachment through integrins [30]. Its increased synthesis has been shown to induce wound healing [22]. Tenasin-C functions as a link between cells and the fibronectin. It is thought to inhibit the expression of integrin cell adhesion proteins [19, 21, 30], and to interfere with the attachment of cells to fibronectin and other ECM components [31].

The presence of the ECM components found in native ligament can be used as a marker of ligament differentiation in engineered tissue, but these components are not specific. Collagen type I is expressed by most types of musculoskeletal tissue cells (e.g. skin, tendon, bone), and the other components (e.g. elastin and fibronectin) can also be found in different tissues [21]. Tenasin-C is found in other tissues, but commonly is used as a marker of ligament because it is found in higher amounts in tendon and ligament [19]. Other musculoskeletal tissues have specific markers – collagen type II for cartilage [32] and osteocalcin for bone [33] – but ligament/tendon only has selective markers, including scleraxis and tenomodulin, that have recently been identified. Scleraxis is a transcription factor – expressed during the early stages of musculoskeletal development [34] – that is necessary for development of mature tendon tissue

[35]. It may be considered an early marker of the ligament phenotype. Tenomodulin is a transmembrane glycoprotein [36] that is induced by scleraxis [37], and is thought to aid in the organization of collagen into fibrils [38] and the suppression of ligament vascularization [39].

1.3.2 Ligament Organization

1.3.2.1 Collagen fibril formation

Ligaments are organized in a hierarchical structure with collagen triple helices at the most basic level. This triple helical structure provides collagens with resistance to degradation by many proteases (e.g. pepsin, trypsin, and chymotrypsin); however, the collagens are degraded by matrix metalloproteinases (MMP)s [26]. For fibrillar collagen, the triple helices assemble into fibrils under physiological conditions [19]. In this process, pro-collagen is secreted into the ECM where a section of the pro-collagen is cleaved to produce the collagen triple-helix [40]. Collagen then self-assembles to form fibrils, likely due to hydrophobic interactions [19, 22]. The collagen triple helices assemble in a “quarter staggered array” where they are staggered by approximately 64 nm (i.e. $\frac{1}{4}$ of their total length) [22]. **(Figure 1.2)** The formation of covalent crosslinks in this collagen is important for the strength of the resulting collagenous tissues. Types of crosslinks include disulfide bonds that form at cysteine residues and crosslinks formed by the enzyme lysyl oxidase [19, 22]. In older tissue these crosslinks are converted to irreversible pyridinoline and pyrrole forms [19].

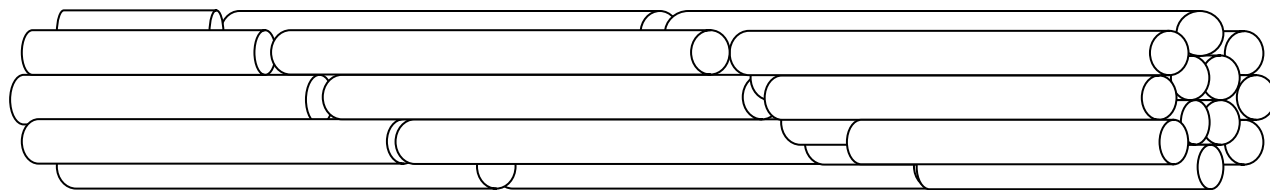


Fig. 1.2. Illustration of the assembly of collagen fibrils in a “quarter-staggered array”

The diameter of native collagen type fibrils in the ECM is approximated as 50 nm for a healthy human ACL [41]. However, human ligaments have been shown to have a bi-modal distribution of collagen fibrils (i.e. fibril diameters 40–75 nm and 100–150 nm) [15]. The exact

size of the fibrils will vary from patient to patient and with age, where younger patients will have more uniform small fibrils and older patients will have a more bi-modal distribution of sizes [22]. The collagen type III homotrimer will form smaller, less organized fibrils [22, 26]. The proteoglycans in ECM have also been shown to affect the fibril diameter of the collagen [19].

1.3.2.2 Higher level organization

In native ligament tissue, collagen fibrils (primarily collagen type I) are arranged in parallel bundles that provide high tensile strength and direct attached fibroblasts to align parallel to the direction of the collagen fibrils (**Figure 1.3**) [19]. These fiber bundles form fascicles with a sinusoidal wave-like structure known as the “crimp” pattern [19]. Finally, at least two fascicles comprise the complete ligament [19, 42]. Additional levels of ligament hierarchy (e.g. the sub-fibril [19] and the tertiary fiber bundle [22]) have been described in some articles. Fibrils of collagen type III are found primarily around bundles of collagen type I fibrils [22]. Many ligaments, such as the ACL, have a synovial sheath surrounding them to protect them [8]. The synovial sheath consists of two membranes surrounding a layer of fluid, and is used to reduce friction with the surrounding tissue [22]. With all of the ACL’s components assembled, the average length of a human ACL ranges from 27 to 32 mm [16].

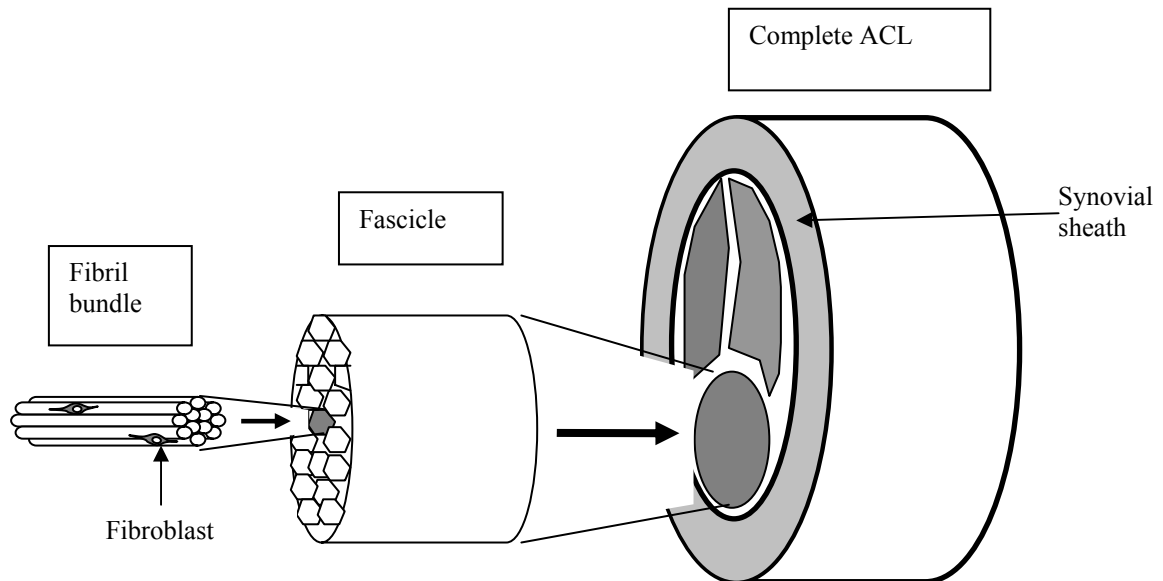


Fig. 1.3. Ligament architecture for the ACL (adapted from the diagrams by Wang et al. and Dorski et al. [19, 22])

1.3.3 Functional Properties

The ligament components and structure provides the properties necessary to withstand the biomechanical forces that are exerted on the ligament daily. A human ACL performs an average of 1 to 2 million cycles per year (2,700 – 5,500 cycles/day) [16], a loading rate that will cause fatigue in many grafts [20]. Fatigue is reduced in native ligament by the fibroblasts that slowly repair the ligament over time [21]. The rate of repair and remodeling has been shown to increase with exercise in the Achilles tendon resulting in a 46% increase in collagen deposition after 8 weeks of endurance training [43]. Further, during knee movement the ACL is commonly exposed to loads of 67 N for ascending stairs and up to 630 N for jogging [44]. The ACL is able to withstand these common loads because it has a modulus of approximately 111 MPa [10] and equal load distribution throughout knee rotation (as the ACL twists 90° during rotation) [16].

Native ligament exhibits three different regions of its stress-strain curve (i.e. the “toe-in” region, the linear region, and the yield region) during loading (**Figure 1.4**) [5]. The crimp pattern in collagen fibrils provides a “toe-in” (i.e. initial non-linear region of the stress strain curve) as the fibrils are straightened and elongated with strain [16]. After 2 to 4 % strain, all of the crimp pattern is straightened and further strain leads to stretching of the collagen triple helices and intrafibrillar slippage occurs between crosslinks (i.e. the linear region) [5, 22, 45]. For 7 to 16% strain, defibrillation of the ligament occurs (i.e. the yield or failure region) [5, 16]. The ACL is typically stretched 4-5% during normal activity – through the “toe-in” region and part of the linear region [46].

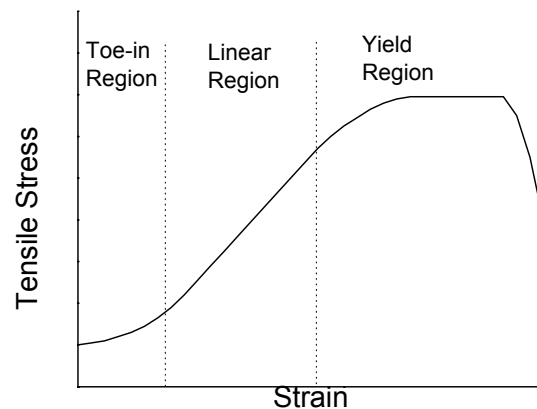


Fig. 1.4. Ligament behavior under tensile load.

1.3.4 Other Considerations

Other components of a native ACL include the presence of microvasculature, nerves, and, fibrocartilage tissue. While ligament is not a highly vascular tissue, some microvasculature as well as the synovial fluid are necessary to provide nutrient transport to the ligament. At the bony insertion ends of the ACL it transitions from ligament to fibrocartilage to mineralized fibrocartilage and finally to bone [15, 19]. The fibrocartilage consists of alternating layers of hyaline cartilage matrix and thick layers of collagen fibers with some calcified sections, and is the section of the ACL where aggrecan, collagen type II, and chondrocytes are found [15, 19, 21, 22].

1.4 Tissue Engineering

Tissue engineering incorporates a biodegradable scaffold and a cellular component to induce tissue generation through the deposition of ECM [1, 2]. Specific strategies involve seeding cells on a biodegradable polymeric scaffold, using a bioreactor to generate ligament-like tissue *in vitro* [16], and adding growth factors to the medium to promote differentiation of stem cells to a ligament-like phenotype [47, 48]. These tissue engineering strategies can produce many of the functional properties (e.g. mechanical properties and cell differentiation) of native ACL *in vitro* [49, 50].

1.4.1 Cell Type

The type of cells used in tissue engineering must be able to proliferate, exhibit a ligament-like phenotype, deposit appropriate ECM, and not induce an immune response *in vivo*. Adult stem cells are a promising cell type, and are commonly employed in ligament tissue engineering studies [16]. These cells can be derived from many types of tissue including bone marrow, adipose tissue, muscle, and synovial membrane [32, 51]. Adult stem cells derived from bone marrow – typically from the iliac crest – are referred to as bone marrow stromal cells (BMSCs) [52, 53]. These cells are proliferative progenitor cells [9] that can differentiate into bone, cartilage, muscle, fat, or ligament-like fibroblasts [54]. In addition, BMSCs have been shown to reduce inflammation in healing tissue [51]. Disadvantages of BMSCs are that they require an additional, often painful, surgery to collect [52, 53] and they can differentiate into undesired cell phenotypes (e.g. osteoblasts and chondrocytes). For engineering ligament tissue,

differentiation of these cells with the expression and synthesis of ligament-like ECM (e.g. collagen types I and III, elastin, decorin, and tenascin-C [22]) without markers of other phenotypes (e.g. collagen type II [32] and osteocalcin [33]) is desired. Multiple markers are required to determine ligament-like differentiation because ligaments and tendons lack specific markers. Another indication of ligament-like fibroblastic differentiation is the cell shape. Mesenchymal stem cells have either an irregular star or spindle shape and cover a large surface area with thin cytoplasmic extensions and pronounced oval-shaped nuclei [21]. With differentiation into mature ligament fibroblasts, the cell area and the nucleus significantly decrease and elongate. Fibroblasts active in wound healing have characteristics of both primitive mesenchymal cells (i.e. more rounded nuclei) and mature fibroblasts (i.e. smaller cell area, but still more spread than mature fibroblasts) [21].

Immortalized xenogeneic cell lines including mouse NIH 3T3 fibroblasts [55], mouse L929 fibroblasts [56], and rainbow trout RTG-2 fibroblasts [57] are easier and less expensive to work with than BMSCs. Therefore, they are often used in initial studies to assess biocompatibility and cell behavior on biomaterials [55, 58, 59]. However, these cells are not suitable for *in vivo* studies because they have a different phenotype than healthy ligament cells and they can induce a host immune response.

Another cell option is terminally differentiated cells removed directly from the patient [9, 32, 60]. Studies have demonstrated autologous fibroblasts can proliferate for ligament repair [60]; however, fibroblasts in ligament tissue (e.g. ACL and MCL fibroblasts) have a lower rate of ECM synthesis than BMSCs [9, 61]. Further, they have relatively low mitotic activity (like most terminally differentiated cells) that prevents their efficient expansion in culture necessary for ligament tissue engineering applications [19].

1.4.2 Growth Factors

For ligament tissue engineering, growth factors are frequently added to induce a ligament fibroblast phenotype in BMSCs. Families of growth factors – including fibroblastic growth factor (FGF), transforming growth factor β (TGF- β), insulin-like growth factor (IGF), vascular endothelial growth factor (VEGF), and platelet-derived growth factor (PDGF) – have been added to induce proliferation and differentiation *in vitro* for ligament tissue engineering and *in vivo* with native ligament tissue [9, 22, 32, 62].

Each of these families of growth factors include several different proteins that are up-regulated during different stages of tendon or ligament healing [22] and serve different functions including increasing cell proliferation, ECM protein expression, and angiogenesis [9, 22]. IGF, PDGF, FGF, and VEGF isotypes have all been shown to increase cell proliferation [63-65], and VEGF isotypes have also been shown to increase angiogenesis [66]. TGF- β isotypes, which are up-regulated late in the healing process, and IGF isotypes have both been shown to increase ECM synthesis [9, 22, 67]. TGF- β has been shown to enhance both markers of the ligament phenotype (e.g. collagen type I [9, 22] and proteoglycans [9]) as well as markers of cartilage (e.g. collagen type II [32]), suggesting that TGF- β alone is not enough to ensure the ligament phenotype. TGF- β has also been shown to be required for the induction of α -smooth muscle actin in fibroblasts with contractile function [68].

1.4.3 Stretch Bioreactor

Bioreactors for ligament tissue engineering use cyclic mechanical stretch, simulating the stretching that occurs naturally in a ligament [16]. In native ligaments and tendons, exercise produces mechanical stretch in the tissue. Importantly, this stimulus has been shown to increase tissue repair, while a lack of this stimulus has been shown to lead to the formation of irregular collagen fibers, increased expression of MMPs, and decreased tensile strength of the tissue [22, 69]. The mechanical stimulus from uniaxial cyclic stretch in a bioreactor has also been shown to stimulate tissue growth by inducing differentiation and ECM deposition *in vitro* [49]. This result is expected as cyclic stretching and the corresponding changes in the cell cytoskeleton have been shown to affect cell proliferation, migration, and ECM deposition through mechanotransduction [70, 71]. While the mechanism of mechanotransduction is partially understood (described further in Section 1.7), its effects in different *in vitro* situations require further investigation. For instance, the number of MSCs and ligament fibroblasts has generally been shown to increase in response to stretch. However, some studies have shown negligible cell growth or even a decline with the application of stretch [4, 49, 72, 73]. This discrepancy may partially be observed because magnitudes of strain above a certain level have been shown to increase the rate of cell apoptosis [74, 75]. Also, cells do not exhibit proliferation and differentiation at the same time [22], and this may be another reason for differences in cell number and proliferation.

The differentiation of MSCs and fibroblasts in response to stretch has been determined through the increased expression and deposition of ligament-like ECM components, growth factors, and other more specific markers. Cyclic mechanical stretch has been shown to increase the expression and synthesis of collagen types I and III in MSCs and ligament fibroblasts [4, 49, 76, 77]. The ratio of the two types of collagen has also been measured in response to stretch because it is one distinction between tendons, ligaments, and other supporting tissue (see section 1.3.1). However, these results are inconclusive because some studies found that collagen type III was induced more than collagen type I, while another study found that collagen type III was not significantly induced even though collagen type I was [4, 76, 77]. Studies have also found that the expression and synthesis of TGF- β – a growth factor that increases the synthesis of collagen type I – by human ACL fibroblasts also increased with mechanical stretch [4]. TGF- β has been shown to increase α -smooth muscle actin expression [68], so expectedly, expression of α -smooth muscle actin by human patellar tendon fibroblasts has also been found to increase with stretch [78]. Increases in expression of MMPs – which are involved in the turnover of ECM – by fibroblasts have also been shown in response to high magnitudes of strain [22, 79]. The expression of other components of ligament-like ECM (e.g. tenascin-C and elastin) has also been shown to be upregulated with stretch [49, 80]. Scleraxis, a selective marker of ligament-like fibroblasts, was shown to be induced in MSCs in response to uniaxial cyclic stretch in a study by Kuo et al. indicating a ligament-like phenotype [81].

1.4.4 Biomaterial Scaffolds

Three-dimensional biocompatible scaffolds for tissue engineering have several requirements that include providing the surface for cell attachment, enabling cell infiltration, and supporting the initial loads placed on a tissue engineered graft. First, surface characteristics are important because they can guide cell attachment and alignment – and consequently the alignment of the ECM [82-84] – through topographical cues [85, 86]. Second, the scaffold must have an adequate porosity and effective pore diameter to allow for cell infiltration [87]. Third, the scaffold must provide the mechanical stability (e.g. both strength and fatigue resistance) in a bioreactor and *in vivo* until the deposited ECM is able to support applied loads. Specific biomaterials and processing techniques are discussed (in Section 1.5).

1.5 Biomaterial Choice and Scaffold Fabrication

1.5.1 Biomaterials

A biomaterial for ligament tissue engineering must meet several requirements, including biocompatibility, degradability, mechanical strength, and fatigue resistance. Several synthetic polymers have been shown to be biocompatible and are used for tissue engineering applications (e.g. α -hydroxyl esters and segmented polyurethanes and polyureas) [88-90]. Commonly used α -hydroxyl esters (e.g. poly (lactic acid) (PLA), poly (glycolic acid) (PGA), poly (ϵ -caprolactone) (PCL)) have rates of hydrolytic degradation that vary from 1 or 2 months for PGA to 2 or 3 years for PCL [89, 91-93], with the longer degradation time of PCL better matching the healing rate of ligament tissue. The tensile properties (e.g. yield strength, percent elongation, and modulus) of these polymers vary, and they should be similar to those of native ligament (described in Section 1.3.3). The tensile properties also vary significantly with different processing techniques, as poly (L-lactic acid) fiber meshes have been reported with moduli from 4 to 8 GPa and percent elongation from 18 to 73% [92]. In addition, one porous poly (lactic-co-glycolic acid) (PLGA) fiber mesh was reported by Li et al. to have an ultimate tensile strength of 323 MPa and 96% percent elongation [90]. These meshes may have a high enough modulus for ligament applications with native human ACL having a modulus of approximately 111 MPa [10]; however, one limitation is that they will fatigue during the repetitive cyclic loading that is applied to a ligament graft both in a bioreactor and *in vivo* [94].

A promising strategy to provide the fatigue resistance required during cyclic loading is to use a thermoplastic elastomer (e.g. poly (ester-urethane urea)s (PEUURs)) [88, 95]. PEUURs consist of a hard segment and a soft segment which are able to micro-phase separate and produce elastomeric properties through physical crosslinks [96, 97]. These materials frequently contain an α -hydroxyl ester segment (e.g. PCL), and the degradation rates may be similar to that of the corresponding ester [88]. These elastomers have been found to have percent elongations of 820% for films and 220% for meshes [88]. A benefit of these materials is that the moduli can be adjusted by varying the molecular weight of one of the segments – while keeping the same chemistry for the individual segments [96]. However, the moduli of these elastomers are lower than that of human ACL [10, 88]. For example, a modulus of 60 MPa has been reported for a poly (ester-urethane urea) (PEUUR) film [88], and the modulus of the same material was

decreased to 8 MPa when processed into a porous mesh [88]. These properties demonstrate the importance of mechanical conditioning to induce tissue deposition prior to implantation *in vivo*.

Many natural proteins have also been used for ligament tissue engineering (e.g. collagen, silk, and gelatin) [1, 98]. In contrast to hydrolytically degradable synthetic polymers [91], natural proteins are degraded enzymatically [99]. These natural polymers are degraded *in vivo* through proteases including MMPs secreted by fibroblasts [22]. In addition, these materials have high moduli but possess limited elasticity [1, 98]. For example, collagen has been electrospun with a dry tensile modulus of 262 MPa and a percent elongation of 8 to 10% [98]. Further, a silk cord has been shown to have a strain at break of 38.6% [1]. Gelatin has been used for ligament tissue engineering applications, but requires crosslinking to prevent dissolution in aqueous environments [100]. After 3 days of crosslinking, Zhang et al. found that the modulus of dry electrospun gelatin meshes increased from 46.5 to 424 MPa and the strain at break increased from 32.4 to 48.8% [100]. However, the modulus of gelatin decreases after hydration [101, 102], and the gelatin would be hydrated during *in vitro* culture.

1.5.2 Processing Techniques

Different structures of porous materials for tissue engineering include foams [96], fibers [103], and sintered microspheres [104]. For ligament tissue engineering, high strength in the direction of tension can be achieved with aligned fibrous meshes. Fibrous scaffolds can be produced with melt extrusion [105], wet spinning processes [106, 107], and electrospinning [108, 109]. In melt extrusion, the polymer is melted and then forced through a die [105]. The dimensions of the die are used to control the diameter of the fibers [110]. This process requires a melt viscosity low enough for the polymer to be forced through the die [111], and can lead to significant degradation in polymers such as PLA. Wet-spinning is used for polymers that will degrade at the temperatures required for melt extrusion. In wet spinning, a solvent is added to lower the viscosity and therefore lower the temperature required for extrusion. The tensile moduli of PLA fibers produced through these two techniques have been compared, and the fibers have been shown to have higher moduli after wet-spinning than melt extrusion [111]. However, extrusion and wet spinning techniques are only able to produce fiber diameters as low as 28 μm [105-107].

1.5.3 Electrospinning

Electrospinning is a common method for fabricating fibrous meshes and can be performed both in the melt [108] or in solution [109]. This process involves the use of an electric field to eject a charged polymer fiber from a syringe, and then deposit it randomly onto a grounded target. Electrospun fibers have been produced with diameters of 100 nm to 7 μm [108, 112-114]. The range of fibers that can be produced through electrospinning include the upper range of collagen fibril diameters found in ligament ECM (i.e. 150 nm) [10, 15] and includes the range of feature sizes, 200 nm to 5 μm , known to induce contact guidance [85, 115, 116]. With electrospinning, the fiber diameter can be controlled by varying electrical potential, throw distance (i.e. the distance between the tip of the needle and the target), needle diameter, and solution concentration [108, 112, 113, 117, 118].

Electrospun fibers can be macroscopically oriented by electrospinning onto a rotating drum [119] or disc [120], between two grounded rods [121], or by subsequently stretching the resultant mesh [122]. A diagram of a common electrospinning system with a rotating drum is shown below (**Figure 1.5**). In this system, the polymer deposits on the grounded drum as it rotates. The degree of macroscale fiber orientation can be increased by increasing the speed of the rotating drum.

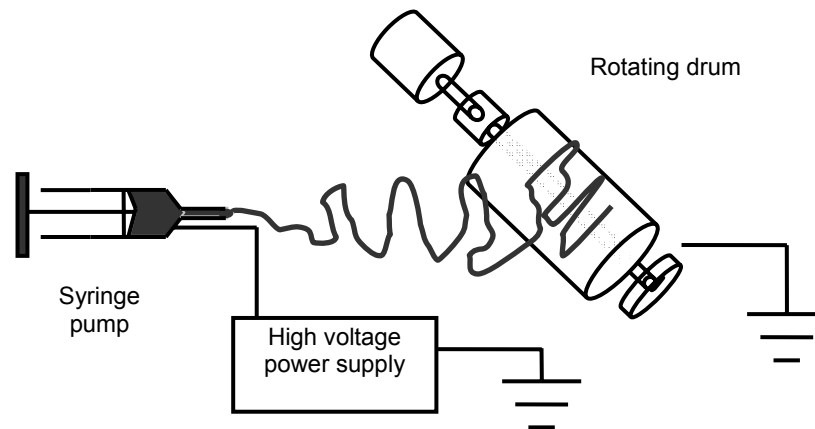


Fig. 1.5. Diagram of an electrospinning system.

Mesh thickness is primarily controlled by the length of time that the polymer is electrospun, and typically ranges from 140 μm to 0.5 mm [88, 118, 123]. Thicker scaffolds can be produced, but the formation of very thick scaffolds by electrospinning is not practical, as a

thickness of approximately 1 mm requires hours of electrospinning [98]. The primary three dimensional structure that has been produced with electrospinning is a tube. This is produced by electrospinning on a mandrel and then sliding the mesh off the mandrel [124]. Multiple layers have also been electrospun in sequence to produce a tube with layers of different composition [102]. This technique has been used for nerve regeneration [125] and vascular grafts [114, 126].

Electrospun meshes have porosities of 56 to 93% [118, 127-129], and Kwon et al. showed that the porosity of electrospun meshes increases with increasing fiber diameter [118]. Even though electrospun meshes have a high porosity, the effective pore diameters for electrospinning, assuming circular pores, is typically smaller than 10 μm [10, 130]. These effective pore diameters appear to geometrically restrict cell infiltration because the width of the cells is approximately 10 μm [87]. Electrospinning heterogeneous a mesh is one technique that has been used to increase cell infiltration [131].

Most electrospinning research has focused on electrospinning one polymer, but multiple polymers can be electrospun simultaneously to produce heterogeneous meshes. For example, Gupta et al. electrospun two polymers from separate syringes that mixed at the tip of the needle to produce a polymer blend in the fibers [132]. This technique enables the production of polymer blends using two different solvents. Alternatively, Zhao et al. was able to create a fiber consisting of a PCL core coated by a gelatin shell [133]. In this system, the electrospinning solutions were added to concentric tubes with the gelatin solution on the outside [133]. These solutions come in contact at the tip of the needle similar to the system used by Gupta et al. Finally, two polymers may be electrospun separately and deposited on the same target to form an integrated, heterogeneous mesh [124, 134-136]. Fiber-fiber repulsion from the positively charged individual fibers makes integration of the different fibers a challenge, but Kidoaki et al. was able to achieve better integration by moving the target in the transverse direction during electrospinning instead of keeping it stationary [124].

Simultaneous electrospinning has been used in recent research by Baker et al. to produce a gradient of co-electrospun components PCL and poly (ethylene oxide) (PEO) with the goal of increasing cell infiltration into the mesh. The sacrificial PEO fibers dissolve in aqueous media to effectively open larger pore diameters [131]. MSC penetration was increased into the meshes with 50% or greater PEO, but as a result, the mechanical properties of the mesh were significantly reduced. One other technique that has been used to increase cell penetration is to

add salt crystals during the electrospinning process – that are subsequently dissolved – and make larger pores than with traditional one component electrospinning [137]. These larger pores were able to increase the infiltration of cells into an electrospun mesh [137].

Many different polymers, both natural and synthetic [132, 138], have been electrospun for tissue engineering applications. Natural polymers include collagen [98, 127, 139, 140], elastin [98, 139], tropo-elastin [98], gelatin [98, 141], and silk [1]. Synthetic polymers that have been electrospun for tissue engineering including PGA [122, 142], PCL [143], poly (L-lactide-*co*-epsilon-caprolactone) copolymer [138], and PLGA [144].

1.6 Cell differentiation with stretch

The expression of ECM components and phenotypic markers has been shown to be induced by stretch [49]. This includes the induction of the selective ligament marker scleraxis in MSCs in response to uniaxial cyclic stretch [81]. However, MSC expression of markers of several different types of musculoskeletal tissue (e.g. bone and cartilage) has also been found to be induced by the application of mechanical stretch, indicating that other factors are important in determining how the cells differentiate [145, 146]. For example, Altman et al. found that only ligament markers – and not the cartilage marker collagen type II or the bone marker bone sialoprotein – were induced in BMSCs by stretch. In contrast, Haasper et al. showed that transcription factors Runx2 and FosB (which promote osteoblastic differentiation) were induced by a combination of mechanical stretch and osteogenic media [145], and Sumanasinghe et al. found that the osteogenic growth factor bone morphogenic protein-2 (BMP-2) was induced by stretch in BMSCs without the addition of osteogenic supplements to the media [146]. These studies indicate that the differentiation of BMSCs into different phenotypes cannot always be explained by the addition of growth factors. The scaffold that the cells attach to and the stretch parameters (e.g. frequency, duration, and magnitude of strain) have also been shown to affect the cell differentiation.

1.6.1 Effect of the Scaffold

Mechanical stretch has been performed with several different types of scaffolds – including smooth and micro-grooved poly(dimethyl-siloxane) (PDMS) surfaces [84], collagen hydrogels [49], and large diameter fibers [50]. The scaffold has been shown to guide the

orientation of the cells through contact guidance, and the cells have been shown to remain oriented after stretch is applied. This phenomenon is important because oriented cells will deposit oriented ECM [84, 147, 148], and oriented ECM has a higher tensile strength than unoriented ECM (e.g. scar tissue) [83]. Aligned tissue does exhibit anisotropic properties (e.g. higher tensile strength in the direction of orientation), so the directions of alignment of the ECM and the biodegradable scaffold should be the same for ligament tissue engineering applications.

Many mechanical stretch studies have been performed on smooth surfaces where mechanical stretch in the absence of topographic cues has been shown to orient cells perpendicular to the direction of stretch [75, 149]. This is thought to be an avoidance reaction to the stretching of the cell cytoskeleton by focal adhesion contacts [75]. The degree of re-alignment of the cells may be an indication of how much the cells are stimulated, because it has been shown that the alignment of fibroblasts increased with increasing magnitudes of strain from 0 to 12% [75]. Importantly, the topographic cues presented by parallel grooves have been shown to keep cells oriented parallel to the direction of the stretch if the surfaces are stretched parallel to the alignment of the grooves [3, 78, 119]. This produces an alignment similar to that exhibited in fibroblasts in natural ligament [19]. Cells have also been shown to remain oriented in the direction of microgrooves even if the grooves were at a 45 or 90° angle to the direction of stretch [78], indicating that the topographic cues override the mechanism of cellular reorientation in response to stretch. Lee et al. observed a similar response on aligned electrospun surfaces with human ACL fibroblasts that remained oriented in the direction of fiber alignment [3]. However, the effect of different surfaces on cell differentiation with stretch is not as well understood.

Mechanically stretching fibroblasts on different surfaces can affect the morphology of the cells [3], and consequently may influence the cell phenotype (see section 1.4.1) [21]. However, little is understood about the effects of the combination of stretch and different surfaces on gene expression and protein synthesis. Differences in gene expression between smooth surfaces and electrospun meshes with the application of cyclic stretch is expected because these differences have been shown previously in static culture [150]. In addition, the orientation of the fibers appears to affect differentiation, with human ACL fibroblasts depositing more total collagen when the fibers are oriented instead of random [3]. An increase in α -smooth muscle actin expression also occurred when the microgrooves were parallel compared to perpendicular to the direction of stretch [78]. Combined with the application of stretch, differences in the mechanical

properties of the surfaces may also affect gene expression by the cells attached to them, as they have been shown to have an effect in static culture [18, 86, 151].

1.6.2 Effect of Stretch Parameters

Gene expression and orientation of MSCs and ligament fibroblasts can be affected by the cyclic stretch parameters, including (1) magnitude of strain, (2) duration, and (3) frequency. First, increasing the magnitude of strain induces a corresponding increase in collagen type I mRNA expression of ACL fibroblasts on microgrooved surfaces [4]. In addition, an increased deposition or maturation of ECM by fibroblasts was inferred through an increase in modulus of a construct [50]. However, in one study the expression of collagen type I by MSCs was found to be independent of the magnitude of strain (2 and 8%) even though the expression of other genes was dependant. These results indicate that cell response to strain magnitudes between 0 and 8% is complex. Importantly, strains above a certain level have been shown to increase the rate of cell apoptosis [4, 75], and lower strains that do not cause apoptosis can still lead to inflammation (e.g. induction of cyclooxygenase-2 (COX-2) and prostoglandin) [152]. Second, increasing the duration of stretch has been shown to increase the expression of collagen type I, collagen type III, and tenacin-C by MSCs [49, 81, 145, 153]. This dependence was shown with both continuously and intermittently stretching the samples [81, 153]. Third, increasing the frequency from 0.1 to 0.5 Hz increased mRNA expression of collagen type I but decreased the expression of collagen type III [154]. However, the effect of frequency has been shown to have less affect than the strain magnitude on cell alignment [155]. Wang et al. found that endothelial cell realignment on smooth silicone surfaces was more dependant on strain magnitude (5% to 10%) than strain rate (5%/s to 10%/s). The cells were also found to exhibit significant alignment even without cyclically stretching using a static strain of 10% [155].

1.7 Interaction between Cells and the Biomaterial

Cell attachment, spreading, and orientation are affected by the surface chemistry, mechanical properties, and topology of the biomaterial. In turn, cell alignment and spreading on a surface can affect other cell functions, including cell proliferation and ECM deposition through biochemical signaling pathways [156]. One important signaling pathway involves focal adhesions (i.e. the points where the cell anchors to the biomaterial).

1.7.1 Cell Attachment and Spreading

Cell attachment to ECM proteins – either adsorbed onto a synthetic biomaterial surface or present in a natural biomaterial – is mediated through integrin adhesion receptors. These receptors consist of α and β subunits. At least 18 α and 8 β subunits have been found in at least 24 different dimer combinations [18]. Common pairings include $\alpha_5\beta_1$ that attaches to fibronectin, $\alpha_v\beta_1$ that attaches to fibronectin and vitronectin, and $\alpha_6\beta_1$ that attaches to laminin [22]. The integrins are transmembrane proteins, and the outer section of the β subunit recognizes one or more binding sites on ECM proteins [18]. After binding, the β subunits mediate “outside in” signaling to recruit more integrins to the adhesion site. The β subunits also recruit both structural and regulatory proteins in the cytoplasm to form a focal adhesion plaque (**Figure 1.6**). Structural proteins in these focal adhesions (e.g. talin and α -actinin) bind with β integrin subunits and hold focal the adhesion together [18]. Vinculin, another structural protein found in focal adhesions, binds to actin and enables force transduction from the focal adhesion to the actin cytoskeleton. Regulatory proteins at a focal adhesion include focal adhesion kinase (FAK), paxillin, Src, and members of the Rho and Ras families [18], most of which are phospho-kinases that are involved in cell signaling pathways. FAK and Src regulate the formation of focal adhesion plaques, while Rho and Ras can initiate mitogen-activated kinase (MAPK) signaling pathways that lead the mRNA expression [28, 157]. Rho and Ras, specifically, are involved in actin assembly and the generation of cellular contractile forces [46]. Another member of the Rho family of GTPases, Cdc42, has been shown in fibroblasts to trigger the formation of filipodia that are involved in cell spreading [46].

Forces exerted on the focal adhesion plaque have been shown to the initiate MAPK pathways (**Figure 1.6**) [18, 28, 157], and this is one mechanism that induces cellular expression of ligament-like ECM proteins. A simplified description of these pathways is that kinases (e.g. Ras) are activated and lead to the phosphorylation of MAPKs (e.g. extra-cellular regulated kinase (ERK)). The MAPKs eventually activate transcription factors, such as activator protein-1 (AP-1) leading to gene expression. Cell migration, cytoskeletal reorganization, and changes in gene expression can occur after this intercellular signaling [85].

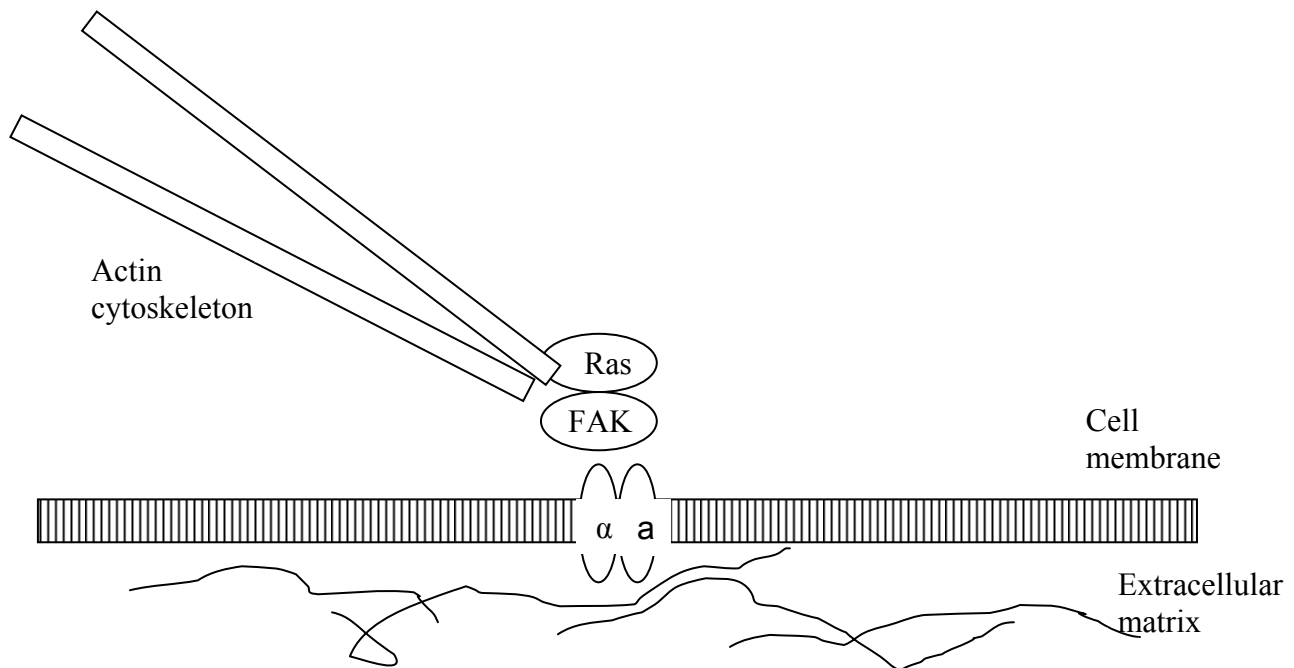


Fig. 1.6. Illustration of cell adhesion through integrin receptors and the resulting focal adhesion plaque (adapted from Goldstein [18]).

1.7.2 Surface Chemistry

Cell spreading is affected by both specific attachment sites (i.e. recognized amino acid sequences) on the surface and differences in surface chemistry. Modifying a substrate with specific attachment sites or adsorbing natural ECM proteins on a surface is commonly used to increase integrin-mediated cell adhesion. Surfaces have been frequently modified with the arginine-glycine-aspartic acid (RGD) sequence that is recognized by several integrin receptors and is sufficient to promote cell adhesion [18]. Patterning a surface with the RGD sequence has been shown to control cell shape and proliferation [18]. For example, Lauer et al. produced micrometer scale adhesive regions using RGD sequences to control the orientation of neuronal cells [158]. Other sequences that have been studied include tyrosine-isoleucine-glycine-serine-arginine (YIGSR) [159] and isoleucine-lysine-valine-alanine-valine (IKVAV) [160] that are the integrin binding sites on laminin.

Non-specific surface chemistry has also been shown to affect cell adhesion. Hydrophilic surfaces promote cell attachment and spreading through increased serum protein deposition. Hydrophobic materials such as poly-ethylene glycol prevent protein deposition and consequently

cell attachment [161]. Further, terminal amine and carboxylic acid groups on surfaces have been shown to produce less protein denaturation than hydrophobic methyl groups [162].

1.7.3 Surface Compliance

Surface compliance can affect cell alignment, spreading, and migration because fibroblastic cells maintain forces that can deform compliant surfaces. These forces are maintained in the actin cytoskeleton through non-muscle myosin. Cells exert traction forces on the surface through the formation of hundreds of focal adhesions. The tension on the actin stress fibers increases as the cells spread [86]. Different cell types exert very different tensile forces. For example, forces from fully developed focal adhesions of cardiac fibroblasts are between 10 to 30 nN, and the overall force is in the μN range [86]. In comparison, canine kidney cells have been shown to exert forces ranging from 20 to 230 nN in total on a surface [163]. The cellular traction forces exerted by fibroblasts have been shown to deform silicone rubbers [86, 151]. The cells become rounded and less spread after contracting the surface. In addition, a reduction in level of cell spreading – with a corresponding reduction of tension on the integrin attachments – has been shown to induce a decrease in the expression of α -smooth muscle actin by contractile fibroblasts [25, 68]. This suggests that fibroblastic differentiation may be reduced on compliant surfaces.

1.7.4 Surface Topography

Oriented surface features have been shown to affect cell spreading and alignment. This phenomenon was first called contact guidance in 1945 when cells were found to align with fibrin [164]. Recently, studies have been primarily performed on model microgrooved surfaces [85, 165]. Several types of cells (e.g. macrophages, fibroblasts, and neurons) have been aligned on a variety of surfaces including silicones, polymethylmethacrylates, and metals [85] – indicating that contact guidance is a generalized cell phenomenon. Further, when cells are oriented through contact guidance they are able to deposit an oriented ECM [121, 147, 148]. On microgrooved surfaces the groove width and depth of the grooved surfaces are two parameters that have been shown to affect cell spreading and orientation. For ridges and grooves of equal widths from 2 to 10 μm , fibroblast orientation was found to increase with decreasing width [115, 166], and the time required for cells to orient was significantly decreased for the smallest 1 μm repeating

groove compared to the other conditions [167]. These results suggest that the smaller features have more affect on cell alignment. Nanoscale grooves have also been shown to orient neural cells [168, 169]. Surface features of 100 nm were too small for axons to sense; however, neuron orientation was guided by surface features 200 nm and larger [168, 169]. Cells for ligament tissue engineering (i.e. ligament fibroblasts and MSCs) may also align best on a surface with an ideal feature size.

Two different cellular mechanisms for cell alignment on grooved surfaces have been proposed. First, cells may orient because of the geometry of the focal adhesion plaque which requires a minimum width of 2 μm to establish adhesion [166, 170]. With this hypothesis, fewer orientations of the focal adhesion become possible as the groove width decreases, leading to more oriented cells. Second, cells will seek a biomechanical equilibrium with the net sum of forces minimized [166, 171]. This equilibrium may not occur if the cell crosses the groove gaps, so this would favor cell alignment.

Fibrous meshes have also been shown to induce contact guidance [58, 98, 123], but these surfaces differ from grooved surfaces in several respects. First, unlike the precise orientation of grooved surfaces, fiber alignment can vary throughout the mesh. Second, the fibers provide a rounded surface for cell attachment, unlike the straight walls on grooved surfaces. Third, electrospun meshes have thin fibers that can be more easily deformed by cellular traction forces. For contact guidance on fibrous meshes, fiber diameter and fiber alignment are the two parameters that control cell attachment and spreading. For fiber diameter, MC3T3-E1 osteoblasts have been found to exhibit greater cell aspect ratio on 2.1 μm diameter fibers instead of 0.14 μm diameter fibers [58]. For fiber orientation, oriented poly (D,L-lactic-co-glycolic acid) PLGA fibrous scaffolds have been shown to orient NIH 3T3 fibroblasts [82] and PLLA scaffolds have been shown to orient neural stem cells [120].

Cell orientation and spreading through contact guidance is important in ligament tissue engineering. First, cell spreading is required for cell proliferation in anchorage dependant cells [172, 173]. Second, increases in cell orientation can affect ECM deposition, as Lee et al. found that collagen expression for human ligament fibroblasts was higher on fibers with alignment than on randomly oriented meshes [3].

1.8 Experimental Plan

The overall goal of this project was to develop a tissue engineered approach to produce a ligament graft. Cells should exhibit the ligament phenotype and deposit organized fibril-forming ECM that is necessary for ligament tissue growth and maturation. With this in mind, three complimentary tasks were performed: (1) determining scaffold topographies that induce cell orientation and ligament-like phenotype in cells, (2) determining bioreactor conditions that stimulate the expression of ECM mRNA in oriented cells, and (3) developing an approach to produce more clinically relevant constructs.

The first task was to determine a range of fiber diameters and fiber alignments that induce cell orientation and stimulate ECM deposition (Chapters 2 and 3). To accomplish this, a series of fiber meshes with different fiber diameters and fiber alignments were prepared and seeded with fibroblasts and mesenchymal progenitor cells. Projected area, aspect ratio, cell number, and mRNA expression of ligament-like markers were measured. The mechanical properties of unsupported meshes with different fiber diameters and orientations were also determined (Chapter 4).

The second task was to determine the effect of mechanical stretch on cell orientation and differentiation by cyclically stretching cell seeded electrospun fibers (Chapter 5). To accomplish this, a mechanical stretch bioreactor was designed and constructed. Mesenchymal progenitor cells were seeded on electrospun scaffolds and either static or cyclic stretch was applied. Projected cell area, aspect ratio, orientation, and mRNA expression of ligament-like markers were measured on the surfaces after applying stretch.

The third task was to develop a simultaneous electrospinning (i.e. co-electrospinning) technique for the purpose of improving cell infiltration (Chapter 6). Co-electrospinning of enzymatically degradable gelatin and slowly hydrolysable PEUUR was performed. Next, the scaffolds were embedded with a hydrolytically degradable poly (ethylene glycol – diacrylate) (PEG-DA) hydrogel and processed into a three dimensional construct.

The conclusions from these studies and their contributions to the field of ligament tissue engineering are described at the end of the document (Chapter 7). The results summarized there demonstrate the feasibility of the tissue engineering strategy for ligament repair. The results also demonstrate three important areas of further research that are then described (Chapter 7).

1.9 Material within Appendices

Studies performed that are not closely linked to the overall goal of this dissertation are included in the appendices. These include studies on the effect of electrospun meshes of different diameters and orientation on neural cells (Appendix A), and the effect of electrically conductive fibers on neural cells (Appendix B). Appendix C contains a mathematical model of the mechanical property of three-dimensional electrospun meshes based on topographic and mechanical properties of the PEUUR meshes used in this research project. Finally, ImagePro computer macros for taking and working with fluorescent images are included (Appendix D). While these appendices are not closely linked to ligament tissue engineering, they contribute to other fields of tissue engineering.

Chapter 2: Effect of Fiber Diameter and Orientation on Fibroblast Morphology and Proliferation on Electrospun Poly (D,L-lactic-co-glycolic acid) Meshes

Chris A. Bashur¹, Linda A. Dahlgren^{2,3}, Aaron S. Goldstein^{1,2}

¹Department of Chemical Engineering and
²School of Biomedical Engineering and Sciences,
Virginia Polytechnic Institute and State University
Blacksburg, VA 24061

³Department of Large Animal Clinical Sciences,
Virginia-Maryland Regional College of Veterinary Medicine
Blacksburg, VA 24061

Abstract

Engineered ligament tissues are promising materials for the repair of tears and ruptures, but require the development of biomaterial scaffolds that not only support physiologically relevant loads, but also possess architectures capable of orienting cell adhesion and extracellular matrix deposition. Based on evidence that micron-scale topographic features induce cell orientation through a contact guidance phenomenon, we postulate that oriented micron-scale fiber meshes – formed by the electrospinning process – can regulate cell morphology. To test this, fused fiber meshes of poly (D,L-lactic-co-glycolic acid) (PLGA) were electrospun onto rigid supports under conditions that produced mean fiber diameters of 0.14 – 3.6 μm , and angular standard deviations of 31 – 60°. Analysis of the morphology of adherent NIH 3T3 fibroblasts indicated that projected cell area and aspect ratio increased systematically with both increasing fiber diameter and degree of fiber orientation. Importantly, cell morphology on 3.6 μm fibers was similar to that on spincoated PLGA films. Finally, cell densities on electrospun meshes were not significantly different from spincoated PLGA, indicating that cell proliferation is not sensitive to fiber diameter or orientation.

2.1 Introduction

The anterior cruciate ligament (ACL) is the most commonly injured ligament in the knee, and – due to limited vascularization and poor clotting ability that hinder healing [8] – more than 100,000 surgeries are performed annually in the United States to treat tears and ruptures [7]. Currently autologous transplant of patellar or hamstring tendons [13] or allogeneic transplant of cadaveric tissue [16] are the only surgical options for ACL replacement. However, the former involves additional injury to the patient and risks donor site morbidity [15, 20], while the latter risks disease transmission [16] and inflammatory responses that undermine healing [174]. Currently, synthetics are not used for ACL replacement as they have success rates of 30–60%, and fail due to flexural and rotational fatigue and creep [20].

A potential alternative material for ACL replacement is an engineered ligament tissue, which may be formed by culturing cells within a fibrous scaffold [1, 2] under the appropriate combination of biochemical [48, 175] and mechanical conditions [4, 77] to induce synthesis of a ligament-like extracellular matrix (ECM) containing oriented collagen fibrils. Central to this strategy is achievement of an oriented ECM because poor mechanical properties of healed ligament tissue are associated with a disorganized ECM [83]. Therefore, within this approach the biomaterial scaffold should not only provide extensive surface area for cell attachment and matrix deposition, but should induce cell orientation. Cell orientation then will guide the formation of an oriented ECM [84, 147, 148].

One strategy for achieving cell orientation is through the use of contact guidance, a phenomenon by which topographical features of the biomaterial substratum regulate the spatial distribution of adhesive contacts and the direction of cell spreading [165, 176]. Model studies on micropatterned substrates have shown that parallel microgrooves with feature sizes of 1–5 microns can orient multiple cell types [4, 115, 177-179], while submicron grooves orient axonal outgrowth of neurons [168]. However, the extension of this phenomenon from a model two-dimensional system to a three-dimensional scaffold suitable for tissue engineering has been limited.

Recently, electrospinning has gained momentum as a method for fabricating porous biomaterial scaffolds. This process involves the use of an electric field to eject a polymer fiber from solution to a grounded target. The fiber deposits randomly to form a fused fiber mesh, and fiber diameter can be controlled over a range from 100 nm to 5 μm by varying electrical

potential, throw distance, needle diameter, and solution concentration [108, 112, 113]. Importantly, the range of fiber diameters that can be achieved are two to three orders of magnitude smaller than those formed by conventional extrusion [105] and wet spinning [106] processes, and includes the range of feature sizes known to induce contact guidance. In addition, fiber orientation can be induced by electrospinning onto a rotating disc [120], drum [119], between two grounded rods [121], or by stretching the resultant mesh [122].

The objective of this study was to determine how diameter and orientation of electrospun poly (D,L-lactic-*co*-glycolic acid) (PLGA) fibers affect morphology, orientation, and proliferation of NIH 3T3 fibroblasts. Fiber diameter was systematically varied from 140 nm to 3.6 μm and fiber orientation was introduced by electrospinning onto a drum rotating at surface velocities of 1.9, 3.3, and 4.7 m/s. Cell proliferation was inferred from measurements of cell number at 3, 7, and 14 days of culture, and projected cell area, aspect ratio, and length and angle of the long axis were measured at 2 days of culture from fluorescent cell images.

2.2 Materials and Methods

2.2.1 Materials

All materials were purchased from Fisher Scientific (Pittsburgh, PA), all chemicals were purchased from Sigma-Aldrich (St. Louis, MO), and all biological supplies were purchased from Invitrogen (Gaithersburg, MD) unless otherwise noted. The 75/25 PLGA (inherent viscosity 0.55–0.75 dL/g) was purchased from Lactel Biodegradable Polymers (Birmingham, AL), and dichloromethane was purchased from Burdick and Jackson (Muskegon, MI).

2.2.2 Electrospinning

PLGA was electrospun onto 18 mm circular glass coverslips to form fused fiber meshes with controlled fiber diameters and degrees of fiber orientation as described previously [58]. Briefly, glass coverslips were sonicated in ethanol and allowed to air dry. Next, a 0.30 mL volume of a 3.5 wt% solution of PLGA in dichloromethane was spincoated onto the glass at 2500 rpm for 30 s to form a smooth polymer film. Films were allowed to dry in a vacuum oven at 50°C for two days. To form meshes comprised of randomly oriented fibers, the PLGA-coated coverslips were mounted onto a stationary target and PLGA was electrospun under ambient

conditions from a syringe equipped with a 22 gauge Teflon tipped needle using a 15 kV potential, a throw distance of 15 cm, and a syringe flow rate of 5 mL/h. PLGA concentrations of 5, 11, and 16 wt% in 1,1,1,3,3,3-hexafluoro-2-propanol (HFIP) were used to produce meshes with different fiber diameters. To form meshes comprised of oriented fibers, coverslips were mounted onto a 6.2 cm diameter wire mesh drum and electrospun under identical conditions except that a throw distance of 12 cm was used. The drum was rotated at 580, 1010, and 1450 rpm (corresponding to surface velocities of 1.9, 3.3, and 4.7 m/s, respectively) to achieve different degrees of fiber orientation. All meshes were dried under vacuum for 2 days to remove residual HFIP.

For cell culture studies electrospun meshes and spincoated films (controls) were placed into 12-well plates, sterilized by overnight exposure to UV light, and incubated for 1 h at room temperature with 2 mL of a 1 µg/mL solution of fibronectin in phosphate buffered saline (PBS).

2.2.3 Cell Culture and Cell Seeding

Cell studies were performed using NIH 3T3 fibroblasts. Cells were maintained in Dulbecco's Modified Eagle's Medium (DMEM) with 10% fetal bovine serum (FBS Gemini, Calabasas, CA) and 1% antibiotic/antimycotic in a 37°C and 5% CO₂ incubator, lifted every 3 or 4 days with trypsin/EDTA, and replated at a density of 1.5 x 10⁵ cells per 100 mm Petri dish. Cells were seeded onto meshes, spincoated (control) surfaces, and tissue culture polystyrene (TCPS) well bottoms at a density of 2.5×10⁴ cells/well (6.6×10³ cells/cm²), and maintained in 2 mL of medium. Medium was replaced twice weekly. Cells were analyzed 2 days after seeding to characterize cell morphology, and 3, 7, and 14 days after seeding to determine cell number.

2.2.4 Scanning Electron Microscopy (SEM)

The diameter and degree of orientation of the electrospun fibers were determined by analysis of SEM images. Briefly, electrospun meshes were mounted onto studs and sputtercoated with a 10 nm layer of palladium (Model 208HR, Cressington Scientific Instruments, Cranberry Township, PA). Images were acquired using a LEO 1550 Field Emission SEM (Carl Zeiss SMT, Thornwood, NY) operating at 5kV with a 16 mm working distance. Resultant images were imported into ImagePro Plus software (ICube, Crofton, MD) for analysis of fiber diameter and fiber orientation. Fiber diameter and angle of orientation (relative to the

vertical axis of the image) was determined manually. The degree of orientation was characterized by the angular standard deviation, σ , for a wrapped normal distribution:

$$f(\theta) = \frac{1}{\pi} \left(1 + 2 \sum_{p=1}^{\infty} \rho^{p^2} \cos(2p(\theta - \mu)) \right) \quad (2.1)$$

Here, the probability distribution function has been adapted from Fisher [180] for a periodicity of π radians, where μ is the mean angle and ρ is the mean resultant length. These parameters were determined from a set of n measured fiber orientations, θ_i , by the following equations:

$$\rho = \frac{1}{n} \sqrt{\left(\sum_{i=1}^n \cos 2\theta_i \right)^2 + \left(\sum_{i=1}^n \sin 2\theta_i \right)^2} \quad (2.2)$$

$$\mu = \tan^{-1} \left(\frac{\sum_{i=1}^n \sin 2\theta_i}{\sum_{i=1}^n \cos 2\theta_i} \right) \quad (2.3)$$

Finally, the angular standard deviation was calculated from the mean resultant length:

$$\sigma = \frac{1}{2} \sqrt{-2 \ln \rho} \quad (2.4)$$

2.2.5 Cell Morphology

Cell morphology was determined by image analysis of calcein-stained cells. Briefly, calcein-AM (1 mg/mL in dimethyl sulfoxide, Molecular Probes, Eugene, OR) was added to a concentration of 0.5 μ g/mL in medium and allowed to incubate at 37°C for 30 min. The coverslips were washed twice with 2 mL PBS, and then 2 mL minimal essential medium, α modification (α -MEM), without phenol red was added to each well. Images were obtained at 60 \times with a wide blue filter using an Olympus IX50 fluorescence microscope (Opelco, Sterling,

VA) equipped with a cooled CCD camera (Hamamatsu C4742-98-12NRB). The images were then imported into ImagePro and the cell outline was determined using a variance edge detection algorithm. From this outline the projected cell area, aspect ratio, length, and angle of cell orientation were measured. Aspect ratio, length, and angle were calculated using an ellipse equivalent of the cell (i.e, an ellipse with the same area, first and second degree moments as the cell). Length and angle were calculated from the major axis, and aspect ratio was calculated as the ratio of major to minor axes of the ellipse equivalent. Morphological analysis was limited to isolated cells; cells in physical contact with one another were not examined.

2.2.6 Cell Number

After 3, 7, and 14 days cell number was determined using Hoechst 33258 (Sigma-Aldrich St. Louis, MO) to fluorescently label DNA as described in detail elsewhere [58].

2.2.7 Statistical Analysis

Results are presented as mean \pm standard deviation for $n \geq 200$ fibers , $n \geq 25$ cells for morphology, and $n = 4$ substrates for cell number. Studies were replicated to ensure experimental reproducibility of trends. Statistical significance was determined in SAS 9.1 (SAS Institute Inc. Cary NC) using a one-way analysis of variance (ANOVA) and Fisher's protected least significant difference with a significance criterion of $p \leq 0.05$.

2.3 Results

2.3.1 Electrospun Fiber Architecture

PLGA was electrospun onto a stationary screen at solution concentrations of 5, 11, and 16 wt% to produce meshes with varying fiber diameters (**Figure 2.1**). Fibers appear to be smooth and regular; however, bead formation occasionally was noted at the lowest concentration. Quantitative analysis indicated fiber diameters of 0.14 ± 0.07 , 0.76 ± 0.36 , and $3.6 \pm 0.6 \mu\text{m}$ for concentrations of 5, 11, and 16 wt%, respectively.

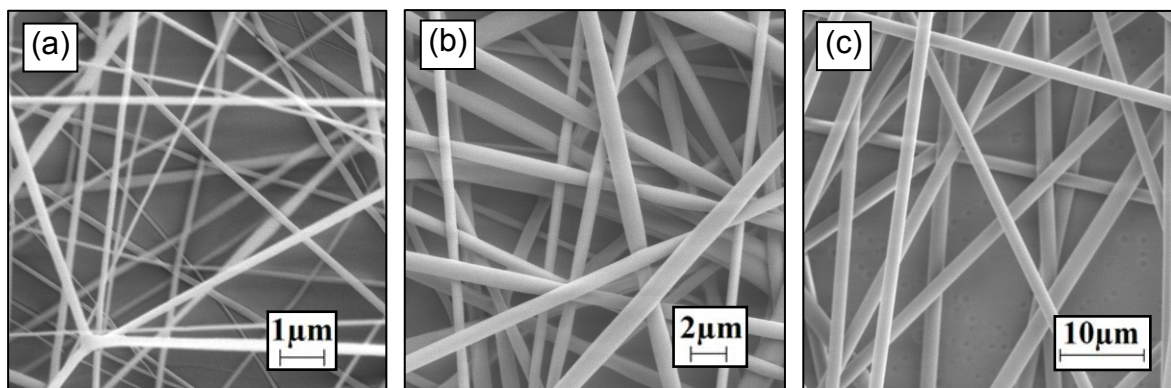


Fig.2.1. SEM images of PLGA fibers electrospun from different solution concentrations: (a) 5 wt, (b) 11 wt%, and (c) 16 wt%.

Fiber meshes with different degrees of orientation were produced by electrospinning 5 and 11 wt% solutions onto a barrel rotating at rates of 580, 1010 and 1450 rpm (corresponding to linear velocities of 1.9, 3.3, and 4.7 m/s, respectively). Representative SEM images for the 11 wt% solution (**Figure 2.2**) show increased fiber orientation when PLGA was electrospun onto a rotating drum at rates of 1010 and 1450 rpm. Histograms for orientation of fibers electrospun from the 5 wt% solution (**Figure 2.3**) indicate a close agreement between fiber distribution (bars) and the wrapped normal distribution function (curve). At the lowest rate of rotation, the degree of fiber orientation – characterized as the angular standard deviation (Eq. 4) – did not differ from that for the stationary target (**Table 2.1**). In contrast, the angular standard deviation was markedly lower at the higher rotational rates. Concurrently, fiber diameter systematically decreased from 0.76 to 0.52 μm with increasing rotational rate for PLGA electrospun from 11 wt% solutions. However, this effect was not observed with 5 wt% solutions.

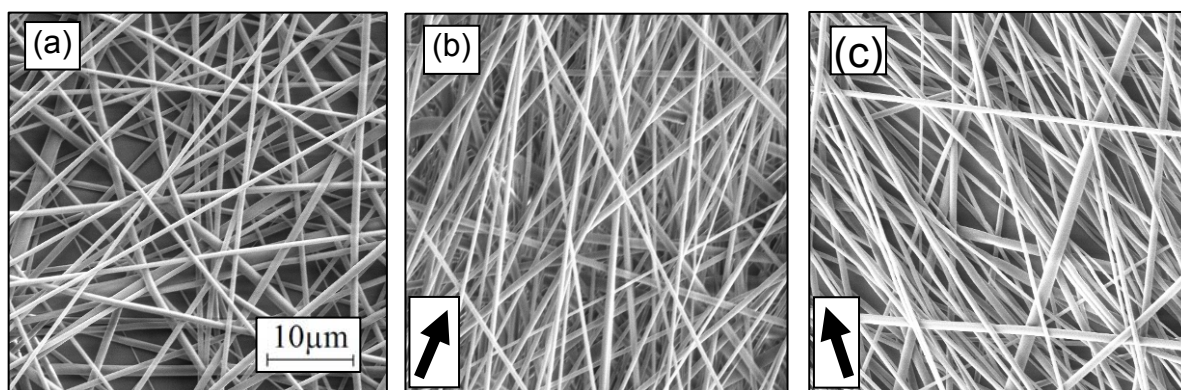


Fig. 2.2. SEM images of PLGA fibers electrospun from 11 wt% solutions onto moving target: (a) stationary target, (b) 1010 rpm, and (c) 1450 rpm. Arrows corresponds to the average orientation of fibers.

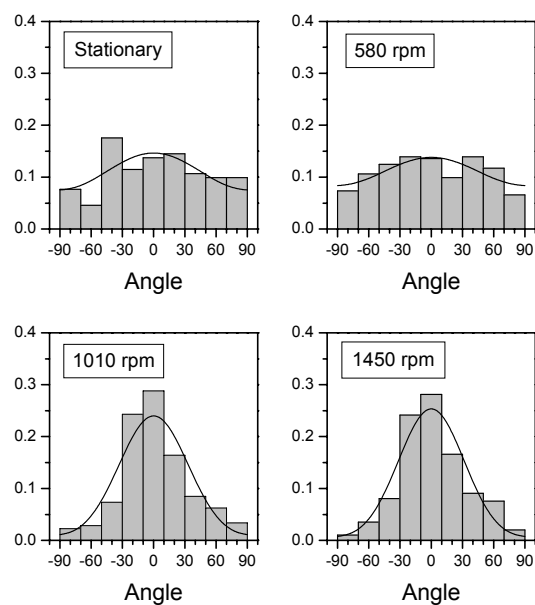


Fig. 2.3. Normalized histograms of fiber angle for the different rates of rotation: (a) stationary, (b) 580 rpm, (c) 1010 rpm, and (d) 1450 rpm. Curves correspond to the wrapped normal distributions for a given mean and angular standard deviation. Fibers were electrospun from a 5 wt% solution.

Table 2.1. Fiber diameter and angular standard deviation for PLGA electrospun from 5 and 11 wt% solutions at different rotation rates

Solution Concentration (wt%)	Speed (rpm)	Fiber angular deviation (°)	Fiber Diameter (μm)
5	stationary	59.7	0.14 ± 0.07
	580	58.6	0.13 ± 0.05
	1010	32.8	0.15 ± 0.10
	1450	31.0	0.16 ± 0.07
11	stationary	59.4	0.76 ± 0.36
	1010	36.6	0.66 ± 0.31
	1450	32.0	0.52 ± 0.22

2.3.2 Cell Morphology on Electrospun Fibers

Fluorescent images of the fibroblasts on randomly oriented fibers were acquired to determine the effect of fiber diameter on cell morphology. In general, it was noted that cell

spreading was diminished on the smaller diameter fibers (**Figure 2.4**). Quantitative analysis indicated that projected cell area, aspect ratio, and length of the long axis were significantly lower for cells on 0.14 and 0.76 μm fibers compared to cells on control surfaces (**Figure 2.5**). Projected cell area and aspect ratio were found to increase systematically with increasing fiber diameter, and fibroblast morphology on 3.6 μm was not statistically different from that on spincoated PLGA (control) surfaces.

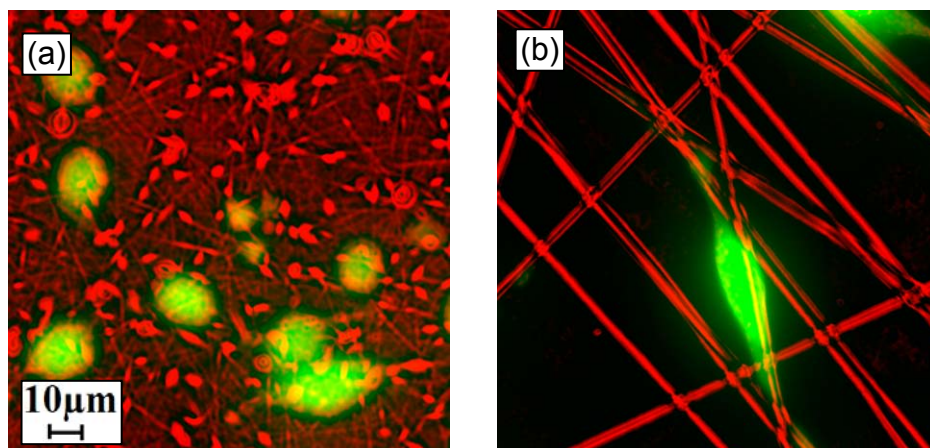


Fig. 2.4. NIH 3T3 morphology on fiber meshes with diameters of (a) $0.14 \pm 0.07 \mu\text{m}$, and (b) $3.6 \pm 0.6 \mu\text{m}$. Images were constructed by merging phase contrast (red) and fluorescence (green) images of calcein-loaded cells attached to fibers. Bead formation during the electrospinning process is evident in (a).

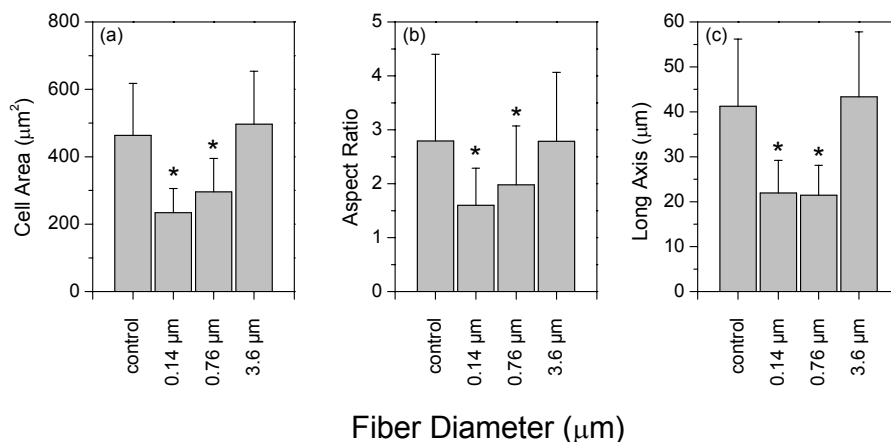


Fig. 2.5. Effect of PLGA fiber diameter on (a) projected cell area, (b) aspect ratio, and (c) length of long axis. Controls were spincoated PLGA films. Bars correspond to the mean \pm standard deviation for $n = 82, 84, 25,$ and 46 cells for spincoated surfaces, and fibers with diameters of $0.14, 0.76,$ and $3.6 \mu\text{m}$, respectively. An asterisk indicates statistical difference from control.

Analysis of cell morphology on oriented fibers formed from 11 wt% solutions showed that the projected cell area, aspect ratio, and length of the long axis increased systematically with increasing degree of fiber orientation (i.e., decreasing σ) and approached that of spincoated (control) surfaces (**Figure 2.6**). The substrates were also analyzed to determine mean orientation and angular standard deviation of the adherent cells (**Table 2.2**). In general, cells were aligned with fibers: the mean angle of the cells was within 15° of the mean angle of the fibers. Further, the angular standard deviation of the cells decreased systematically with decreasing angular standard deviation of the fibers.

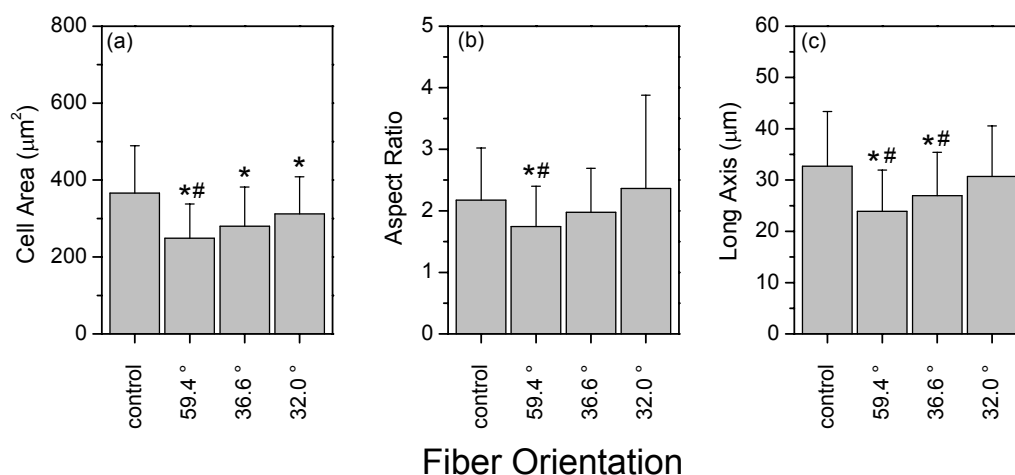


Fig. 2.6. Effect of PLGA fiber orientation on (a) projected cell area, (b) aspect ratio, and (c) length of long axis. Controls were spincoated PLGA films. Bars correspond to the mean \pm standard deviation for $n = 107, 40, 81,$ and 89 cells for spincoated surfaces, and fibers with angular standard deviations of $59.4^\circ, 36.6^\circ,$ and $32.0^\circ,$ respectively. An asterisk indicates statistical difference from control, and a pound symbol indicates statistical difference from the most oriented fibers (i.e., $\sigma = 32.0^\circ$).

Table 2.2 Angular standard deviation of cells and cell orientation relative to fibers on electrospun surfaces with different degrees of orientation.

Fiber angular deviation (°)	Cell angular deviation (°)	Mean angle (° from fibers)
No fibers	72.4	
57.7	42.5	15.2
39.6	36.1	3.5
36.7	22.1	14.6

2.3.3 Cell Density on Electrospun Fibers

Cells were cultured on electrospun PLGA fibers to determine the effects of fiber diameter and fiber orientation on cell proliferation. Analysis of cell number on randomly oriented fibers indicated that cell density increased from day 3 through day 14 in a manner insensitive to fiber diameter; all of the surfaces, including both tissue culture polystyrene and spincoated PLGA controls, had comparable cell densities (**Figure 2.7a**). The only noted exception was at day 14 for 3.6 μm fibers, which exhibited a significantly higher cell number than the spincoated control. Cell density on oriented fibers formed from 11 wt% solutions also increased with time (**Figure 2.7b**) and no statistical difference was measured for oriented fibers.

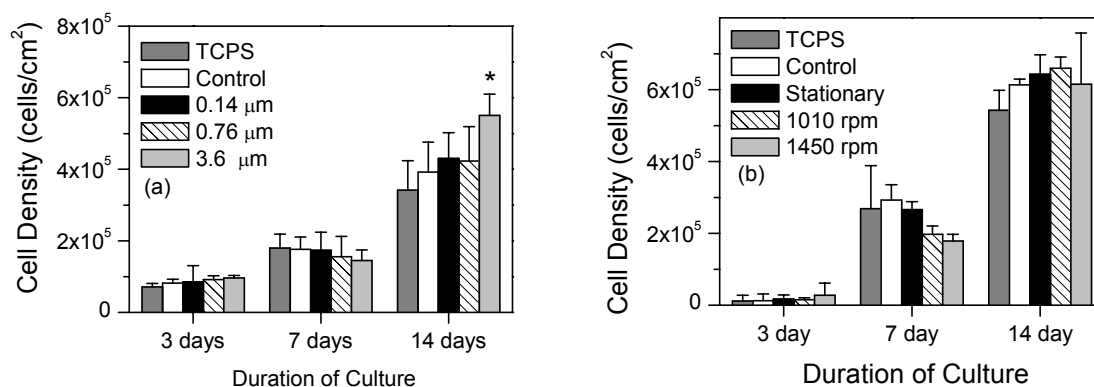


Fig. 2.7. Cell number on PLGA fibers as a function of culture duration: (a) effect of fiber diameter, and (b) effect of fiber orientation. An asterisk indicates statistically significant difference from the spincoated control group for $n = 4$ substrates.

2.4 Discussion

In this study PLGA meshes were formed with different fiber diameters (0.14 - 3.6 μm) and degrees of fiber orientation (32-60° angular standard deviation). NIH 3T3 cells adhered to and proliferated well on all surfaces, and analysis of cell morphology showed that projected cell area, aspect ratio, and the length of the long axis increased with both increasing fiber diameter and increasing fiber orientation. Finally, cells aligned with fibers and the angular standard deviation for cells decreased with decreasing angular standard deviation of fibers.

Cell morphology on randomly oriented fibers showed that cell area, aspect ratio, and the length of the long axis were sensitive to fiber diameter. In particular, all three parameters were decreased relative to smooth surfaces when fibers were less than 1 μm , but were comparable to

smooth surfaces for fiber diameters of 3.6 μm . Diminished projected cell area is consistent with Badami et al [58] who reported smaller projected areas for MC3T3-E1 pre-osteoblasts on both 0.14 and 2.1 μm fibers compared to smooth surfaces. Two plausible explanations for diminished cell spreading on sub-micron fibers are related to the role of focal adhesions complexes in mediating cell adhesion to biomaterials. Focal adhesions contain clusters of integrin transmembrane adhesion receptors – that bind the extracellular matrix proteins (e.g., fibronectin, collagen) adsorbed to the biomaterial surface – and serve as termini for the actin cytoskeleton [18]. Immunohistochemical staining for vinculin has shown that focal adhesions can be larger than 1 μm [58, 115]; consequently it is plausible that the sub-micron fibers studied here undermine cell spreading by limiting the size of focal adhesions. In addition, the density of fibronectin adsorbed to the sub-micron fibers may be less than that on larger fibers or spincoated films, which would diminish the number of integrin receptors engaged in cell adhesion.

Because adhesion and spreading of anchorage-dependent cells is a prerequisite for cell viability [181] and proliferation [182], decreased projected cell area on smaller electrospun fibers could be expected to result in lower cell densities, especially at earlier timepoints in culture. Although such an effect has been shown in previous studies [58, 118, 142], in the study presented here fibroblast cell density was not sensitive to fiber diameter; measurements at 3, 7 and 14 days indicated that cells proliferate equally well on all substrates. Such differences may be a consequence of cell type (e.g., endothelial [118], pre-osteoblastic cells [58]), suggesting that electrospun fiber scaffolds may be preferentially suited for development of particular tissues. Further, it was noted that at the latest time point cell density was greatest with the largest fiber diameter. This has been observed previously [58] and likely is a consequence of cell penetration into the fiber mesh, resulting in multilayer coverage.

When cells were cultured on oriented submicron fibers cell spreading increased with increasing fiber orientation (Figure 6). In particular this trend occurred even though fiber diameter decreased from 0.76 to 0.52 μm (Table I). This increased cell spreading has been reported both on oriented electrospun meshes [120] and on parallel microgrooved surfaces, and is consistent with a contact guidance phenomenon. Concurrently, fibroblast density was found to be insensitive to fiber orientation. This is consistent with Lee et al [3] who showed similar ligament fibroblast cell densities on both oriented and random 700 nm fibers, but differs from Xu et al [123] who reported greater densities of smooth muscle cells on oriented surfaces.

This study represents an initial effort to characterize fibroblast response to electrospun architecture, and indicates that fibroblast spreading is enhanced with both larger fibers and increased fiber orientation. However, caveats with these results indicate the need for additional studies. First, although morphological studies suggest fibroblasts prefer larger or more oriented fibers, phenotypic analyses (e.g., deposition and organization of type I collagen) are required to evaluate the suitability of fiber mesh architectures for ligament tissue engineering. Second, because the model cells used in this study are not suitable for clinical application, future studies will require the testing of primary cells derived from tissue explants, perhaps including progenitor cells (e.g., bone marrow stromal cells [48]). Third, electrospinning of meshes thicker than 100 μm is time-consuming and difficult. Consequently, methods must be developed to process thin electrospun sheets into considerably thicker scaffolds. Fourth, although PLGA is a well-characterized, biocompatible, resorbable material used in many tissue engineering applications, its tendency to deform plastically under applied strains undermines its suitability for ligament tissue engineering. Degradable elastomeric materials, such as poly(ester urethane)ureas [88] and poly(ϵ -caprolactone-co-lactide) [118, 183] may prove more applicable.

2.5 Conclusions

This study demonstrated that meshes could be formed with fiber diameters of 0.14 to 3.6 μm , and angular standard deviations – indicative of fiber orientation – of 32 to 60°. When cultured on these substrates NIH 3T3 fibroblasts grew equally well on all fiber topographies. However, projected cell area, aspect ratio, and the length of the long axis were diminished on submicron fibers. In contrast, these morphologic characteristics increased systematically with fiber orientation. These studies suggest that electrospun fiber meshes may be suitable for development of an engineered ligament tissue.

2.6 Acknowledgements

The authors thank Dr. Garth L. Wilkes for the use of the electrospinning device, and funding from the Charles E. Culpeper Foundation (03-130) and the Institute for Critical Technologies and Sciences at Virginia Tech.

Chapter 3: Effect of Fiber Diameter and Alignment of Electrospun Polyurethane Meshes on Mesenchymal Progenitor Cells

Chris A. Bashur, B.S.¹, Robyn D. Shaffer, B.S.², Linda A. Dahlgren, D.V.M, Ph.D.³, Scott A. Guelcher, Ph.D.⁴, Aaron S. Goldstein, Ph.D.^{1,2}

¹ Department of Chemical Engineering, and
² School of Biomedical Engineering and Sciences,
Virginia Polytechnic Institute and State University,
Blacksburg, VA 24061

³ Department of Large Animal Clinical Sciences,
Virginia-Maryland Regional College of Veterinary Medicine,
Blacksburg, VA 24061

⁴ Department of Chemical Engineering, Vanderbilt University
Nashville, TN 37235

Abstract

Effective strategies to guide cell alignment and the deposition of an oriented extracellular matrix are critical for the development of anisotropic engineered tissues suitable for the repair of ligament defects. Electrospinning is a promising means to create meshes that can align adherent cells, but the effect of fiber mesh architecture on differentiation has not been examined closely. Therefore, the goal of this study was to determine the effect of fiber diameter and the degree of fiber alignment on mesenchymal progenitor cell morphology, proliferation and ligament gene expression. Specifically, a poly (ester urethane)urea elastomer was electrospun onto rigid supports under conditions designed to independently vary the mean fiber diameter (from 0.28 to 2.3 μm) and the degree of fiber alignment. Bone marrow stromal cells – seeded onto supported meshes – adhered to and proliferated on all surfaces. Cells assumed a more spindle-shaped morphology with increasing fiber diameter and degree of fiber alignment, and oriented parallel to fibers on aligned meshes. Expression of the ligament markers collagen 1 α 1, decorin, and tenomodulin appeared to be sensitive to fiber diameter and greatest on the smallest fibers. Concurrently, expression of the transcription factor scleraxis appeared to decrease with increasing fiber alignment. These results suggest that the formation of a ligament-like tissue on electrospun scaffolds is enhanced when the scaffolds consist of aligned submicron fibers.

3.1 Introduction

Approximately 150,000 surgical procedures are performed annually in the United States to treat injured anterior cruciate ligament (ACL) tissue [7], and current materials for ACL replacement include autologous and allogeneic grafts. Both options, however, have intrinsic limitations. Autologous tissue – the preferred material for ACL replacement – exists in limited quantities, requires a secondary surgery to obtain donor tissue, and risks morbidity at the donor site [15]. Allogeneic tissue – typically from cadaveric sources [16] – avoids donor site complications, but risks disease transmission and host inflammatory response [17]. Given these limitations, ligament tissue engineering holds promise as a method to create new materials for ACL reconstruction.

In its most generic form, ligament tissue engineering involves the combination of biomaterial, biologic, and pharmaceutical ingredients to form a composite material that is capable of integrating with the host bone and ligament tissues, stimulating normal tissue remodeling, and providing mechanical stability to the joint [1, 2]. Within this general paradigm, an approach for achieving an engineered ACL tissue involves *in vitro* culture of mesenchymal progenitor cells on a biomaterial scaffold under the appropriate conditions to stimulate cell differentiation toward the ligament phenotype. Two complementary *in vitro* strategies to accomplish this are the use of growth factors (e.g., EGF, IGF-II, FGF-2, TGF- β 1 [48, 184]) and mechanical stimulation [49]. However both strategies require a biomaterial scaffold that is capable of deforming elastically under physiologically relevant strains, controlling the alignment of the adherent cells, and supporting cell differentiation into the ligament phenotype.

For tissue engineering applications the biomaterial must be both degradable and elastomeric, which limits the number of suitable candidate materials. In particular, many degradable polyesters that are commonly employed in tissue engineering applications (e.g., poly(lactic acid), poly(glycolic acid), poly(ϵ -caprolactone) (PCL)) are not sufficiently elastic (yield strains < 10% [185]). However, a number of segmented polyurethanes have been described in the literature that are biocompatible, elastomeric, and degradable [88, 96, 186-189]. These materials are formed by end-capping low molecular weight polyesters (e.g., PCL) with a diisocyanate and then chain-extending them to produce a high molecular weight linear polymers with ester, urethane, and urea linkages (i.e., poly (ester urethane) ureas (PEUURs)). Further,

some of these polymers can be processed into micron-scale fiber meshes by electrospinning [88, 190].

Electrospinning is an attractive method for producing fiber meshes with anisotropic properties suitable for musculoskeletal [191], cardiac [94, 122], and nerve regeneration [120] applications. In particular, the alignment of electrospun fibers produces topographic cues that orient adherent cells [3, 82, 192] through the phenomenon of contact guidance [165]. However, analysis of cell morphology on electrospun meshes has indicated that projected cell area and aspect ratio are sensitive to the diameter and degree of fiber alignment of underlying mesh [82]. Because cell shape and cell function are interdependent [193], the architecture of electrospun meshes may affect cell phenotype.

The primary goal of this study was to determine the effect of electrospun mesh architectures on mesenchymal progenitor cell differentiation into the ligament phenotype. Morphologically, ligament fibroblasts exhibit an elongated cell body – that is oriented parallel to collagen bundles in vivo – and a network of cytoplasmic extensions that mediate cell-cell and cell-ECM interactions. Ligament fibroblasts express a variety of ECM proteins, including collagen types I and III, biglycan, decorin, elastin, and tenascin-C [16]. Although these proteins are common to many soft tissues, scleraxis and tenomodulin have been recently identified as selective markers of ligament fibroblasts. Scleraxis is a transcription factor – expressed during the early stages of musculoskeletal development [34] – that is necessary for development of mature tendon tissue [35], and may be considered an early marker of the ligament phenotype. Tenomodulin is a transmembrane glycoprotein [36] that is induced by scleraxis [37], and is thought to aid in the organization of collagen into fibrils [38] and the suppression of ligament tissue vascularization [39].

In this study an elastomeric PEUUR was electrospun onto rigid substrates with mean fiber diameters of 0.28 to 2.3 μm and varying degrees of fiber alignment. To determine how fiber diameter and the degree of fiber alignment affect development of the ligament phenotype, bone marrow stromal cells (BMSCs) were cultured under static conditions on the resultant meshes, and cell morphology, cell density, and expression of the ligament proteins collagen 1 α 1 (*Colla1*), decorin, tenomodulin, and scleraxis were measured.

3.2 Materials and Methods

3.2.1 Polyurethane Synthesis

A linear segmented degradable PEUUR elastomer, consisting of alternating PCL soft segment and a urethane- and urea-containing hard segment, was synthesized using a standard two-step technique in a three-neck, round-bottom flask equipped with argon inlet and outlet, condenser, and stirrer [189]. In the first step, the flask was charged with anhydrous dimethyl sulfoxide (DMSO, < 50 ppm water; Acros Organics, Morris Plains, NJ) and 1,6-diisocyanatohexane (HDI, Sigma-Aldrich, St. Louis, MO), immersed in a 75°C oil bath, purged with argon, and stirred with a Teflon blade stirrer turned by an electric motor. Next, PCL diol (average molecular weight 1250 Da, PCL1250, Sigma, St Louis, MO) – that had been dried for 24 h at 80°C under vacuum (10 mm Hg) and dissolved in DMSO – was charged into the reactor by means of an addition funnel. The prepolymer content in the reactor was controlled at 14 wt%, and the relative masses of HDI and PCL1250 were selected to achieve a prepolymer NCO:OH equivalent ratio of 2.0:1.0. Dibutyltin dilaurate (DBTDL, Sigma) was added to the flask at 1000 ppm and the reaction was allowed to proceed for 3 h to produce a HDI.PCL1250.HDI prepolymer. In the second step, a solution of 1,3-propanediol bis (4-aminobenzoate) (PDAB, Sigma-Aldrich) in DMSO was prepared at 50°C and added to the resultant prepolymer in the reaction vessel. The NCO:OH equivalent ratio of the polyurethane was controlled at 1.03:1.0 and the polymer concentration was 12 wt%. DBTDL was added to a concentration of 1000 ppm. The reaction was allowed to proceed at 80°C for 20 h. The final polymer was then precipitated in diethyl ether (Sigma) and dried in a vacuum oven for 24 h at 80°C under 10 mm Hg vacuum.

3.2.2 Electrospinning

The PEUUR was electrospun onto rigid glass supports to form fused-fiber meshes with controlled fiber diameters and degrees of fiber alignment as described previously [82]. Briefly, 18 mm glass coverslips (Fisher Scientific, Pittsburgh, PA) were sonicated in ethanol and allowed to air dry. To facilitate adhesion of electrospun fibers a thin film of PEUUR was deposited onto coverslips. For each coverslip, 0.30 mL of a 2.75 wt% solution of PEUUR in 50:50 isopropanol:1,1,1,3,3,3-hexafluoro-2-propanol (HFIP, Sigma) was placed in the center, and the coverslip was spun at 2,500 rpm for 30 s using a Model 1-EC101D-R485 spincoater (Headway

Research, Garland, TX). Coverslips were allowed to dry under vacuum for two days. Two sets of electrospun meshes were prepared concurrently. First, to study the effect of fiber diameter, unaligned fiber meshes were prepared by electrospinning PEUUR onto spincoated coverslips that were mounted onto a stationary target. Electrospinning was performed on three different occasions and PEUUR concentrations of 7.5 to 8.0 wt%, 12.0 to 13.5 wt%, and 20.0 wt% in HFIP were used to achieve three ranges of fiber diameters. These concentrations were selected using a trial-and-error approach with the objective of producing meshes consisting of regularly shaped fibers with the smallest and largest possible diameters, and one intermediate fiber diameter. Second, to study the effect of fiber alignment, spincoated coverslips were mounted onto a 6 cm diameter drum that was rotated at linear velocities of 2.6 ± 0.29 and 4.6 ± 0.26 m/s. For this study, only the intermediate PEUUR concentration (12.0 to 13.5 wt% PEUUR in HFIP) was used. All electrospinning was performed under ambient conditions using a 22 gauge Teflon tipped needle, a 15 kV potential, a throw distance of 15 cm, and a syringe flow rate of 5 mL/h. Because HFIP is toxic, meshes were soaked in ethanol for 7 days followed by deionized water for 2 days to remove residual HFIP. The meshes were then dried and stored in a desiccator – to minimize degradation – until use.

Prior to cell culture studies electrospun PEUUR meshes and spincoated PEUUR films (the control group) were placed into 12-well tissue culture plates (Fisher Scientific) and sterilized by overnight exposure to UV light. To facilitate cell adhesion, substrates were incubated for 1 h with 2 mL of a 2 μ g/mL solution of fibronectin (Fisher Scientific) in phosphate buffered saline (PBS, Fisher Scientific) at room temperature. Substrates were kept wet in PBS until cell seeding.

3.2.3 Scanning Electron Microscopy (SEM) Analysis

For SEM analysis of fiber diameter and alignment electrospun meshes were mounted onto studs and sputtercoated with a 20 nm layer of palladium (Model 208HR, Cressington Scientific Instruments, Cranberry, PA). These surfaces were then imaged with a LEO 1550 Field Emission SEM (Carl Zeiss SMT, Thornwood, NY) operating at 5kV with a 16 mm working distance. Resultant images were imported into ImagePro Plus software (ICube, Crofton, MD) and the orientation and diameter of individual fibers was measured manually using the interactive measurement tools. (At least 100 fibers were analyzed per sample and care was taken to measure only fibers that had clearly defined edges.) Mean angle of orientation relative to the

direction of rotation, μ , and average angular standard deviation, σ , were calculated from a wrapped normal distribution [82]. Briefly, μ and mean resultant length, ρ , were determined using the following equations.

$$\mu = \tan^{-1} \left(\frac{\sum \sin 2\theta_i}{\sum \cos 2\theta_i} \right) \quad (3.1)$$

$$\rho = \frac{\sqrt{\left(\sum \cos 2\theta_i\right)^2 + \left(\sum \sin 2\theta_i\right)^2}}{n} \quad (3.2)$$

Here θ_i is the angle of orientation for an individual fiber. Finally, angular standard deviation was calculated from mean resultant length by the following equation.

$$\sigma = \frac{1}{2} \sqrt{-2 \ln \rho} \quad (3.3)$$

3.2.4 Cell Culture and Cell Seeding

Cell studies were performed using rat bone marrow stromal cells (BMSC) isolated from male 125-150 g Sprague-Dawley rats (Harlan, Dublin, VA) in accordance with the Institutional Animal Care and Use Committee at Virginia Tech [96]. Dispersed whole marrow extracts were grown on 100 mm tissue culture polystyrene Petri dishes (Fisher Scientific) for 10 days in growth medium consisting of Minimal Essential Medium α modification (α -MEM, Invitrogen, Bethesda, MD) with 10% fetal bovine serum (FBS, Gemini, Calabasas, CA) and 1% antibiotic/antimycotic (Invitrogen). Cells were then enzymatically lifted using trypsin/ethylenediamine tetraacetic acid (EDTA) (Invitrogen), split 1:2 and seeded into fresh 100 mm Petri dishes. (This process selectively increases the concentration of the proliferative, marrow-adherent fraction, which includes a population of mesenchymal progenitor cells. However, it does not select for specific antigen markers nor achieve a homogeneous cell population.)

After four days of expansion, first passage cells were enzymatically lifted, and seeded onto PEUUR meshes and PEUUR films in 12 well plates. Cells were added as a suspension of 1.9×10^4 cells in 2 mL of growth medium to achieve a uniform distribution of cells across the well bottom of 5.0×10^3 cells/cm². After 24 h, medium was replaced with growth medium supplemented with 2 mM ascorbate-2-phosphate (Sigma). Thereafter, medium was replaced twice weekly. Samples were then collected and analyzed for cell morphology, cell density, and mRNA expression of ligament proteins decorin, *Colla1*, tenomodulin, and scleraxis.

3.2.5 Cell Morphology

After 3 days of culture on fibers, cell morphology was determined by imaging fluorescently labeled cells. Briefly, medium was replaced with 2 mL fresh medium containing 15 μ L of 1 mg/mL calcein-AM (Molecular Probes, Eugene, OR) in DMSO and incubated for 30 min at 37 °C in the dark. Next, cell-seeded substrates were washed two times with 2 mL/well PBS, and 2 mL α -MEM without phenol red was added to each well. Fluorescent images were obtained at 20 \times magnification with a wide blue filter using an Olympus IX50 microscope (Opelco, Sterling, VA) equipped with a cooled CCD camera (Hamamatsu C4742-98-12NRB). Phase contrast images of each field were also collected. Sixteen pairs of images per substrate were then imported into ImagePro Plus software and length of the long axis, aspect ratio, projected area, and angle of orientation of each cell were measured from fluorescent images using ImagePro algorithms. (These algorithms calculate long axis, aspect ratio, and angle of orientation by approximating the cell as an ellipse.) On average, 100 cells were analyzed per substrate, although the smallest sample size was $n = 18$ cells. Concurrently, the angle of fiber orientation was measured for at least 100 fibers per substrate from phase contrast images. Mean values for projected cell area, aspect ratio, length of the long axis, and angle for both fibers and cells were calculated per substrate. Angular standard deviations for both cell and fiber orientation were calculated for each substrate using Equations 1 - 3. Statistical analyses were performed using the mean properties of each substrate.

3.2.6 Cell Number

Cell number was calculated from fluorescence measurements of DNA as described in detail elsewhere [58]. Briefly, meshes were mechanically disrupted using cell scrapers and

collected in 10 mM EDTA (pH 12.3). Samples were sonicated for 10 min on ice, neutralized with the addition of KH_2PO_4 , and combined with a solution of Hoechst 33258 (Sigma) in 100 mM NaCl and 10 mM Tris (pH 7.0, Sigma). Fluorescence was measured with a DyNAQuant 200 fluorimeter (Hoefer, San Francisco, CA) and cell number was calculated from measurements of fluorescence intensity using a set of DNA standards and a conversion factor of 10.4 pg DNA/cell [194].

3.2.7 mRNA Expression

Expression of *Colla1*, decorin, scleraxis and tenomodulin was determined quantitatively by real-time polymerase chain reaction (PCR). Briefly, total RNA was isolated from the cells on days 7 and 14 using the RNeasy Mini Kit (Qiagen, Valencia, CA) according to the manufacturer's instructions. Lysates were first homogenized with QIASHredder columns (Qiagen) and then were subjected to on-column DNase digestion using DNase I (Qiagen). RNA was quantified using Quant-It RiboGreen kit (Molecular Probes) and a fluorescent plate reader (SpectraMax M2, Molecular Devices, Sunnyvale, CA). Equal masses of RNA – approximately 0.5 μg – were reverse-transcribed to cDNA using SuperScript[®] First-Strand Synthesis kit (Invitrogen) with random hexamers as primers according to manufacturer's protocol. Real-time PCR was performed in the ABI 7300 Real Time PCR System (Applied Biosystems, Foster, CA) using 50 ng cDNA, Power Sybr[®]Green Master Mix (Applied Biosystems), and specific primers for *Colla1*, decorin, scleraxis, tenomodulin and β -actin (the internal reference). Primer sequences were designed in Primer Express[®] software (Applied Biosystems) using the NCBI database accession numbers as shown in (**Table 3.1**) and purchased from Integrated DNA Technologies (Coralville, IA). Primers for the reference gene, β -actin, were developed as described previously [195]. Quantification of target gene expression, relative to spincoated substrates on day 7, was performed using the comparative threshold cycle ($\Delta\Delta\text{Ct}$) method [196]. Relative gene expression was reported as $2^{-\Delta\Delta\text{Ct}}$. Control reactions (e.g., amplification without cDNA template, amplification of isolated RNA) were performed to verify the fidelity of the amplification process.

Table 3.1: Primer sequences for real-time polymerase chain reaction amplification.

Gene	Forward primer sequences	Reverse primer sequences	Product Size
<i>Col1a1</i> NM_053304	5' GAGGGCGAGTGCTGTCCTT 3'	5' GGTCCCTCGACTCCTATGACTTC 3'	74 bp
Decorin NM_024129	5' CATCTCCGAGTGGTGCAGTGT 3'	5' GCAATGTTGTGTCAGGTGGAA 3'	76 bp
Scleraxis NM_001130508	5' TCTGCCTCAGCAACCAGAGAAAGT 3'	5'ACTCTTCAGTGGCTTCCACCTTCA 3'	130 bp
Tenomodulin NM_022290	5' CCCACAAGTGAAGGTGGAGAA 3'	5'AACAGTAACCTCTCTCATCCAGCAT 3'	125 bp
Beta Actin NM_031144	5' CGTGAAAAGATGACCCAGATCA 3'	5' CACAGCCTGGATGGCTACGT 3'	72 bp

3.2.8 Statistical Analysis

All studies were performed two or three times using separate batches of PEUUR meshes and BMSCs. Results are presented as the mean \pm standard deviation for $n = 2$ or 3 substrates for SEM analysis of fiber diameter and orientation, $n = 6$ or 9 coverslips per condition for cell morphology, $n = 8$ or 12 coverslips per condition for cell number. Results are presented as the mean \pm standard error of the mean, with $n = 6, 9,$ or 12, for mRNA expression of *Colla1* and decorin, and with $n = 4, 6,$ or 8, for scleraxis and tenomodulin. Statistical significance was determined in SAS 9.1.3 (SAS Institute Inc. Cary NC) and mixed model analysis of variance (ANOVA) was used with post-hoc comparisons using the Tukey-Kramer method with a significance criterion of $p \leq 0.05$.

3.3 Results

3.3.1 Electrospun Meshes

SEM images were analyzed to determine fiber diameter and degree of alignment for each electrospinning condition. When electrospun onto a stationary target, PEUUR solution concentrations of 7.5-8.0, 12.0-13.5, and 20.0 wt%, resulted in mean fiber diameters of 0.28, 0.82, and 2.3 μm , respectively (**Table 3.2, Figure 3.1**). When electrospun from a 12.0-13.5 wt% solution onto a rotating drum, the angular standard deviation decreased from 49.5° to 27.8° and the mean fiber diameter decreased from 0.72 to 0.46 μm (**Table 3.2, Figure 3.2**) as the drum speed was increased from 0 to 4.6 m/s.

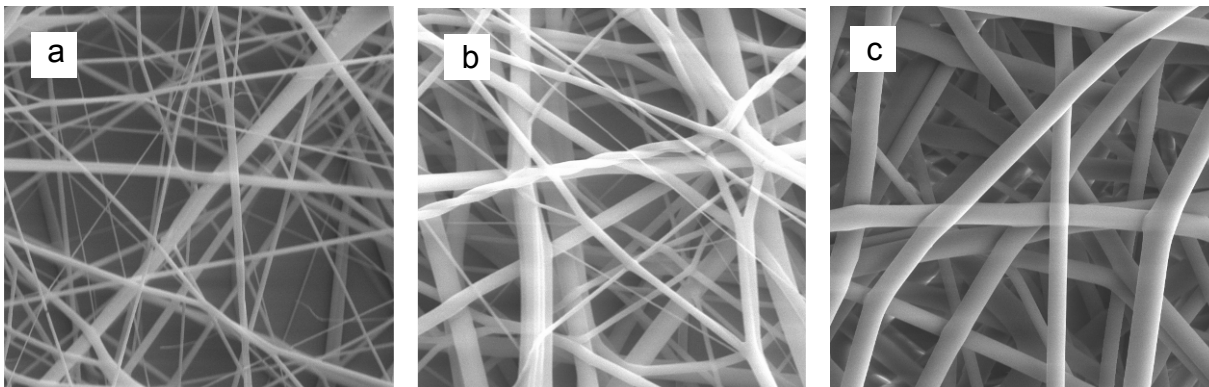


Fig. 3.1: SEM images of PEUR fibers electrospun from different solution concentrations: a) 8 wt%, b) 12 wt%, and c) 20 wt%.

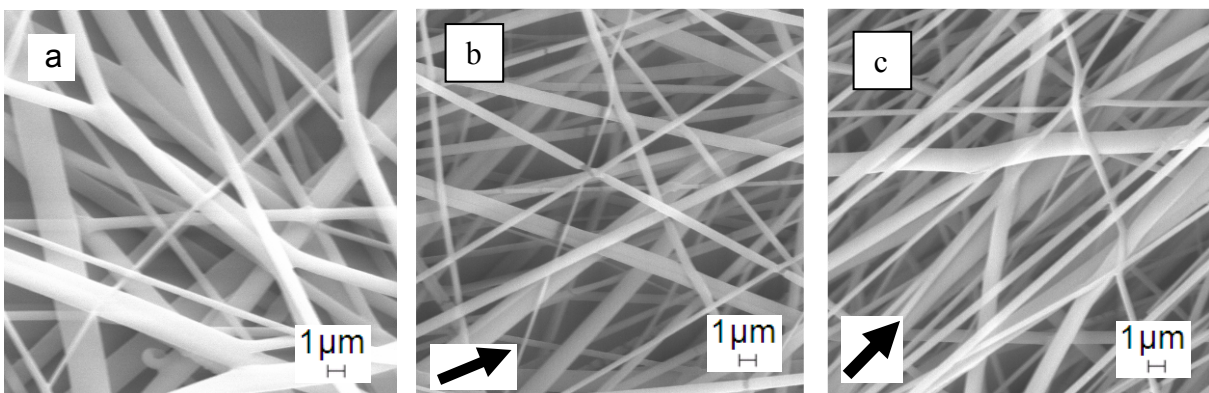


Fig. 3.2: SEM images of PEUR fibers electrospun from 12 wt% solutions onto a) a stationary target, or a rotating target at b) 2.4 m/s, and c) 4.4 m/s. Arrows corresponds to the average orientation of fibers.

Table 3.2: Fiber diameter and angular standard deviation for meshes electrospun from PEUR solutions of different concentrations and at different rotation rates. Mean \pm standard deviation for $n = 3$ replicates (except $n = 2$ for 2.6 m/s drum speed) with greater than 100 fibers per sample.

Concentration (%)	Rotational speed (m/s)	Fiber angular deviation ($^{\circ}$)	Fiber Diameter (μm)
7.8 ± 0.2	Stationary	61.9 ± 4.4	0.28 ± 0.07
12 ± 0.9	Stationary	49.9 ± 3.7	0.82 ± 0.14
20 ± 0.0	Stationary	60.3 ± 5.2	2.3 ± 0.15
12 ± 0.9	Stationary	49.5 ± 3.2	0.72 ± 0.21
11 ± 1.1	2.6 ± 0.3	33.7 ± 1.0	0.53 ± 0.15
12 ± 0.9	4.6 ± 0.3	27.8 ± 2.5	0.46 ± 0.12

3.3.2 Cell Orientation and Morphology on Meshes

BMSCs were cultured on electrospun meshes for three days, and then fluorescent images were collected to characterize cell morphology. Representative images of cells (green) on meshes (red) showed that cells were rounder and exhibited random orientations on unaligned fiber meshes (**Figure 3.3a**) compared to cells on more aligned fiber meshes (**Figure 3.3b**). Quantitative image analysis was performed to characterize the projected cell area, aspect ratio, and length of the long axis as a function of fiber diameter (**Figure 3.4**) and degree of fiber alignment (**Figure 3.5**). Projected cell area was diminished on fibers relative to spincoated films (**Figures 3.4a and 3.5a**), and this difference was significant for the 0.28 and 2.3 μm fibers ($p = 0.008$ and 0.046 , respectively). However, projected cell area did not appear to vary systematically with either fiber diameter (**Figure 3.4a**) or degree of fiber alignment (**Figure 3.5a**). In contrast, cell aspect ratio was increased on all fibers relative to spincoated films (**Figure 3.4b and 3.5b**), and differences were statistically significant for diameters of 0.82 and 2.3 μm , ($p = 0.003$ and 0.006 , respectively, **Figure 3.4b**) and all degrees of fiber alignment ($p = 0.005$, <0.001 , and <0.001 for $\sigma = 49.5^\circ$, 33.7° , and 27.8° , respectively, **Figure 3.5b**). Further, cells on the more aligned fiber meshes ($\sigma = 33.7^\circ$ and 27.8°) had significantly greater aspect ratios than cells on the unaligned fiber meshes ($p = 0.002$ and <0.001 , respectively, **Figure 3.5b**). Finally, the length of the long axis was unaffected by fiber diameter and angular standard deviation (**Figure 3.4c and 3.5c**, respectively).

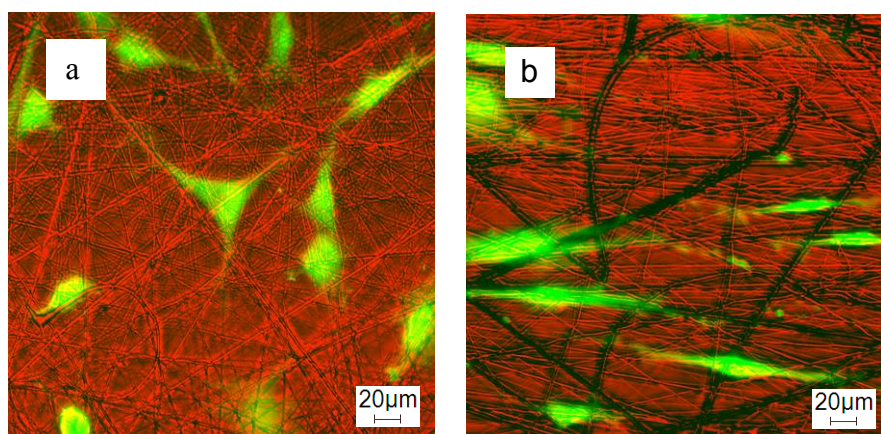


Fig. 3.3: BMSC morphology on fiber meshes electrospun onto a) a stationary target and b) a drum rotating at 4.4 m/s. Images were constructed by merging phase contrast (red) and fluorescence (green) images of calcein-loaded cells attached to fibers.

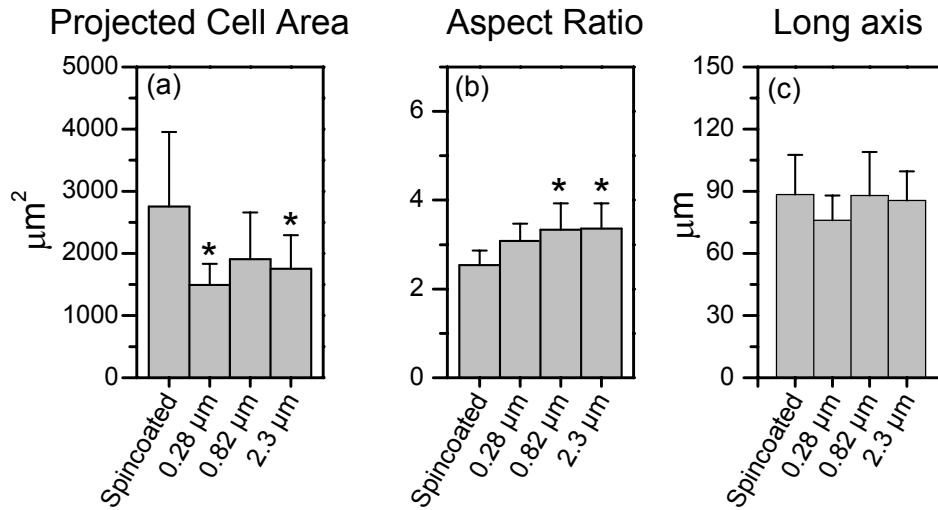


Fig. 3.4. Effect of PEUUR fiber diameter on a) projected cell area, b) aspect ratio, and c) length of long axis. Controls surfaces were spincoated PEUUR films. An asterisk indicates statistical difference relative to control for $n = 9$ coverslips.

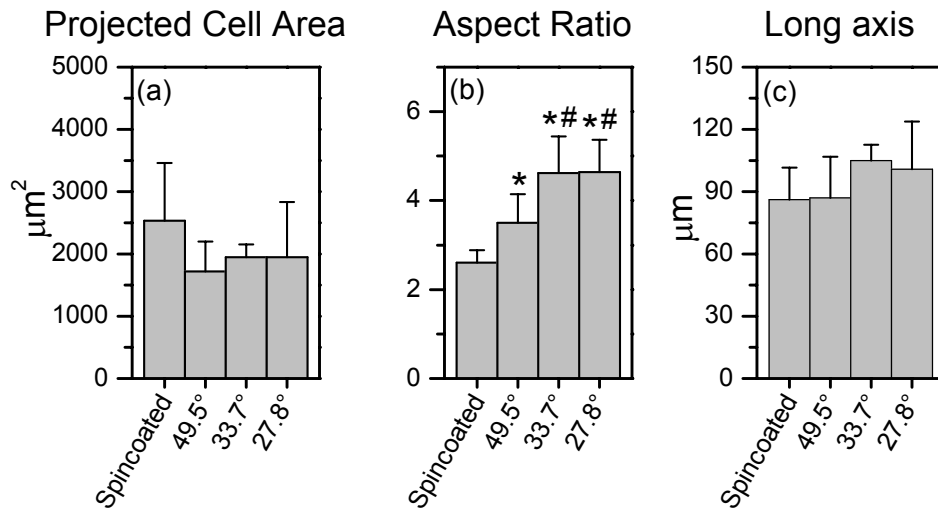


Fig. 3.5. Effect of PEUUR fiber orientation on a) projected cell area, b) aspect ratio, and c) length of long axis. Control surfaces were spincoated PEUUR films. An asterisk indicates statistical difference relative to control, and a pound symbol indicates statistical difference relative to the randomly oriented fibers for $n = 9$ coverslips (except $n = 6$ for the group $\sigma = 33.7^\circ$).

Fluorescent images (e.g., **Figure 3.3**) were analyzed quantitatively to compare the orientation of BMSCs to that of the underlying fibers. Cells seeded onto spincoated surfaces and unaligned fiber meshes were unoriented, as indicated by angular standard deviations of $\sigma = 50^\circ$ and 38° , respectively (**Table 3.3**). In contrast, cells cultured on aligned fiber meshes oriented parallel to the fibers. Specifically, the mean angle of cell orientation differed from that of the fibers by 7° and the angular standard deviations for the cells were $\sigma = 22^\circ$ and 15° for linear velocities of 2.6 and 4.6 m/s, respectively (**Table 3.3**).

Table 3.3: Cell alignment and orientation on aligned meshes. Angular standard deviation of cells for $n = 3$ replicates (except $n = 2$ for 2.6 m/s drum speed) and mean angle of cell orientation relative to fibers on electrospun surfaces with different degrees of orientation for $n = 9$ coverslips (except $n = 6$ for 2.6 m/s rotational speed).

Drum Speed (m/s)	Fiber Angular Deviation ($^\circ$)	Cell Angular Deviation ($^\circ$)	Difference in Mean Angle ($^\circ$)
–	No fibers	49.6 ± 17.8	–
–	53.3 ± 7.4	38.7 ± 6.5	35 ± 27
2.6	44.1 ± 7.4	22.4 ± 9.7	6.4 ± 6.9
4.6	33.7 ± 5.2	15.1 ± 4.5	7.1 ± 6.5

3.3.3 Cell Density on Meshes

Cell density was measured at days 3, 7, and 14 to characterize BMSC attachment and proliferation on the electrospun meshes. On day 3 the cell densities on the 0.28 and 0.82 μm fiber meshes were similar to those on the spincoated films (**Figure 3.6a**). In contrast cell density on the 2.3 μm fiber meshes was significantly lower than on the 0.28 and 0.82 μm fibers ($p = 0.035$ and 0.001 , respectively). Between days 3 and 7 similar increases in cell density were noted on 0.28 and 0.82 μm fiber meshes and spincoated films, while no change in cell density was noted between 7 and 14 days. Cell density on the 2.3 μm fiber meshes was significantly lower than on the 0.28 μm fiber meshes at day 7 ($p = 0.035$). However, by day 14 cell density on the 2.3 μm fiber meshes was comparable to that on the other surfaces. On meshes with similar fiber diameters (0.46 to 0.82 μm) but with different degrees of fiber alignment, cell densities were comparable to the spincoated films at all time points (**Figure 3.6b**).

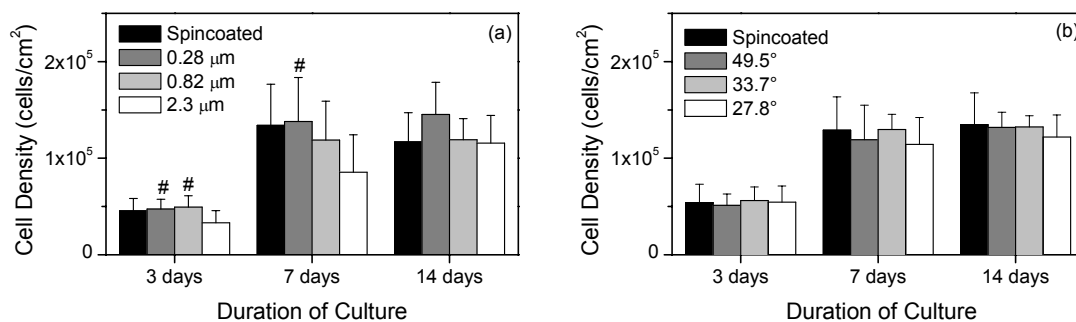


Fig. 3.6. Cell density on PEUUR fibers as a function of culture duration: a) effect of fiber diameter, and b) effect of fiber orientation. A pound symbol indicates a statistical difference relative to the largest diameter fibers on the same day for $n = 12$ substrates (except $n = 8$ for the group $\sigma = 33.7^\circ$).

3.3.4 Ligament Protein Expression

Real-time PCR was performed to determine the effect of fiber architecture on the expression of ligament proteins *Colla1*, decorin, tenomodulin, and scleraxis. At day 7 BMSCs cultured on 0.82 and 2.3 μm fiber meshes exhibited lower expressions of *Colla1*, decorin, and tenomodulin relative to BMSCs cultured on 0.28 μm fiber meshes and spincoated films (**Figure 3.7**). In particular, *Colla1* expression by BMSCs on both 0.82 and 2.3 μm fibers was significantly lower than by BMSCs on spincoated films ($p = 0.008$ and 0.028 , respectively) and the expression of decorin on 2.3 μm fibers was significantly lower than on both spincoated films and 0.28 μm fibers ($p = 0.039$ and 0.047 , respectively). When BMSCs were cultured on meshes with similar fiber diameters but with different degrees of fiber alignment, expression of *Colla1*, decorin, and tenomodulin were lowest for BMSCs on the randomly oriented fibers ($\sigma = 49.5^\circ$, **Figure 3.8**). Although the differences were not statistically significant, these lower levels of mRNA expression for $\sigma = 49.5^\circ$ relative to spincoated surfaces are consistent with **Figure 3.7**, while the lower levels for $\sigma = 49.5^\circ$ relative to the more aligned fibers ($\sigma = 33.7^\circ$ and 27.8°) may be related to differences in both fiber alignment and fiber diameter. Scleraxis expression at day 7 was not significantly affected by either fiber diameter or degree of fiber alignment; however scleraxis expression increased with increasing fiber diameter (Figure 7) and decreasing degree of fiber alignment (**Figure 3.8**). Finally, expression of these four genes was also measured on day 14 (**Figures 3.9-3.11**). Although no differences between groups were significant, expression of *Colla1* and tenomodulin were lower on all surfaces at day 14 relative to day 7, and tenomodulin expression was slightly higher on fiber meshes than on the spincoated films.

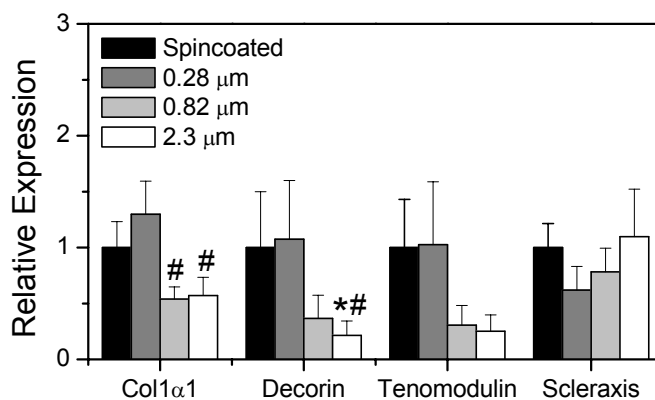


Fig. 3.7. Effect of fiber diameter on mRNA expression of *Colla1*, decorin, tenomodulin, and scleraxis after 7 days of culture. Data was normalized relative to cells on spincoated PEUUR films. An asterisk indicates statistical difference relative to the spincoated control group and a pound symbol indicates significant difference relative to the smallest diameter fibers. All studies were performed in triplicate for a total of $n = 9$ to $n = 12$ samples per condition for *Colla1* and decorin. A subset of these samples were analyzed for tenomodulin and scleraxis ($n = 6$ to $n = 8$).

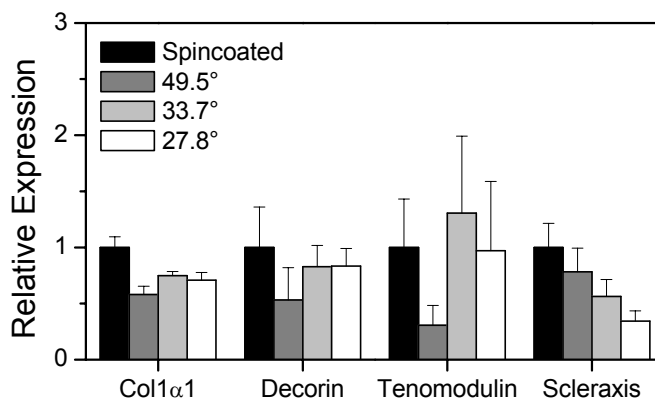


Fig. 3.8. Effect of fiber orientation on mRNA expression of *Colla1*, decorin, tenomodulin, and scleraxis after 7 days of culture. Data was normalized relative to cells on spincoated PEUUR films. All studies were performed in triplicate (except $\sigma = 33.7^\circ$ which was performed in duplicate) for a total of $n = 6$ to $n = 12$ samples per condition for *Colla1* and decorin. A subset of these samples were analyzed for tenomodulin and scleraxis ($n = 4$ to $n = 8$).

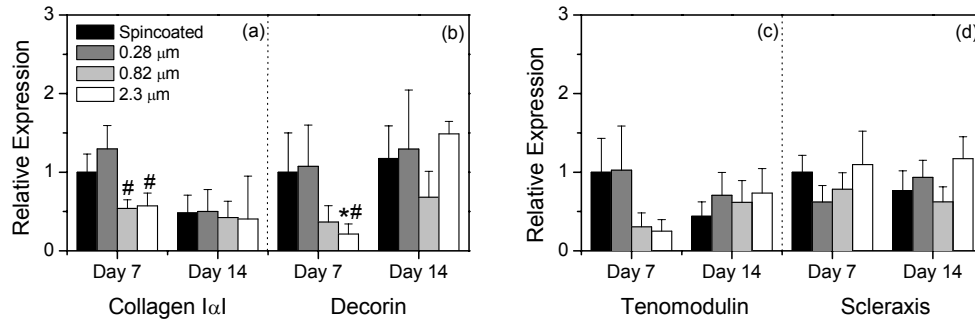


Fig. (supplemental) 3.9. Effect of fiber diameter on mRNA expression of a) collagen 1α1, b) decorin, c) tenomodulin, and d) scleraxis after 7 and 14 days of culture. Data was normalized relative to cells on spincoated PEUR films at day 7. An asterisk indicates statistical difference relative to the spincoated control group and a pound symbol indicates statistical difference relative to the smallest diameter fibers at the same time point. All studies were performed in triplicate for a total of $n = 9$ to $n = 12$ samples per condition for collagen 1α1 and decorin. A subset of these samples were analyzed for tenomodulin and scleraxis ($n = 6$ to $n = 8$).

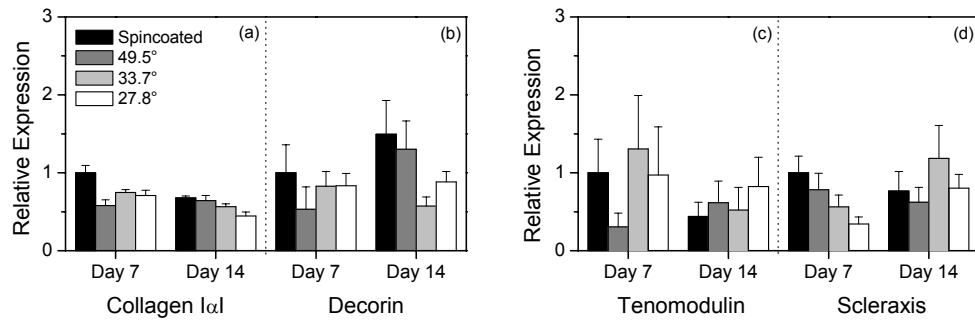


Fig. (supplemental) 3.10. Effect of fiber orientation on mRNA expression of a) collagen 1α1, b) decorin, c) tenomodulin, and d) scleraxis after 7 and 14 days of culture. Data was normalized relative to cells on spincoated PEUR films at day 7. All studies were performed in triplicate (except $\sigma = 33.7^\circ$ which was performed in duplicate) for a total of $n = 6$ to $n = 12$ samples per condition for collagen 1α1 and decorin. A subset of these samples were analyzed for tenomodulin and scleraxis ($n = 4$ to $n = 8$).

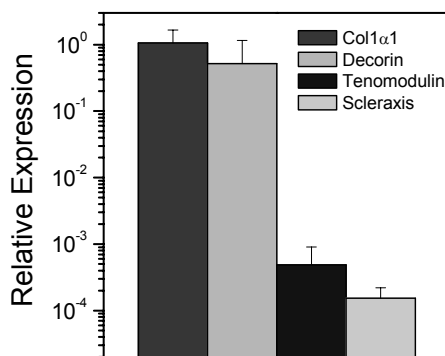


Fig. (supplemental) 3.11: Comparison of mRNA expression on spincoated PEUUR films for collagen 1 α 1, decorin, tenomodulin, and scleraxis after 7 days of culture. Data is reported as $2^{-\Delta\Delta C_t}$ with β -actin as the internal control. All studies were performed in triplicate and error bars correspond to the standard error of the mean for $n = 12$ (collagen 1 α 1, decorin) or $n = 8$ (tenomodulin, scleraxis) samples.

3.4 Discussion

In this study BMSCs were cultured on electrospun PEUUR meshes to determine the effect of fiber diameter and alignment on cell morphology, proliferation, and ligament gene expression. Meshes with mean fiber diameters of 0.28 to 2.3 μm were achieved by using PEUUR solution concentrations of 7.5 to 20 wt%, while differing degrees of fiber alignment – characterized angular standard deviation of 27.8° to 49.5° – were achieved by varying the velocity of the target from 0 to 4.6 m/s. When BMSCs were cultured on resultant meshes, the projected cell areas were smaller than on spincoated PEUUR films; however cell aspect ratios were significantly greater on larger (0.82 and 2.3 μm diameter) unaligned fiber meshes and were further increased when the fibers were aligned ($\sigma = 33.7$ and 27.8°). In addition, cells oriented parallel to fibers on aligned fiber meshes. Cells proliferated on all surfaces, but expression of *Colla1*, decorin, and tenomodulin were diminished at day 7 on the larger (0.82 and 2.3 μm diameter) unaligned fiber meshes relative to the smallest (0.28 μm diameter) unaligned fiber meshes and spincoated films.

The primary goal of this study was to determine the effects of electrospun mesh architecture on the expression of ligament genes, and a body of evidence is emerging to indicate that fiber diameter and alignment have pronounced effects on cell phenotype. For example, recent work by Kumbar et al showed that the expression of *Colla1* is suppressed when human dermal fibroblasts are grown on larger fibers but that expression of collagen type III and elastin

are enhanced when cells are grown on fibers with intermediate diameters (0.35 to 1.1 μm) [197]. The study presented here shows a decrease in the expression of *Colla1* with increasing fiber diameter (**Figure 3.7**), consistent with Kumbar et al, but it also demonstrates decreases in expression of decorin and tenomodulin, which have not been examined previously. In particular, the expressions of these three proteins as a function of substrate properties are remarkably similar, suggesting a common mechanism of gene regulation. In another study, Lee et al. examined the effect of fiber alignment and showed that collagen deposition is increased when ligament fibroblasts are grown on aligned fibers [3]. Although the study presented here does not demonstrate a change in *Colla1* (**Figure 3.8**, which is consistent with Baker et al [192]) it does show increases in expression of decorin and tenomodulin (both involved in collagen bundle formation) and a decrease in scleraxis (an early marker of the ligament phenotype) with increasing fiber alignment. These data, while not statistically significant, suggest that fiber alignment promotes phenotypic maturation. Importantly, a similar observation was reported by Chew et al. for Schwann cells on aligned fiber meshes [198].

The ability to control electrospun mesh architecture has been described extensively and fiber diameters from as small as 0.03 μm to greater than 6 μm [117] have been achieved by changing spinning conditions such as electric potential, throw distance, flow rate of the metering pump, diameter of the syringe tip, and solution concentration [108, 112, 113, 117, 138]. Variation of the solution concentration is an effective means to control mean fiber diameter, but the range of achievable diameters is limited by bead formation [82, 138] and electrospaying [117] at low concentrations and viscous resistance to flow at high concentrations [117]. Because the goal of this study was to evaluate the biological effects of fiber diameter and degree of alignment, PEUUR solutions of 7.5 to 20 wt% in HFIP were selected to ensure that meshes were comprised of regularly shaped fibers. However, future examination of a broader range of fiber diameters may be both prudent and feasible. In this study, the expression of *Colla1*, decorin, and tenomodulin were maximal on the smallest (0.28 μm) diameter fiber meshes (Figure 7), suggesting further increases in expression of these ligament proteins can be achieved by decreasing the fiber diameter. This may be testable as the addition of salts and the reduction of the throw potential have been reported to reduce bead formation at low solution concentrations. Concurrently, the limited penetration of cells into electrospun meshes that has been noted in the literature [192] may be overcome by the use of larger fibers, which provide larger interfiber

spaces for cell migration.. Such larger fibers may be achieved by shortening of the throw distance [117].

Methods to align electrospun fibers also have been described extensively in the literature, and include depositing fibers on a rotating drum [82, 119], rotating disc [88, 120], between two grounded targets [121], and by stretching the resultant mesh [122]. In this study, partial alignment – marked by angular standard deviations of 33.7° and 27.8° – was achieved using a rotating drum. Better alignment of electrospun fibers has been reported previously [3, 120], but the partial alignment demonstrated in this study was sufficient to achieve aspect ratios in excess of 4 (**Figure 3.5**) and to induce alignment of adherent BMSCs (**Table 3.3**). Further, the achievement of highly aligned electrospun fibers may not be beneficial for development of engineered ligament tissues because fiber packing density increases with fiber alignment, reducing interfiber pore size and the ability for cells to infiltrate [131].

A caveat of these studies is that the measured cell properties may reflect the mechanical properties of the PEUUR meshes. The rationale for electrospinning PEUUR meshes onto rigid glass supports was to isolate the effects of the mesh architecture. However, mechanical testing of the PEUUR meshes indicates that the modulus is approximately 1 MPa [190]. This relatively low modulus may contribute to the diminished projected cell areas, as previous studies have shown that cell spreading decreases with increasing substratum compliance [199]. Indeed, fibroblastic cells on rigid microgrooved titanium substrates are well-spread [166], in contrast to the BMSCs on PEUUR meshes in this study (**Figures 13-15**). In addition, when electrospun fibers are deposited on a rotating drum the resultant mesh can be as much as five times stiffer in the direction of fiber orientation than in the direction perpendicular [190]. This mechanical anisotropy may contribute to BMSC alignment as cells have been shown to align their actin cytoskeleton parallel the axis of greatest substratum stiffness [191, 200].

Previous work has shown that differentiation of progenitor cells and the achievement of a target phenotype is sensitive to the compliance of the underlying biomaterial [201]. Although an optimal modulus for stimulating BMSCs to differentiate into tendon/ligament fibroblasts has not been identified, the PEUUR used in this study has a Young's modulus of 2.7 MPa [190], which is nearly two orders of magnitude lower than human adult ACL tissue (111-144 MPa [202, 203]). This suggests that new elastomers with higher Young's moduli may need to be identified in order to fabricate clinically useful engineered ligaments. However, processing conditions

remain important, as the modulus of PEUUR meshes is sensitive to both fiber diameter and the degree of fiber alignment [190].

Finally, the results of this study suggest that electrospun fiber meshes consisting of smaller and more aligned fibers are attractive over larger unaligned fiber for ligament tissue engineering applications. The smaller fibers achieve higher expression of ligament proteins *Colla1*, decorin, and tenomodulin, and the more aligned fibers stimulate alignment and elongation of adherent cells. However, differences in gene expression among the different electrospun meshes were modest, which suggests that additional stimuli (e.g. mechanical stretch [49] and growth factors [48, 184]) are required to achieve clinically effective engineered ligament tissues. Therefore, future studies, will concern the effect of uniaxial mechanical strain, which has been shown to induce expression of several ECM proteins, including collagen types I and III, decorin, and tenascin-C [40, 154, 204].

3.5 Conclusions

This study demonstrates that electrospun PEUUR meshes with fibers diameters of 0.28 to 2.3 μm and angular standard deviation of 27.8 to 49.5° support attachment and spreading of BMSCs. In addition, cell morphology was sensitive to fiber diameter and alignment, and adherent cells oriented parallel to fibers on aligned fiber meshes. Expression of collagen 1 α 1, decorin, and tenomodulin was suppressed on the larger fibers. Together, these results suggest that aligned electrospun meshes consisting of submicron fibers may be preferable for ligament tissue engineering.

3.6 Acknowledgments

This research was funded by the ASPIRES grant program and through the Institute for Critical Technologies and Sciences at Virginia Tech.

Chapter 4: Characterization of Segmented Poly (ester-urethane urea)s for Ligament Tissue Engineering Applications

Chris A. Bashur¹, Scott A. Guelcher², Aaron S. Goldstein^{1,3}

¹ Department of Chemical Engineering, and
² Department of Chemical Engineering, Vanderbilt University
Nashville, TN 37235

³ School of Biomedical Engineering and Sciences,
Virginia Polytechnic Institute and State University,
Blacksburg, VA 24061

4.1 Introduction

A biomaterial for ligament tissue engineering must meet several requirements, including biocompatibility, degradability, mechanical strength, and fatigue resistance. The biomaterial must also have the ability to be processed into a porous scaffold (e.g. electrospun fibrous scaffold) that will guide cell alignment and allow for cell infiltration. Several synthetic polymers have been shown to have the biocompatibility necessary for tissue engineering applications (e.g. poly (lactic acid), poly (glycolic acid) (PGA), poly (ϵ -caprolactone) (PCL), and segmented polyurethanes and polyureas) [88-90]. The degradation rates of these polymers vary from 1 or 2 months for PGA to 2 or 3 years for PCL [89, 92, 93], with the longer degradation time of PCL better matching the healing rate of ligament tissue. In addition, the tensile properties (e.g. yield strength, percent elongation, and modulus) of these polymers vary and are important considerations for ligament tissue engineering applications.

One limitation with many biocompatible polymers is that they will fatigue during the repetitive cyclic loading that is applied to a ligament graft both in a bioreactor and *in vivo* [94]. A promising strategy to provide the fatigue resistance required during cyclic loading is to use a thermoplastic elastomer (e.g. poly (ester-urethane urea)s (PEUURs)) [88, 95]. PEUURs consist of a hard segment and a soft segment which are able to micro-phase separate and produce elastomeric properties through physical crosslinks [96, 97]. For PEUURs with a crystalline segment (e.g. PCL), the molecular weight of that segment can be adjusted to vary the crystallinity – and consequentially the moduli – of these materials while keeping the same chemistry in the individual segments [96]. However, the moduli of these elastomers are lower than that of human anterior cruciate ligament (ACL) (i.e. approximately 111 MPa) [10, 88]. For

example, a modulus of 60 MPa has been reported for a PEUUR film [88], and the modulus of the same material was decreased to 8 MPa when processed into a porous electrospun mesh [88].

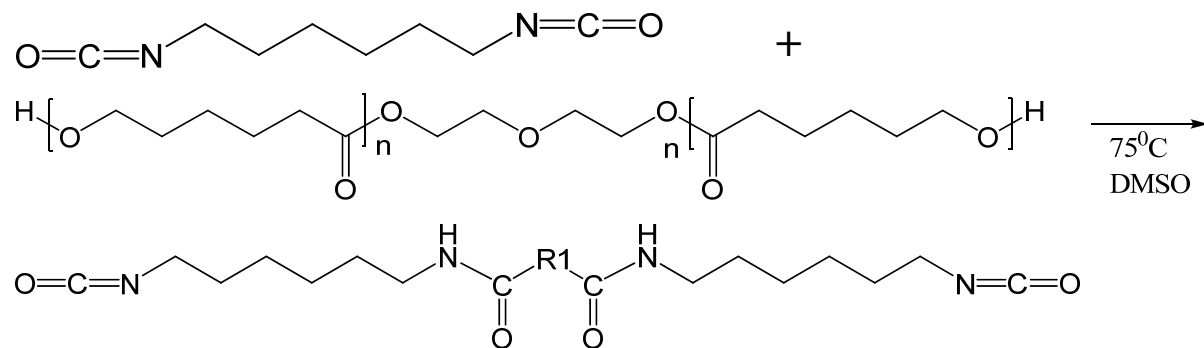
In this study, two different PEUURs were characterized to determine which segmented copolymer would work best for ligament tissue engineering applications. These polymers were synthesized with slowly degrading PCL as the soft segment. The amount of the crystalline PCL soft segment was varied to produce two polymers with similar chemistries. Afterward, the densities, thermal properties, and mechanical properties were measured. Finally, the mechanical properties of the polymers processed into electrospun scaffolds with different diameters and alignments were measured to determine their effect on the mechanical strength of the scaffold.

4.2 Materials and Methods

4.2.1 PEUUR Synthesis

The synthesis of the PEUURs by Dr. Scott Guelcher is described in detail elsewhere (Section 3.2.1) [150]. Briefly, a linear segmented degradable PEUUR elastomer was synthesized using a standard two-step technique [189]. PCL diols with different molecular weights ($M_n = 1250$ or 2000 Da) were end-capped with hexamethylene diisocyanate (HDI), and this prepolymer was chain extended with 1,3-propanediol bis (4-aminobenzoate) (PDAB) (**Figure 4.1**). First, the PCL and the HDI were reacted at a ratio of 1.0:2.0 to produce an HDI.PCL.HDI prepolymer. Second, the prepolymer was reacted with PDAB at a ratio of 1:03:1:0 to produce PEUURs with alternating PCL soft segments and urethane and urea containing hard segments. The theoretical weight percent soft segment, predicted from the molecular weights of the hard and soft segments, for polymers synthesized with either $M_n = 1250$ or 2000 Da was 65% or 74%, respectively. In this polymer, the PCL segments are important for the properties because of their ability to crystallize, and the percent crystallinity of the PEUURs is expected to increase with a larger PCL segment. Therefore, the use of different molecular weights of PCL were expected to produce polymers with different mechanical properties but similar chemistries, densities, and overall molecular weights [96].

(a) Pre-polymer synthesis



where R1 is the PCL segment.

(b) Chain extending to produce PEUUR

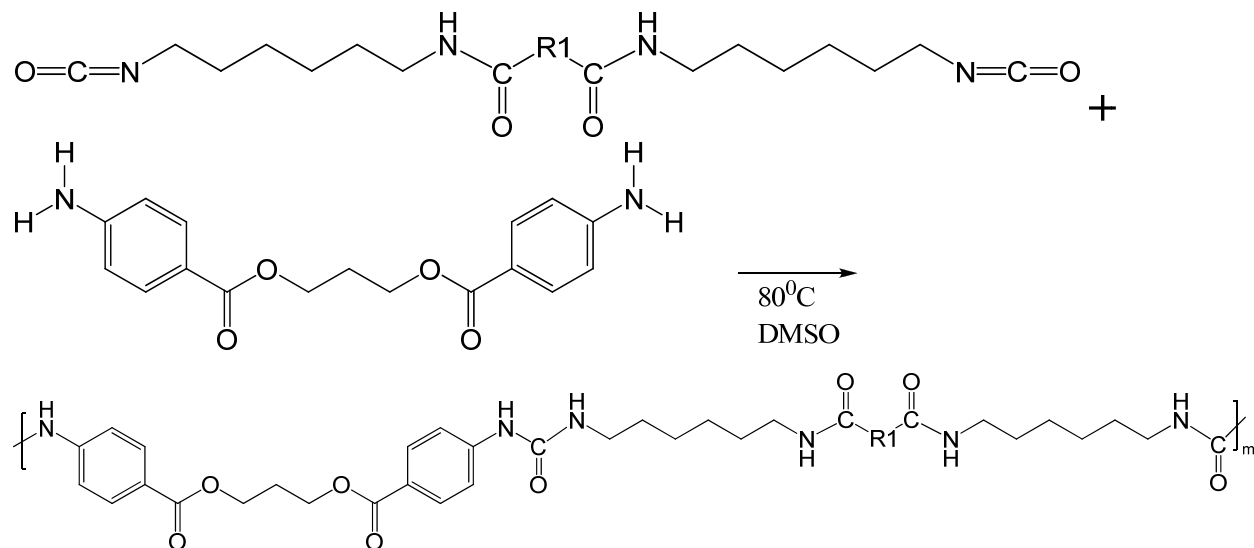


Fig. 4.1. Synthesis scheme for forming PEUUR elastomers for a) formation of the HDI.PCL.HDI prepolymer and b) formation of the PEUUR

4.2.2 Measurement of Polymer Density

The density of the PEUUR polymers was measured with an Accu Pyc 1330 pycnometer (Norcross, GA). A standard (AccuPyc, Norcross, GA) of known volume was added to the 1 cm³ chamber to calibrate the equipment. Next, samples (0.5 g or less) were weighed and added to the

chamber, and then the chamber was filled with helium to determine the volume of the samples. Finally, the polymer density was calculated from the measured mass and volume for $n = 4$ samples.

4.2.3 Polymer Processing

Cast films of PEURs with both 1250 M_n (PEUR1250) and 2000 M_n (PEUR2000) PCL segments were prepared for mechanical testing. Briefly, PEUR1250 and PEUR2000 were dissolved in dimethylformaldehyde (DMF) to produce 9 wt% solutions, and then heated in a 60°C water bath overnight. The solution was cast in a Teflon dish, and allowed to dry under 25 in Hg vacuum at 60°C at for two days. A punch was used to create dogbones with a 10 mm gauge distance and a 2.5 mm width. The thickness of individual samples was measured with digital calipers.

PEUR1250 was also electrospun onto aluminum foil with controlled fiber diameters and degrees of alignment as described elsewhere (Appendix C.2.3) [190]. To form random, isotropic meshes, aluminum foil was mounted onto a stationary target and electrospinning was performed with a 22 gauge Teflon tipped needle using a 15 kV potential, a throw distance of 15 cm, and a syringe flow rate of 5 mL/h. PEUR concentrations of 7.5, 11.0 and 13.5 wt% in 1,1,1,3,3,3-hexafluoro-2-propanol (HFIP) were made to produce meshes with different fiber diameters. To form meshes comprised of aligned fibers, aluminum foil was mounted on a 6.2 cm diameter wire mesh drum and a 13.5 wt% PEUR1250 solution was electrospun under the conditions described above. The drum was rotated at rates of 600 and 1300 rpm (corresponding to linear velocities of 2.0 and 4.4 m/s, respectively) to produce meshes with different degrees of fiber alignment. After electrospinning, the meshes were carefully peeled off of the aluminum foil for imaging and mechanical testing.

4.2.4 Scanning Electron Microscopy (SEM)

The diameter and degree of alignment of electrospun fiber meshes were determined by analysis of SEM images as described previously (Section 3.2.3) [82]. Briefly, electrospun meshes were mounted, sputtercoated with a 10 nm layer of palladium (Model 208HR, Cressington Scientific Instruments, Cranberry Township, PA), and images were acquired using a LEO 1550 Field Emission SEM (Carl Zeiss SMT, Thornwood, NY) operating at 5 kV with a 16

mm working distance. Resultant images were imported into ImagePro Plus software (ICube, Crofton, MD) for analysis of fiber diameter and alignment. The degree of alignment was characterized by the angular standard deviation as described previously (Section 3.2.2) [82]. The diameter and alignment of at least 150 fibers were analyzed for each sample.

4.2.5 Mechanical Testing

The tensile moduli of the PEUUR1250 and PEUUR2000 were determined, as described elsewhere [190], using ASTM D412-98a with modifications. Cast films were soaked in PBS overnight and then tested at 37°C in PBS. The samples were pulled at a rate of 10 mm/min to 400% strain using a Tytron250 (MTS, Eden Prairie, MN). After testing, the Young's modulus, tensile strength, percent elongation, and yield strain were measured from the stress/strain curve with $n = 3$ samples.

The tensile moduli of electrospun PEUUR meshes were determined using 15×10 mm strips that were incubated in PBS at room temperature for approximately 15 h prior to testing. Cyclic testing was performed under the same conditions that were used in stretch experiments (Section 5.2.6) (e.g. in PBS with a gauge distance of 10 mm, a frequency of 0.5 Hz, and a maximum strain of 20%). The temperature was maintained at 37°C using a heated water bath. Isotropic meshes were tested in only one direction, and samples of oriented meshes were tested either parallel or perpendicular to the direction of fiber alignment. A total of 220 cycles were performed, and the Young's moduli were reported based on the last cycle using the initial linear region of the stress strain curve – typically between 10 and 20% strain. Values for the thickness of the meshes were required for the calculation of stress, and they were calculated from the mesh mass, length, width, and density using an estimated porosity of 60%. This porosity is assumed based on published mercury intrusion porosimetry measurements of electrospun meshes [118]. The thicknesses for these samples were on the order of 0.1 mm. Young's moduli are presented as mean \pm standard deviation for $n = 3$ meshes.

4.2.6 Further Characterization

Differential scanning calorimetry (DSC) (TA Instruments Q100, New Castle, DE) was performed to determine the glass transition temperature, melting temperature, and crystallinity of the PEUUR1250 and PEUUR2000. The samples were heated from 25°C to 120°C (10°/min),

cooled from 120°C to -90°C (5°/min), then reheated from 25°C to 120°C (10°/min), and heat flows were reported on a unit mass basis. The glass transition temperatures were determined at the inflection point of the second heating curves, and percent crystallinities were determined from the integrated melting peaks using Origin software. Percent crystallinity was only measured for the second heating curve because the baselines for the first heating curve could not be determined. Percent crystallinities were calculated using a heat of fusion for PCL with 100% crystallinity of 136 J/g [205].

4.3 Results and Discussion

4.3.1 Bulk Properties

The densities of the two polymers were determined with the pycnometer and then used in calculations of mesh thickness. The densities of the two polymers were similar, with a density of $1.13 \pm 0.022 \text{ g/cm}^3$ for PEUUR1250 [190] and a density of $1.09 \pm 0.011 \text{ g/cm}^3$ for PEUUR2000. These densities are very similar to a published value for PCL from the literature (1.13 g/cm^3) [206] as well as the densities for PDAB and HDI reported by the company (1.14 and 1.04 g/cm^3 , respectively)

Mechanical tests were performed on PEUUR1250 and PEUUR2000 films to characterize the Young's moduli, tensile strengths at break, percent elongations, and yield strains of these elastomers (**Figure 4.2**). The elastic moduli of the cast films in PBS at 37°C for PEUUR1250 was $4.1 \pm 0.31 \text{ MPa}$ [190] and for PEUUR2000 was $18 \pm 0.59 \text{ MPa}$. Furthermore, the PEUUR2000 had a yield point of approximately 15% while the PEUUR1250 did not exhibit a yield point. These materials exhibited percent elongations above 400% for PCL1250 and above 800% for PCL2000. These results suggest that the polymers are able to exhibit elastomeric behavior at strains greater than those exerted on natural ACL [16] and those that are commonly used in stretch bioreactors *in vitro* [3, 78, 119]. However, the moduli are two orders of magnitude lower than natural ligament tissue [10].

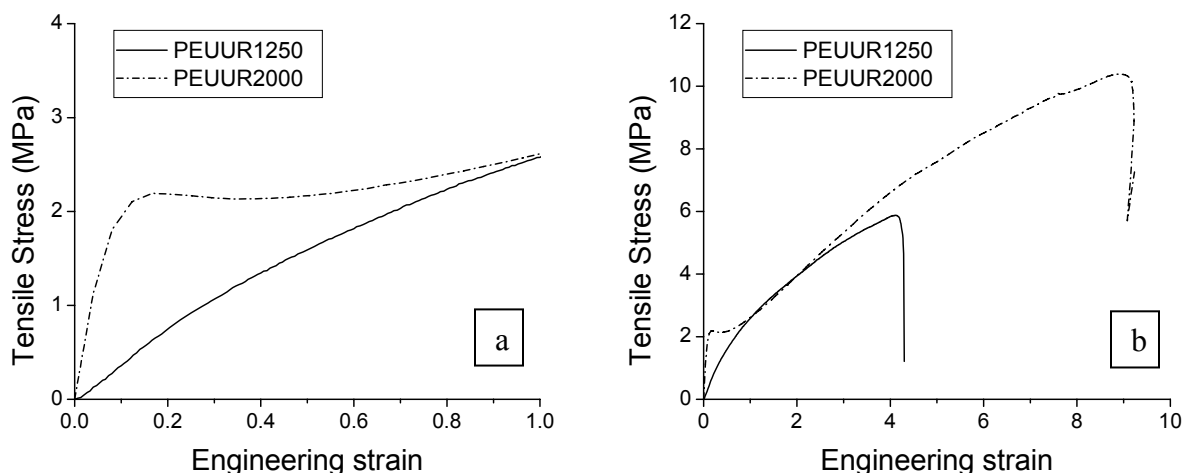


Fig. 4.2. Stress strain curves of both a) the initial linear region and b) the entire curve for cast polymer dogbones tested in PBS at 10 mm/min and 37°C (representative samples).

The thermal properties of the meshes were determined by DSC (**Figure 4.3**). The second heating curve results were analyzed to determine a glass transition temperature (T_g) of -45°C for the polymers and melting points (T_m) of 25°C for PEUUR1250 and 39°C for PEUUR2000; however, the polymers started melting earlier because of broad melting distributions. Compared to the second heating curve, the melting points were elevated to 50°C or greater for the as-processed materials (i.e. the first heating curve). Differences in melting points with thermal history has also been observed previously in other PEUURS [96]. Based on the second heating curve, the PEUUR2000 and the PEUUR1250 had percent crystallinities of 27.6% and 17.8% respectively, indicating that the PEUUR2000 is a more crystalline material. Percent crystallinity was not measured for the first heating curve because the baselines could not be determined.

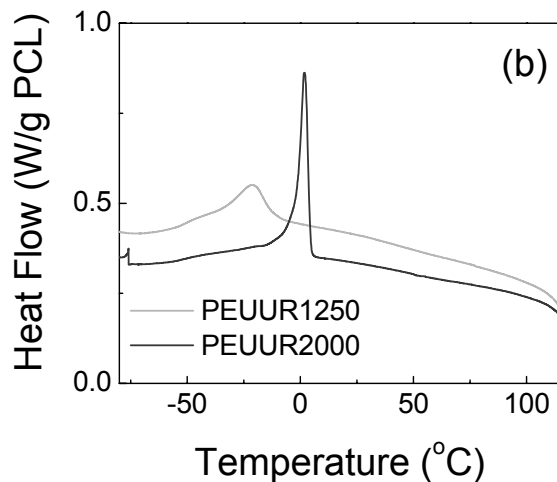
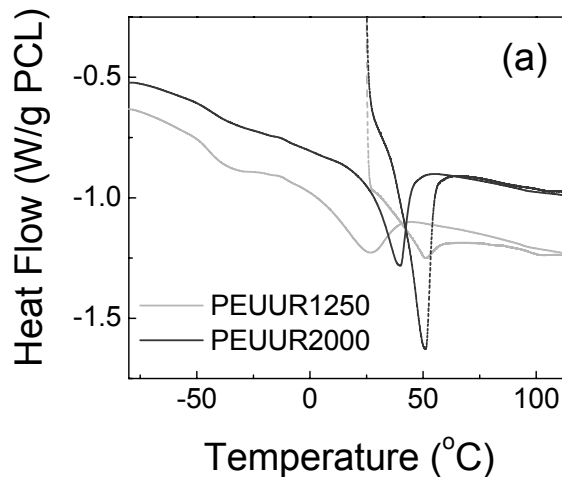


Fig. 4.3. DSC results of the PEUURs showing a) heating curves (dashed line for initial heating and solid line for second heating) and b) the cooling curves.

DSC analysis was also performed on three different batches of PEUUR2000. The melting temperatures for these tests were lower than the value of 39°C determined above and they were found to vary from 32.7 to 36.2°C. Gel permeation chromatography (GPC) was also performed on these same batches of PEUUR2000, and the M_n was found to vary from 67,700 to 89,900 Da. This result indicates that some variation in polymer molecular weight is present between different batches of polymer, and this may result in variation in other properties of the polymer (e.g. glass transition temperature and tensile strength).

4.3.2 Properties of Electrospun Meshes

The Young's modulus of electrospun PEUUR1250 meshes with varying fiber diameters and alignments were determined by testing different samples parallel and perpendicular to the direction of alignment. Briefly, electrospun meshes with fiber diameters from 0.27 to 0.90 μm and angular standard deviation of 54.6 to 29.9° were found to have elastic moduli in PBS at 37°C ranging from 0.43 to 1.2 MPa. The modulus increased with electrospinning conditions that produce increasing fiber alignment (when tested parallel to the direction of alignment) as well as increasing fiber diameter (**Figure 4.4**). However, these trends may also occur because of differences in crystallinity, fiber-fiber contacts, or porosity between electrospinning conditions (discussed further in Appendix C.4) [190]. This result is in agreement with Courtney et al. who showed that the tensile modulus of PEUUR meshes in water at room temperature also increased with electrospinning conditions that produce higher degrees of fiber alignment [94]. In addition, Thomas et al. showed that while individual electrospun PCL fibers had lower Young's moduli with increasing drum rotational speed, the modulus of the overall mesh increased because of increased fiber alignment [207]. These results assumed constant fiber density throughout the mesh when calculating the mesh thickness [190].

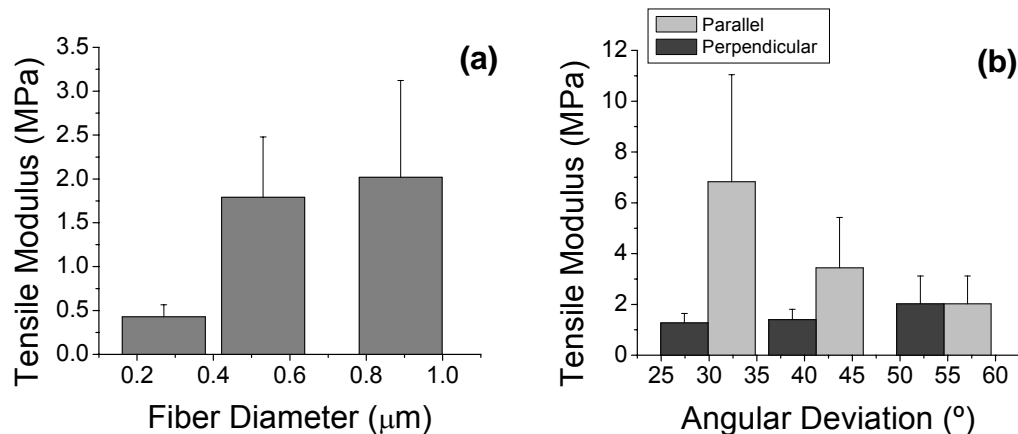


Fig. 4.4. Mesh moduli for a) different fiber diameters ($n = 3$) and b) different degrees of alignment ($n = 3$) tested cyclically in PBS at 37°C and 0.5 Hz.

The PEUUR1250 meshes exhibited hysteresis during cyclic mechanical testing when tested in PBS, consistent with viscoelastic behavior (**Figure 4.5**). Furthermore, the point of maximum stress for each cycle in the electrospun PEUUR1250 meshes decreased during the initial ~100 cycles, possibly due to breaking of fiber-fiber contacts (**Figure 4.6**). However, after approximately 100 cycles further decreases occurred more slowly, suggesting that the polymer may be elastomeric. The profiles were similar for meshes with random and aligned fibers.

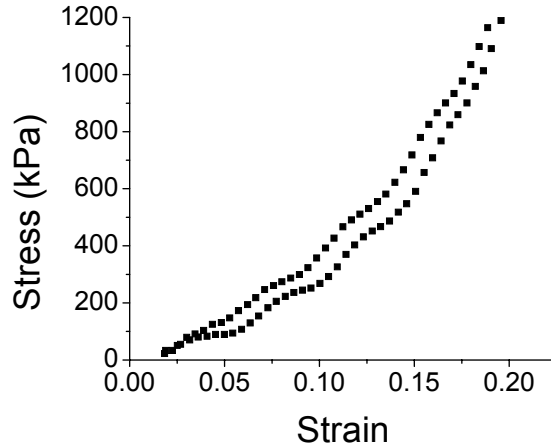


Fig. 4.5. Stress-strain curve showing hysteresis for a representative sample (0.89 μm diameter electrospun PEUUR1250 meshes with 29.9° angular standard deviation tested parallel to the direction of fiber alignment) in PBS at 37°C and 0.5 Hz.

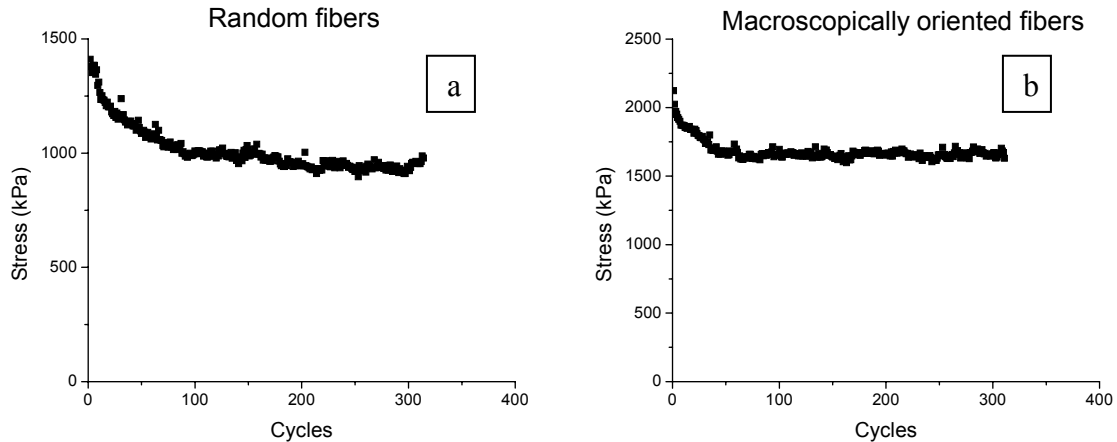


Fig. 4.6. Profile of maximum stress with the number of cycles for PEUUR1250 meshes for a) 0.47 μm diameter randomly oriented fibers and b) 0.61 μm diameter fibers tested parallel to the direction of alignment (33.4° angular standard deviation). Cyclic testing was performed in PBS at 0.5 Hz, 20% maximum strain, and 37°C. Profiles are representative of other fiber diameters and alignments.

4.4 Conclusions

The characterization of the PEURs suggests that they are elastomeric materials which are capable of undergoing repetitive stretch in a bioreactor *in vitro*. The maximum stress for PEUR1250 at 20% maximum strain does decrease after the initial 100 cycles, but afterward no significant reductions occur. In addition, the PEUR2000 has a melting temperature greater than the temperature used for cell culture (37°C) while the PEUR1250 does not. However, with their melting distributions, both polymers start melting before the cell culture temperature. Finally, the most highly aligned meshes have the highest modulus. These results suggest that highly aligned electrospun PEUR2000 meshes are more desirable for future ligament tissue engineering studies (Chapter 5). However, the moduli are still less than 18 MPa and significantly lower than that of native human ligament (i.e. approximately 111 MPa) [10, 88], and would require *in vitro* pre-conditioning for use in a ligament tissue engineering construct. Cyclic mechanical stretch may be able to provide the pre-conditioning required for cells to deposit load-bearing collagen fibrils prior to implantation *in vivo*.

4.5 Acknowledgments

The authors thank Dr. Garth L. Wilkes for the use of the electrospinning device, Sudip Chowdhury for performing DSC measurements, and funding from the Charles E. Culpeper Foundation (03-130) and the Institute for Critical Technologies and Sciences at Virginia Tech.

Chapter 5: The Role of Electrospun Polyurethane Fibers and Mechanical Stretch on Bone Marrow Stromal Cells Orientation and Differentiation

*Chris A. Bashur¹, Linda A. Dahlgren², Scott A. Guelcher³,
Aaron S. Goldstein^{1,4}*

¹ Department of Chemical Engineering, and
²Department of Large Animal Clinical Sciences,
Virginia-Maryland Regional College of Veterinary Medicine,
Blacksburg, VA 24061

³Department of Chemical Engineering, Vanderbilt University
Nashville, TN 37235

⁴School of Biomedical Engineering and Sciences, Virginia Polytechnic Institute
and State University, Blacksburg, VA 24061

Abstract

A tissue-engineered ligament produced using electrospun fibrous surfaces, mesenchymal stem cells, and mechanical stimulation is a promising graft for anterior cruciate ligament reconstruction. The electrospun surfaces have been shown to guide cell orientation in static culture, and the mechanical stimulation has been shown to increase the synthesis of ligament-like extracellular matrix. One article to our knowledge has been performed to test the affect of the topographic features presented by electrospun fibers on cell alignment and behavior in conjunction with mechanical stretch. However, this article – along with other articles on model silicone surfaces – has focused on the expression of non-specific markers of the ligament phenotype including collagen types I and III. Therefore, in this study electrospun fibers and smooth surfaces have been stretched to determine the effect of mechanical stimulation on cell orientation and the selective ligament markers scleraxis and tenomodulin. This study shows that cells are able to attach and express ligament-like extracellular matrix components (i.e. collagen type I and decorin) as well as other markers of fibroblastic and myofibroblastic differentiation (i.e. scleraxis, tenomodulin, and α -smooth muscle actin) on both smooth poly (dimethylsiloxane) and electrospun surfaces with the application of uniaxial mechanical stretch. On electrospun surfaces the cells were directed to orient parallel to the direction of fiber orientation through topographic cues, and they remained oriented with the application of stretch. On silicone surfaces cells responded to stretch by orienting perpendicular the direction of stretch. Finally, while the expression of α -smooth muscle actin appeared to be elevated on electrospun surfaces, no significant effects of cyclic stretch on gene expression were observed after two days. Future work is to apply a longer duration of mechanical stimulation.

5.1 Introduction

More than 150,000 reconstructive anterior cruciate ligament (ACL) surgeries are performed annually in the United States [7]. Autologous graft taken from a patient is currently the primary choice for ACL replacement, but drawbacks with this grafting material include limited donor tissue supply and donor site morbidity [15, 16]. A tissue-engineered ligament is a promising alternative to autograft for ACL reconstruction [1, 2, 7, 16]. With this strategy, cells are seeded onto a biomaterial scaffold that provides the area for cell attachment. The scaffold also provides the initial mechanical properties of the graft before the extracellular matrix (ECM) deposited by the cells is able to organize and provide mechanical strength. The cellular component is frequently mesenchymal stem cells (MSCs) because of their high proliferative activity and ability to differentiate into the ligament like fibroblastic phenotype [9, 54]. Further, the scaffolds are commonly produced through the electrospinning process because electrospun meshes are able to guide cell attachment through the contact guidance phenomenon, unlike meshes produced through other conventional techniques (e.g. extrusion) [82, 150]. Finally, the additional component of mechanical stimulation is commonly employed using a stretch bioreactor to increase the expression and deposition of ligament-like ECM by MSCs and ligament fibroblasts [3, 4, 78, 81].

A ligament-like ECM would contain components of natural ligament organized to form oriented collagen fibrils that are strong in the direction of tension [16]. Components of natural ligament include proteins (e.g. collagen types I, III, and V, and elastin), proteoglycans (e.g. decorin), and glycoproteins (e.g. tenascin-C and fibronectin) [19, 22]. Importantly, while these components comprise the ECM of ligaments, they are not ligament specific and are common to many types of soft tissues [19, 21]. Therefore, other markers must also be examined. Recently, scleraxis and tenomodulin have been identified as selective markers of ligament fibroblasts. Scleraxis is a transcription factor that is expressed during the early stages of musculoskeletal development [34] and is necessary for development of mature tendon tissue [35]. Tenomodulin is a transmembrane glycoprotein [36] that is induced by scleraxis [37], and is thought to aid in the organization of collagen into fibrils [38].

In static culture, cellular deposition of oriented collagen fibrils has been shown on aligned topographic features with sizes less than 10 μm [3, 84]. In these studies, the topographic features are able to guide cell orientation through the contact guidance phenomenon [115, 165-

167, 208], and oriented cells have been shown to produce orientated ECM [84]. Both model micro-grooved poly(dimethyl-siloxane) (PDMS) surfaces [115, 166, 168, 169] and porous electrospun meshes [82] have topographic features small enough to guide cell attachment, morphology, and orientation. Recent research has shown that different topographic features may effect the expression of ECM components [150], in agreement with the established link between changes in cell morphology and changes in mRNA expression [156].

The application of mechanical stimulation has been shown to increase the expression and deposition of markers of ligament-like ECM by MSCs and ligament fibroblasts [3, 4, 49]. For example, the deposition of both total collagen and collagen type I – the primary component of ligament ECM – have been shown to be increased with stretch [3, 4]. The expression of α -smooth muscle actin, a marker of contractile fibroblasts, has also been shown to be induced in fibroblastic cells in response to stretch [78]. In addition, tenascin-C and elastin expression have also been shown to be induced with stretch [49, 80]. The expression of the more specific marker scleraxis (*scx*) was found to be induced with mechanical stretch in a collagen gel [81], but has not been measured on electrospun fibers in response to stretch.

Ligament fibroblasts and MSCs cultured on different types of scaffolds – including smooth and micro-grooved PDMS surfaces [84], collagen hydrogels [49], and large diameter fibers [50] – have been shown to respond to mechanical stretch. However, the effects of the different scaffold chemistries, topographies, and mechanical properties on cell behavior in combination with the application of stretch still need to be elucidated. Differences in these scaffold properties have been shown to affect both cell orientation and differentiation in static culture [18, 82, 86, 151], and they may also affect cell orientation and differentiation in response to stretch. The effect of topography on cyclically stretched cells has been studied on model PDMS surfaces with and without micro-grooves. On smooth PDMS surfaces, cells have been shown to reorient perpendicular to the direction of stretch [75]. Consequently, this cell realignment will result in the deposition of aligned ECM that is weak in the direction of stretch [84]. The addition of micro-grooves aligned in the direction of stretch has been shown to keep the cells oriented parallel to the stretch direction [78, 84].

Electrospun scaffolds present topographic cues similar to the micro-grooved surfaces, however when strain is applied, the topographic features of electrospun meshes will not deform in the same manner as a solid microgrooved surfaces. Differences in the deformation of the

surfaces should result in different mechanical stimuli being placed on the cells. In the only study on the effect of mechanical stretch on electrospun fibers, Lee et al. found that ACL fibroblasts remained oriented on the fibers when mechanical stretch was applied, and that the amount of total collagen that was deposited on the substrate increased when stretch was applied to aligned electrospun meshes [3]. They found that ACL fibroblasts will respond positively to uniaxial mechanical stretch, but total collagen deposition cannot be used to determine the specific phenotype of the cells. MSCs can differentiate into several types of supporting tissue, so for MSCs the expression and synthesis of more specific markers of ligament-like fibroblast differentiation are important to ensure that a functional ligament-like graft is being produced.

In this study, bone marrow stromal cells (BMSCs) were seeded onto oriented scaffolds and cyclic stretch was applied to the cell-seeded mesh to determine if MSCs differentiate into oriented ligament-like fibroblasts on electrospun fibers with the application of mechanical stretch. Electrospinning of an elastomeric poly (ester-urethane urea) (PEUUR) onto a rotating target was performed to create an oriented fiber mesh to guide cell alignment and suppress cell reorientation in response to stretch. The expression of α -smooth muscle actin, markers of ligament-like ECM (i.e. collagen type I and decorin), and more specific markers of ligament differentiation (i.e. scleraxis and tenomodulin) were measured.

5.2 Materials and Methods

5.2.1 Materials

All materials were purchased from Fischer Scientific (Pittsburgh, PA), all chemicals were purchased from Sigma-Aldrich (St. Louis, MO), and all biological supplies were purchased from Invitrogen (Gaithersburg, MD) unless otherwise noted. A linear segmented PEUUR – consisting of 2000 Mw poly (ϵ -caprolactone) (PCL) end-capped with 1,6-diisocyanatohexane and chain extended with 1,3-propanediol bis (4-aminobenzoate) – was synthesized. The segmented degradable PEUUR elastomer was synthesized using a standard two-step technique as previously described [150]. The PCL is the degradation tie of the PEUUR, so the polymer is expected to degrade between 2 to 3 years similar to pure PCL [93].

5.2.1 Electrospinning

The PEUUR was electrospun to form fused-fiber meshes with controlled fiber diameters and degrees of fiber orientation as described previously [82]. Briefly, a 6 cm diameter drum was wrapped with aluminum foil and rotated at a linear velocity of 7.9 m/s to induce orientation in the electrospun fibers. Electrospinning was performed under ambient conditions using a 22 gauge steel needle, a 15 kV potential, a throw distance of 15 cm, and a syringe flow rate of 3 mL/h. Electrospinning was performed on three different occasions using 10 wt% solutions of PEUUR in 1,1,1,3,3,3-hexafluoro-2-propanol (HFIP). These concentrations were used because they have been shown to produce average fiber diameters of approximately 0.5 microns with a similar polymer, PEUUR1250, and within the range known to induce contact guidance [142]. Following electrospinning, meshes were peeled off of the aluminum foil and soaked in ethanol for 5 days followed by deionized water for 2 days to remove residual HFIP. The meshes were then air dried and stored in a desiccator until use.

5.2.2 Scanning Electron Microscopy (SEM) Analysis

For SEM analysis of fiber diameter and orientation, the electrospun surfaces were mounted onto studs and sputtercoated with a 20 nm layer of palladium (Model 208HR, Cressington Scientific Instruments, Cranberry, PA). These surfaces were then imaged with a LEO 1550 Field Emission SEM (Carl Zeiss SMT, Thornwood, NY) operating at 5kV with a 16 mm working distance. Resultant images were imported into ImagePro Plus software (ICube, Crofton, MD) and the orientation and diameter were determined for at least 100 fibers per sample. The surfaces were measured manually for all fibers in the SEM image with clearly defined edges. Fiber orientation was characterized by average angular standard deviation, with the mean angle of orientation – relative to the direction of rotation – and average angular standard deviations (ASDs) calculated from a wrapped normal distribution [82].

5.2.3 Stretch Bioreactor Design

Prototype mechanical stretch bioreactors were designed to perform mechanical stimulation of electrospun meshes and smooth PDMS controls. The bioreactors include a poly(carbonate) chamber that is gas sterilized with ethylene oxide and a removable sample holder that is sterilized separately by γ -irradiation and then loaded into the chamber (**Figure 5.1**). The

space inside the holder is 11.3×4.00 cm and can hold up to 6 samples that can be loaded individually prior to sterilization. Further, ports allow for both the sterile exchange of gases between the air and the inside of the box as well as the changing of medium. The moveable arm is sealed with a neoprene bellow and driven by a Tytron250 (MTS, Eden Prairie, MN).

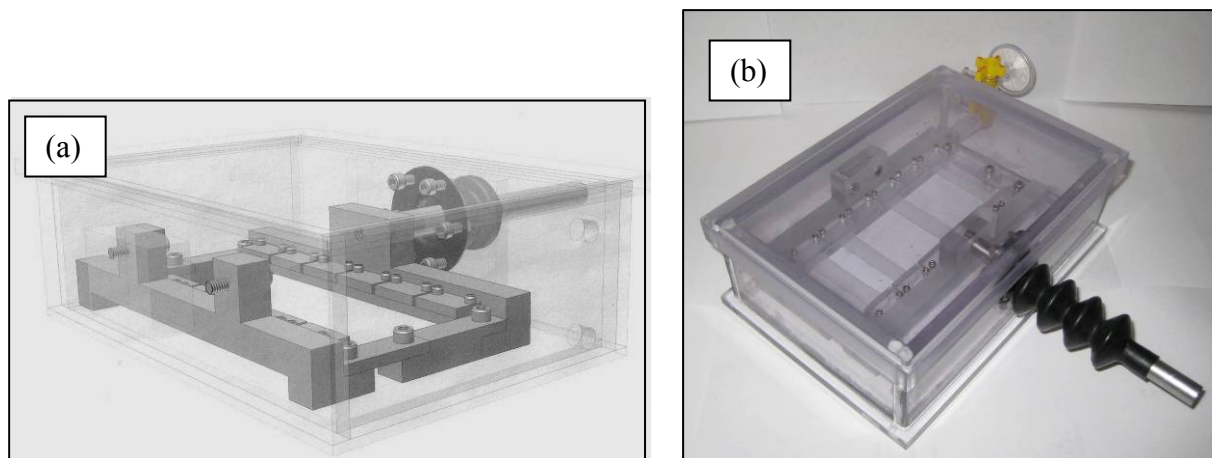


Figure 5.1: a) Diagram and b) an image of the stretch bioreactor

5.2.4 Bioreactor Assembly and Sterilization

For cell culture studies four chambers and holders were assembled and sterilized. Prior to sterilization, electrospun PEUUR meshes and medical grade smooth PDMS films were cut into strips (1×5 cm) and mounted in the sample holders with the fibers oriented parallel to the direction of stretch. Mesh samples were pre-stretched approximately 33% (1 cm) when loaded into the holder and PDMS samples were pre-stretched 17% (0.5 cm) to ensure that the surfaces were in tension. The 33% pre-stretch for the meshes was chosen because it provided a similar degree of alignment to the as-electrospun meshes (i.e. prior to subsequent processing). The holders were inserted in the chambers and then the bioreactors were placed under ultraviolet (UV) light for 30 min for further sterilization. To facilitate cell adhesion $2 \mu\text{g/mL}$ fibronectin (Fisher) in phosphate buffered saline (PBS, Fisher) was added to surfaces at room temperature and allowed to adsorb for 2 hours. Substrates were kept wet in PBS until cell seeding.

5.2.5 Cell Culture and Cell Seeding

Cell studies were performed using rat bone marrow stromal cells (BMSC) isolated from male 125-150 g Sprague-Dawley rats (Harlan, Dublin VA) in accordance with the Institutional

Animal Care and Use Committee at Virginia Tech [96]. Dispersed whole marrow extracts were grown on 100 mm tissue culture poly(styrene) Petri dishes (Fisher) until confluence (approximately 10 days) in growth medium consisting of Minimal Essential Medium α modification (α -MEM, Invitrogen, Bethesda, MD) with 10% fetal bovine serum (FBS Gemini, Calabasas, CA) and 1% antibiotic/antimycotic. Cells were then enzymatically lifted using trypsin/EDTA, split 1:2, and seeded into fresh 100 mm Petri dishes for cell morphology studies. For mRNA expression studies, the cells were lifted and frozen in growth media with 10% dimethylsulfoxide (DMSO) at 1:2, and then replated when ready for use. (This process selectively increases the concentration of the proliferative, plastic-adherent fraction, which includes a population of mesenchymal progenitor cells. However, it does not select for specific antigen markers nor achieve a homogeneous cell population.) When the cells were close to confluence, they were passaged again and allowed to grow for 3 or 4 days.

Second passage cells were enzymatically lifted, and then seeded onto electrospun meshes and PDMS strips inside of the bioreactor chamber at a density of approximately 5.0×10^4 cells/sample (1.2×10^4 cells/cm²) using approximately 0.5 mL of growth medium. The samples were incubated at 37°C and 5% carbon dioxide for 2 h prior to filling the entire chamber with 175 mL of media and then incubating again. To determine cell morphology, the mesh area was filled with the cell suspension, so the extra 2 h incubation step was not required. Thereafter, half of the medium was replaced after 3 days, and samples were stretched after 3 and 4 days.

5.2.6 Mechanical Stretch

Cyclic stretch studies were performed on two bioreactors on days 3 and 4 (for 1 h daily). Cyclic stretch was performed uniaxially at 0.5 Hz frequency with 8% strain (in addition to the 33% static strain already applied). These conditions are within the range that has been shown to elicit a cell response in previous stretch studies for mature ligament fibroblasts and MSCs [4, 75, 145, 154, 155]. The ambient temperature was 25°C, but media remained warm throughout stretch. Two control bioreactors with 33% static stretch were also removed from the incubator during this time. After stretch on day 4, the bioreactors were stored in the incubator for approximately 0.5 hours and then media was drained from the bioreactors. Cells were analyzed to determine cell morphology and mRNA expression of ECM proteins *Colla1*, decorin, tenomodulin, scleraxis, and α -smooth muscle actin.

5.2.7 Cell Morphology

After mechanical stretch, cell morphology and orientation was determined by imaging fixed and fluorescently labeled cells. Briefly, 1 mL of 3.7% methanol free formaldehyde (Polysciences, Inc., Warrington, PA) in PBS was added to the top of the samples and incubated for approximately 15 min at room temperature. The surfaces were washed one time in PBS, and then placed in 0.1% Triton×100 in DI water for approximately 1 h. The surfaces were washed three times with PBS. Next, the samples were cut out of the holder and stained with 1 mL of 15 $\mu\text{L}/\text{mL}$ rhodamine-phalloidin (Molecular Probes, Eugene, OR) on a slide for approximately 1 h to stain filamentous-actin. Finally, the extra liquid was removed and the samples were mounted using soft mount with 4',6-diamidino-2-phenylindole (DAPI) to stain the nuclei (Vector Laboratories, Inc., Burlingame, CA).

Fluorescence images were obtained at 20× magnification with a near UV filter for the nuclei and a wide green filter for the filamentous-actin using an Olympus IX50 microscope (Opelco, Sterling, VA) equipped with a cooled CCD camera (Hamamatsu C4742-98-12NRB). Images were focused in phase contrast or in fluorescence with the near UV filter prior to taking images. At least ten pairs of images per substrate were then imported into ImagePro Plus software and an ellipse was fitted to the cells. Cells were only outlined if a nucleus was also visible. Length of the long axis, aspect ratio, projected area, and angle of orientation were measured from fluorescence images for greater than 65 cells per substrate. Mean values for projected cell area, aspect ratio, length of the long axis, and angle for both fibers and cells were calculated per substrate. In addition, the degree of cell alignment – characterized by angular standard deviation – was calculated for each substrate. Statistical analyses were performed using the mean properties of each substrate.

5.2.8 mRNA Expression

Expression of *Coll1a1*, decorin, tenomodulin, scleraxis, and α -smooth muscle actin was determined quantitatively by real-time polymerase chain reaction (PCR). Total RNA was isolated from the cells on day 4 after stretch using the RNeasy Mini Kit (Qiagen, Valencia, CA) according to the manufacturer's instructions. Briefly, lysates were first homogenized with QIAshredder columns (Qiagen) and then were subjected to on-column DNase digestion using DNase I (Qiagen). RNA was quantified using the Quant-It RiboGreen kit (Molecular Probes)

and a fluorescent plate reader (SpectraMax M2, Molecular Devices, Sunnyvale, CA). Equal masses of RNA (50 or 100 ng) were reverse-transcribed to cDNA using SuperScript[®] First-Strand Synthesis kit with random hexamers as primers according to manufacturer's protocol. Real-time PCR was performed in the ABI 7300 Real Time PCR System (Applied Biosystems, Foster, CA) using 50 ng cDNA, Power Sybr[®]Green Master Mix (Applied Biosystems), and specific rat primers for *Colla1*, decorin, α -smooth muscle actin, scleraxis, tenomodulin, and β -actin (the internal reference). *Colla1*, decorin, scleraxis, and tenomodulin primer sequences were designed as previously described (**Table 5.1**) [150]. α -smooth muscle actin primer sequences were designed in Primer Express[®] software (Applied Biosystems) using the NCBI database accession number, and primers for the reference gene, β -actin were developed as described previously [195]. Quantification of target gene expression, relative to smooth PDMS substrates on day 7, was performed using the comparative threshold cycle ($\Delta\Delta C_t$) method [196]. Relative gene expression was reported as $2^{-\Delta\Delta C_t}$, and statistical analysis was performed on the ΔC_t values. Control samples (i.e., total RNA, no template) were used to verify the fidelity of the amplification process.

Table 5.1: Primers for PCR

Gene	Forward primer sequences	Reverse primer sequences	Product Size
Collagen 1 α 1 NM_053304	5' GAGGGCGAGTGCTGTCCTT 3'	5' GGTCCCTCGACTCCTATGACTTC 3'	74 bp
Decorin NM_024129	5' CATCTCCGAGTGGTGCAGTGT 3'	5' GCAATGTTGTGTCAGGTGGAA 3'	76 bp
Scleraxis NM_001130508	5' TCTGCCTCAGCAACCAGAGAAAGT 3'	5' ACTCTTCAGTGGCTTCCACCTTCA 3'	130 bp
Tenomodulin NM_022290	5' CCCACAAGTGAAGGTGGAGAA 3'	5' AACAGTAACCTCTCTCATCCAGCAT 3'	125 bp
α -smooth muscle actin a2 NM_007392	5' CAGGATGCAGAAGGAGATCACA 3'	5' CCGCCGATCCAGACAGAA 3'	56 bp
β -actin NM_031144	5' CGTGAAAAGATGACCCAGATCA 3'	5' CACAGCCTGGATGGCTACGT 3'	72 bp

5.2.9 Statistical Analysis

Results are presented as the mean \pm standard deviation for $n > 60$ fibers/substrate for SEM analysis of fiber diameter and orientation, $n = 3$ coverslips per condition for cell morphology, and $n = 6$ for gene expression. Two replicates were performed for mRNA

expression to prove reproducibility with different batches of cells. Statistical significance was determined in SAS 9.1.3 (SAS Institute Inc. Cary NC) and mixed-model analysis of variance (ANOVA) was used with post-hoc comparisons using the Tukey method with a significance criterion of $p \leq 0.05$.

5.3 Results

5.3.1 Electrospun Meshes

SEM images were analyzed to determine fiber diameter and degree of alignment for the stretch studies. Highly oriented meshes (angular standard deviation of 16.5°) for mRNA measurements were electrospun with an average fiber diameter of $0.89 \pm 0.31 \mu\text{m}$ before they were peeled off the aluminum (**Figure 5.2a**). The meshes contracted after peeling off the aluminum and soaking in ethanol, so in this study they were statically stretched in the bioreactor sample holder to 33% of their current length for SEM analysis (**Figure 5.2b**). The contraction of the PEUUR meshes suggests that initial stresses from the electrospinning process remain in the fibers. While 33% static stretch produced fibers with similar degree of alignment (ASD of 21.5°) to the as-electrospun material, the individual fibers exhibited significant bending (**Figure 5.2b**). SEM analysis also indicated that the average fiber diameter ($0.94 \pm 0.28 \mu\text{m}$) after this additional processing was similar to the as-electrospun material.

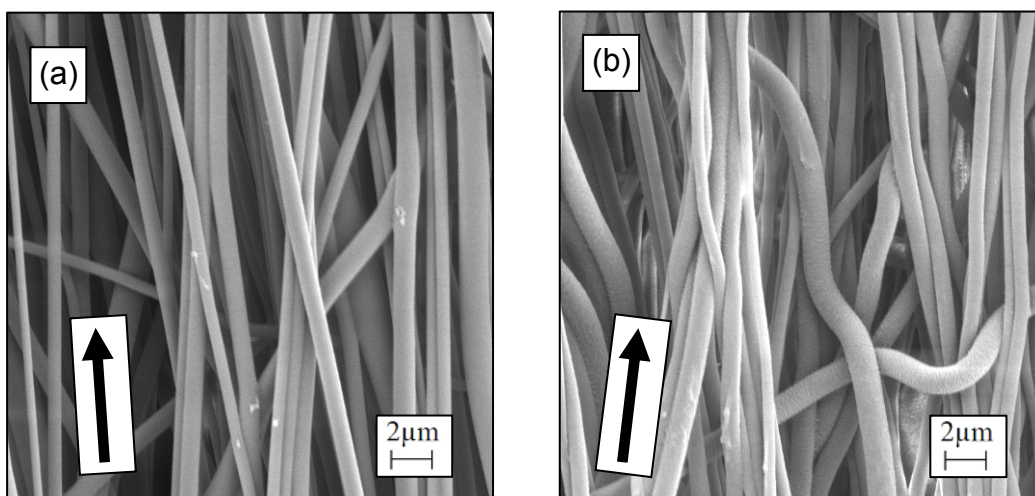


Figure 5.2: Representative images of oriented meshes electrospun both a) as-electrospun on aluminum and b) further processed and statically stretched 25%.

5.3.2 Cell Orientation and Morphology on Meshes

BMSCs were allowed to attach, spread, and proliferate on statically stretched electrospun meshes and PDMS controls for 4 days. In addition, cyclically stretched samples were stretched an additional 8% (at 0.5 Hz for 1 h a day) on days 3 and 4. BMSCs seeded on both smooth PDMS films and electrospun fibers attached to all static surfaces and remained attached following cyclic stretch (**Figure 5.3**). On PDMS films, BMSCs were randomly oriented in the absence of stretch (ASD = 61°); however, BMSCs partially oriented perpendicular to the direction of stretch (orientation 86.3° from the stretch direction and ASD = 41°) (**Table 5.2**). On electrospun meshes, BMSCs aligned with the fibers independent of stretch (orientation < 3° from the stretch direction and ASD < 16 °). These results demonstrate that the cells exhibit good alignment on electrospun surfaces, but poor alignment on the smooth surfaces.

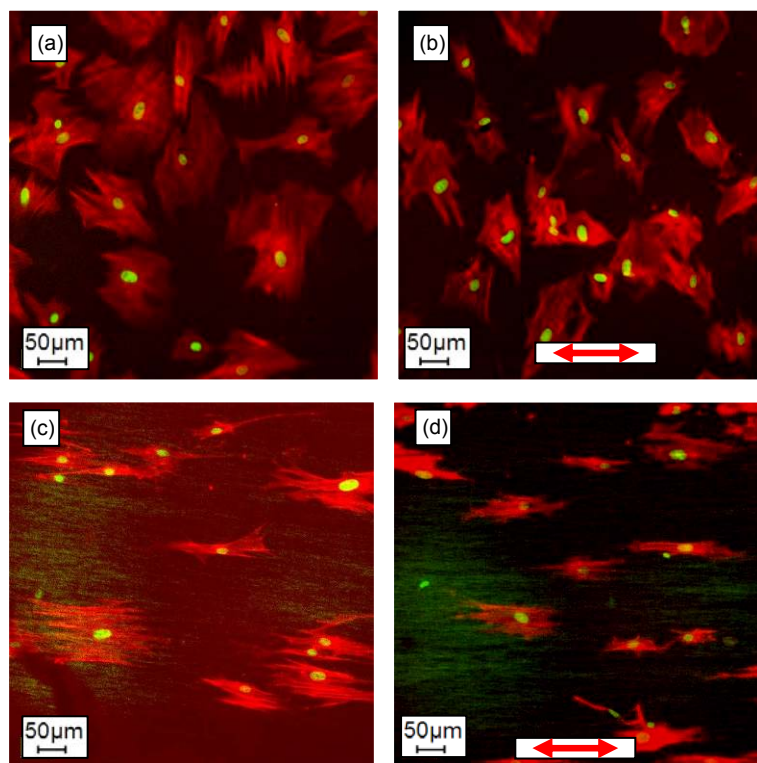


Figure 5.3: Representative images of BMSCs after 4 days on silicone surfaces with and without stretch (a and b respectively) and on electrospun meshes with and without stretch (c and d respectively). Overlay images were constructed by merging the actin-cytoskeleton (red) and the nuclei (green) images of fixed cells. For meshes, some electrospun fibers also appear as faint green in the background.

Table 5.2. Cell alignment on meshes and PDMS control surfaces. Angular standard deviation of cells for and cell orientation relative to the direction of fibers or stretch for $n = 3$ samples.

Condition	Cell Angular Deviation (°)	Difference in Mean Angle (°)
PDMS Static	61.0	–
Stretch	41.0	86.3
Mesh Static	12.7	2.2
Stretch	15.3	0.1

Cell morphology was affected by both mechanical stretch and the type of surface (**Figure 5.4**). The projected cell area was lower ($p < 0.03$) and the aspect ratio higher ($p < 0.002$) on the fibrous surfaces, consistent with the cells assuming a spindle shaped morphology. With the application of stretch, the BMSCs projected cell area and long axis decreased ($p = 0.01$ and 0.03 respectively for smooth control surfaces), while the aspect ratio was not affected. The projected cell area decreased with the application of stretch by 30% on the PDMS surfaces compared to only 21% on the meshes.

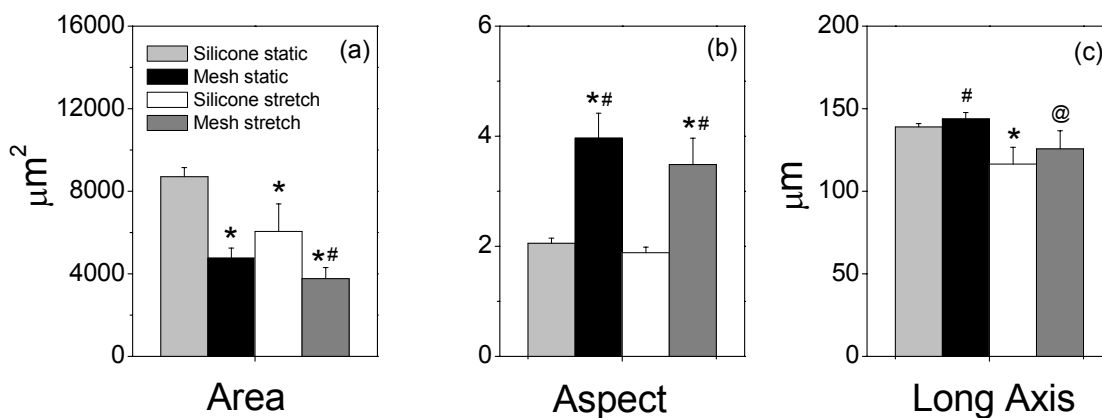


Figure 5.4: Effect of mechanical stretch and type of surface on BMSC a) projected cell area, b) aspect ratio, and c) length of long axis. Statistical significance is denoted by an asterisk from PDMS static, a pound sign from PDMS stretch, and @ from mesh static for $n = 3$ samples.

5.3.3 ECM Expression

Real-time PCR was performed to determine the effect of fiber architecture on the expression of ECM proteins Coll1 α 1, decorin, tenomodulin, scleraxis, and α -smooth muscle actin. The results indicate that α -smooth muscle actin expression appeared to be induced on meshes compared to PDMS surfaces, although this difference is not statistically significant. However, the other genes do not have significantly different expression with different surfaces and with or without stretch (**Figure 5.5**).

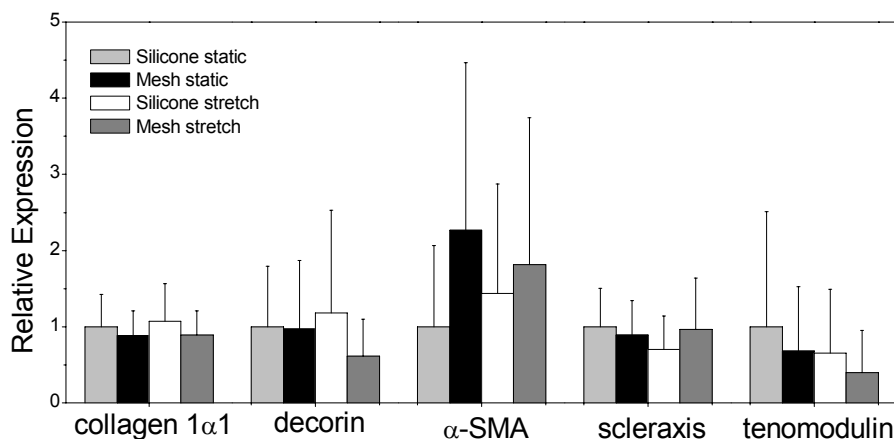


Figure 5.5: PCR results normalized by the β -actin housekeeping gene for the different surfaces with and without stretch for $n = 6$ substrates.

5.4 Discussion

In this study, electrospun PEUUR meshes were produced with an average fiber diameter of $0.94 \pm 0.28 \mu\text{m}$ and an alignment (characterized by ASD) of 21.5° . BMSCs were seeded on these electrospun meshes and smooth PDMS control surfaces to determine the effect of electrospun meshes on the cell orientation, morphology, and mRNA expression with the application of cyclic stretch. On cyclically stretched and statically stretched electrospun meshes, BMSCs aligned with the fibers – average orientations $<3^\circ$ from the direction of fiber orientation and average angular standard deviations (ASDs) $<16^\circ$. On PDMS films, BMSCs were randomly oriented in the absence of stretch (ASD of 61.0°), but after the application of stretch, BMSCs partially oriented perpendicular to that direction – orientation 86.3° from the stretch direction and ASD of 41.0° . Further, BMSCs projected cell area and long axis decreased on both the electrospun and smooth control surfaces with the application of stretch. The projected cell area

was lower and the aspect ratio higher on the fibrous surfaces. In addition, the expression of α -SMA appeared to be induced on electrospun meshes compared to PDMS surfaces. Finally, the application of stretch did not have a significant effect on mRNA expression in this study.

Common electrospinning techniques were used in this study to produce highly oriented meshes with diameters within the range known to induce contact guidance [82, 150]. However, these meshes contracted and lost alignment when they were peeled off the aluminum mandrel. This contraction was not observed in other studies with oriented poly (lactic-*co*-glycolic acid) scaffolds (Appendix B). This suggests that the elastomeric PEUUR meshes are able to exhibit significant elastic deformation in response to the mechanical forces produced by the rotating mandrel, and the meshes are able to retain part of forces without undergoing stress relaxation. To reestablish the aligned fiber topography of the meshes, they were stretched to 133% of their contracted length. The resultant orientation of these stretched surfaces was similar to the orientation of the as-spun materials (21.5° compared to 16.5°).

In this study, the electrospun meshes were able to guide cell alignment without the application of cyclic stretch, consistent with previous results [82, 150]. In addition, the electrospun meshes were able to orient cells parallel to the direction of fiber alignment independent of cyclic mechanical stretch – in agreement with results by Lee et al. using human ligament fibroblasts [3]. The presence of oriented topographic cues allowed the cells to remain aligned with the fibers – similar to previous work on model micro-grooved surfaces [84]. However on smooth PDMS surfaces, the cells aligned perpendicular to the direction of stretch (Figure 5.3, Table 5.2) consistent with previous work [75, 209]. However, greater cell reorientation on smooth surfaces has been observed previously [155], suggesting that in this study less mechanical stimulus was translated to the cells. The tendency for cells to reorient perpendicular to the direction of stretch on smooth surfaces is thought to be an avoidance reaction by the cells to the stretching of their cytoskeleton and focal adhesion contacts [75]. Cells have been shown to lose some of their focal adhesion contacts with the application of mechanical stretch – and round up if too much strain is applied [75]. The results from this study suggest that the phenomenon of contact guidance has a greater role of in the reestablishment of cell contacts on electrospun meshes than the tendency for cells to resist the deformation of their cytoskeleton.

In addition to BMSC orientation, electrospun fibers also affected the morphology of the cells both with and without stretch. The projected cell area was lower and the aspect ratio higher on the fibrous surfaces, consistent with previous research where electrospun fibers were not stretched but instead supported on coverslips [150]. This result suggests that on meshes BMSCs assume a smaller and more spindle shaped morphology – the characteristic shape of ligament-like fibroblastic cells [176, 210]. However, on smooth surfaces BMSCs are more spread and exhibit a more rounded morphology – consistent with the shape of progenitor cells [21]. Further, the primary effect of stretch was that the BMSCs projected cell area and long axis decreased. This result indicates that the BMSCs are more rounded after stretch, and suggests that cells may not have time to fully reestablish focal adhesion contacts between the cessation of cyclic stretch and the analysis of cell morphology.

The mRNA expression of markers of the ligament-like phenotype (e.g. collagen type I, decorin, scleraxis, and tenomodulin) and the expression of α -smooth muscle actin – which has been shown to be induced by stress in fibroblastic cells [25, 68, 78] – were not significantly affected by mechanical stretch in this study. The only effect of the surface on BMSCs appeared to be a non-significant increase in α -smooth muscle actin expression on electrospun meshes compared to PDMS surfaces. The mRNA expression and cell morphology results may indicate that the cells on the electrospun fibers have differentiated more than cells on the smooth surfaces. However, the application of mechanical stretch did not appear to have a significant affect on mRNA expression, contrary to most studies [4, 49, 76, 77]. The lack of significant induction of mRNA expression – and limited cell orientation on smooth surfaces – after the application of cyclic stretch suggests that either the cells were not provided with the same level of cyclic mechanical stimulation as in previous studies or the level of static pre-stretch in the surfaces may have induced more expression than the subsequent cyclic mechanical stimulation [155]

Supporting the hypothesis that not enough stimulus was provided is the fact most studies have performed stretch for longer times from 12 h to 21 days [49, 153], although induction of collagen type I mRNA expression and orientation responses on smooth surfaces have been observed on PDMS surfaces after 1 h of stretch [145, 155]. ACL fibroblasts have been found to deposit collagen on electrospun fibers after 24 h of stretch [3]. Therefore, in future work stretch will be performed for longer than 24 h to determine if stretching cells on electrospun meshes will

significantly induce the cellular expression of the selective ligament-like markers and if this response is different than that on smooth PDMS surfaces.

5.5 Conclusions

This study shows that cells are able to attach to both smooth PDMS and electrospun surfaces and express the ligament-like ECM components (collagen type I and decorin) as well as other markers of fibroblastic and myofibroblastic differentiation (scleraxis, tenomodulin, and α -SMA). When cyclic mechanical stretch was applied, the cells remained oriented parallel to the direction of fiber orientation. In contrast, cells exhibited a limited reorientation in response to stretch on PDMS surfaces. Finally, no significant effects of stretch were observed on electrospun meshes, suggesting that the stimulus needs to be applied for a longer total time (e.g. for a longer time each day or for more days) to induce the production of ECM by mesenchymal progenitor cells.

5.6 Acknowledgments

This research was funded by the ASPIRES grant program and through the Institute for Critical Technologies and Sciences at Virginia Tech. We would also like to acknowledge Dr. Joseph Freeman for the use of his MTS, Dr. Yong Woo Lee for the use of his PCR equipment, and Dr. Garth Wilkes for the use of his electrospinning power supply and syringe pump.

Chapter 6: Simultaneously Electrospinning Two Components to Improve Cellular Infiltration

Chris A. Bashur¹, Robyn D. Shaffer², Linda A. Dahlgren³, Scott A. Guelcher⁴, Mariah S. Hahn⁵, Aaron S. Goldstein^{1,2}

¹ Department of Chemical Engineering, and
² School of Biomedical Engineering and Sciences,
Virginia Polytechnic Institute and State University,
Blacksburg, VA 24061

³ Department of Large Animal Clinical Sciences,
Virginia-Maryland Regional College of Veterinary Medicine,
Blacksburg, VA 24061

⁴ Department of Chemical Engineering, Vanderbilt University
Nashville, TN 37235

⁵ Department of Biomedical Engineering, Texas A&M University
College Station, TX 77843

6.1 Introduction

Electrospun scaffolds are attractive for the construction of oriented soft tissue (e.g. tendon, ligament, and muscle) because of their ability to guide cell alignment. However, while electrospun scaffolds have high porosities of 56 to 93% [118, 127-129], they allow limited cell infiltration because of low effective pore diameters – typically smaller than 10 μm [130, 191]). This is especially a concern for the thicker, more three dimensional scaffolds that are required for clinical applications. One strategy that has been used to increase cell infiltration is to co-electrospin a sacrificial polymer that can be dissolved out of the resultant mesh, and consequentially create larger pores. In a study by Baker et al. [131], a coelectrospun scaffold of poly (ϵ -caprolactone) (PCL) and poly (ethylene oxide) (PEO) increased the effective pore diameter of a mesh when the sacrificial PEO component was dissolved in aqueous medium. They found that PEO composition of 50% or greater were required for significant cell infiltration. This high percentage of water solubilized PEO resulted in significantly reduced mechanical properties. In addition, limited integration of the co-electrospun components has

been achieved because the positive charges applied to both of them during the electrospinning process repel each other [124, 131].

Another possible strategy to increase cell infiltration involves incorporating a sacrificial component that does not dissolve instantaneously but instead is degraded enzymatically by cells as they infiltrate into the scaffold. The natural polymer gelatin is able to degrade enzymatically [99], and it may be used as the sacrificial component if it is crosslinked to reduce its solubility in water [100]. The other component (e.g. poly (ester-urethane urea) (PEUUR)) should degrade slowly through hydrolysis [93] and provide structural integrity for the scaffold until the cells deposit organized, load-bearing collagen fibrils. An additional step of embedding the co-electrospun meshes in a degradable hydrogel may prevent the pores from collapsing and aid in increasing cell infiltration. The hydrogel may also be able to hold electrospun meshes together if they are processed into three-dimensional structures required for clinical applications.

In this study, three steps were performed with the goal of developing methods to produce more clinically relevant electrospun constructs (i.e. more three-dimensional and with improved cell infiltration). In the first step co-electrospun scaffolds were prepared with a PEUUR and gelatin with the aim of producing larger pores and increasing cell infiltration. The polarity of the electrical charge applied to the individual components was varied to determine what configuration achieves the best integration. In the second step meshes and cells were embedded in a hydrogel to determine the feasibility of using this process to produce more three dimensional constructs. In the third step three dimensional constructs were prepared and the cell viability in these constructs was determined.

6.2 Materials and Methods

6.2.1 Materials

All lab supplies were purchased from Fisher Scientific (Pittsburgh, PA), and all biological supplies were purchased from Invitrogen (Gaithersburg, MD) unless otherwise noted. The 75/25 mol ratio poly (lactic-*co*-glycolic acid) (PLGA) (inherent viscosity 0.55–0.75 dL/g) was purchased from Lactel Biodegradable Polymers (Birmingham, AL), and a poly-ester-urethane-urea (PEUUR) was synthesized with amounts of hard and soft segments as described elsewhere (Section 4.2.1) and as discussed in a previous report [190]. Briefly, a PCL diol ($M_n =$

2000 Da) was end-capped with hexamethylene diisocyanate (HDI), and this pre-polymer was chain extended with 1,3-propanediol bis (4-aminobenzoate) (PDAB). Poly (ethylene glycol) – oligo (lactide) – diacrylate (PEG-LA-DA) was also synthesized. The PEG-LA-DA hydrogel material was synthesized by a ring opening polymerization of D,L-lactide monomers (Sigma-Aldrich, St. Louis, MO) using the hydroxyl ends of a 6 kDa M_w poly (ethylene glycol) (PEG) pre-polymer (Sigma-Aldrich, St. Louis, MO) as the initiator to produce hydrolytically degradable sections of the molecule that are approximately 2 lactide unit long. This was then reacted with acryloyl chloride (Sigma-Aldrich, St. Louis, MO) to form the diacrylate ends (**Figure 6.1**). The double bonds at the ends are able to undergo free-radical polymerization.

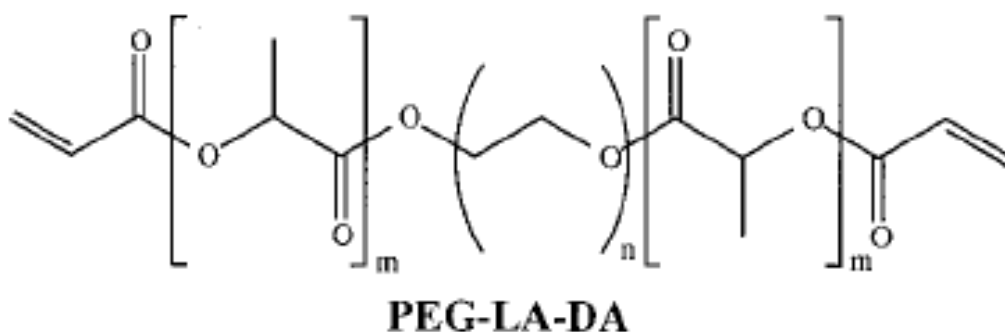


Fig.6.1. Chemical structure of the PEG-LA-DA hydrogel prior to photo-crosslinking.

6.2.2 Electrospinning One Component

PLGA, PEUUR, and gelatin type B (~225 Bloom) (Sigma-Aldrich, St. Louis, MO) were electrospun to form fused-fiber meshes with controlled fiber diameters and degrees of fiber orientation as described previously (Section 5.2.1) [82]. Briefly, a 6 cm diameter drum was wrapped with aluminum foil and rotated at linear velocities less than 1 m/s (i.e. < 250 rpm) to produce a scaffold with consistent properties along the circumference of the drum but to avoid inducing orientation in the electrospun fibers. Electrospinning was also performed on glass coverslips to aid in imaging of the resulting samples. Electrospinning was performed under ambient conditions using a 22 gauge steel needle, a 15 kV potential, a throw distance of 15 cm, and a syringe flow rate of 3 mL/h. Positive charges were always applied to the polymer if only one component was electrospun. Electrospinning was performed with solutions of the three different polymers (9 wt% for (1) PEUUR and (2) PLGA and 10w/v for (3) gelatin) dissolved in

1,1,1,3,3,3- hexafluoro-2-propanol (HFIP). Following electrospinning, meshes were peeled off of the aluminum foil, allowed to air dry, and then stored in a desiccator until use.

6.2.3 Co-electrospinning

Simultaneous electrospinning (i.e. co-electrospinning) was performed by dispensing components from two separate syringes placed on opposite sides of a rotating drum (**Figure 6.2**). Here, the components were on opposite sides of the drum to reduce the interaction of the charges from the two individual components (i.e. reduce the effect of charge repulsion or attraction). The drum was rotated at less than 1 m/s to integrate the components without inducing fiber alignment. The two component polymer systems were PLGA/PLGA, gelatin/PLGA, or gelatin/PEUUR dissolved in HFIP as described in Section 6.2.2. To distinguish between the two components, the fluorescent dyes DiO or DiI (Molecular Probes – Invitrogen, Eugene, OR) were added to the solutions. Next, the solutions were electrospun onto the drum using the previously described electrospinning conditions (Section 6.2.2). However, for co-electrospinning the polarity of the electrical charge applied to individual components was switched between positive 15 kV and negative 15 kV through a switch on the power supplies. In this study, two different configurations were used where either both components were positively charged or the individual components were charged with opposite polarities.

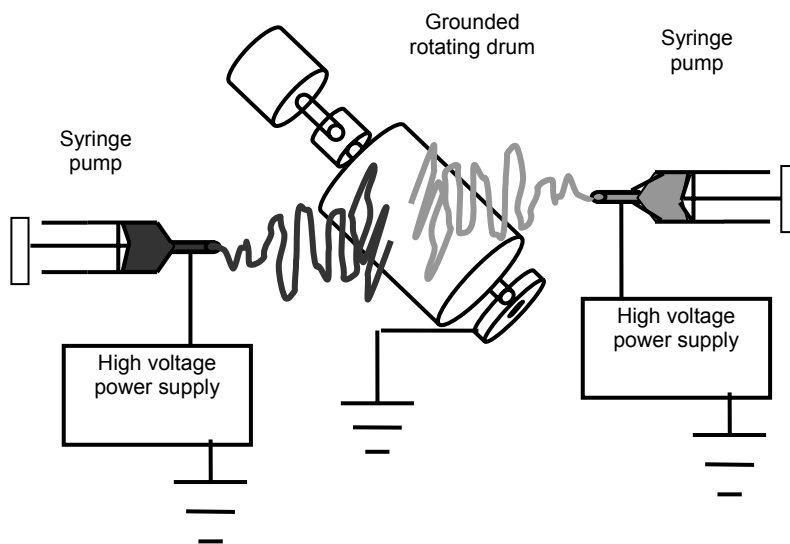


Fig.6.2. Diagram of the co-electrospinning system with two syringes on opposite sides of a rotating drum

6.2.4 Characterization of Mesh Morphology

The morphology, diameter, and orientation of co-electrospun meshes were determined by quantitative analysis of scanning electron microscopy (SEM) images. For SEM analysis, electrospun surfaces were mounted onto studs and sputtercoated with a 20 nm layer of palladium (Model 208HR, Cressington Scientific Instruments, Cranberry, PA). These surfaces were then imaged with a LEO 1550 Field Emission SEM (Carl Zeiss SMT, Thornwood, NY) operating at 5kV with a 16 mm working distance. Resultant images were imported into ImagePro Plus software (ICube, Crofton, MD) and the alignment and diameter were determined for at least 100 fibers per sample. The individual fibers in the SEM images with clearly defined edges were measured manually. Fiber alignment was characterized by angular standard deviation, with the mean angle of orientation and average angular standard deviation calculated from a wrapped normal distribution [82].

Fluorescent microscopy was used to distinguish the degree of integration of fibers from the two components for both meshes electrospun onto coverslips and meshes peeled off aluminum foil. Fluorescence images were obtained at 20× magnification with a wide green filter (excitation 535 nm/ mirror 565 nm/ emission 590 nm) to identify fibers loaded with DiI, and with a wide blue filter (excitation 455 nm/ mirror 500 nm/ emission 515 nm) to identify fibers loaded with DiO using an Olympus IX50 microscope (Opelco, Sterling, VA) equipped with a cooled CCD camera (Hamamatsu C4742-98-12NRB). Images were taken along the length of the drum to determine if a gradient was present.

The extent of integration of the components and the presence of a gradient was quantified through the use of the fluorescent images. Pixel intensities of the wide green image and the wide blue image at the same location along the length of the drum were measured in ImagePro, and then the ratio of the two were calculated. This ratio was used to characterize the extent of integration of the two components.

6.2.5 Crosslinking Gelatin

Co-electrospun meshes containing gelatin were crosslinked with glutaraldehyde (50% in water) (Sigma-Aldrich, St. Louis, MO) to decrease the solubility of the gelatin fibers in aqueous media. Briefly, 3 mL of glutaraldehyde was diluted with 3 mL of ethanol. The meshes were then elevated above the glutaraldehyde solution container inside a desiccator to allow the

glutaraldehyde vapors to crosslink the gelatin, as described elsewhere [100]. The meshes were removed after 24 h and then stored in a desiccator until use. Single component electrospun gelatin meshes were also vapor crosslinked with the same procedure. The structure of the fibers was characterized by SEM before and after crosslinking to ensure that the fibers did not fully dissolve. The percent mass loss after ~24 h in deionized water for the gelatin-containing meshes was measured for both crosslinked and non-crosslinked samples to quantitatively assess the stability of gelatin in aqueous solution.

6.2.6 Production of PEG-LA-DA Hydrogels

PEG-LA-DA hydrogels were produced using a procedure described in detail elsewhere [211]. Briefly, 20 and 25 vol% hydrogels were prepared by adding a sufficient mass of PEG-LA-DA to PBS, vortexing, and allowing it to dissolve for 30 min. Next, a volume of 10 μ L of the photoinitiator (2,2-dimethoxy-2-phenylacetophenone in 1-vinyl-2-pyrrolidinone) (Sigma, St. Louis, MO) in *N*-vinyl-2-pyrrolidone (NVP) (Sigma, St. Louis, MO) was added for each 1 mL of solution and vortexed. Finally, the solution was poured into a dish and then exposed to a 365 nm UV light (UVP B-100ap, Upland, CA) for 5 min to crosslink and form a gel.

To incorporate cells, the hydrogel solution in PBS was sterilized overnight by short-wavelength UV light, and then the initiator was added to the solution. Next, one plate of NIH 3T3 fibroblasts maintained in a 37 °C and 5% CO₂ incubator were enzymatically lifted using trypsin/ ethylenediamine tetraacetic acid (EDTA) (Invitrogen) and added to the hydrogel and initiator solution. This was then quickly poured into a Petri dish and crosslinked for 5 min as described previously. Afterward, Dulbecco's Modified Eagle's Medium (DMEM) with 10% fetal bovine serum (FBS Gemini, Calabasas, CA) and 1% antibiotic/antimycotic was added to the Petri dish and the constructs were cultured at 37 °C and 5% CO₂ for 3 days. To confirm the presence of live cells throughout the gel at 3 days, calcein-AM (20 μ L/mL of media) and DAPI (2 μ L/mL of media) were added to the hydrogel. Fluorescent images of the cells were taken with a wide green and wide blue filter.

Meshes were also embedded in the hydrogel, the hydrogel was crosslinked as previously described, and then cross-sections of the resulting construct were produced. Initially, the hydrogel and initiator solution was poured on an electrospun mesh in a Petri dish. The sample

was then crosslinked as previously described. Afterward, slices of the sample were made using a razor blade and the sections were visualized under phase contrast at 20× magnification.

6.3 Results and Discussion

6.3.1 Co-electrospinning

Simultaneous electrospinning of two different components – one loaded with the fluorescent dye DiI and the other with DiO – was performed for three different polymer systems: PEUUR/gelatin, PLGA/gelatin, and PLGA/PLGA (**Figure 6.3**). The PLGA/gelatin and PEUUR/gelatin systems (**Figure 6.3b** and **Figure 6.3c**) were designed to try to increase cell infiltration. However, the gelatin component was more difficult to electrospin reproducibly because the polymer dries on the tip of the needle for the 8 to 10 w/v% concentration range used in this study. The system of 10 wt% PLGA/ 9 wt% PLGA (**Figure 6.3a**) was easier to electrospin and therefore was used to determine the effect of different co-electrospinning parameters on the resultant mesh. For all polymer systems, co-electrospinning with the syringes on opposite sides of the rotating drum allowed the components to better integrate, likely due to reduce repulsion of the two positively charge components.

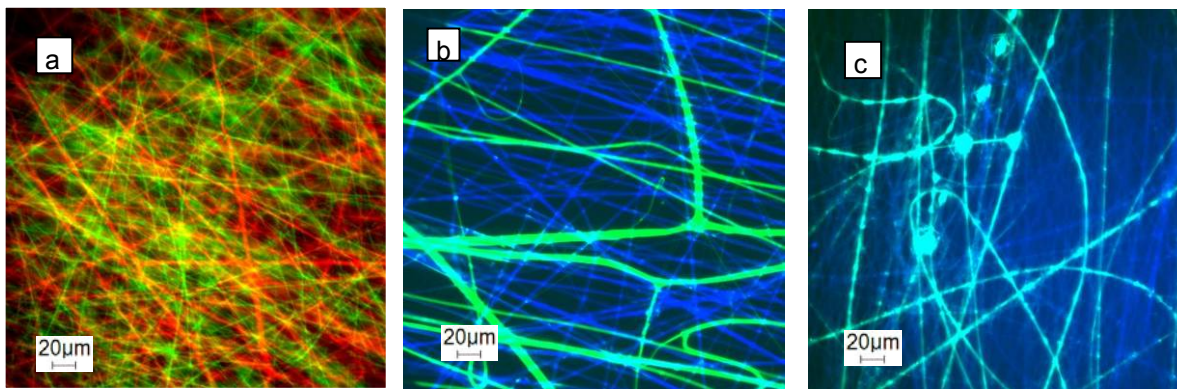


Fig. 6.3. Superimposed fluorescent images of a coelectrospun a) 9 wt% PLGA/ 9 wt% PLGA peeled mesh, b) 9 wt% PLGA/ 10 w/v% gelatin fibers on a coverslip, and c) 9 wt% PEUUR/ 10 w/v% gelatin fibers on a coverslip. For images (b and c) the gelatin is stained green and the other polymer is stained blue.

One parameter that has an effect on the co-electrospinning results is the polarity of the electrical charge applied to the two components. For PLGA/gelatin studies, applying a positive charge to both polymers created a gradient (**Figure 6.4**). The fibers were mixed in a small area at the center (**Figure 6.4a**) but on either side they were primarily composed of fibers from the individual components (**Figure 6.4b**). The gradient was produced because the charges remain in the fibers after deposition on the target and can repel other fibers of the like charge [121]. A gradient may be useful for the production of a composite ACL graft that promotes fibrocartilage differentiation on the ends. However, for many applications the creation of a highly uniform scaffold such as the one shown in **Figure 6.3c** is desired.

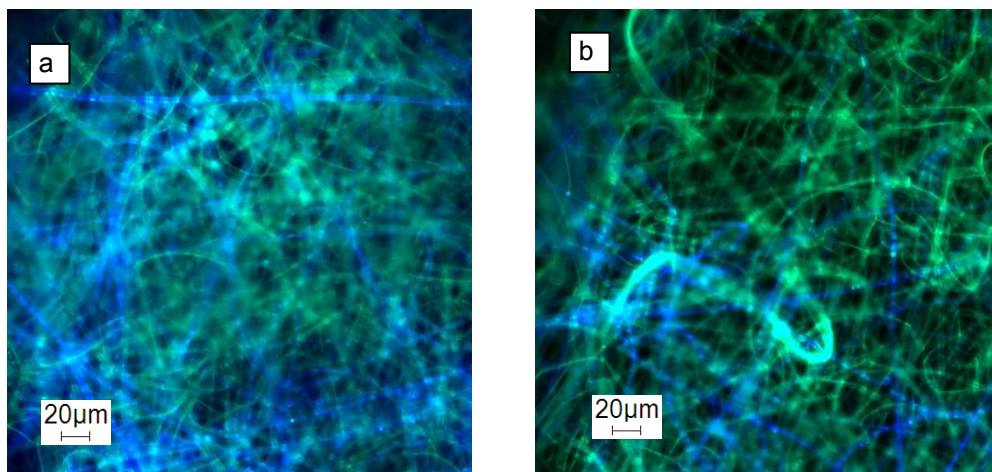


Fig. 6.4. Superimposed fluorescent images of a coelectrospun PLGA/gelatin fiber mesh imaged along the length of the rotating drum from a) to c). For these images, the gelatin is green and the PLGA is blue.

A highly uniform scaffold was produced using the PLGA/PLGA system by applying a positive charge to one component and a negatively charge the other. The uniformity of mixing of the components along the length of the drum was quantified using fluorescent images of the meshes (**Figure 6.5**). The ratio of the pixel intensities of the wide green and wide blue images were consistent along the majority of the length of the drum (>20 cm), with the exception of approximately 5 cm on the edge where the ratio transitioned to higher intensity for the wide green filter. These quantified results indicate that **Figure 6.3c** is representative of the mixing of the fibers throughout most of the drum except for region at the edge the composition transition to primarily gelatin fibers.

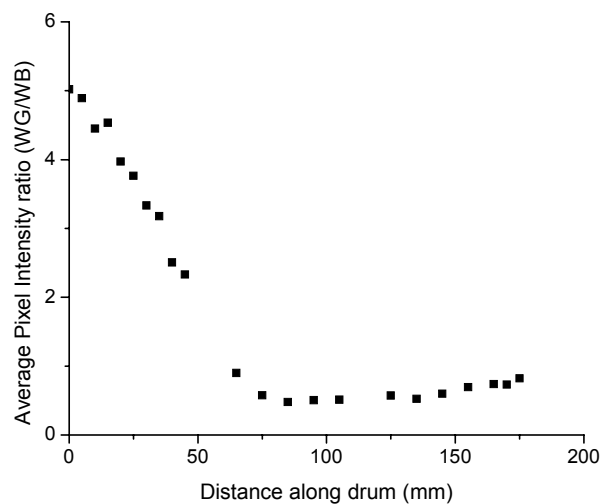


Fig. 6.5. Average pixel intensity ratios for fluorescent images of a well integrated PLGA/PLGA composite mesh.

6.3.2 Crosslinking Gelatin Fibers

Glutaraldehyde crosslinking was performed for electrospun meshes containing gelatin to prevent the gelatin fibers from completely dissolving after 1 h. Initially, single component electrospun gelatin meshes were prepared, and their solubility in aqueous media was found to decrease with crosslinking (**Figure 6.6**). However, the meshes did appear to partially dissolve after the crosslinking process. In addition, the meshes developed a yellow color after this process that made fluorescent imaging difficult. This yellowish color can be attributed to the formation of aldimine linkages ($R-CH=N-R'$) between the amine groups of gelatin and glutaraldehyde [212].

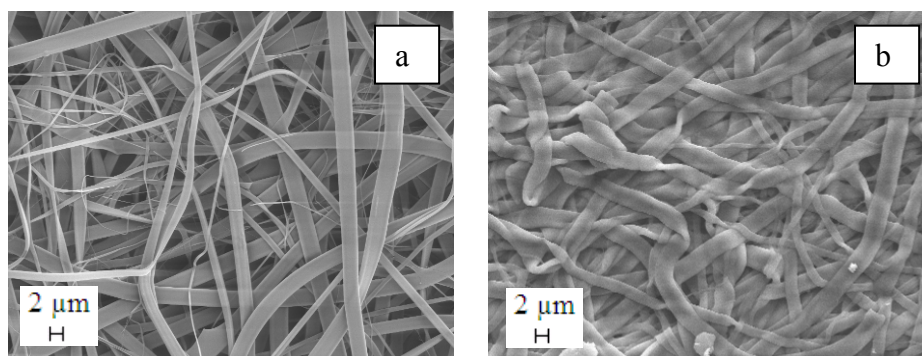


Fig. 6.6. SEM images of electrospun gelatin a) before and b) after crosslinking.

The crosslinking of co-electrospun meshes was performed using 50% glutaraldehyde to decrease the amount of water present during crosslinking and consequentially decrease changes to the structure of the fibers. In co-electrospun meshes, the fiber structure of the gelatin fibers was similar both with and without crosslinking (**Figure 6.7**). **Figure 6.7b** contains more of the smaller diameter gelatin fibers because a gradient was present in these meshes. In addition, the percent mass loss for gelatin/PEUUR co-electrospun samples in aqueous solution was 0% for crosslinked meshes but 34% for non-crosslinked samples. These results indicate that coelectrospun meshes containing gelatin can retain their fiber structure in aqueous solutions for tissue engineering application. Importantly, future work must still be performed to determine if the crosslinked-scaffolds are biocompatible and if there is a maximum percent crosslinking before adverse cellular responses from toxicity are observed.

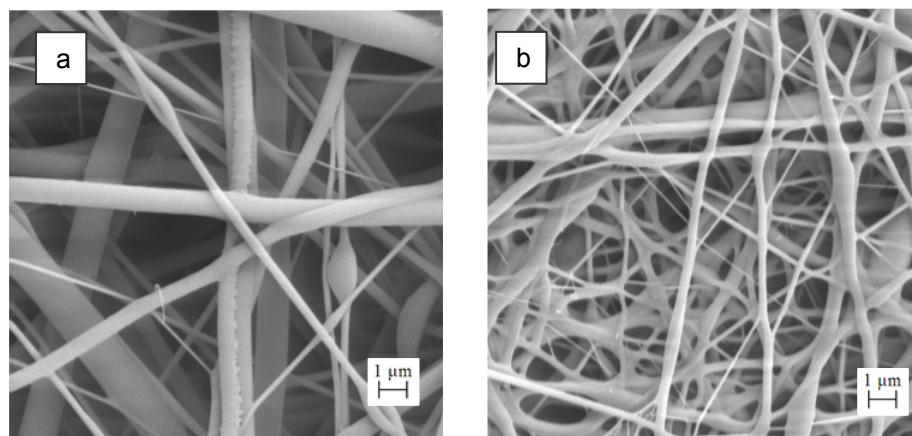


Fig. 6.7. SEM images of electrospun PEUUR/gelatin meshes a) before and b) after crosslinking. The crosslinked samples were soaked in DI water.

6.3.3 Embedding in a Hydrogel

Cells have been shown to have limited infiltration into single component PEUUR electrospun meshes (**Figure 6.8**). In addition, while **Figure 6.8** shows that some meshes remain mostly intact after sectioning in paraffin, many meshes started to fall apart after sectioning. Therefore, in this study meshes were embedded in PEG-LA-DA hydrogels in the hope of holding the meshes together during any subsequent processing, including sectioning (**Figure 6.9**). NIH 3T3 cells seeded in the hydrogel were distributed throughout the gel and remained viable after 3

days of culture (**Figure 6.10**). However, these cells appeared to be rounded and were not spread in the hydrogel. For this reason, in the future cells could be seeded on the meshes prior to embedding instead of being suspended in the hydrogel.

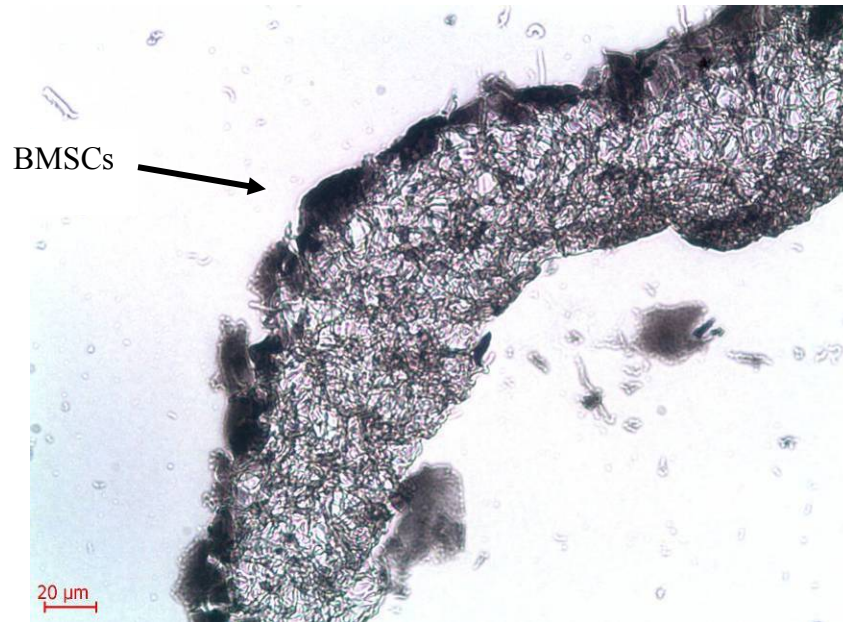


Fig. 6.8. Histological paraffin section of randomly oriented electrospun PEUR fibers stained with hematoxylin (blue) for cell nuclei and VectaStain ABC kit for collagen type I (brown).

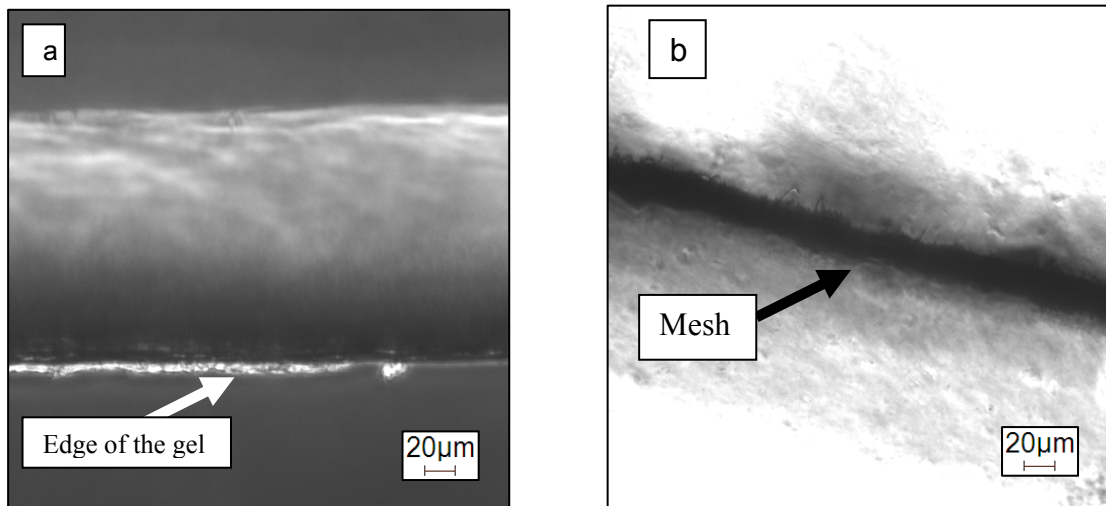


Fig. 6.9. Sections of a crosslinked PEG hydrogel a) without and b) with an embedded electrospun mesh

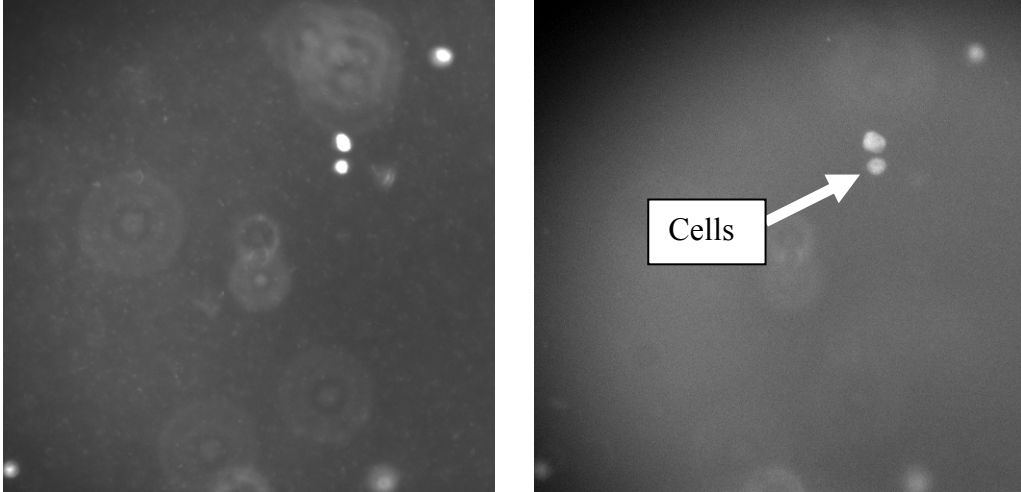


Fig. 6.10. NIH 3T3 cells in a crosslinked PEG hydrogel stained with a) DAPI and b) calcein-AM after 3 days in culture.

6.3.3 Processing Three-dimensional Samples

The PEG-LA-DA hydrogel can also aid in the production of three-dimension constructs for tissue engineering applications. For example, an electrospun PEUR mesh was seeded with cells, rolled into a hollow cylindrical shape, and then embedded in the hydrogel (**Figure 6.11**). Composites were mechanically robust, did not unroll, and could be easily cut into segments. In addition, cells were viable on the mesh after the embedding process (**Figure 6.11b**). This technique could also be used to produce a cord-like ligament construct.

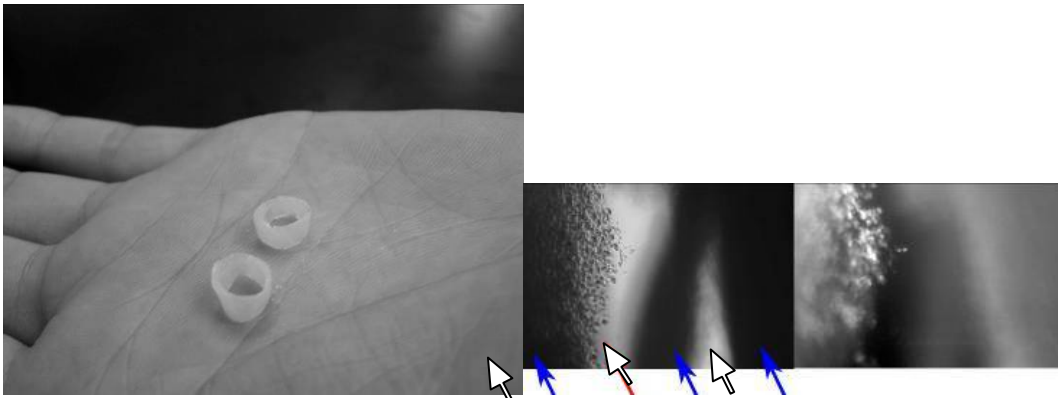


Fig. 6.11. Image of a) PEUR1250 mesh embedded in hydrogel and b) cell inside an embedded hydrogel with brightfield and fluorescent images. The solid arrow indicates cells and the hollow arrow indicates the PLGA mesh.

6.4 Conclusions

The results of this study show that co-electrospinning can be used to produce scaffolds for ligament tissue engineering investigations. A sacrificial component gelatin was incorporated into the co-electrospun meshes with the goal of increasing cell infiltration into the scaffold. Its dissolution in water was prevented by crosslinking with glutaraldehyde. In addition, single component meshes were seeded with cells, processed, and embedded in a PEG hydrogel to show the feasibility of producing three dimensional constructs. Co-electrospun meshes with different degrees of integration (i.e. well integrated or as a gradient) of the individual components were produced by applying different polarities. While a well integrated mesh was desired in this study, in future studies a gradient structure may be useful for the production of a composite ACL graft that promotes fibrocartilage differentiation on the ends. Several areas must be developed before this composite graft can be produced. Three of these areas include systematically controlling the gradient of co-electrospun meshes, processing the meshes into three-dimensional cord structures, and determining the biocompatibility and mechanical properties of these cords.

6.5 Acknowledgments

The authors thank Dr. Garth L. Wilkes for the use of the electrospinning device, and funding from the Charles E. Culpeper Foundation (03-130) and the Institute for Critical Technologies and Sciences at Virginia Tech.

Chapter 7: Conclusions and Future Work

7.1 Conclusions

The overall goal of this research project was to develop methods to produce a tissue engineered ligament construct with MSCs that differentiate into ligament-like fibroblasts and have the ability to deposit organized fibril-forming ECM. Towards this goal, three complimentary tasks were performed: (1) the determination of scaffold topographies that induce cell orientation and expression of the ligament phenotype, (2) the examination of mechanical stretch to stimulate the expression of ECM mRNA in oriented cells, and (3) the development of an approach to produce three-dimensional constructs with improved cell infiltration.

The first task was to determine scaffold topographies that induce cells to orient and differentiate into the ligament-like phenotype in static culture. The effect of topographic features of electrospun scaffolds (i.e. fiber diameter and alignment) on cell behavior was determined in two separate studies. The first study was performed with PLGA scaffolds and NIH 3T3 fibroblasts, and the second study was performed with the clinically relevant system of PEUR scaffolds and BMSCs. In both studies, the surfaces were supported on coverslips to isolate the effect of topography. The results demonstrated that electrospun scaffolds with fiber diameters from 0.14 to 3.6 μm and angular standard deviations (ASDs) of 27.8 to 60° could be formed. These substrates were able to guide cell attachment and support cell growth. Importantly, the topographic cues presented by aligned electrospun scaffolds were able to align the cells in the direction of fiber alignment and induce a more spindle shaped morphology. In addition, the degree of cell orientation and cell elongation increased with increasing fiber alignment. Examination of the expression of the ECM components collagen type I and decorin on the different electrospun surfaces showed that topography affects cell phenotype. Specifically, expression of the ECM components was elevated on smaller diameter 0.28 μm PEUR fibers. These findings suggest that smaller and more oriented fiber scaffolds enhance BMSC differentiation into a ligament-like phenotype and may be preferred for the manufacture of engineered ligament tissues.

The second task was to determine the effect of dynamic mechanical stimulation of oriented electrospun scaffolds on ligament-like differentiation of MSCs. Oriented PEUR scaffolds (average diameter of 0.65 μm or 0.89 μm and ASDs < 22°) were suspended in a

prototype mechanical stretch bioreactor, pre-stretched to ensure that both the static and cyclically stretched scaffolds were in tension, and then seeded with BMSCs. This study showed that cells are able to express ligament-like ECM components (e.g. collagen type I and decorin) as well as other markers of fibroblastic and myofibroblastic differentiation (e.g. scleraxis, tenomodulin, and α -SMA). On fibrous surfaces, the cells aligned parallel to the direction of fiber alignment in static culture and remained aligned with the application of cyclic stretch. However, no significant effects of stretch on BMSC mRNA expression were observed, and cells seeded on smooth silicone surfaces only exhibited a limited reorientation in response to stretch. These results demonstrate the feasibility of conditioning BMSCs on fibers under intermittent cyclic stretch, but they suggest that more stimulation (e.g. longer durations of stretch) may be needed to stimulate ECM deposition.

The third task was to produce three-dimensional constructs with improved cell infiltration that are necessary for a clinical application. Two complimentary studies were performed for this task: (1) simultaneous electrospinning of two components to create larger pores and (2) processing the scaffolds into more three-dimensional constructs and holding them together with a photo-crosslinkable hydrogel. In the first study a sacrificial component gelatin was incorporated into co-electrospun scaffolds with the goal of increasing cell infiltration into the scaffold. Co-electrospun scaffolds with a high degree of integration of the individual components were produced by applying different polarities (i.e. positive to one component and negative to the other). With these scaffolds, dissolution of gelatin in water was prevented by crosslinking with glutaraldehyde. In the second task single component scaffolds were seeded with cells, processed into a tubular structure, and embedded in a degradable PEG-LA-DA hydrogel to demonstrate the feasibility of producing three dimensional constructs. These results show that electrospun scaffolds can be processed into three-dimensional constructs for clinical applications and co-electrospinning can be used to produce scaffolds with the potential for greater cell infiltration. However, additional research is required to determine specific co-electrospinning conditions that can produce scaffolds with improved cell infiltration and to develop a strategy to process the scaffolds into three dimensional ligament-like structures.

Through the tasks performed in this research project, three important results were achieved: (1) desirable scaffold characteristics for the production of a tissue engineered ligament have been determined, (2) aligned electrospun scaffolds have been shown to guide cell alignment

in a cyclic stretch bioreactor, and (3) the feasibility of producing more clinically relevant three dimensional constructs with improved cell infiltration has been established.

7.2 Future Work

While the results of this research project are promising, they also demonstrate important areas where further research is required. Three of these areas include: (1) enhancing the expression of ligament-like ECM with cyclic stretch, (2) increasing cell infiltration with co-electrospinning, and (3) processing the scaffolds into three-dimensional cord structures.

7.2.1 Enhance Expression of ECM with Cyclic Stretch

This area of future work is to determine cyclic stretch conditions that increase the expression and deposition of organized fibril-forming ECM. While BMSC expression of collagen types I and III, tenascin-C, elastin, fibronectin, and scleraxis have been found to be elevated with the application of cyclic stretch [49, 80, 81], the results presented in Chapter 5 suggest that the expression of ligament-like ECM components is not always elevated in response to cyclic stretch. Therefore, determining appropriate stretch parameters for cell-seeded electrospun scaffolds is important to the preparation a future tissue engineered ligament. These parameters (e.g. magnitude of strain) should have different effects on cells seeded on various electrospun scaffolds or other types of surfaces, partially because similar magnitudes of strain will not translate to the same effective strain felt by the cells [3, 78]. However, the application of cyclic stretch has induced BMSCs and ligament fibroblasts – seeded on a range of surfaces (e.g. collagen gels, large diameter extruded fibers, and microgrooved surfaces) – to express ECM components in response to cyclic stretch [4, 49, 80, 81], suggesting that other stretch conditions (e.g. duration of cyclic stretch) may also contribute to differences in mRNA expression. Durations from 1 h to 21 days have been shown to induce the expression of ligament-like ECM [49, 145, 153]. However, the cellular response and mechanical properties have been shown to increase with increasing durations (e.g. numbers of hours of stimulus per day and the number of consecutive days of mechanical stimulation) [49, 213], and longer durations may be required to induce a significant cellular response compared to non-stretched controls [49].

Future work can be performed to determine if a longer duration of cyclic stretch is required to induce the expression and deposition of ligament-like tissue, and if the induction is

different for cells seeded on different scaffolds. One strategy to accomplish this involves seeding BMSCs on aligned electrospun PEUR scaffolds, mechanically stimulating the constructs, and then determining if ligament-like ECM is produced. The experiment can be performed with different types of stretch (i.e. static and cyclic), and smooth silicone control surfaces can also be included to determine how different the level of stimuli necessary is for clinically relevant electrospun surfaces. All cyclically stretched samples can be stretched after 3 days of culture at the same conditions as in Chapter 5 (i.e. 8% strain and 0.5 Hz), but for a longer duration per day and over more consecutive days (e.g., 2 h/day for 7 days). Afterward, mRNA expression of ligament-like markers (e.g. collagen type I, decorin, tenomodulin, and scleraxis) and the deposition of collagen type I can be determined. Day 3 samples – prior to performing cyclic stretch – can also be included as a control.

This future work is expected to show that longer durations of cyclic stretch (e.g. 2 h/day for 7 days) will induce higher levels of expression and deposition of ligament-like ECM compared to controls. This result is expected because, although 1 h of stretch has been shown to induce expression of ECM components [145], longer durations from 12 h to 21 days have more commonly been used [49, 153]. In addition, the induction of ECM expression by cells on collagen gels with the application of cyclic stretch has been shown to increase with increasing duration [49]. Further complicating ligament tissue engineering is that the same applied macroscopic strain magnitude that is applied to the biomaterial scaffold may be transmitted to the attached cells differently, and depend on the modulus and architecture of the scaffold. Consequently, the cellular expression on model silicone control surfaces and clinically relevant fibrous scaffolds in response to stretch are expected to vary [3, 75]. Therefore, an important next step would be to determine what percentage of the applied overall strain is transmitted to cells and how this varies with the surface properties.

7.2.2 Increase Cell Infiltration with Co-electrospinning

This area of future work is to apply the technique of co-electrospinning developed in Chapter 6 to improve cell infiltration into electrospun scaffolds. Recently, the co-electrospinning technique has been used to produce composite scaffolds [124, 131, 135, 136], and a co-electrospun scaffold of PCL and PEO was able to increase cell infiltration through the creation of larger pores [131]. The PEO was the sacrificial component, and its role was to dissolve away

and reveal larger and more open pores. However, PEO compositions of 50% or greater were required to achieve infiltration of a few cells into the center of the scaffold, and with these large amounts of PEO, the scaffolds started to visually deform after the PEO dissolved. In chapter 6, a different sacrificial component (i.e. gelatin) – one that can be crosslinked to avoid rapid dissolution – was co-electrospun with PLGA. The underlying rationale is that the gelatin fibers may be enzymatically degraded by cells as they infiltrate inside. This may prevent the scaffolds – and consequentially the pores – from collapsing prior to cell infiltration. To use this strategy, scaffolds with controlled ratios of each component must be co-electrospun, and consistent integration of the fibers from each component must be produced throughout the sample. Chapter 6 has shown that producing well integrated co-electrospun scaffolds is feasible, and other studies have demonstrated that varying the ratio of the two components can be achieved by changing the number of syringes for each individual component [136]. Connecting syringes in parallel effectively multiplies the applied voltage, so another way to change the component ratio may be to apply different voltages to the individual components.

Future work can be performed to determine how the ratio of the gelatin – the sacrificial component – and PLGA affects cell infiltration. Constructs consisting of BMSCs seeded on co-electrospun scaffolds with different ratios of gelatin and PLGA can be produced, and the degree of cell infiltration into the scaffolds can be determined. Well integrated scaffolds can be produced by charging two components with opposite polarities, while varying the voltage potentials (e.g. +20kV / -10kV, +10kV / -10kV, and +10kV / -20kV) should produce different ratios of gelatin/PLGA. These ratios can be determined by incorporating fluorescent dyes into the fibers and then analyzing images of the scaffolds. These scaffolds would then be crosslinked with glutaraldehyde and seeded with BMSCs. After the cells have been allowed to migrate during 3 and 7 days of culture, the nuclei can be stained with DAPI, cross-sections of the samples can then prepared with a cryotome, and then the sections can be imaged.

This future work is expected to show that scaffolds with higher ratios of gelatin to PLGA allow greater cell infiltration. This result has been achieved previously with co-electrospun scaffolds containing a 50% or greater of a water soluble PEO component [131]. However, with enzymatically degradable gelatin, cell infiltration is expected to occur at lower ratio of gelatin to PLGA because the fibers are prevented from contracting prior to cell infiltration. A reduction in the percentage of sacrificial fibers should lead to better maintenance of the shape and tensile

strength of the ligament tissue engineering construct. Therefore, a logical next step would be to determine the tensile properties of constructs with different ratios of gelatin to PLGA.

7.2.3 Three-dimensional Processing and the Effect of Embedding in a Hydrogel

This area of future research is to process electrospun scaffolds into three-dimensional ligament-like cord structures that are required for ACL replacement and assess their performance *in vitro*. Electrospun scaffolds have been processed into other cylindrical constructs in previous work [114, 126]; however, methods to process the scaffolds into a clinically relevant ligament-like construct still need to be developed. Requirements for a ligament construct include the following: (1) electrospinning scaffolds with aligned fibers to direct cell alignment, (2) processing the scaffold into a stable cord structure with fiber alignment along the length of the construct, (3) distributing ECM-depositing cells throughout the construct, and (4) producing a construct with the appropriate dimensions for a human ACL graft (i.e. approximately 7 mm in diameter and 32 mm long [16, 214]). The first requirement has already been addressed in Chapters 3 and 4, where the feasibility of producing aligned fatigue resistant, electrospun fibers with a rotating drum is described. In addition, one method to improve the distribution of cells with the use of co-electrospinning has been discussed (Section 7.2.2); however, the distribution of cells may also be improved by seeding the cells on the sheet of electrospun fibers prior to processing. To our knowledge this processing of an electrospun scaffold into a stable cord structure has not been published and is one specific area of future work.

One strategy for forming a cord-shaped constructs is to seed an aligned electrospun scaffold with BMSCs, process the construct into a three dimensional cord-like structure with dimensions similar to current autologous ligament grafts (i.e. 7 mm in diameter and 32 mm long), and embed the construct in an enzymatically degradable PEG hydrogel to prevent it from unraveling. However, the presence of the hydrogel may reduce the transport of nutrients in the medium to the cells and change the mechanics of the construct [215]. Therefore, cell viability throughout the cross-section of the construct and the mechanical properties (e.g. tensile modulus and stress relaxation) should be determined for constructs with different solution concentrations of the PEG hydrogel (e.g. no hydrogel, 20 vol%, and 30 vol%). After 0, 7, and 14 days of culture, the cell viability throughout the cross-section can be determined by staining dead cells

with ethidium bromide and the nuclei of all cells with DAPI, preparing cross-sections with a cryotome, and then imaging the sections.

This future work is expected to show that cord-like constructs can be produced with techniques similar to those used in Chapter 6: cells seeded prior to processing the electrospun sheet will be distributed throughout the cross-section of the construct, and the hydrogel will prevent the construct from unraveling. Cell viability is expected to be reduced in the inside of the construct even without embedding in a hydrogel, and further reduced with the hydrogel due to the slow rate of diffusion of oxygen and nutrients [215]. However, the concurrent application of cyclic stretch could drive flow of fluid in and out of the hydrogel. In addition, the transport of fluid is expected to provide a reversible route of relieving stresses in the construct [216], and examination of differences in the mechanics of the constructs (e.g. tensile modulus and stress relaxation) with and without the presence of the hydrogel is a logical next step.

7.2.4 Conclusions

The focus of this research project was to develop a ligament tissue engineering strategy that combines BMSCs, electrospun scaffolds, and cyclic stretch bioreactors. Through this project, ligament-like cell behavior on different scaffold topographies and with mechanical stretch was determined and techniques (e.g. co-electrospinning) were developed that may be used to produce three-dimensional structures with improved cell infiltration. Important areas of future work include determining stretch conditions that induce the production of a ligament-like tissue, developing methods to increase cell infiltration into electrospun scaffolds, and producing a ligament-like three-dimensional construct. Successful completion of these next steps is envisioned to result in a ligament-like tissue that will be suitable for *in vivo* testing.

References

1. Altman GH, Horan RL, Lu HH, Moreau J, Martin I, Richmond JC, et al. Silk matrix for tissue engineered anterior cruciate ligaments. *Biomaterials* 2002 Oct;23(20):4131-4141.
2. Lu HH, Cooper Jr. JA, Manuel S, Freeman JW, Attawia MA, Ko FK, et al. Anterior cruciate ligament regeneration using braided biodegradable scaffolds: in vitro optimization studies. *Biomaterials* 2005;26:4805-4816.
3. Lee CH, Shin HJ, Cho IH, Kang YM, Kim IA, Park KD, et al. Nanofiber alignment and direction of mechanical strain affect the ECM production of human ACL fibroblast. *Biomaterials* 2005 Apr;26(11):1261-1270.
4. Yang GG, Crawford RC, Wang JHC. Proliferation and collagen production of human patellar tendon fibroblasts in response to cyclic uniaxial stretching in serum-free conditions. *Journal of Biomechanics* 2004 Oct;37(10):1543-1550.
5. Freeman JW, Woods MD, Laurencin CT. Tissue engineering of the anterior cruciate ligament using a braid-twist scaffold design. *Journal of Biomechanics* 2007;40(9):2029-2036.
6. Nirmalanandhan VS, Dressler MR, Shearn JT, Juncosa-Melvin N, Rao M, Gooch C, et al. Mechanical stimulation of tissue engineered tendon constructs: effect of scaffold materials. *J Biomech Eng* 2007 Dec;129(6):919-923.
7. Cooper JA, Lu HH, Ko FK, Freeman JW, Laurencin CT. Fiber-based tissue-engineered scaffold for ligament replacement: design considerations and in vitro evaluation. *Biomaterials* 2005 May;26(13):1523-1532.
8. Murray MM, Spindler KP. Anterior cruciate ligament healing and repair. *Sports Medicine and Arthroscopy Review* 2005;13(3):151-155.
9. Petrigliano FA, McAllister DR, Wu BM. Tissue engineering for anterior cruciate ligament reconstruction: A review of current strategies. *Arthroscopy-the Journal of Arthroscopic and Related Surgery* 2006 Apr;22(4):441-451.
10. Ge Z, Yang F, Goh JC, Ramakrishna S, Lee EH. Biomaterials and scaffolds for ligament tissue engineering. *J Biomed Mater Res A* 2006 Jun;77(3):639-652.
11. Zhao J, Peng X, He Y, Wang J. Two-bundle anterior cruciate ligament reconstruction with eight-stranded hamstring tendons: four-tunnel technique. *Knee* 2006 Jan;13(1):36-41.
12. Brand J, Weiler A, Caborn DNM, Brown CH, Johnson DL. Graft fixation in cruciate ligament reconstruction. *American Journal of Sports Medicine* 2000 Sep-Oct;28(5):761-774.
13. Goldblatt JP, Fitzsimmons SE, Balk E, Richmond JC. Reconstruction of the anterior cruciate ligament: Meta-analysis of patellar tendon versus hamstring tendon autograft. *Arthroscopy* 2005 Jul;21(7):791-803.
14. Rose T, Engel T, Bernhard J, Hepp P, Josten C, Lill H. Differences in the rehabilitation period following two methods of anterior cruciate ligament replacement: semitendinosus/gracilis tendon vs. ligamentum patellae. *Knee Surg Sports Traumatol Arthrosc* 2004 May;12(3):189-197.
15. Rahaman MN, Mao JJ. Stem cell-based composite tissue constructs for regenerative medicine. *Biotechnology and Bioengineering* 2005 Aug 5;91(3):261-284.
16. Vunjak-Novakovic G, Altman G, Horan R, Kaplan DL. Tissue engineering of ligaments. *Annual Review of Biomedical Engineering* 2004;6:131-156.
17. Jackson DW, Windler GE, Simon TM. Intraarticular reaction associated with the use of freeze-dried, ethylene oxide-sterilized bone-patella tendon-bone allografts in the reconstruction of the anterior cruciate ligament. *American Journal of Sports Medicine* 1990 Jan-Feb;18(1):1-11.

18. Anderson JM. Inflammatory and Immune Responses to Tissue Engineered Devices. In Bronzino JD, editor. *The biomedical engineering handbook: tissue engineering and artificial organs*. 3rd ed. Boca Raton: Taylor & Francis Group. 2006.
19. Doroski DM, Brink KS, Temenoff JS. Techniques for biological characterization of tissue-engineered tendon and ligament. *Biomaterials* 2007 Jan;28(2):187-202.
20. Guidoin MF, Marois Y, Bejui J, Poddevin N, King MW, Guidoin R. Analysis of retrieved polymer fiber based replacements for the ACL. *Biomaterials* 2000 Dec;21(23):2461-2474.
21. Barbara Young JH. *Wheater's Functional Histology*, 4th edition, Churchill Livingstone. New York. 2000.
22. Wang JHC. Mechanobiology of tendon. *Journal of Biomechanics* 2006;39(9):1563-1582.
23. Amiel D, Frank C, Harwood F, Fronck J, Akeson W. Tendons and ligaments: a morphological and biochemical comparison. *J Orthop Res* 1984;1(3):257-265.
24. Murray MM, Spector M. Fibroblast distribution in the anteromedial bundle of the human anterior cruciate ligament: the presence of alpha-smooth muscle actin-positive cells. *J Orthop Res* 1999 Jan;17(1):18-27.
25. Tomasek JJ, Gabbiani G, Hinz B, Chaponnier C, Brown RA. Myofibroblasts and mechano-regulation of connective tissue remodelling. *Nat Rev Mol Cell Biol* 2002 May;3(5):349-363.
26. Gelse K, Poschl E, Aigner T. Collagens--structure, function, and biosynthesis. *Adv Drug Deliv Rev* 2003 Nov 28;55(12):1531-1546.
27. Yoon JH, Halper J. Tendon proteoglycans: biochemistry and function. *J Musculoskeletal Neuronal Interact* 2005 Mar;5(1):22-34.
28. Silver FH, Siperko LM, Seehra GP. Mechanobiology of force transduction in dermal tissue. *Skin Research and Technology* 2003 Feb;9(1):3-23.
29. Halasz K, Kassner A, Morgelin M, Heinegard D. COMP acts as a catalyst in collagen fibrillogenesis. *J Biol Chem* 2007 Oct 26;282(43):31166-31173.
30. Farach-Carson MC, Wagner RC, Kiich KL. *Extracellular Matrix: Structure, Function, and Applications to Tissue Engineering*. Chapter 32, *Tissue Engineering and Artificial Organs*. ed. Bronzino, J.D., Taylor & Francis, Boca Raton, FL. 2006
31. Chiquet M, Renedo AS, Huber F, Fluck M. How do fibroblasts translate mechanical signals into changes in extracellular matrix production? *Matrix Biol* 2003 Mar;22(1):73-80.
32. Chung C, Burdick JA. Engineering cartilage tissue. *Advanced Drug Delivery Reviews* 2007 in press.
33. Lian JB, Stein GS. Concepts of Osteoblast Growth and Differentiation - Basis for Modulation of Bone Cell-Development and Tissue Formation. *Critical Reviews in Oral Biology & Medicine* 1992;3(3):269-305.
34. Schweitzer R, Chyung JH, Murtaugh LC, Brent AE, Rosen V, Olson EN, et al. Analysis of the tendon cell fate using Scleraxis, a specific marker for tendons and ligaments. *Development (Cambridge, England)* 2001 Oct;128(19):3855-3866.
35. Murchison ND, Price BA, Conner DA, Keene DR, Olson EN, Tabin CJ, et al. Regulation of tendon differentiation by scleraxis distinguishes force-transmitting tendons from muscle-anchoring tendons. *Development (Cambridge, England)* 2007 Jul;134(14):2697-2708.
36. Shukunami C, Oshima Y, Hiraki Y. Molecular cloning of tenomodulin, a novel chondromodulin-I related gene. *Biochem Biophys Res Commun* 2001 Feb 9;280(5):1323-1327.

37. Shukunami C, Takimoto A, Oro M, Hiraki Y. Scleraxis positively regulates the expression of tenomodulin, a differentiation marker of tenocytes. *Developmental biology* 2006 Oct 1;298(1):234-247.
38. Docheva D, Hunziker EB, Fassler R, Brandau O. Tenomodulin is necessary for tenocyte proliferation and tendon maturation. *Mol Cell Biol* 2005 Jan;25(2):699-705.
39. Oshima Y, Shukunami C, Honda J, Nishida K, Tashiro F, Miyazaki J, et al. Expression and localization of tenomodulin, a transmembrane type chondromodulin-I-related angiogenesis inhibitor, in mouse eyes. *Invest Ophthalmol Vis Sci* 2003 May;44(5):1814-1823.
40. Chen J, Horan RL, Bramono D, Moreau JE, Wang Y, Geuss LR, et al. Monitoring mesenchymal stromal cell developmental stage to apply on-time mechanical stimulation for ligament tissue engineering. *Tissue Engineering* 2006;12:3085-3095.
41. Ochi M, Murao T, Sumen Y, Kobayashi K, Adachi N. Isolated posterior cruciate ligament insufficiency induces morphological changes of anterior cruciate ligament collagen fibrils. *Arthroscopy-the Journal of Arthroscopic and Related Surgery* 1999 Apr;15(3):292-296.
42. Mommersteeg TJA, Kooloos JGM, Blankevoort L, Kauer JMG, Huijkes R, Roeling FQC. The Fiber Bundle Anatomy of Human Cruciate Ligaments. *Journal of Anatomy* 1995 Oct;187:461-471.
43. Curwin SL, Vailas AC, Wood J. Immature Tendon Adaptation to Strenuous Exercise. *Journal of Applied Physiology* 1988 Nov;65(5):2297-2301.
44. Chen EH, Black J. Materials Design Analysis of the Prosthetic Anterior Cruciate Ligament. *Journal of Biomedical Materials Research* 1980;14(5):567-586.
45. Pioletti DP, Rakotomanana LR, Leyvraz PF. Strain rate effect on the mechanical behavior of the anterior cruciate ligament-bone complex. *Medical Engineering & Physics* 1999 Mar;21(2):95-100.
46. Wang JH, Thampatty BP, Lin JS, Im HJ. Mechanoregulation of gene expression in fibroblasts. *Gene* 2007 Apr 15;391(1-2):1-15.
47. Bosch U, Krettek C. Tissue engineering of ligaments and tendons. A new challenge ahead. *Unfallchirurg* 2002 Feb;105(2):88-94.
48. Moreau J, Chen JS, Horan RL, Kaplan DL, Altman GH. Sequential growth factor application in bone marrow stromal cell ligament engineering. *Tissue Engineering* 2005;11:1887-1897.
49. Altman GH, Horan RL, Martin I, Farhadi J, Stark PR, Volloch V, et al. Cell differentiation by mechanical stress. *FASEB J* 2002 Feb;16(2):270-272.
50. Joshi SD, Webb K. Variation of cyclic strain parameters regulates development of elastic modulus in fibroblast/substrate constructs. *Journal of Orthopaedic Research* 2008 Aug;26(8):1105-1113.
51. Krampera M, Pizzolo G, Aprili G, Franchini M. Mesenchymal stem cells for bone, cartilage, tendon and skeletal muscle repair. *Bone* 2006 Oct;39(4):678-683.
52. Kuroda R, Ishida K, Matsumoto T, Akisue T, Fujioka H, Mizuno K, et al. Treatment of a full-thickness articular cartilage defect in the femoral condyle of an athlete with autologous bone-marrow stromal cells. *Osteoarthritis and Cartilage* 2007 Feb;15(2):226-231.
53. Haynesworth SE, Goshima J, Goldberg VM, Caplan AI. Characterization of Cells with Osteogenic Potential from Human Marrow. *Bone* 1992;13(1):81-88.
54. Martin I, Shastri VP, Padera RF, Yang J, Mackay AJ, Langer R, et al. Selective differentiation of mammalian bone marrow stromal cells cultured on three-dimensional polymer foams. *Journal of Biomedical Materials Research* 2001 May;55(2):229-235.

55. Chen M. Role of fiber diameter in adhesion and proliferation of NIH3T3 fibroblasts on electrospun polycaprolactone scaffolds. 2007.
56. Sun J, Dai ZW, Zhao Y, Chen GQ. In vitro effect of oligo-hydroxyalkanoates on the growth of mouse fibroblast cell line L929. *Biomaterials* 2007 Sep;28(27):3896-3903.
57. DeWitte-Orr SJ, Leong JAC, Bols NC. Induction of antiviral genes, Mx and vig-1, by dsRNA and Chum salmon reovirus in rainbow trout monocyte/macrophage and fibroblast cell lines. *Fish & Shellfish Immunology* 2007 Sep;23(3):670-682.
58. Badami AS, Kreke MR, Thompson MS, Riffle JS, Goldstein AS. Effect of fiber diameter on spreading, proliferation, and differentiation of osteoblastic cells on electrospun poly(lactic acid) substrates. *Biomaterials* 2006 Feb;27(4):596-606.
59. Donahue TLH, Haut TR, Yellowley CE, Donahue HJ, Jacobs CR. Mechanosensitivity of bone cells to oscillating fluid flow induced shear stress may be modulated by chemotransport. *Journal of Biomechanics* 2003 Sep;36(9):1363-1371.
60. Cooper JA, Bailey LO, Carter JN, Castiglioni CE, Kofron MD, Ko FK, et al. Evaluation of the anterior cruciate ligament, medial collateral ligament, achilles tendon and patellar tendon as cell sources for tissue-engineered ligament. *Biomaterials* 2006 May;27(13):2747-2754.
61. Ge ZG, Goh JCH, Lee EH. Selection of cell source for ligament tissue engineering. *Cell Transplantation* 2005;14(8):573-583.
62. Lee SC, Shea M, Battle MA, Kozitza K, Ron E, Turek T, et al. Healing of large segmental defects in rat femurs is aided by RhBMP-2 in PLGA matrix. *J Biomed Mater Res* 1994 Oct;28(10):1149-1156.
63. Abrahamsson SO, Lohmander S. Differential effects of insulin-like growth factor-I on matrix and DNA synthesis in various regions and types of rabbit tendons. *Journal of Orthopaedic Research* 1996 May;14(3):370-376.
64. Banes AJ, Tsuzaki M, Hu PQ, Brigman B, Brown T, Almekinders L, et al. PDGF-BB, IGF-I and mechanical load stimulate DNA synthesis in avian tendon fibroblasts in vitro. *Journal of Biomechanics* 1995 Dec;28(12):1505-1513.
65. Chan BP, Chan KM, Maffulli N, Webb S, Lee KKH. Effect of basic fibroblast growth factor - An in vitro study of tendon healing. *Clinical Orthopaedics and Related Research* 1997 Sep(342):239-247.
66. Ferrara N. Role of vascular endothelial growth factor in the regulation of angiogenesis. *Kidney International* 1999 Sep;56(3):794-814.
67. Murphy DJ, Nixon AJ. Biochemical and site-specific effects of insulin-like growth factor I on intrinsic tenocyte activity in equine flexor tendons. *American Journal of Veterinary Research* 1997 Jan;58(1):103-109.
68. Arora PD, Narani N, McCulloch CAG. The compliance of collagen gels regulates transforming growth factor-beta induction of alpha-smooth muscle actin in fibroblasts. *American Journal of Pathology* 1999 Mar;154(3):871-882.
69. Lavagnino M, Arnoczky SP, Tian T, Vaupel Z. Effect of amplitude and frequency of cyclic tensile strain on the inhibition of MMP-1 mRNA expression in tendon cells: an in vitro study. *Connect Tissue Res* 2003;44(3-4):181-187.
70. Chiquet M, Matthisson M, Koch M, Tannheimer M, ChiquetEhrismann R. Regulation of extracellular matrix synthesis by mechanical stress. *Biochemistry and Cell Biology-Biochimie Et Biologie Cellulaire* 1996;74(6):737-744.
71. Ingber DE, Dike L, Hansen L, Karp S, Liley H, Maniotis A, et al. Cellular Tensegrity - Exploring How Mechanical Changes in the Cytoskeleton Regulate Cell-Growth, Migration, and

Tissue Pattern during Morphogenesis. *International Review of Cytology - a Survey of Cell Biology*, Vol 150 1994;150:173-224.

72. Zeichen J, van Griensven M, Bosch U. The proliferative response of isolated human tendon fibroblasts to cyclic biaxial mechanical strain. *Am J Sports Med* 2000 Nov-Dec;28(6):888-892.

73. Song GB, Ju Y, Shen XD, Luo Q, Shi YS, Qin J. Mechanical stretch promotes proliferation of rat bone marrow mesenchymal stem cells. *Colloids and Surfaces B-Biointerfaces* 2007 Aug 1;58(2):271-277.

74. Sanchez-Esteban J, Wang YL, Cicchiello LA, Rubin LP. Pre- and postnatal lung development, maturation, and plasticity - Cyclic mechanical stretch inhibits cell proliferation and induces apoptosis in fetal rat lung fibroblasts. *American Journal of Physiology-Lung Cellular and Molecular Physiology* 2002 Mar;282(3):L448-L456.

75. Neidlinger-Wilke C, Grood ES, Wang JHC, Brand RA, Claes L. Cell alignment is induced by cyclic changes in cell length: studies of cells grown in cyclically stretched substrates. *Journal of Orthopaedic Research* 2001 Mar;19(2):286-293.

76. Nakatani T, Marui T, Hitora T, Doita M, Nishida K, Kurosaka M. Mechanical stretching force promotes collagen synthesis by cultured cells from human ligamentum flavum via transforming growth factor-beta 1. *Journal of Orthopaedic Research* 2002 Nov;20(6):1380-1386.

77. Kim SG, Akaike T, Sasagawa T, Atomi Y, Kurosawa H. Gene expression of type I and type III collagen by mechanical stretch in anterior cruciate ligament cells. *Cell Struct Funct* 2002 Jun;27(3):139-144.

78. Wang JHC, Yang GG, Li ZZ. Controlling cell responses to cyclic mechanical stretching. *Annals of Biomedical Engineering* 2005 Jan;33(3):337-342.

79. Archambault J, Tsuzaki M, Herzog W, Banes AJ. Stretch and interleukin-1 beta induce matrix metalloproteinases in rabbit tendon cells in vitro. *Journal of Orthopaedic Research* 2002 Jan;20(1):36-39.

80. Noth U, Schupp K, Heymer A, Kall S, Jakob F, Schutze N, et al. Anterior cruciate ligament constructs fabricated from human mesenchymal stem cells in a collagen type I hydrogel. *Cytotherapy* 2005 Nov;7(5):447-455.

81. Kuo CK, Tuan RS. Mechanoactive Tenogenic Differentiation of Human Mesenchymal Stem Cells. *Tissue Engineering Part A* 2008 Oct;14(10):1615-1627.

82. Bashur CA, Dahlgren LA, Goldstein AS. Effect of fiber diameter and orientation on fibroblast morphology and proliferation on electrospun poly(D,L-lactic-co-glycolic acid) meshes. *Biomaterials* 2006 Nov;27(33):5681-5688.

83. Frank C, Woo SLY, Amiel D, Harwood F, Gomez M, Akeson W. Medial Collateral Ligament Healing - a Multidisciplinary Assessment in Rabbits. *American Journal of Sports Medicine* 1983;11(6):379-389.

84. Wang JHC, Jia FY, Gilbert TW, Woo SLY. Cell orientation determines the alignment of cell-produced collagenous matrix. *Journal of Biomechanics* 2003 Jan;36(1):97-102.

85. Flemming RG, Murphy CJ, Abrams GA, Goodman SL, Nealey PF. Effects of synthetic micro- and nano-structured surfaces on cell behavior. *Biomaterials* 1999 Mar;20(6):573-588.

86. Safran SA, Gov N, Nicolas A, Schwarz US, Tlusty T. Physics of cell elasticity, shape and adhesion. *Physica a-Statistical Mechanics and Its Applications* 2005 Jul 1;352(1):171-201.

87. Boudriot U, Dersch R, Greiner A, Wendorff JH. Electrospinning approaches toward scaffold engineering - A brief overview. *Artificial Organs* 2006 Oct;30(10):785-792.

88. Stankus JJ, Guan JJ, Wagner WR. Fabrication of biodegradable elastomeric scaffolds with sub-micron morphologies. *Journal of Biomedical Materials Research Part A* 2004 Sep 15;70A(4):603-614.
89. Gupta AP, Kumar V. New emerging trends in synthetic biodegradable polymers - Polylactide: A critique. *European Polymer Journal* 2007 Oct;43(10):4053-4074.
90. Li WJ, Laurencin CT, Cateson EJ, Tuan RS, Ko FK. Electrospun nanofibrous structure: A novel scaffold for tissue engineering. *Journal of Biomedical Materials Research* 2002 Jun 15;60(4):613-621.
91. Miller RA, Brady JM, Cutright DE. Degradation Rates of Oral Resorbable Implants (Polylactates and Polyglycolates) - Rate Modification with Changes in Pla-Pga Copolymer Ratios. *Journal of Biomedical Materials Research* 1977;11(5):711-719.
92. Gupta B, Revagade N, Hilborn J. Poly(lactic acid) fiber: An overview. *Progress in Polymer Science* 2007 Apr;32(4):455-482.
93. Nair LS, Laurencin CT. Biodegradable polymers as biomaterials. *Progress in Polymer Science* 2007 Aug-Sep;32(8-9):762-798.
94. Courtney T, Sacks MS, Stankus J, Guan J, Wagner WR. Design and analysis of tissue engineering scaffolds that mimic soft tissue mechanical anisotropy. *Biomaterials* 2006 Jul;27(19):3631-3638.
95. El Fray M, Altstadt V. Fatigue behaviour of multiblock thermoplastic elastomers. 3. Stepwise increasing strain test of poly (aliphatic/aromatic-ester) copolymers. *Polymer* 2004 Jan 1;45(1):263-273.
96. Kavlock KD, Pechar TW, Hollinger JO, Guelcher SA, Goldstein AS. Synthesis and characterization of segmented poly(esterurethane urea) elastomers for bone tissue engineering. *Acta Biomaterialia* 2007;3:475-484.
97. Stevens. MP. *Polymer Chemistry An Introduction: Third Edition*. Oxford University Press, New York, . 1999.
98. Li MY, Mondrinos MJ, Gandhi MR, Ko FK, Weiss AS, Lelkes PI. Electrospun protein fibers as matrices for tissue engineering. *Biomaterials* 2005 Oct;26(30):5999-6008.
99. vanderZee E, Everts V, Beertsen W. Cytokines modulate routes of collagen breakdown - Review with special emphasis on mechanisms of collagen degradation in the periodontium and the burst hypothesis of periodontal disease progression. *Journal of Clinical Periodontology* 1997 May;24(5):297-305.
100. Zhang YZ, Venugopal J, Huang ZM, Lim CT, Ramakrishna S. Crosslinking of the electrospun gelatin nanofibers. *Polymer* 2006 Apr 5;47(8):2911-2917.
101. Nickerson MT, Farnworth R, Wagar E, Hodge SM, Rousseau D, Paulson AT. Some physical and microstructural properties of genipin-crosslinked gelatin-maltodextrin hydrogels. *International Journal of Biological Macromolecules* 2006 Feb 28;38(1):40-44.
102. Thomas V, Zhang X, Catledge SA, Vohra YK. Functionally graded electrospun scaffolds with tunable mechanical properties for vascular tissue regeneration. *Biomedical Materials* 2007 Dec;2(4):224-232.
103. WojciakStothard B, Denyer M, Mishra M, Brown RA. Adhesion orientation, and movement of cells cultured on ultrathin fibronectin fibers. *In Vitro Cellular & Developmental Biology-Animal* 1997 Feb;33(2):110-117.
104. Cheng P, Wang C, Zan QF, Dong LM, Tian J. Fabrication of calcium phosphate-based tissue-engineering porous microspheres. *Rare Metal Materials and Engineering* 2007 Aug;36:65-67.

105. Hutmacher DW, Schantz T, Zein I, Ng KW, Teoh SH, Tan KC. Mechanical properties and cell cultural response of polycaprolactone scaffolds designed and fabricated via fused deposition modeling. *Journal of Biomedical Materials Research* 2001 May;55(2):203-216.
106. Williamson MR, Coombes AGA. Gravity spinning of polycaprolactone fibres for applications in tissue engineering. *Biomaterials* 2004 Feb;25(3):459-465.
107. Nelson KD, Romero A, Waggoner P, Crow B, Borneman A, Smith GM. Technique paper for wet-spinning Poly(L-lactic acid) and poly(DL-lactide-co-glycolide) monofilament fibers. *Tissue Engineering* 2003 Dec;9(6):1323-1330.
108. Gupta P, Elkins C, Long TE, Wilkes GL. Electrospinning of linear homopolymers of poly(methyl methacrylate): exploring relationships between fiber formation, viscosity, molecular weight and concentration in a good solvent. *Polymer* 2005 Jun 17;46(13):4799-4810.
109. Dalton PD, Grafahrend D, Klinkhammer K, Klee D, Moller M. Electrospinning of polymer melts: Phenomenological observations. *Polymer* 2007 Nov 2;48(23):6823-6833.
110. Moroni L, Schotel R, Sohler J, de Wijn JR, van Blitterswijk CA. Polymer hollow fiber three-dimensional matrices with controllable cavity and shell thickness. *Biomaterials* 2006 Dec;27(35):5918-5926.
111. Eling B, Gogolewski S, Pennings AJ. Biodegradable materials of poly(L-lactic acid) .1. melt-spun and solution-spun fibers. *Polymer* 1982;23(11):1587-1593.
112. Nair LS, Bhattacharyya S, Bender JD, Greish YE, Brown PW, Allcock HR, et al. Fabrication and optimization of methylphenoxy substituted polyphosphazene nanofibers for biomedical applications. *Biomacromolecules* 2004 Nov-Dec;5(6):2212-2220.
113. Fong H, Chun I, Reneker DH. Beaded nanofibers formed during electrospinning. *Polymer* 1999 Jul;40(16):4585-4592.
114. Inoguchi H, Kwon IK, Inoue E, Takamizawa K, Maehara Y, Matsuda T. Mechanical responses of a compliant electrospun poly(L-lactide-co-epsilon-caprolactone) small-diameter vascular graft. *Biomaterials* 2006 Mar;27(8):1470-1478.
115. den Braber ET, de Ruijter JE, Ginsel LA, von Recum AF, Jansen JA. Orientation of ECM protein deposition, fibroblast cytoskeleton, and attachment complex components on silicone microgrooved surfaces. *J Biomed Mater Res* 1998 May;40(2):291-300.
116. den Braber ET, de Ruijter JE, Smits HTJ, Ginsel LA, von Recum AF, Jansen JA. Quantitative analysis of cell proliferation and orientation on substrata with uniform parallel surface micro-grooves. *Biomaterials* 1996 Jun;17(11):1093-1099.
117. Subbiah T, Bhat GS, Tock RW, Pararneswaran S, Ramkumar SS. Electrospinning of nanofibers. *Journal of Applied Polymer Science* 2005 Apr 15;96(2):557-569.
118. Kwon IK, Kidoaki S, Matsuda T. Electrospun nano- to microfiber fabrics made of biodegradable copolyesters: structural characteristics, mechanical properties and cell adhesion potential. *Biomaterials* 2005 Jun;26(18):3929-3939.
119. Riboldi SA, Sampaolesi M, Neuenschwander P, Cossu G, Mantero S. Electrospun degradable polyesterurethane membranes: potential scaffolds for skeletal muscle tissue engineering. *Biomaterials* 2005 Aug;26(22):4606-4615.
120. Yang F, Murugan R, Wang S, Ramakrishna S. Electrospinning of nano/micro scale poly(L-lactic acid) aligned fibers and their potential in neural tissue engineering. *Biomaterials* 2005 May;26(15):2603-2610.
121. Li D, Wang YL, Xia YN. Electrospinning of polymeric and ceramic nanofibers as uniaxially aligned arrays. *Nano Letters* 2003 Aug;3(8):1167-1171.

122. Zong XH, Bien H, Chung CY, Yin LH, Fang DF, Hsiao BS, et al. Electrospun fine-textured scaffolds for heart tissue constructs. *Biomaterials* 2005 Sep;26(26):5330-5338.
123. Xu CY, Inai R, Kotaki M, Ramakrishna S. Aligned biodegradable nanofibrous structure: a potential scaffold for blood vessel engineering. *Biomaterials* 2004;25:877-886.
124. Kidoaki S, Kwon IK, Matsuda T. Mesoscopic spatial designs of nano- and microfiber meshes for tissue-engineering matrix and scaffold based on newly devised multilayering and mixing electrospinning techniques. *Biomaterials* 2005 Jan;26(1):37-46.
125. Bini TB, Gao SJ, Tan TC, Wang S, Lim A, Hai LB, et al. Electrospun poly(L-lactide-co-glycolide) biodegradable polymer nanofibre tubes for peripheral nerve regeneration. *Nanotechnology* 2004 Nov;15(11):1459-1464.
126. Vaz CM, van Tuijl S, Bouten CV, Baaijens FP. Design of scaffolds for blood vessel tissue engineering using a multi-layering electrospinning technique. *Acta Biomater* 2005 Sep;1(5):575-582.
127. Rho KS, Jeong L, Lee G, Seo BM, Park YJ, Hong SD, et al. Electrospinning of collagen nanofibers: Effects on the behavior of normal human keratinocytes and early-stage wound healing. *Biomaterials* 2006 Mar;27(8):1452-1461.
128. Min BM, Lee G, Kim SH, Nam YS, Lee TS, Park WH. Electrospinning of silk fibroin nanofibers and its effect on the adhesion and spreading of normal human keratinocytes and fibroblasts in vitro. *Biomaterials* 2004 Mar-Apr;25(7-8):1289-1297.
129. Moroni L, Licht R, de Boer J, de Wijn JR, van Blitterswijk CA. Fiber diameter and texture of electrospun PEOT/PBT scaffolds influence human mesenchymal stem cell proliferation and morphology, and the release of incorporated compounds. *Biomaterials* 2006 Oct;27(28):4911-4922.
130. Eichhorn SJ, Sampson WW. Statistical geometry of pores and statistics of porous nanofibrous assemblies. *Journal of the Royal Society Interface* 2005 Sep 22;2(4):309-318.
131. Baker BM, Gee AO, Metter RB, Nathan AS, Marklein RA, Burdick JA, et al. The potential to improve cell infiltration in composite fiber-aligned electrospun scaffolds by the selective removal of sacrificial fibers. *Biomaterials* 2008 May;29(15):2348-2358.
132. Gupta P, Wilkes GL. Some investigations on the fiber formation by utilizing a side-by-side bicomponent electrospinning approach. *Polymer* 2003 Sep;44(20):6353-6359.
133. Zhao PC, Jiang HL, Pan H, Zhu KJ, Chen W. Biodegradable fibrous scaffolds composed of gelatin coated poly(epsilon-caprolactone) prepared by coaxial electrospinning. *Journal of Biomedical Materials Research Part A* 2007 Nov;83A(2):372-382.
134. Wu L, Li H, Li S, Li X, Yuan X, Zhang Y. Composite fibrous membranes of PLGA and chitosan prepared by coelectrospinning and coaxial electrospinning. *J Biomed Mater Res A* 2009 Feb 20.
135. Ding B, Kimura E, Sato T, Fujita S, Shiratori S. Fabrication of blend biodegradable nanofibrous nonwoven mats via multi-jet electrospinning. *Polymer* 2004 Mar 15;45(6):1895-1902.
136. Duan B, Wu L, Yuan X, Hu Z, Li X, Zhang Y, et al. Hybrid nanofibrous membranes of PLGA/chitosan fabricated via an electrospinning array. *J Biomed Mater Res A* 2007 Dec 1;83(3):868-878.
137. Nam J, Huang Y, Agarwal S, Lannutti J. Improved cellular infiltration in electrospun fiber via engineered porosity. *Tissue Engineering* 2007 Sep;13(9):2249-2257.

138. Mo XM, Xu CY, Kotaki M, Ramakrishna S. Electrospun P(LLA-CL) nanofiber: a biomimetic extracellular matrix for smooth muscle cell and endothelial cell proliferation. *Biomaterials* 2004 May;25(10):1883-1890.
139. Buttafoco L, Kolkman NG, Engbers-Buijtenhuijs P, Poot AA, Dijkstra PJ, Vermes I, et al. Electrospinning of collagen and elastin for tissue engineering applications. *Biomaterials* 2006 Feb;27(5):724-734.
140. Lee CK, Kim SL, Kim SJ. The influence of added ionic salt on nanofiber uniformity for electrospinning of electrolyte polymer. *Synthetic Metals* 2005;154(1-3):209-212.
141. Ayres C, Bowlin GL, Henderson SC, Taylor L, Shultz J, Alexander J, et al. Modulation of anisotropy in electrospun tissue-engineering scaffolds: Analysis of fiber alignment by the fast Fourier transform. *Biomaterials* 2006 Jul 19.
142. Boland ED, Telemeco TA, Simpson DG, Wnek GE, Bowlin GL. Utilizing acid pretreatment and electrospinning to improve biocompatibility of poly(glycolic acid) for tissue engineering. *Journal of Biomedical Materials Research Part B-Applied Biomaterials* 2004 Oct 15;71B(1):144-152.
143. Lee KH, Kim HY, Khil MS, Ra YM, Lee DR. Characterization of nano-structured poly(epsilon-caprolactone) nonwoven mats via electrospinning. *Polymer* 2003 Feb;44(4):1287-1294.
144. Sahoo S, Ouyang H, Goh JCH, Tay TE, Toh SL. Characterization of a novel polymeric scaffold for potential application in tendon/ligament tissue engineering. *Tissue Engineering* 2006 Jan;12(1):91-99.
145. Haasper C, Jagodzinski M, Drescher M, Meller R, Wehmeier M, Krettek C, et al. Cyclic strain induces FosB and initiates osteogenic differentiation of mesenchymal cells. *Experimental and Toxicologic Pathology* 2008;59:355-363.
146. Sumanasinghe RD, Bernacki SH, Lobo EG. Osteogenic differentiation of human mesenchymal stem cells in collagen matrices: Effect of uniaxial cyclic tensile strain on bone morphogenetic protein (BMP-2) mRNA expression. *Tissue Engineering* 2006 Dec;12(12):3459-3465.
147. Glass-Brudzinski J, Perizzolo D, Brunette DM. Effects of substratum surface topography on the organization of cell and collagen fibers in collagen gel cultures. *Journal of Biomedical Materials Research* 2002;61:608-618.
148. Engelmayer GC, Papworth GD, Watkins SC, Mayer JE, Sacks MS. Guidance of engineered tissue collagen orientation by large-scale scaffold microstructures. *Journal of Biomechanics* 2006;39(10):1819-1831.
149. Joung IS, Iwamoto MN, Shiu YT, Quam CT. Cyclic strain modulates tubulogenesis of endothelial cells in a 3D tissue culture model. *Microvascular Research* 2006 Jan;71(1):1-11.
150. Bashur CA, Shaffer R, Dahlgren LA, Guelcher SA. Effect of Fiber Diameter and Alignment of Electrospun Polyurethane Meshes on Mesenchymal Progenitor Cells. *Tissue Engineering* (in press).
151. Harris AK, Wild P, Stopak D. Silicone-Rubber Substrata - New Wrinkle in the Study of Cell Locomotion. *Science* 1980;208(4440):177-179.
152. Yang G, Im HJ, Wang JH. Repetitive mechanical stretching modulates IL-1beta induced COX-2, MMP-1 expression, and PGE2 production in human patellar tendon fibroblasts. *Gene* 2005 Dec 19;363:166-172.

153. Zhang L, Kahn CJF, Chen HQ, Tran N, Wang X. Effect of uniaxial stretching on rat bone mesenchymal stem cell: Orientation and expressions of collagen types I and III and tenascin-C. *Cell Biology International* 2008 Mar;32(3):344-352.
154. Gilbert TW, Stewart-Akers AM, Sydeski J, Nguyen TD, Badylak SF, Woo SL. Gene expression by fibroblasts seeded on small intestinal submucosa and subjected to cyclic stretching. *Tissue Eng* 2007 Jun;13(6):1313-1323.
155. Wang JH, Goldschmidt-Clermont P, Wille J, Yin FC. Specificity of endothelial cell reorientation in response to cyclic mechanical stretching. *J Biomech* 2001 Dec;34(12):1563-1572.
156. Sarkissian M, Lafyatis R. Integrin engagement regulates proliferation and collagenase expression of rheumatoid synovial fibroblasts. *Journal of Immunology* 1999 Feb 1;162(3):1772-1779.
157. Dzamba BJ, Bolton MA, Desimone DW. The integrin family of cell adhesion molecules. *Cell adhesion frontiers in molecular biology* 2001;Oxford Press.
158. Lauer L, Klein C, Offenhausser A. Spot compliant neuronal networks by structure optimized micro-contact printing. *Biomaterials* 2001 Jul;22(13):1925-1932.
159. Iwamoto Y, Robey FA, Graf J, Sasaki M, Kleinman HK, Yamada Y, et al. Yigrs, a Synthetic Laminin Pentapeptide, Inhibits Experimental Metastasis Formation. *Science* 1987 Nov 20;238(4830):1132-1134.
160. Tashiro K, Sefhel GC, Weeks B, Sasaki M, Martin GR, Kleinman HK, et al. A Synthetic Peptide Containing the Ikvav Sequence from the α -Chain of Laminin Mediates Cell Attachment, Migration, and Neurite Outgrowth. *Journal of Biological Chemistry* 1989 Sep 25;264(27):16174-16182.
161. Khang G, Choe JH, Rhee JM, Lee HB. Interaction of different types of cells on physicochemically treated poly(L-lactide-co-glycolide) surfaces. *Journal of Applied Polymer Science* 2002 Aug 8;85(6):1253-1262.
162. Cheng SS, Chittur KK, Sukenik CN, Culp LA, Lewandowska K. The Conformation of Fibronectin on Self-Assembled Monolayers with Different Surface-Composition - an Ftir/Atr Study. *Journal of Colloid and Interface Science* 1994 Jan;162(1):135-143.
163. Zeng DH, Ferrari A, Ulmer J, Veligodskiy A, Fischer P, Spatz J, et al. Three-dimensional modeling of mechanical forces in the extracellular matrix during epithelial lumen formation. *Biophysical Journal* 2006 Jun;90(12):4380-4391.
164. Curtis A, Riehle M. Tissue engineering: the biophysical background. *Physics in Medicine and Biology* 2001 Apr;46(4):R47-R65.
165. Curtis A, Wilkinson C. Topographical control of cells. *Biomaterials* 1997 Dec;18(24):1573-1583.
166. den Braber ET, Jansen HV, de Boer MJ, Croes HJ, Elwenspoek M, Ginsel LA, et al. Scanning electron microscopic, transmission electron microscopic, and confocal laser scanning microscopic observation of fibroblasts cultured on microgrooved surfaces of bulk titanium substrata. *J Biomed Mater Res* 1998;40(3):425-433.
167. Walboomers XF, Ginsel LA, Jansen JA. Early spreading events of fibroblasts on microgrooved substrates. *Journal of Biomedical Materials Research* 2000 Sep 5;51(3):529-534.
168. Johansson F, Carlberg P, Danielsen N, Montelius L, Kanje M. Axonal outgrowth on nano-imprinted patterns. *Biomaterials* 2006 Mar;27(8):1251-1258.
169. Clark P, Connolly P, Curtis ASG, Dow JAT, Wilkinson CDW. Cell Guidance by Ultrafine Topography In vitro. *Journal of Cell Science* 1991 May;99:73-77.

170. Izzard CS, Lochner LR. Cell-to-Substrate Contacts in Living Fibroblasts - Interference Reflection Study with an Evaluation of Technique. *Journal of Cell Science* 1976;21(1):129-159.
171. Ward MD, Hammer DA. A Theoretical-Analysis for the Effect of Focal Contact Formation on Cell-Substrate Attachment Strength. *Biophysical Journal* 1993 Mar;64(3):936-959.
172. Chen CS, Mrksich M, Huang S, Whitesides GM, Ingber DE. Geometric control of cell life and death. *Science* 1997 May 30;276(5317):1425-1428.
173. Trinkausrandall V, Capecchi J, Newton A, Vadasz A, Leibowitz H, Franzblau C. Development of a Biopolymeric Keratoprosthetic Material - Evaluation In vitro and In vivo. *Investigative Ophthalmology & Visual Science* 1988 Mar;29(3):393-400.
174. Jackson DW, Groot ES, Goldstein JD, Rosen MA, Kurzweil PR, Cummings JF, et al. A comparison of patellar tendon autograft and allograft used for anterior cruciate ligament reconstruction in the goat model. *American Journal of Sports Medicine* 1993 Mar-Apr;21(2):176-185.
175. Moreau JE, Chen JS, Bramono DS, Volloch V, Chernoff H, Vunjak-Novakovic G, et al. Growth factor induced fibroblast differentiation from human bone marrow stromal cells in vitro. *Journal of Orthopaedic Research* 2005 Jan;23(1):164-174.
176. Singhvi R, Kumar A, Lopez GP, Stephanopoulos GN, Wang DIC, Whitesides GM, et al. Engineering cell shape and function. *Science* 1994;264:696-698.
177. Teixeira AI, Abrams GA, Bertics PJ, Murphy CJ, Nealey PF. Epithelial contact guidance on well-defined micro- and nanostructured substrates. *Journal of Cell Science* 2003;116:1881-1892.
178. Walboomers XF, Croes HJE, Ginsel LA, Jansen JA. Contact guidance of rat fibroblasts on various implant materials. *Journal of Biomedical Materials Research* 1999 Nov;47(2):204-212.
179. Zhu BS, Lu QH, Yin J, Hu J, Wang ZG. Alignment of osteoblast-like cells and cell-produced collagen matrix induced by nanogrooves. *Tissue Engineering* 2005 May;11(5-6):825-834.
180. Fisher NI. *Statistical analysis of circular data*. New York: Cambridge University Press, 1993.
181. Chen CS, Mrksich M, Huang S, Whitesides GM, Ingber DE. Micropatterned surfaces for control of cell shape, position, and function. *Biotechnology Progress* 1998;14:356-363.
182. Singhvi R, Stephanopoulos G, Wang DIC. Effects of substratum morphology on cell physiology. *Biotechnology and Bioengineering* 1994 Apr 5;43(8):764-771.
183. Jeong SI, Kim SH, Kim YH, Jung Y, Kwon JH, Kim BS, et al. Manufacture of elastic biodegradable PLCL scaffolds for mechano-active vascular tissue engineering. *Journal of Biomaterial Science, Polymer Edition* 2004;15:645-660.
184. Moreau JE, Chen J, Kaplan DL, Altman G. Sequential growth factor stimulation of bone marrow stromal cells in extended culture. *Tissue Engineering* 2006;12:2905-2912.
185. Rezgui F, Swistek M, Hiver HM, G'Sell C, Sadoun T. Deformation and damage upon stretching of degradable polymers (PLA and PCL). *Polymer* 2005;46:7370-7385.
186. Skarja GA, Woodhouse KA. Synthesis and characterization of degradable polyurethane elastomers containing an amino-acid based chain extender. *Journal of Biomaterials Science Polymer Edition* 1998;9(3):271-295.
187. Spaans CJ, De Groot JH, Dekens FG, Pennings AJ. High molecular weight polyurethanes and a polyurethane urea based on 1,4-butanediisocyanate. *Polymer Bulletin* 1998;41:131-138.

188. Guan J, Sacks M, Beckman E, Wagner W. Synthesis, characterization, and cytocompatibility of elastomeric, biodegradable poly(ester-urethane)ureas based on poly(caprolactone) and putrescine. *Journal of Biomedical Materials Research* 2002;61:493-503.
189. Guelcher SA, Gallagher K, Didier JE, Klinedinst D, Doctor JS, Goldstein A, et al. Synthesis of biocompatible segmented polyurethanes from aliphatic diisocyanates and diurea diol chain extenders. *Acta Biomaterialia* 2005;1:471-484.
190. Stylianopoulos T, Bashur CA, Goldstein AS, Guelcher SA, Barocas VH. Computational predictions of the tensile properties of electrospun fibre meshes: Effect of fibre diameter and fibre orientation. *Journal of the Mechanical Behavior of Biomedical Materials* 2008 Oct;1(4):326-335.
191. Li WJ, Mauck RL, Cooper JA, Yuan X, Tuan RS. Engineering controllable anisotropy in electrospun biodegradable nanofibrous scaffolds for musculoskeletal tissue engineering. *J Biomech* 2007;40:1683-1693.
192. Baker BM, Mauck RL. The effect of nanofiber alignment on the maturation of engineered meniscus constructs. *Biomaterials* 2007 Apr;28(11):1967-1977.
193. Liu WF, Chen CS. Cellular and multicellular form and function. *Adv Drug Deliv Rev* 2007;59:1319-1328.
194. Goldstein AS, Juarez TM, Helmke CD, Gustin MC, Mikos AG. Effect of convection of osteoblastic cell growth and function in biodegradable polymer foam scaffolds. *Biomaterials* 2001;22:1279-1288.
195. Kreke MR, Huckle WR, Goldstein AS. Fluid flow stimulates expression of osteopontin and bone sialoprotein by bone marrow stromal cells in a temporally dependent manner. *Bone* 2005;36:1047-1055.
196. Livak KJ, Schmittgen TD. Analysis of relative gene expression data using real-time quantitative PCR and the 2(-Delta Delta C(T)) Method. *Methods* 2001;25:402-408.
197. Kumbhar SG, Nukavarapu SP, James R, Nair LS, Laurencin CT. Electrospun poly(lactic acid-co-glycolic acid) scaffolds for skin tissue engineering. *Biomaterials* 2008 Oct;29(30):4100-4107.
198. Chew SY, Mi R, Hoke A, Leong KW. The effect of the alignment of electrospun fibrous scaffolds on Schwann cell maturation. *Biomaterials* 2008 Feb;29(6):653-661.
199. Thomas TW, DiMilla PA. Spreading and motility of human glioblastoma cells on sheets of silicone rubber depend on substratum compliance. *Medical and Biological Engineering and Computing* 2000;38:360-370.
200. Saez A, Ghibaudo M, Buguin A, Silberzan P, Ladoux B. Rigidity-driven growth and migration of epithelial cells on microstructured anisotropic substrates. *Proc Natl Acad Sci USA* 2007;104:8281-8286.
201. Engler AJ, Sen S, Sweeney HL, Discher DE. Matrix elasticity directs stem cell lineage specification. *Cell* 2006;126:677-689.
202. Kasprczyk WJ, Rosocha S, Bosch U, Oestern HJ, Tscherne H. Age, activity and strength of knee ligaments. *Unfallchirurg* 1991;94:372-375.
203. Noyes FR, Grood ES. The strength of the anterior cruciate ligament in humans and Rhesus monkeys. *J Bone Joint Surg Am* 1976;58:1074-1082.
204. Lee I, Wang JH, Lee YT, Young TH. The differentiation of mesenchymal stem cells by mechanical stress or/and co-culture system. *Biochemical and Biophysical Research Communications* 2007;352:147-152.

205. Choi WY, Lee CM, Park HJ. Development of biodegradable hot-melt adhesive based on poly-epsilon-caprolactone and soy protein isolate for food packaging system. *Lwt-Food Science and Technology* 2006;39(6):591-597.
206. Mooney DJ, Cima L, Langer R, Johnson L, Hansen LK, Ingber DE, et al. Principles of Tissue Engineering and Reconstruction Using Polymer-Cell Constructs. *Tissue-Inducing Biomaterials* 1992;252:345-352
391.
207. Thomas V, Jose MV, Chowdhury S, Sullivan JF, Dean DR, Vohra YK. Mechano-morphological studies of aligned nanofibrous scaffolds of polycaprolactone fabricated by electrospinning. *Journal of Biomaterials Science-Polymer Edition* 2006;17(9):969-984.
208. Wang JH, Yang G, Li Z, Shen W. Fibroblast responses to cyclic mechanical stretching depend on cell orientation to the stretching direction. *J Biomech* 2004;37:573-576.
209. Davis MJ, Sikes PJ. Myogenic Responses of Isolated Arterioles - Test for a Rate-Sensitive Mechanism. *American Journal of Physiology* 1990 Dec;259(6):H1890-H1900.
210. Ralphs JR, Waggett AD, Benjamin M. Actin stress fibres and cell-cell adhesion molecules in tendons: organisation in vivo and response to mechanical loading of tendon cells in vitro. *Matrix Biology* 2002 Jan;21(1):67-74.
211. Hahn MS, McHale MK, Wang E, Schmedlen RH, West JL. Physiologic pulsatile flow bioreactor conditioning of poly(ethylene glycol)-based tissue engineered vascular grafts. *Annals of Biomedical Engineering* 2007 Feb;35(2):190-200.
212. Akin H, Hasirci N. Preparation and Characterization of Cross-Linked Gelatin Microspheres. *Journal of Applied Polymer Science* 1995 Oct 3;58(1):95-100.
213. Webb K, Hitchcock RW, Smeal RM, Li WH, Gray SD, Tresco PA. Cyclic strain increases fibroblast proliferation, matrix accumulation, and elastic modulus of fibroblast-seeded polyurethane constructs. *Journal of Biomechanics* 2006;39(6):1136-1144.
214. Woo SL, Kanamori A, Zeminski J, Yagi M, Papageorgiou C, Fu FH. The effectiveness of reconstruction of the anterior cruciate ligament with hamstrings and patellar tendon . A cadaveric study comparing anterior tibial and rotational loads. *J Bone Joint Surg Am* 2002 Jun;84-A(6):907-914.
215. Fournier R. *Basic Transport Phenomena in Biomedical Engineering*, Taylor & Francis, Philadelphia. 1999.
216. Buckwalter JA, HJ M. Articular cartilage: Tissue design and chondrocyte matrix interactions. *Instructional Course Lectures* 47. American Academy of Orthopaedic Surgeons, Rosemont, IL. 1998.

Appendix A: Enhanced Polarization of Embryonic Hippocampal Neurons on Micron Scale Electrospun Fibers

Jae Young Lee¹, Chris A. Bashur², Natalia Gomez¹, Aaron S. Goldstein^{2} and Christine E. Schmidt^{1, 3-5}*

¹Department of Chemical Engineering, The University of Texas at Austin, Austin, Texas

²Department of Chemical Engineering, Virginia Polytechnic Institute and State University, Blacksburg, Virginia

³Department of Biomedical Engineering, The University of Texas at Austin, Austin, Texas

⁴Texas Materials Institute, The University of Texas at Austin, Austin, Texas

⁵Center for Nano- and Molecular Science and Technology, The University of Texas at Austin, Austin, Texas

Abstract

Electrospun fibers have been fabricated for wide use as artificial tissue engineering scaffolds. In particular, fibers smaller than a cell body have been extensively employed to mimic natural extracellular matrix (ECM) and to explore specific responses by various cell types. We investigated the effects of various poly(lactic acid-*co*-glycolic acid) (PLGA) fiber features on embryonic hippocampal neurons in the early developmental stages in terms of initial axon formation (i.e., polarization) and axon orientation. We produced PLGA fibers that have average diameters ranging from 0.44 μm to 2.2 μm and different degrees of fiber alignment (16-58° in angular standard deviation). After 22 h in culture, embryonic hippocampal neurons grown on PLGA fibers exhibited more axon formation with a 30-50% increase over those on spin-coated smooth PLGA films. This improvement was independent of fiber diameter and alignment; however, slightly more polarization was observed on the smaller fibers and the more aligned fibers. In addition, average axon length of the polarized embryonic hippocampal neurons was not significantly different among the PLGA fibers when compared to cells grown on spin-coated PLGA films. These findings suggest that fibers of subcellular diameters stimulate initial axon establishment and guide the direction of axonal extension; however these fibers do not appear to affect overall axon length. This information will be valuable in understanding the roles of subcellular features on neuron development and for the design of biomaterials for neural tissue interfacing.

A.1 Introduction

Electrospun fibers have been widely studied for a number of tissue engineering applications because of their attractive features such as high surface area, interconnecting pores, and good mechanical support.^{1,2} In particular, electrospinning techniques have allowed the production of fibers smaller than a cell body and even down to several nanometers, and are thus capable of mimicking architectural and topographic features of the extracellular matrix (ECM).¹ These small fibers not only provide high surface area, but also present a means to control cellular behaviors, such as adhesion and proliferation. In addition to fiber diameter, fiber alignment has been found to regulate cellular behaviors including contact guidance and differentiation.^{3,4} Electrospinning can be used to create fibers bearing various features and chemical compositions using numerous materials, such as synthetic polymers [e.g., PLGA, polycaprolactone (PCL)] and natural polymers (e.g., collagen, hyaluronic acid).⁵⁻⁸ For cell culture, a number of studies have demonstrated that electrospun fibers are able to support and regulate cell growth and differentiation *in vivo* and *in vitro*.^{1,2} For example, nanofibrous poly (L-lactic acid) (PLLA) scaffolds supported adhesion and proliferation of human vein endothelial cells,⁹ and PCL nanofibers induced chondrogenesis of adult bone marrow-derived mesenchymal stem cells.¹⁰

For neural tissue applications, Ramakrishna and coworkers demonstrated that electrospun PLLA nanofibers supported neuron growth and differentiation *in vivo* and *in vitro*.^{4,11} Subsequent studies have also shown that electrospun fibers are suitable and even beneficial for neuron cultures, where growth and differentiation on electrospun fibers were observed for dorsal root ganglion (DRG) neurons, Schwann cells, and cortical neurons.^{12,13} Hence, fibers of various diameters and degrees of alignment create topographical features that influence neuronal behavior. However, little has been explored with respect to the effects of various fibers of micron scales on neural differentiation (i.e., axon formation) and an axonal alignment (i.e., contact guidance) at early developmental stages, of which an understanding will be beneficial for neuroscientists and bioengineers studying nerve tissue repair and regeneration.

To investigate the initial formation of an axon in response to various fiber features, we have used embryonic hippocampal neurons, which have been widely used because of their spontaneous establishment of a highly polarized morphology with a single axon and multiple dendrites.¹⁴ Also, hippocampal neurons have been reported to show specific responses to topographical features, such as pores and microgrooves.^{15,16} Hippocampal differentiation *in vitro*

involves five developmental stages.¹⁷ First, an adherent neuron forms a motile lamellipodium (stage 1). Then, the neuron differentiates by forming multiple neurites (stage 2), followed by establishment of a single axon among the immature neuritis (neuron polarization, stage 3) after 24–48 h in culture. This is followed by maturation with further extension of the axon and formation of multiple dendrites (stages 4 and 5). At this stage, the mature hippocampal neurons form synaptic contacts and communicate with other neurons, establishing neural networks. In tissue culture, neuron polarization occurs spontaneously, although the rate of polarization is affected by the cellular environment, including various biochemical molecules such as neurotrophins and calcium ions.^{14,18–20}

Importantly, neuron polarization can also be modulated in tissue culture by nonbiochemical signals including mechanical and topographical properties of the biomaterial substrate.^{16,21} In a recent study, we showed that poly(dimethyl siloxane) (PDMS) microchannels of both 1 and 2 μm width promoted polarization of embryonic hippocampal neurons compared with smooth PDMS substrates.¹⁶ However, although the extent of polarization was similar for 1- μm and 2- μm patterns, axons preferentially crossed the 1- μm ridges, whereas they were aligned along the direction of 2- μm ridges. On the basis of this previous study, we hypothesize that topographies created by electrospun fibers of micron sizes may play a similar role to the micropatterned substrates in supporting axon initiation and alignment of embryonic hippocampal neurons.

To determine the effects of fiber features in initial neuronal differentiation, PLGA meshes were electrospun with various fiber diameters (0.44, 1.5, and 2.2 μm) and alignments (16, 28, and 53°) (**Table A.1**). Rat embryonic hippocampal neurons were cultured for 22 h on these fibers and on spin-coated PLGA films, and analyzed using immunostaining of axonal protein (tau-1) to monitor axonal growth (i.e., polarization and extension) and alignment.

Table A.1. PLGA fibers synthesized and tested for embryonic hippocampal neuron culture

Samples	Synthesis Conditions		Analysis			
	Concentration (wt % PLGA)	Drum Speed (m/s)	No. Fibers Analyzed (n)	Average Diameter \pm STD* (μm)	Angular Standard Deviation ($^{\circ}$)	Fiber Orientation
RD_7	7	0	210	0.44 ± 0.18	57.84	Random
RD_10.5	10.5	0	167	1.51 ± 0.56	52.93	Random
IN_10.5	10.5	4.9	233	1.25 ± 0.52	27.67	Intermediate
HI_10.5	10.5	10	189	0.97 ± 0.32	15.89	High
RD_13	13	0	115	2.22 ± 0.55	50.07	Random

STD*=standard deviation

A.2 Materials and Methods

A.2.1 Electrospinning

A 75/25 poly(D,L lactic-co-glycolic acid) (PLGA) (inherent viscosity 0.55–0.75 dL/g) was purchased from Lactel Biodegradable Polymers (Birmingham, AL) and electrospun onto 18-mm circular glass coverslips (Sigma, St. Louis, MO) to form fused-fiber meshes with controlled fiber diameters and degrees of fiber alignment as described previously.²² Briefly, glass coverslips were sonicated in ethanol and allowed to air dry. Next, a 0.30 mL volume of a 3.5 wt% solution of PLGA in dichloromethane (Sigma) was deposited with a Model 1-EC101D-R485 spincoater (Headway Research, Garland, TX) onto the glass to form a smooth spin-coated polymer film. The spincoater was operated at a rotational speed of 2500 rpm for 30 s, and the samples were allowed to air dry. For fiber scaffolds, the spin-coated coverslips were then mounted onto a stationary stand and PLGA was electrospun under ambient conditions to form fiber meshes with random fiber orientation. Fiber diameter was controlled by using PLGA concentration in hexafluoro-2-propanol (HFIP) (Sigma) of 7.0, 10.5, and 13.0 wt%. Electrospinning was performed with a syringe equipped with a 22-gauge Teflon-tipped needle using a 15 kV potential, a throw distance of 15 cm, and a syringe flow rate of 5 mL/h. To form oriented meshes, the spin-coated coverslips were mounted onto a 7.6 cm diameter drum rotated at linear velocities of 4.9 and 10.0 m/s and PLGA was electrospun. After electrospinning, PLGA coverslips were air dried for 2 days to remove residual HFIP. Representative scanning electron microscopy (SEM) images of PLGA fibers on coverslips are displayed in **Figure A.1**.

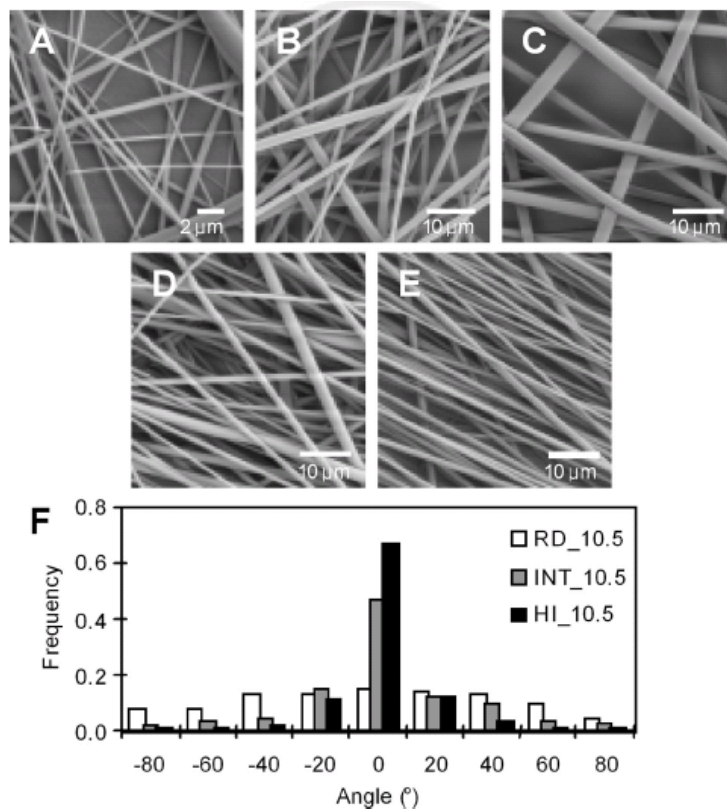


Fig. A.1. Scanning electron micrographs of PLGA fibers electrospun using different concentrations and rotation speeds of a collector: Random fibers of (A) RD_7, (B) RD_10.5, and (C) RD_13 were electrospun using 7%, 10.5%, and 13% polymer solution at a stationary mode, respectively. Aligned fibers were produced from 10.5% concentration on a rotating collector: (B) 0 m/s (random fibers, RD_10.5), (D) 4.9 m/s (intermediately oriented fibers, INT_10.5), and (E) 10 m/s (highly oriented fibers, HI_10.5). (F) Normalized histograms of fiber angles for the fibers (B, D, and E). At least 100 individual fibers were analyzed from a representative sample for each substrate.

A.2.2 Hippocampal Cell Culture

For cell culture experiments, electrospun meshes and spin-coated films were transferred to a 12-well cell culture plate (BD, Franklin Lakes, NJ), and sterilized by exposure to UV for 2 h. The samples were incubated in 0.2 mg/mL poly-D-lysine (Sigma) overnight, and washed twice with sterile double deionized (ddI) water. The substrates were dried in a laminar flow bench, and stored at 4°C until use. Rat embryonic hippocampal neurons (E-18) were isolated from commercial rat hippocampal tissue (BrainBits, Springfield, IL) according to the manufacture's protocol. In brief, a hippocampus was incubated in 4 mg/mL papain (Worthington, Lakewood, NJ) solution in Hibernate E medium (BrainBits) at 30°C for 20 min. A fire-polished Pasteur pipette was used to triturate the hippocampal tissue, followed by centrifugation (200g, 1 min).

The cell pellet was suspended in 1 mL of warm culture medium, containing Neurobasal medium (Invitrogen, Gaithersburg, MD), 2% B-27 supplement (Invitrogen), 0.5 mM L-glutamine (Fisher, Pittsburgh, PA), 0.025 mM glutamic acid (Sigma), and 1% antibiotic-antimycotic solution (Sigma). Totally, 2×10^4 cells/cm² were inoculated onto different samples of PLGA fibers and spin-coated coverslips. The cells were incubated at 37°C in a humid, 5% CO² incubator for 22 h. For each substrate, data were collected from at least five experiments performed on separate days.

A.2.3 SEM

SEM was used to analyze electrospun PLGA fibers and hippocampal neurons on the substrates for cellular morphologies and interaction with fibers. For the characterization of the fibers, high-resolution images of electrospun meshes were acquired using a LEO1550 Field Emission SEM (Carl Zeiss SMT, Thornwood, NY). Briefly, samples were mounted onto studs and sputtercoated with 20 nm of palladium using a Cressington Scientific Instruments Model 208HR (Cranberry Township, PA).

For cell images, the fixed hippocampal neurons were dehydrated by successive treatment with increasing ethanol concentrations in water (30% for 45 min; 50% for 30 min, 70%, 85%, 90%, 95%, and absolute ethanol (Pharmco, Brookfield, CT) for 10 min each). Water was completely removed by adding hexamethyl disilazane (HMDS) (Sigma) and drying in air. The dried samples were coated with a 10 nm thick layer of platinum/palladium using a sputter coater (Cressington 208HR). SEM images were acquired with a Zeiss SUPRA 40 VP Scanning Electron Microscope. Fiber characterization The diameter and degree of orientation of the electrospun fibers were measured from already defined SEM images using ImagePro Plus software (ICube, Crofton, MD) as previously described.²² At least 100 individual fibers were measured from a representative sample for each substrate. The degree of fiber alignment was characterized by a wrapped normal distribution and expressed as angular standard deviation (ASD), in which a smaller value of ASD indicates a greater alignment of the individual fibers. Histograms of individual fibers were plotted (relative to the mean) by adjusting for a period of 290° to 90°. Immunofluorescence Embryonic hippocampal neurons cultured on the PLGA substrates were fixed with 4% paraformaldehyde (Sigma) and 4% sucrose (Sigma) in phosphate buffered saline (PBS, pH 7.2) for 20 min at room temperature. Fixed samples were

permeabilized with 0.1% Triton X-100 (Fluka, St. Louis, MO) and 3% goat serum (Sigma) in PBS buffer for 20 min, washed twice with PBS, and treated with blocking solution of 3% goat serum in PBS for 1 h at 37°C. Tau-1, a microtubule protein expressed in axons, was labeled as an axonal marker.²³ Mouse tau-1 antibody (Chemicon, Temecula, CA) was diluted to 1:200 in blocking solution, and added to the samples. After overnight incubation at 4°C, the samples were washed with PBS two times, and treated with a secondary antibody solution of Alexa 488-labeled goat anti-rat IgG (Invitrogen) (1:200 dilution in blocking solution) at 4°C for 5 h, followed by two PBS washes (5 min, each) and storage at 4°C until analysis.

Fluorescence images of cells and axons were acquired using a fluorescence microscope (IX-70, Olympus, Center Valley, PA). Ten to 20 images were randomly captured per sample using a color CCD camera (Optronics MagnaFire, Goleta, CA). The cell images were analyzed using Image J (NIH) software. Axon length was measured as a linear distance between the cell junction and the tip of an axon. When axons were branched from a single neuron, the longest axon was measured. Also, a neuron was considered to be polarized only when the axon was two times longer than the cell body.^{16,17} The fraction of polarized neurons on each substrate was calculated from the total cell number and reported. Axon alignment was also analyzed in an analogous manner as that for fiber alignment. The orientation of each axon (the straight line from the axon-soma junction to the end of the axon) was measured relative to the vertical direction of the sample and then ASD was calculated from the resultant angles.

A.2.4 Statistics

The percentage of polarized neurons and average axon lengths were calculated from analysis of at least 100 neurons per substrate. Experiments were repeated on different days and the data were reported as the mean \pm standard deviation for $n = 5$ independent substrates. Statistical significance was calculated using a Student's t-test with Origin software (MicroCal, Northampton, MA) and the criterion for statistical significance was $p < 0.05$. Also, axonal alignment was determined using at least 100 axons from a representative sample for each substrate.

A.3 Results

A.3.1 Fabrication of Electrospun PLGA Fibers

We fabricated various PLGA fibers having diameters smaller than a neuron cell body ($\sim 15 \mu\text{m}$) by controlling polymer concentrations of PLGA (**Table A.1**). We obtained PLGA fibers of 2.22 ± 0.55 , 1.51 ± 0.56 , and $0.44 \pm 0.18 \mu\text{m}$ in diameter by simply employing different PLGA concentrations (13% (w/w), 10.5%, and 7%, respectively) (**Figure A.1**). High concentration of the PLGA solution increases the number of chain entanglements. This leads to increased solution viscosity and larger average diameter of the PLGA fibers when the solution is electrospun.¹ Production of differently aligned fibers was achieved by varying the rotation speed of a collector drum (**Figure A.1**). PLGA was electrospun using 10.5% (w/w) polymer solution at different rotation speeds of 0 m/s, 4.9 m/s, and 10 m/s, to produce randomly aligned fibers (RD_10.5), intermediately aligned fibers (INT_10.5), and highly aligned fibers (HI_10.5), respectively (Table I). A smaller ASD indicates a narrower distribution of fiber orientations, and thus more alignment of the fibers; whereas a higher value is closer to random orientation. At a higher rotating speed, fibers exhibited a smaller diameter ($0.97 \pm 0.32 \mu\text{m}$) compared with those spun at lower speed or on a stationary stage ($1.25 \pm 0.52 \mu\text{m}$ in INT_10.5 and $1.51 \pm 0.56 \mu\text{m}$ in RD_10.5) even with the same polymer concentration (10.5%). This trend may be attributed to the stretching of fibers by the rotating collector drum, and has been reported by other groups.^{4,12,22}

A.3.2 Effects of Fiber Sizes

Rat embryonic hippocampal neurons were cultured on PLGA fibers having different fiber sizes and spin-coated substrates as controls. After 22 h, axon formation and length were analyzed on each substrate. Because tau-1 is widely used as an axonal marker, immunostaining for tau proteins allowed investigation of the axonal development process of embryonic hippocampal neurons. **Figure A.2** shows representative tau-1 immunostaining images of hippocampal neurons grown on the spin-coated PLGA substrate and PLGA nanofibers (RD_7) after 22 h in culture.

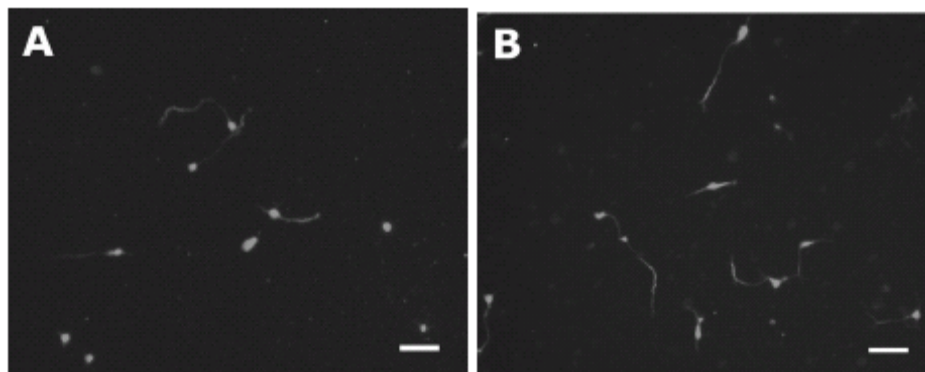


Fig. A.2. Immunostaining of hippocampal neurons on (A) a spin-coated PLGA film and (B) PLGA nanofibers (RD_7). After 22 h in culture, the cells were fixed using paraformaldehyde, and stained for tau-1 (axonal marker). Scale bars are 50 μm . [Color figure can be viewed in the online issue, which is available at www.interscience.wiley.com.]

More axon establishment was observed on PLGA fibers than on spin-coated controls. **Figure A.3(A)** shows that 35–40% of hippocampal neurons polarized on the fibers, which is significantly different from controls (27%) ($p < 0.05$). We observed a trend that the smallest PLGA fibers (RD_7) promoted greater polarization of hippocampal cells compared with larger fibers (RD_10.5 and RD_13); however, the differences were not statistically significant. Fiber diameters did not affect the overall average axon length of polarized neurons (**Fig. A.3(B)**).

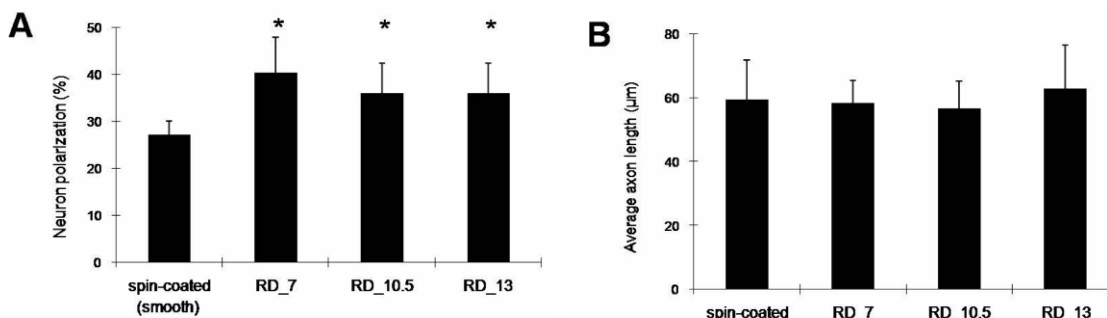


Fig. A.3. Effects of fiber diameter on neuron polarization and average axon lengths of polarized hippocampal neurons cultured for 22 h. (A) Polarization of rat embryonic hippocampal neurons on spin-coated substrates (controls) and different PLGA fibers (0.44, 1.51, and 2.22 μm for diameters of RD_7, RD_10.5, and RD_13, respectively). Polarization of hippocampal neurons was significantly higher on all PLGA fibers than on smooth spin-coated PLGA substrates; however, no significant difference in neuron polarization was observed among PLGA fibers. (B) Fiber diameters and fibrous topographies did not significantly affect axonal length among the samples. Each bar represents the average \pm the standard deviation from six experiments ($n = 6$), and an asterisk denotes a statistically significant difference relative to cells on spin-coated substrates ($p < 0.05$).

A.3.3 Effects of Fiber Orientation

We investigated the effects of fiber orientation on embryonic hippocampal neurons using differently oriented PLGA fibers (RD_10.5, INT_10.5, and HI_10.5) and spin-coated controls. As shown in **Figure A.4(A)**, after 22 h in culture, hippocampal neurons cultured on the fibers established significantly more axons (34–40%) than neurons on spin-coated controls ($p < 0.05$). No significant difference was observed within the fiber samples, indicating that fiber orientation had negligible effects on axonal establishment within these size ranges. However, an overall trend of larger numbers of cells polarized on the more oriented fibers was observed. In addition, similar to the results described in section Effects of fiber sizes, overall axon length was not different among the cells cultured on the oriented fibers and controls (**Figure A.4(B)**). Fiber orientation itself does not appear to considerably influence axonal formation and elongation of embryonic hippocampal neurons. Immunofluorescence images of hippocampal neurons in **Figure A.5** show axonal alignment in the major direction of fibers. Neurons extended their axons along fibers, which resulted in a narrower axonal angle distribution (**Figure A.6**). Axons mostly were found to grow along the fiber strands and often crossed over to other fibers but kept following the new strands near fiber junctions, which are indicated by arrows in **Figure A.5**. Therefore, the ability to guide axons in a certain direction appears to be proportional to the degree of fiber orientation. As seen in **Figure A.6**, the polarized neurons on the spin-coated substrates and random PLGA fibers (RD_10.5) extended their axons in random directions, resulting in a broad distribution of axon angles, whereas narrower ASDs were observed on the more aligned fibers (INT_10.5 and HI_10.5). ASDs of the hippocampal axons cultured were 27.5°, 33.9°, 71.0°, and 70.4° on HI_10.5, INT_10.5, RD_10.5, and spin-coated controls, respectively. These axon distributions were slightly broader than the fiber orientations (**Table A.1**), but close to them, which suggests that micron scale fibers were able to guide the orientation of the axons.

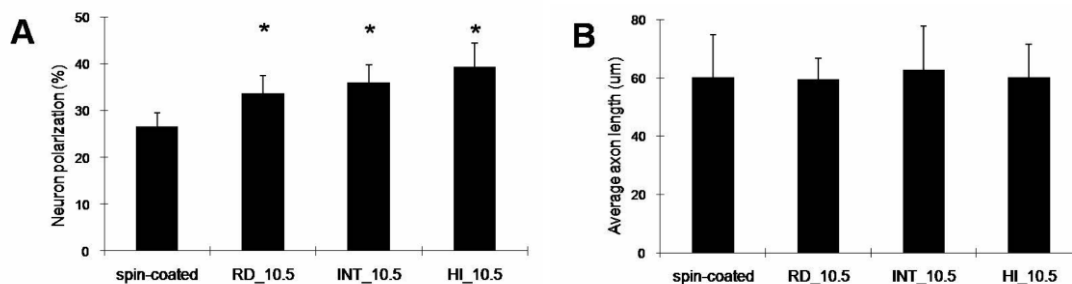


Fig. A.4. Effects of fiber alignment on neuronal polarization and elongation of hippocampal neurons. (A) Polarization on controls and on differently oriented PLGA fibers (RD_10.5, INT_10.5, and HI_10.5). The fibers of different alignments increased neuron polarization compared with the controls. However, the increase in polarization was independent of the degree of fiber alignment, resulting in similar polarization of hippocampal neurons cultured on PLGA fibers. (B) Average axon lengths of hippocampal neurons cultured on differently oriented PLGA fibers and controls. Results suggest that orientations of micron-scaled fibers did not influence initial axon establishment and axon elongation, whereas fibrous meshes enhanced axon establishment of neurons compared with the smooth controls. Each bar represents the average \pm the standard deviation of the means from five experiments ($n = 5$), and an asterisk denotes a statistically significant difference relative to cells on spin-coated substrates ($p < 0.05$).

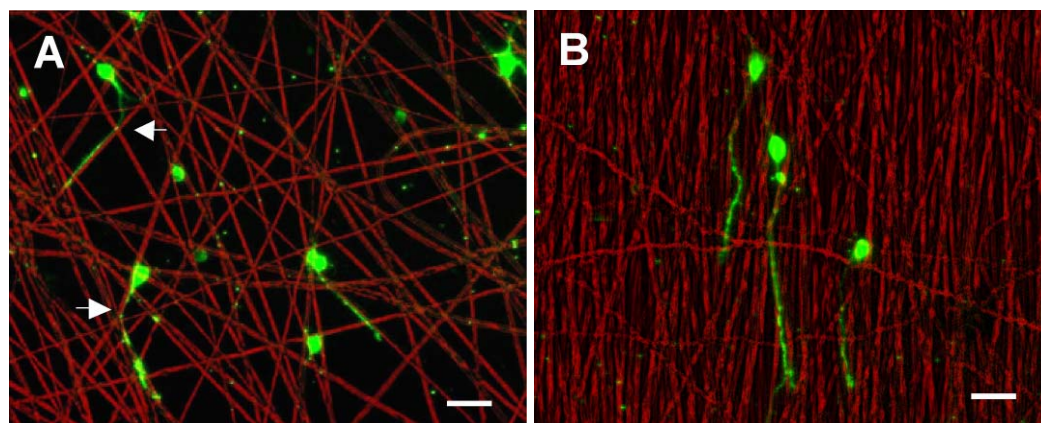


Fig. A.5. Hippocampal neurons cultured on (A) random fibers (RD_10.5) and (B) aligned fibers (HI_10.5). Images were constructed by merging phase contrast (red) and immunofluorescence (green) images. Axons on the fibers were observed to grow mostly along the fibers and often to change directions from one fiber to a closely adjacent fiber (arrows indicate changes near fiber junctions). Scale bars are 50 μm . [Color figure can be viewed in the online issue, which is available at www.interscience.wiley.com.]

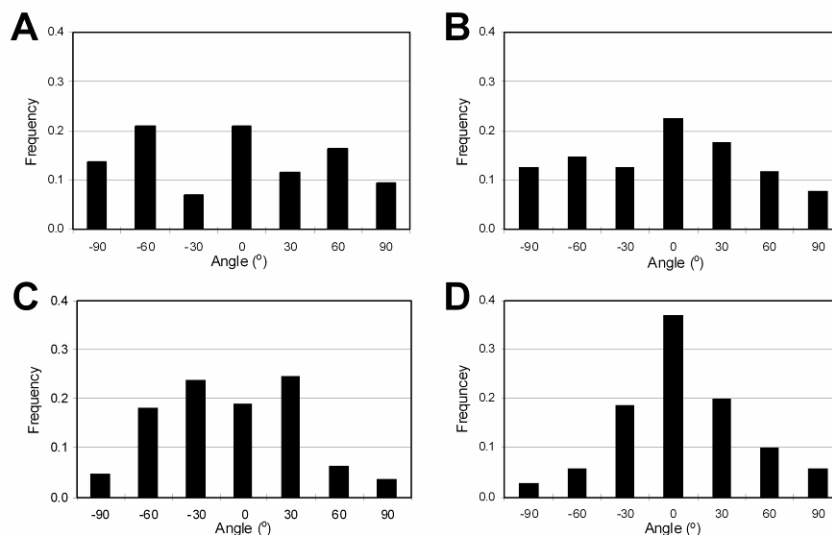


Fig. A.6. Normalized histograms of axon angles on various substrates: (A) the spun-coated films (controls), (B) randomly aligned fibers (RD_10.5), (C) intermediately aligned fibers (INT_10.5), and (D) highly aligned fibers (HI_10.5). At least 100 axons were analyzed from a representative sample for each substrate. Mean values of axon angle on each substrate were adjusted to 0°.

A.4 Discussion and Conclusion

Micron and submicron scale features can be employed for in vitro and in vivo cell culture to mimic the natural cellular surroundings of the ECM for various biomedical applications including nerve tissue regeneration.^{1,2} We are interested in the roles of topographical features of fiber meshes on neuron polarization for the purpose of improved understanding and thus improved design of biomaterials for neural applications. Therefore, in this article, we examined the effects of electrospun fiber diameter and alignment on initial axon establishment of embryonic hippocampal neurons.

We previously studied the polarization of embryonic hippocampal neurons on well-defined microgrooves and found that topographical patterns smaller than a soma have the unique ability to induce axon initiation over other biological cues; however, these microgrooved features had little effect on overall axon length.^{16,24} Hippocampal neurons cultured on PDMS microchannels (1–2 μm distance between ridges, 1–2 μm width, 0.3–0.6 μm depth) polarized approximately two times faster than neurons on smooth PDMS samples.¹⁶ Also, previous studies with other patterned materials have shown similar effects, suggesting that micron-scaled topography is a dominating factor. Specifically, increased neuronal polarization was observed on

polypyrrole microchannels compared with nonpatterned polypyrrole substrates.²⁴ These previous studies emphasized the importance of micron-scaled topography in axon formation of hippocampal neurons. Our results in this study were consistent with these previous findings. The PLGA fibers, ranging from 0.4 μm to 2.2 μm , promoted neuron polarization, but did not have an effect on overall axon elongation after 22 h in culture. In addition, the degree of fiber alignment did not significantly influence neuron polarization. These findings suggest that fibrous features of the tested PLGA samples mainly influence the early developmental stage (axon formation). Overall, the increases in the polarization of the cells on fibrous PLGA substrates (30–50% increase over smooth controls) were not as dramatic as the increases observed on PDMS microgrooves (~100% increase over smooth controls). These differences might result from the irregular patterns of electrospun fibers leading to larger variance in local topographies, compared with precise lithographic microchannels.

Regarding topographical roles in regulating neuronal behaviors, little is known; however, surface topographical features (i.e., porous, grooved, and fibrous structures) interact differently with cells compared with smooth surfaces, influencing adhesion, migration, and differentiation.^{25–27} Neurons appear to sense subtle nanofeatures on surfaces. For example, PDMS replicas of living Schwann cells and the nanometer-scale features of these cells induced the adhesion and orientation of DRG neurons.²⁶ Similarly, human mesenchymal stem cells cultured on nanopatterned PDMS substrata were shown to exhibit selective differentiation into the neuronal lineage compared with the same cells cultured on micro-patterned and smooth substrata.²⁷ In the present studies, we postulate that subcellular-scale fibrous features may provide cells under development (stage 2) with topography and different stresses in a similar way to micropatterns. The scanning electron micro-graphs (**Figure A.7**) illustrate that hippocampal neurons grew mostly on the fibers and interacted with two or more PLGA strands on top of the meshes, suggesting that fibrous topographies of subcellular scales can exert an influence on neurons and neurites/axons. The effects of material topography on cells are not clearly understood. However, one theory is that topographical features in the form of elevation changes facilitate reorganization of focal adhesion complexes (FAC), which mediate cytoskeletal tension, activation of signal transduction, and varied gene expression and phenotypic responses.^{28–30} Presumably, this proposed mechanism may explain the improved polarization of cultured hippocampal neurons on PLGA fibers compared with smooth surfaces in the present studies.

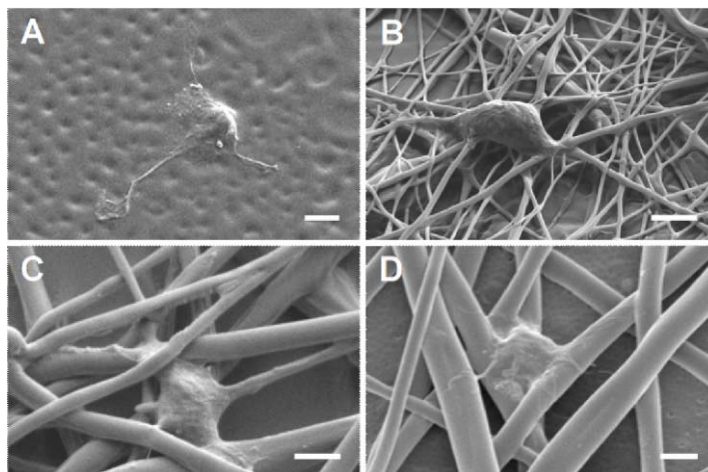


Fig. A.7. SEM images of hippocampal neurons cultured on various PLGA meshes: (A) RD_7, (B) RD_10.5, (C) HI_10.5, and (D) RD_13. Scale bars are 2 μm .

Axon alignment has been widely studied on various grooves and ridges of different substrates.^{16,31,32} Axons and neurites dynamically sense local topographies, allowing the cells to adjust their morphologies and orientation. Other research has shown that hippocampal neurons extend their axons preferentially along wider and deeper ridges while crossing over narrower and shallower patterns, indicating that both parameters are effective for guiding axon growth along the grooves.^{16,31,32} Interestingly, we found that most axons of hippocampal neurons cultured on PLGA fibers were aligned along the fibers regardless of the sizes and orientations of the fibers tested. Our analysis of axon orientation indicated that fiber orientation directly promoted axonal alignment (**Figure A.5**). We found that axons on the random fibers (RD_10.5) often changed to another fiber strand near the crossover points of fibers, which supports the idea that the axons of hippocampal neurons can pass over very small gaps at the fiber junctions.

We fabricated the differently oriented fibers to study the effects of the degree of fiber alignment. The range of fiber sizes was 0.97–1.51 μm . This size is well within the range of 0.44 μm and 2.2 μm over which fiber diameter had little effect on neuron polarization and axon length (**Figure A.3**). Thus, the degree of fiber alignment, and not fiber diameter, appears to be the key factor influencing axon formation and elongation among these differently oriented fibers. We observed increased axon establishment on more aligned fibers; however, it was not significant. Overall axon length was insensitive to fiber orientation (**Figure A.4**). Other researchers have also performed studies to assess the effect of fiber alignment on neurite length and guidance. Aligned PLLA nanofibers caused elongated shapes of cell bodies, and facilitated

neurite elongation of immortalized NSCs with an increase of 25% compared with randomly oriented nanofibers.⁴ Corey et al. cultured DRG explants on differently aligned PLLA nanofibers (524 ± 305 nm in diameter) and found that the aligned PLLA fibers induced neurite alignment and elongation after 3 days in culture.¹² They assumed that the smaller angle between two adjacent fibers in a highly aligned mesh of nanofibers enabled the growth cone to make a decision to select one fiber to follow, resulting in a longer neurite. However, this trend was not observed in our current studies. The different effects of aligned fibers on neuronal behaviors observed by us and other groups may result from inherent differences between embryonic hippocampal neurons and immortalized NSCs and DRG neurons. Also, the short culture time (22 h) used in our studies may not be sufficient to analyze axon elongation after polarization. Although we have not tested other ranges of fiber sizes, oriented fibers of larger or smaller diameters may result in different responses of hippocampal neurons. Also, the degree of fiber alignment may play a synergistic role in neuronal differentiation in combination with other factors, such as ECM proteins and neurotrophins.

For future studies, long-term culture of hippocampal neurons on various electrospun fibers may be useful to explore axon extension and synaptic formation among neurons. Also, tailoring electrospun fibers with bioactive molecules, such as neurotrophins and cell adhesive molecules (i.e., laminin, fibronectin) would be intriguing to understand the combined effects on neurons and to develop better scaffolds for biomedical applications including nerve tissue regeneration scaffolds.

This work may aid an understanding of the topographical effects on neurons during early development stages. In addition, this study on specific interactions between neurons and fibrous meshes will allow us to better design the surface of biomaterials for neural applications, such as nerve tissue engineering scaffolds and neural prostheses.

The authors thank Maeve Cooney for proof reading the manuscript.

A.5 References

1. Pham QP, Sharma U, Mikos AG. Electrospinning of polymeric nanofibers for tissue engineering applications. *Tissue Eng* 2006;12:1197-1211.
2. Murugan R, Ramakrishna S. Nano-featured scaffolds for tissue engineering: a review of spinning methodologies. *Tissue Eng* 2006;12:435-447.
3. Shin M, Ishii O, Sueda T, Vacanti JP. Contractile cardiac grafts using a novel nanofibrous mesh. *Biomaterials* 2004;25:3717-3723.
4. Yang F, Murugan R, Wang S, Ramakrishna S. Electrospinning of nano/micro scale poly(L-lactic acid) aligned fibers and their potential in neural tissue engineering. *Biomaterials* 2005;26, 2603-2610.
5. Yoshimoto H, Shin YM, Terai H, Vacanti JP. A biodegradable nanofiber scaffold by electrospinning and its potential for bone tissue engineering. *Biomaterials* 2003;24:2077-2082.
6. Badami AS, Kreke MR, Thompson MS, Riffle JS, Goldstein AS. Effect of fiber diameter on spreading, proliferation, and differentiation of osteoblastic cells on electrospun poly(lactic acid) substrates. *Biomaterials* 2006;27:596-606.
7. Ji Y, Ghosh K, Shu XZ, Li B, Sokolov JC, Prestwich GD, Clark RA, Rafailovich MH. Electrospun three-dimensional hyaluronic acid nanofibrous scaffolds. *Biomaterials* 2006;27:3782-3792.
8. Matthews JA, Wnek GE, Simpson DG, Bowlin GL. Electrospinning of collagen nanofibers. *Biomacromolecules* 2002;3(2):232-328.
9. Li WJ, Laurencin CT, Cateson EJ, Tuan RS, Ko FK. Electrospun nanofibrous structure: a novel scaffold for tissue engineering. *J Biomed Mater Res A* 2002;60(4):613-621.
10. Li WJ, Tuli R, Okafor C, Derfoul A, Danielson KG, Hall DJ, Tuan RS. A three-dimensional nanofibrous scaffold for cartilage tissue engineering using human mesenchymal stem cells. *Biomaterials* 2005;26:599-609.
11. Bini TB, Gao S, Tan TC, Wang S, Lim A, Hai LB, Ramakrishna S. *et al.*: Electrospun poly(L-lactide-co-glycolide) biodegradable polymer nanofibre tubes for peripheral nerve regeneration. *Nanotechnology* 2004;15:1459-1464.
12. Corey JM, Lin DY, Mycek KB, Chen Q, Samuel S, Feldman EL, Martin DC. Aligned electrospun nanofibers specify the direction of dorsal root ganglia neurite growth. *J Biomed Mater Res A* 2007;83(3):636-645.
13. Schnell E, Klinkhammer K, Balzer S, Brook G, Klee D, Dalton P, Mey J. Guidance of glial cell migration and axonal growth on electrospun nanofibers of poly- ϵ -caprolactone and a collagen/poly- ϵ -caprolactone blend. *Biomaterials* 2007;28:3012-3025.
14. Fukata Y, Kimura T and Kaibuchi K. Axon specification in hippocampal neurons. *Neurosci Res* 2002;43(4):305-315.
15. Sapelkin AV, Bayliss SC, Unal B, Charalambou A. Interaction of B50 rat hippocampal cells with stain-etched porous silicon. *Biomaterials* 2006;27:842-846.
16. Gomez N, Lu Y, Chen S, Schmidt CE. Immobilized nerve growth factor and microtopography have distinct effects on polarization versus axon elongation in hippocampal cells in culture. *Biomaterials* 2007;28:271-284.
17. Dotti CG, Sullivan CA, Banker GA. The establishment of polarity by hippocampal neurons in culture. *J Neurosci* 1988;8(4):1454-1468.

18. Yoshimura T, Arimura N, Kaibuchi K. Signaling networks in neuronal polarization. *J Neurosci* 2006;26(42):10626-10630.
19. Labelle C, Leclerc N. Exogenous BDNF, NT-3 and NT-4 differentially regulate neurite outgrowth in cultured hippocampal neurons. *Brain Res Dev Brain Res* 2000;23:1-11.
20. Ziv NE, Spira ME. Induction of growth cone formation by transient and localized increases of intracellular proteolytic activity. *J Cell Biol* 1998;140(1):223-32.
21. Lamoureux P, Ruthel G, Buxbaum RE, Heidemann SR. Mechanical tension can specify axonal fate in hippocampal neurons. *J Cell Biol* 2002;159(3):499-508.
22. Bashur CA, Dahlgren LA, Goldstein AS. Effect of fiber diameter and orientation on fibroblast morphology and proliferation on electrospun poly(D,L-lactic-co-glycolic acid) meshes. *Biomaterials* 2006;27: 5681-5688.
23. Mandell JW, Banker GA. A spatial gradient of tau protein phosphorylation in nascent axons. *J Neurosci* 1996;16:5727-5740.
24. Gomez N, Lee JY, Nickels JD, Schmidt CE. Micropatterned Polypyrrole: Combination of Electrical and Topographical Characteristics for Stimulation of Cells. *Adv Func Mater* 2007;17:1645-1653.
25. Fan YW, Cui FZ, Hou SP, Xu QY, Chen LN, Lee IS. Culture of neural cells on silicon wafers with nano-scale surface topograph. *J Neurosci Methods* 2002;120:17-23.
26. Bruder JM, Lee AP, Hoffman-Kim D. Biomimetic materials replicating Schwann cell topography enhance neuronal adhesion and neurite alignment in vitro. *J Biomater Sci Polym Ed* 2007;18:967-982.
27. Yim EK, Pang SW, Leong KW. Synthetic nanostructures inducing differentiation of human mesenchymal stem cells into neuronal lineage. *Exp Cell Res* 2007;313:1820-1829.
28. Goldner JS, Bruder JM, Li G, Gazzola D, Hoffman-Kim D. Neurite bridging across micropatterned grooves. *Biomaterials* 2006;27:460-472.
29. Curtis A, Wilkinson C. Topographical control of cells. *Biomaterials* 1997;18:1573-1583.
30. Rajnicek A, Britland S, McCaig C. Contact guidance of CNS neurites on grooved quartz: influence of groove dimensions, neuronal age and cell type. *J Cell Sci* 1997;110:2905-2913.
31. Dalby MJ. Topographically induced direct cell mechanotransduction. *Med Eng & Phys* 2005;27:730-742.
32. Clark P, Connolly P, Curtis AS, Dow JA, Wilkinson CD. Topographical control of cell behaviour: II. Multiple grooved substrata. *Development* 1990;108(4):635-644.

Appendix B: Electroconductive Nanofibers for Neural Tissue Applications: Polypyrrole-Coated Electrospun PLGA Nanofibers

Jae Young Lee¹, Chris A. Bashur², Aaron S. Goldstein^{2} and Christine E. Schmidt^{1, 3-5}*

¹Department of Chemical Engineering, The University of Texas at Austin, Austin, TX

²Department of Chemical Engineering, Virginia Polytechnic Institute and State University, Blacksburg, VA

³Department of Biomedical Engineering, The University of Texas at Austin, Austin, Texas

⁴Texas Materials Institute, The University of Texas at Austin, Austin, TX

⁵Center for Nano- and Molecular Science and Technology, The University of Texas at Austin, Austin, TX

Abstract

Electrospinning is a promising approach to create nanofiber structures that are capable of supporting adhesion and guiding extension of neurons for nerve regeneration. Concurrently, electrical stimulation of neurons in the absence of topographical features also has been shown to guide axonal extension. Therefore, the goal of this study was to form electrically conductive nanofiber structures and to examine the combined effect of nanofiber structures and electrical stimulation. Differently oriented conductive meshes (i.e., random and aligned fibers) were produced by growing polypyrrole (PPy) on random and aligned electrospun poly(lactic-co-glycolic acid) (PLGA) nanofibers. Scanning electron micrographs showed that PLGA nanofibers were uniformly deposited with nano-thick PPy (85 ± 41 nm). X-ray photon spectroscopy confirmed the deposition of PPy on the PLGA fibers. Biocompatibility and suitability of the conductive nanofibers as neuronal tissue scaffolds were studied by culturing rat pheochromocytoma 12 (PC12) cells and rat embryonic hippocampal cells on the PPy-PLGA and the non-coated PLGA template fibers. The PPy-PLGA fibers supported the growth and differentiation of PC12 cells and hippocampal neurons comparable to PLGA controls. Aligned fibers of PPy-PLGA were observed to guide neurites and axons along the fibers. Electrical stimulation studies showed that PC12 cells grown on PPy-PLGA scaffolds and stimulated with a potential of 10 mV/cm exhibited 40-50% longer neurites compared to unstimulated cells on the same scaffolds (PPy-PLGA). In addition, the cells stimulated on aligned PPy-PLGA fibers resulted in longer neurites than the cells stimulated on random PPy-PLGA fibers, suggesting a synergistic effect of electrical stimulation and topographical guidance. In summary, we successfully fabricated biocompatible electroconducting nanofibers and demonstrated their use with electrical stimulation for potential neural tissue applications.

B.1 Introduction

Electroconducting polymers (i.e., polypyrrole (PPy), polythiophene (PT), polyaniline (PANI), poly(3,4-ethylenedioxythiophene) (PEDOT)) exhibit excellent electrical and optical properties and have been explored in the past few decades for a number of applications including microelectronics, polymer batteries, and actuators^{1,2}. In particular, because of its ease of synthesis, biocompatibility, and good conductivity, PPy has been the most extensively studied for biological and medical applications, such as biosensors and tissue engineering scaffolds³. This electroconducting polymer has been recognized as a promising scaffold material to electrically stimulate neurons and nerve tissues for therapeutic purposes such as nerve tissue engineering scaffolds and neural prostheses^{3,4}. Schmidt *et al.* first electrically stimulated PC12 cells through PPy films and observed the promotion of neurite outgrowth from the cells, demonstrating the potential use of electroconducting polymers for nerve tissue engineering scaffolds⁵. Subsequent studies have focused on improving the electroconducting polymer scaffolds by incorporating various cues, such as neurotrophins⁶, cell adhesive molecules^{7,8}, and topographical features⁹, emphasizing the importance of multiple cues for improved modulation of neuronal responses¹⁰. For example, Gomez *et al.* electrochemically synthesized PPy microchannels to fabricate electroconductive, topographical substrates for neural interfacing and found that PPy microchannels facilitated axon establishment of rat embryonic hippocampal neurons⁹. However, these studies involve relatively planar substrates which are ideal model surfaces for characterizing cell responses to electric fields, but lack the three-dimensional architecture necessary for organization of a functional nerve tissue.

Electroconducting nanofibers may be a means to translate model studies on well-defined topographical features into scaffold materials for nerve regeneration. Nanofibers present unique topographical surfaces of which features (i.e., fiber diameter and orientation) affect cellular behaviors of many cells^{11,12,13}. For example, Yang *et al.* found that immortalized neural stem cells cultured on aligned poly(L-lactic acid) nanofibers extended longer neurites than cells on random nanofibers and aligned microfibers of the same composition¹². Several attempts to synthesize conducting nanofibers for tissue engineering applications have been described in the literature. Lelkes and colleagues electrospun polyaniline-gelatin blends to produce electroconducting nanofibers, which displayed good conductivities ranging from 0.01 to 0.02 S/cm. These fibers supported the growth and proliferation of cardiac rat myoblasts¹⁴. Also,

carbon nanofiber composites of polycarbonate urethane were produced for neural and orthopedic interfaces¹⁵. Depending on compositions of the blends, mechanical, and electrical properties as well as cell adhesion were varied. As an alternative, electroconducting polymers, mostly PPy, have been deposited on fiber templates, which can be achieved by in situ chemical oxidation of PPy in a polymerizing solution or by oxidation of monomers deposited on the substrates in vapor phase followed by oxidant treatment. This PPy deposition method enables the simple production of conducting fibers using template fibers^{16,17}. For example, Zhang and colleagues deposited PPy on woven fabrics of poly(ethylene terephthalate) (> 20 μm in diameter, 10^2 - 10^5 ohm/square) for in vitro biocompatibility studies for the application of vascular prostheses^{18,19}. However, there have been fewer studies on nano-scaled fibers for tissue engineering scaffolds. More importantly, application of electrical potential of nerve cells using electroconducting micro-/nano- fibers has not been explored yet.

In this article, we produced polypyrrole-coated electrospun PLGA nanofibers (PPy-PLGA), as electroconducting nanofibers, for neural tissue applications. Because these components, PPy and PLGA, are biocompatible in vivo as well as in vitro^{20,21,22}, the PPy-PLGA product was expected to be appropriate for ultimate use as implantation materials. To retain the fibers under submicron size and to take advantage of submicron scaled features, we deposited nano-thick PPy onto PLGA nanofibers. Also, oriented fibers were electrospun as template meshes for the PPy-coating to study contact guidance (i.e., neurite/axon alignment). For in vitro neuronal culture, we cultured two different types of neurons – PC12 cells and rat embryonic hippocampal neurons. We also performed electrical stimulation of PC12 cells on these biocompatible electroconductive nanofibers according to previous protocols^{6,23} to demonstrate their potential uses as nerve tissue engineering scaffolds for the regeneration of injured peripheral and central nerves.

B.2 Materials and Methods

B.2.1 Materials

All chemicals, cell culture supplements, and disposable tissue culture supplies were purchased from Sigma (St Louis, MO), Hyclone (Logan, UT), and BD (Brookfield, NJ), respectively, unless otherwise noted.

B.2.2 Electrospinning

The 75/25 poly(lactic-co-glycolic acid) (PLGA) (inherent viscosity 0.55–0.75 dL/g, Lactel Biodegradable Polymers, Birmingham, AL) was used for electrospinning as described previously¹³. In brief, PLGA was dissolved in hexafluoro-2-propanol (HFIP). Aluminum foil was wrapped around the 7.6 cm drum. The polymer solution (7.0 or 6.5 wt% PLGA) was electrospun with a syringe equipped with a 22 gauge steel needle using a 15 kV potential, a throw distance of 15 cm, and a syringe flow rate of 3 mL/h. Random fibers (RF) were electrospun from 7.0 wt% polymer solution on a stationary collector, and aligned fibers (AF) were obtained from 6.5 wt% polymer solution on a rotating drum at a linear velocity of 6.4 m/s to achieve similar diameters with different fiber orientations because fibers generally exhibit a smaller diameter on a rotating collector¹³. After electrospinning, PLGA meshes were air dried for 2 days to remove residual HFIP. Meshes were cut into 15 × 15 mm squares, and then carefully removed from the aluminum foil.

B.2.3 Polypyrrole Coating

Differently oriented PPy-PLGA meshes, PPy-RF and PPy-AF, were synthesized by coating PPy on random and aligned PLGA (RF and AF, respectively). To do this, pyrrole was purified by passing it through a column of activated basic alumina before use. A PLGA mesh (15 × 15 mm) was put into 2 mL aqueous solution of 14.4 mM pyrrole and 14.4 mM sodium para-toluene sulfonate (pTS) (Aldrich) in a 15 mL polypropylene tube, followed by ultrasonication for 30 s to allow the meshes to be saturated with pyrrole solution. The mesh was incubated at 4°C for 1 h. Then, 2 mL ferric chloride solution (38 mM) was added to the tube and incubated with shaking at 4°C for 24 h for the polymerization and deposition of PPy on the PLGA meshes. The polymerization of PPy from pyrrole involves the incorporation of chlorine and pTS, of which elements can be detected using XPS. Black PPy-coated mesh was sonicated for 1 min, washed with copious amounts of deionized water, and then transferred onto a clean glass slide. PPy-PLGA was dried in a vacuum oven at room temperature for 2 days.

B.2.4 Fiber Characterization

B.2.4.1 Scanning Electron Microscopy (SEM)

SEM was used to characterize fiber diameter and orientation of electrospun PLGA meshes and PPy-PLGA meshes. SEM images of electrospun PLGA fibers and PPy-PLGA fibers were acquired with a Zeiss SUPRA 40 VP Scanning Electron Microscope (Carl Zeiss SMT, Thornwood, NY). Non-coated PLGA samples were sputter-coated with 5 nm of palladium using a Cressington Scientific Instruments Model 208HR (Cranberry, Township, NY) prior to taking SEM images. PPy-PLGA fibers were imaged using SEM without metal coating. The SEM images were analyzed using ImagePro Plus software (ICube, Crofton, MD) or ImageJ (NIH) for fiber diameter and macroscale fiber orientation as previously described¹³. PPy shell thickness was calculated from the differences of fiber diameters between non-coated fibers and PPy-PLGA fibers. The degree of fiber alignment was characterized by the wrapped normal distribution and reported as angular standard deviation (ASD), in which a smaller value of ASD represents a greater alignment of the individual fibers.

B.2.4.2 Surface Resistance

Surface resistance of PPy-PLGA meshes was measured as previously described²⁴. Two silver wires separated by 1 cm were placed onto the sample. Resistance (R) was measured between the two silver electrodes using a digital multimeter (DM-8A, Sperry Instrument, Milwaukee, WI). Surface resistance (R_s) was calculated as follows:

$$R_s = R \times W / D \quad (\text{B.1})$$

where W is the sample width and D is the distance between the two silver electrodes.

B.2.4.3 X-ray Photon Spectroscopy (XPS)

XPS was used to characterize the surface compositions of PPy-coated PLGA fibers. High-resolution spectra of elements were obtained using a Kratos AXIS Ultra XPS system (Chestnut Ridge, NY). A monochromatic Al $K\alpha_1$ source was employed. Typical operating

conditions were 1×10^{-9} Torr chamber pressure, and 15 kV and 150 W for the Al X-ray source. High-resolution elemental scans were collected with a pass energy of 20 eV at takeoff angles of 90 degrees between the sample and analyzer. Calibration of the binding energy was performed by setting \underline{C} - $\underline{C}/\underline{C}$ -H components in C_{1s} peak at 284.6 eV. Peak deconvolution was performed using XPSPEAK software (The Chinese University of Hong Kong).

B.2.5 Cell Culture

B.2.5.1 Sample Preparation

For cell culture experiments, PPy-PLGA meshes were tested for their ability to support cell growth. Each mesh was placed on a thin poly(dimethylsiloxane) (PDMS, Sylgard® 184, Dow Corning, Midland, MI) film on a glass slide. Two silver wires (round 30 gauge, MELTIK) were then placed on both sides of the mesh, followed by covering them with a thin PDMS well (1 cm \times 1 cm \times 1 mm inner well dimension) to serve as a sealant and to prevent the wires from direct contact with medium. A Plexiglas well (1 cm \times 1 cm \times 1 cm inner well dimension) was placed on top of the assembled system (**Figure B.1**). For the aligned fibers, two electrodes were placed perpendicular to the major direction of the fibers. The assembly was tightly clipped and sterilized by exposure to UV for 1 h. The samples were incubated overnight in a sterile solution of rat tail type I collagen (0.1 mg/mL) for PC12 cells and poly-D-lysine (0.1 mg/mL) for hippocampal cells, respectively. The substrates were washed twice with sterile de-ionized water and incubated in sterile phosphate-buffered saline (PBS) solution for 2 days to remove unreacted compounds.

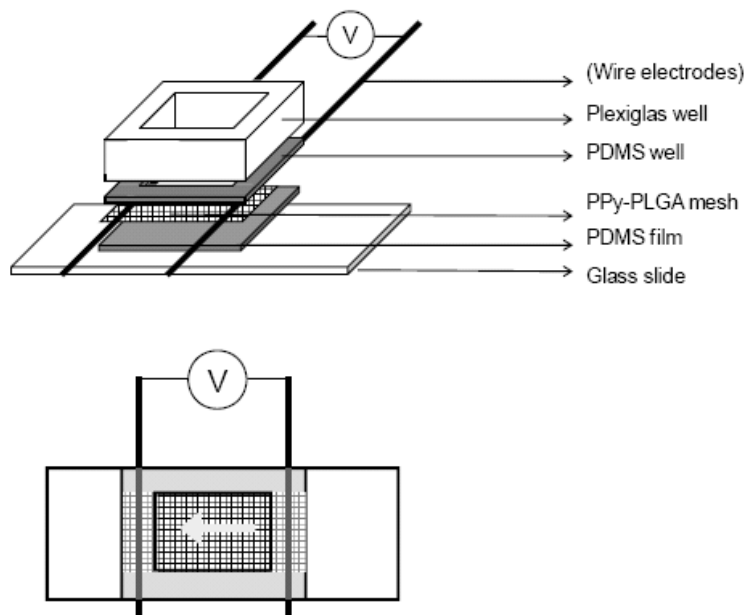


Fig. B.1. Schematics of assembly of a PPy-PLGA mesh for in vitro cell culture study and electrical stimulation. For biocompatibility tests, silver wires were not included in the assemblies.

B.2.5.2 PC12 Cell Culture and Immunostaining

PC12 cells were maintained at 37°C in a humid, 5% CO₂ incubator in F-12K culture medium (Sigma) containing 15% heat-inactivated horse serum (Hyclone), 2.5% fetal bovine serum (Hyclone), and 1% Penicillin-Streptomycin solution (Sigma). Cells were passaged weekly using a 0.25% trypsin-EDTA solution (Sigma). Cells were primed by culturing them in medium containing 50 ng/mL nerve growth factor (NGF) three days prior to an experiment. The primed PC12 cells were inoculated at a density of 2×10^4 cells per well and cultured for 2 days. Four substrates for each condition were tested ($n=4$).

We studied electrical stimulation to demonstrate that conducting nanofibers (PPy-PLGA) may be beneficial as neuronal tissue engineering scaffolds. We performed electrical stimulation of PC12 cells on random and aligned PPy-PLGA meshes and followed the experimental conditions as previously reported^{6,23}. PC12 cells were inoculated (2×10^4 cells per well) in the wells attached to the PPy-PLGA meshes. After 24 h in culture, a constant electrical potential of 100 mV/cm or 10 mV/cm (a Pine Instrument AFRDE5 bipotentostat) was applied to two electrodes for 2 h in the incubator. Cells were analyzed 24 h after electrical stimulation. Four substrates for each condition were employed ($n=4$).

After culture, the PC12 cells were fixed using 4% paraformaldehyde and 4% sucrose in phosphate-buffered saline (PBS) buffer for 15 min. The cells were permeabilized in 0.1% Triton X-100 (Fluka) and 2% bovine serum albumin (Sigma) in PBS for 15 min, followed by blocking with 2% BSA in PBS for 30 min at room temperature. PC12 cells were stained with Alexa Fluor 488-labeled phalloidin (Invitrogen) for 30 min for actin filaments and with 4',6-diamidino-2-phenylindole diacetate (DAPI, Invitrogen) nuclear stain, washed with PBS buffer twice, and stored at 4°C until analysis.

B.2.5.3 Hippocampal Neuron Culture and Immunostaining

Commercial rat hippocampus (E-18) was purchased from BrainBits (Springfield, IL) and used to isolate embryonic hippocampal neurons (E-18) according to the manufacturer's protocol. In brief, hippocampal tissue was treated in papain (Warthington, Likewood, NJ) solution (4 mg/mL in Hibernate E medium (BrainBits)) and triturated using a fire-polished Pasteur pipette. Cells were collected by centrifugation (200 g, 1 min) and suspended in Neurobasal medium, supplemented with 2% B-27 supplement (Invitrogen), 0.5 mM L-glutamine (Fisher), 0.025 mM glutamic acid (Sigma), and 1% Penicillin-Streptomycin solution (Sigma). The cells were inoculated into each well (2×10^4 cells per well) and cultured in medium at 37°C in a humid, 5% CO₂ incubator for 24 h. Four substrates per each condition were employed ($n=3$).

Embryonic hippocampal neurons cultured on the meshes were incubated with the fixing solution (4% paraformaldehyde and 4% sucrose in PBS) for 20 min at room temperature. The cells were permeabilized with 0.1% Triton X-100 and 3% goat serum (Sigma) in PBS for 20 min, and washed twice with PBS, followed by treatment with blocking solution (3% goat serum in PBS buffer) for 1 h at 37°C. Mouse tau-1 antibody (Chemicon, Temecular, CA) (1:200 in blocking solution) was added to the sample, incubated at 4°C overnight, and washed with PBS twice (10 min each). The cells were stained with Alexa Fluor 488-labeled goat anti-rat IgG (Invitrogen) (1:200 dilution in blocking solution) at 4°C for 5 h, washed with PBS twice (10 min, each), and stored at 4°C until analysis.

B.2.6 Immunofluorescence and Image Analysis

Fluorescence images of PC12 cells and hippocampal neurons were acquired using a fluorescence microscope (IX-70, Olympus, Center Valley, PA) equipped with a color CCD

camera (Optronics MagnaFire, Goleta, CA). The fluorescence images were processed and analyzed using Adobe Photoshop and Image J (NIH) software.

The numbers of cells on the sample meshes were determined by counting nuclei stained with DAPI dye from the randomly acquired fluorescence images. Axon/neurite length was measured as a linear distance between the cell junction and the tip of an axon/neurite. For PC12 cells, neurite outgrowth was evaluated and reported in terms of median length because neurite lengths were not normally distributed^{5,6}. More than 300 neurites were measured to obtain the median length for each condition. For hippocampal neurons, axonal establishment and length were investigated as embryonic hippocampal neurons differentiate by forming single axons among immature neurites and elongating the axons in vitro culture. Axon formation (neuron polarization) was defined and counted only when neurite processes were twice as long as the length of the cell body according to previous literature^{9,25}. The averages and standard errors of the means are calculated for the percentages of polarized hippocampal neurons and average axon lengths. More than 100 neurons were analyzed per substrate.

B.2.7 Assessment of Cellular Morphology

SEM was employed to study cellular morphologies on the fibers. The fixed cells were dehydrated using increasing ethanol/water concentrations (30% for 45 min; 50% for 30 min, 70%, 85%, 90%, 95%, and absolute ethanol for 10 min each). Samples were dehydrated with hexamethyl disilazane (HMDS) (Sigma) and dried in air overnight. Platinum/palladium was coated on the sample with 10 nm in thickness using a sputter coater. SEM images were obtained with Zeiss SUPRA 40 VP Scanning Electron Microscope.

B.2.8 Statistics

Averages and standard deviations were calculated and reported from at least four samples per each condition. The statistical significance between two groups was determined using a Student's *t*-test ($p < 0.05$) for the numbers of the cells, polarized hippocampal neurons, and axon lengths of hippocampal neurons. On the other hand, for the evaluation of PC12 neurite extension, median lengths were calculated and reported for each condition because the measured neurite lengths were not normally distributed. Statistical differences between medians were calculated with a Mann-Whitney U test²⁶ ($p < 0.05$).

B.3 Results and Discussion

B.3.1 Electrospinning PLGA Nanofibers

Template PLGA nanofibers for PPy-coating were used in this study because of PLGA's well-investigated biocompatibility, biodegradability, and suitability for various biomedical applications^{11,20}. The PLGA nanofiber meshes were obtained by electrospinning PLGA (75/25) solution as previously described¹³. Highly aligned nanofibers (AF) and random nanofibers (RF) were collected from PLGA polymer solution on a rotating and stationary collector, respectively. The SEM images of the electrospun fibers indicate that both meshes (AF and RF) have uniform fibrous features on the surface and that AF exhibits highly aligned fibers (**Figure B.2**). The fiber diameters, which were determined by analyzing the SEM images, were $0.25 \pm 0.11 \mu\text{m}$ for AF and $0.36 \pm 0.13 \mu\text{m}$ for RF. For degree of fiber orientation, the AF had a value of angular standard deviation (ASD) of 32.9° , whereas the RF had a larger ASD (54.7°). High ASD reflects randomly oriented fibers. These nanofibers, with nanometer scale dimensions, provide highly porous, nanofibrous topographies capable of modulating cellular responses in various cells^{11,27}.

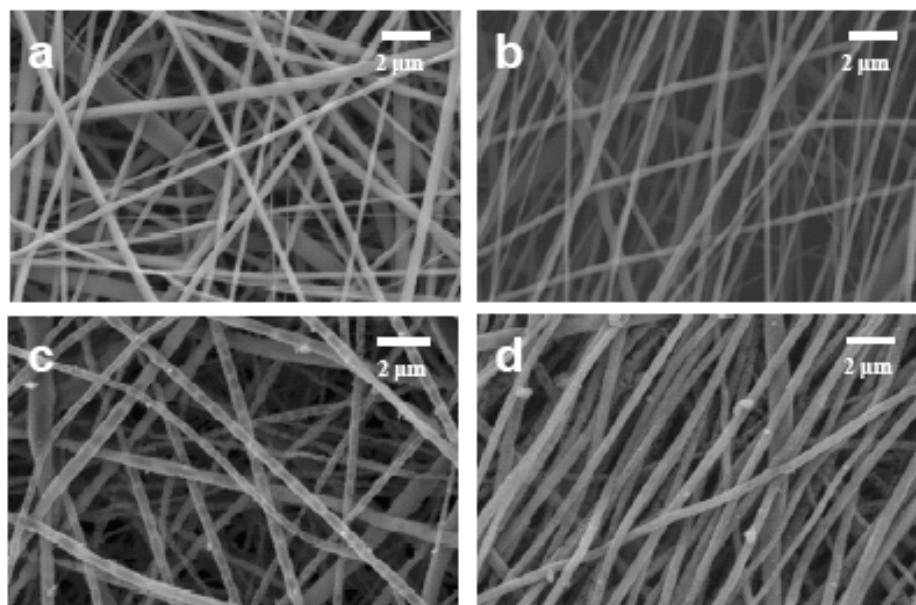


Fig. B.2. Scanning electron micrographs of electrospun PLGA nanofibers, (a) and (b), and their PPy-coated fibers, (c) and (d). (a) Randomly-oriented nanofibers (RF), (b) aligned nanofibers (AF), (c) PPy-coated randomly oriented fibers (PPy-RF), and (d) PPy-coated aligned fibers (PPy-AF).

B.3.2 Synthesis of PPy-Coated PLGA Nanofibers

To produce electroconducting nanofibers, PPy deposition was performed on the electrospun PLGA nanofibers (RF and AF) in a polymerizing solution containing pyrrole, pTS, and FeCl₃ as a monomer, a dopant, and an oxidizing reagent, respectively. As pyrrole was polymerized, polymeric products (PPy) aggregated in solution or deposited on the fiber surfaces, depending on reaction conditions, forming conducting shells. Polymerization condition strongly influenced coating properties of the PPy-PLGA fibers, such as uniformity, conductivity, and morphologies of the PPy shells, which is consistent with other literature^{16,28}. For example, incomplete coverage of PPy, which resulted in non-conducting meshes, was observed at low concentrations of the reactants and/or a short reaction time. On the other hand, high concentrations of the reactants resulted in PPy aggregates in solution and non-uniform deposition of PPy covering on the fibers (data not shown). **Figure B.3** demonstrate that the PPy-PLGA products, synthesized under the optimized condition, consist of PLGA fiber cores and PPy shells. PPy-coated AF meshes (PPy-AF) retained the aligned fiber structures, which were similar to their non-coated template meshes (AF) (**Figure B.2**). The SEM images of the PPy-PLGA were acquired without treatment of the samples with metal coating, inferring qualitatively good electrical conductance of the fibers. Some PPy aggregates were often observed on the fiber surfaces, but they were loosely bound and could be removed by successive washes. The PPy-PLGA fibers had fiber diameters of 520 ± 150 nm for PPy-RF and 430 ± 180 nm for PPy-AF, with 85 ± 41 nm shell thickness. Nanometer-scale thick PPy deposition was accomplished on the template nanofibers, of which features were retained (i.e., fiber orientations).

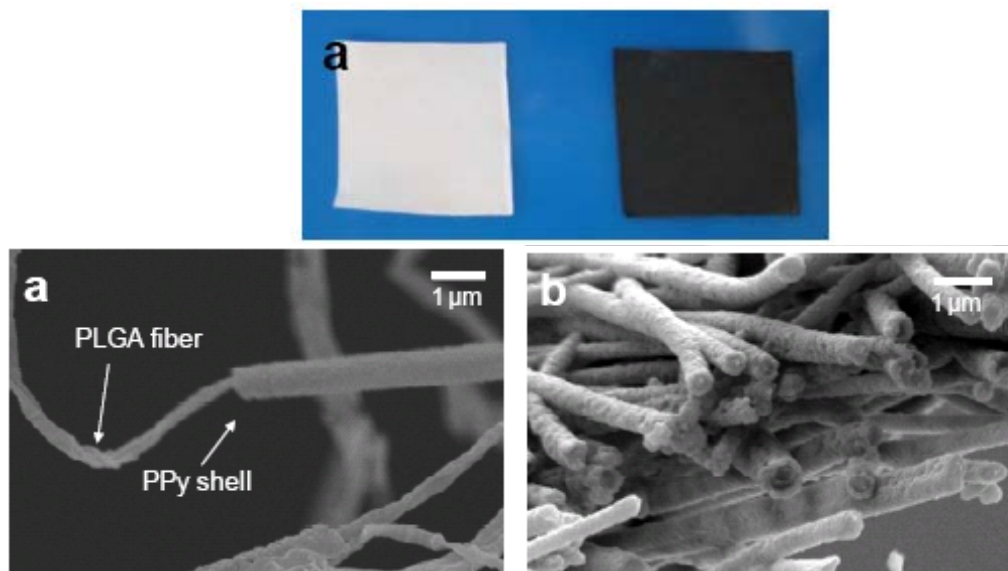


Fig. B.3. PPy-coated PLGA meshes. (a) photographs of uncoated PLGA meshes (white, left) and PPy-PLGA meshes (black, right). (b) SEM micrograph of single strands of PPy-PLGA fibers. (c) SEM image of section of the PPy-PLGA meshes.

B.3.3 Characterization of PPy-coated PLGA Nanofibers

To characterize electroconducting properties of the PPy-PLGA meshes, surface resistance (R_s) was measured. Random PPy-PLGA had an $R_s = 1.7 \pm 0.6 \times 10^4$ Ohm/square. This value was insensitive to the direction of measurement, which was reasonable because the PPy-RF fibers were randomly oriented and had multiple contacts among coated fibers. On the other hand, R_s values of aligned PPy-PLGA varied with direction of the fibers: $R_s = 7.4 \pm 3.2 \times 10^3$ Ohm/square along the fiber direction and $R_s = 9.0 \pm 6.0 \times 10^4$ Ohm/square perpendicular to the major fiber direction. These results suggest that current is conducted primarily along the fiber axis.

To characterize the surfaces of the fibers, XPS analysis was performed. **Table B.1** summarizes the elemental compositions of the sample surfaces. For the PPy-PLGA, nitrogen, chlorine, and sulfur atoms were detected, whereas they were absent in the uncoated PLGA samples. Doping level of the PPy components was calculated from the atomic ratio of Cl and S to N from the high resolution XPS spectra. The doping level of PPy-PLGA was 0.27 and close to that for oxidized PPy (about 0.3), as previously investigated³. pTS and Cl ions accounted for 80% and 20%, respectively, in total molar amounts of dopant. High-resolution spectra of the PPy-PLGA were decomposed according to previous reports^{29,30}. The C_{1s} spectrum of PPy-PLGA (**Figure B.4**) reveals substantial changes in the spectrum after PPy-coating, which can be attributed to new signals at 285.8 eV (\underline{C} -N), 287.2 eV (\underline{C} =N), and 288.9 eV (C=N+). Peaks,

related to the PLGA cores, are diminished, indicating PPy-coating shields the surface of PLGA. In addition, **Figure B.4b** shows changes in the high resolution spectra of N_{1s} after PPy-coating with new signals at 397.8 eV ($=\underline{N}-$), 399.8 eV ($-\underline{NH}-$), 401.2 eV ($C-\underline{N}^+$), and 402.2 eV ($C=\underline{N}^+$). No significant peak was observed in the N_{1s} spectrum of the PLGA sample, as expected. These XPS spectra obtained from the PPy-PLGA are consistent with those from pristine PPy in other literature^{24,29,30}, demonstrating surface deposition of PPy on the PLGA fibers.

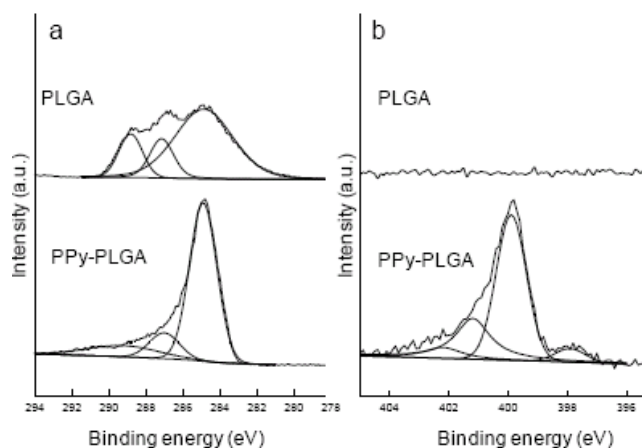


Fig. B.4. High resolution (a) C_{1s} and (b) N_{1s} XPS spectra of PLGA and PPy-PLGA. The C_{1s} spectrum of PPy-PLGA shows typical signals of PPy at 284.6 eV ($\underline{C}-H_x/\underline{C}-C$), 285.8 eV ($\underline{C}-N$), 287.2 eV ($\underline{C}=\underline{N}$), 288.9 eV ($C=N^+$), and 290.1 eV ($\pi-\pi^*$). In tense peaks at 287.1 eV and 288.7 eV in the PLGA spectrum diminished after PPy-coating. (b) New peaks were detected in the N_{1s} spectrum after the PPy-coating at 397.8 eV, 399.8 eV, 401.2 eV, and 402.2 eV, which were assigned to $=\underline{N}-$, $-\underline{NH}-$, $C-\underline{N}^+$, and $C=\underline{N}^+$, respectively.

Table B.1. Elemental compositions and doping levels of PLGA and PPy-coated PLGA (PPy-RF) using XPS analysis.

Sample	Elements (atomic %)				Doping level ^{a)}
	C	N	Cl	S	
PLGA	99.7	0.2	0	0	-
PPy-PLGA ^{b)}	84.9	12.0	1.0	2.2	0.27

a) doping level = $(Cl+S)/N$

b) PPy-RF used.

B.3.4 Cell Culture Experiments

In an effort to study properties of the PPy-PLGA scaffolds for neuronal applications, we cultured PC12 cells and embryonic hippocampal neurons on the scaffold materials. PC12 cells are the most widely studied cell type for neuritogenesis in responses to various extracellular cues such as neurotrophins and electrical stimulation^{5,6}. This cell line has been used as an experimental model of the sympathetic nervous system³¹. On the other hand, the embryonic hippocampal neuron is of CNS origin and plays an important role in learning-and-memory and processing of spatial information in the brain³². Embryonic hippocampal neurons have been widely used for initial axon establishment in neuronal development³³. It has been also noted that the cellular responses of these neurons are influenced by external electrical fields³⁴ and topographical surfaces of substrates (i.e., pores, grooves)^{9,35}. Therefore, we cultured PC12 cells and hippocampal cells on the PPy-PLGA meshes for in vitro cell culture to demonstrate the utility of these meshes bearing nanofibrous topographical features and electrical activities for nerve tissue engineering applications. Non-coated PLGA fibers, displaying similar fiber features (fiber diameters and orientations) to the PPy-PLGA fibers, were also used as controls for comparison.

The PC12 cells were cultured on both PPy-PLGA (PPy-RF and PPy-AF) and uncoated PLGA (RF and AF) in an NGF-containing medium for 2 days. Cell numbers, counted from the numbers of DAPI-stained nuclei from random fluorescence images, were 148 ± 15 (RF), 111 ± 39 (PPy-RF), 112 ± 27 (AF), and 128 ± 18 per image (PPy-AF). These differences were not statistically different, indicating that the PPy-coating does not affect the adhesion or viability of the PC12 cells. Fluorescence images of PC12 cells stained for actin filament (**Figure B.4**) show that the cells formed neurites on all substrates. Analysis of neurite outgrowth was performed from at least 300 neurites. The results indicated that median lengths of the neurites on the meshes were $12.3 \mu\text{m}$ (RF, $n=507$), $12.8 \mu\text{m}$ (PPy-RF, $n=424$), $16.0 \mu\text{m}$ (AF, $n=391$), and $15.3 \mu\text{m}$ (PPy-AF, $n=523$), where n denotes the numbers of analyzed neurites. Longer neurites were formed on the aligned fibers (AF and PPy-AF) than on the random fibers (RF and PPy-RF), $p < 0.01$. The median lengths were similar between the PPy-PLGA fibers and their template PLGA fibers having similar fiber dimensions: $p=0.32$ between RF and PPy-RF; $p=0.31$ between AF and PPy-AF. These results suggest that fiber features played important roles in neurite outgrowth regardless of the PPy-deposition. Other types of neurons have shown similar cellular responses

to fiber orientation, including dorsal root ganglia explants³⁶ and neural stem cells¹², which formed longer neurites/axons on aligned nanofibers and extended their neurites along the fiber strands. Most neurites were aligned along the major direction of the meshes (AF and PPy-AF) (**Figure B.5**). SEM images show that PC12 cells on PPy-PLGA (both PPy-RF and PPy-AF) formed intimate contact with multiple fibers (**Figure B.6**). Cells on the aligned fibers were also found to form more elliptical morphologies elongated in the major fiber direction.

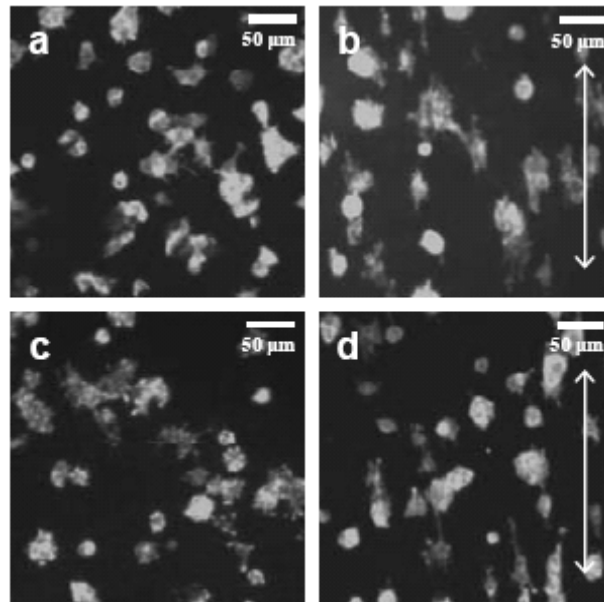


Fig. B.5. Immunostaining of PC12 cells cultured on (a) RF, (b) AF, (c) PPy-RF, and (d) PPy-AF. PC12 cells were cultured for 2 days with an exogenous NGF in the medium and stained with phalloidin-Alexa 488 for F-actin. Arrows indicate major directions of the aligned fibers of (b) and (d) in the images. Scale bars are 50 μm .

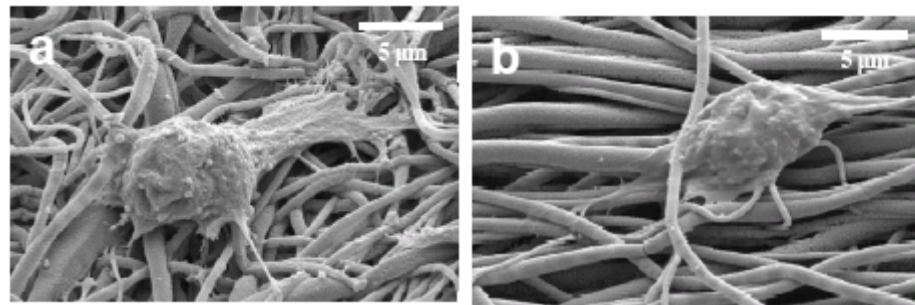


Fig. B.6. SEM images of PC12 cells cultured on (a) PPy-RF and (b) PPy-AF for 2 days.

Likewise, embryonic hippocampal neurons were also cultured on the fiber samples and immuno-stained for analysis (**Figure B.7**). No significant difference was found between PLGA fibers and PPy-coated fibers in terms of the number of the cells and the fraction of cells with established axons (i.e., polarized neurons). After 24 h in culture, $27.8 \pm 3.2\%$, $28.9 \pm 9.7\%$, $30.1 \pm 4.3\%$, and $28.8 \pm 8.8\%$ of the hippocampal neurons established axons on RF, PPy-RF, AF, and PPy-AF, respectively. Average axon lengths were similar with a range of 60-65 μm for all the samples. These results suggest that nano-thick PPy-coating on PLGA nanofibers did not affect initial differentiation (i.e., axon establishment) and resulted in similar results among the substrates. Fiber orientation did not influence axon establishment nor axon elongation of the hippocampal neurons. This finding is consistent with our previous studies with various PLGA fibers (400 nm – 2.4 μm in diameter and different degrees of fiber orientation) for axon formation and elongation of embryonic hippocampal neurons³⁷, where we found that axon establishment and average length were not significantly different among the fibers, although more axons were found on the cells cultured on the fibers compared to smooth PLGA substrates. Contact guidance of hippocampal axons was also observed on the aligned fibers (AF and PPy-AF) similarly to the PC12 cells. Most axons were found to grow along the major direction of the aligned fibers (**Figure B.7**). Consequently, the growth and differentiation of hippocampal neurons (i.e., neuron polarization and axon elongation) were supported by the PPy-PLGA fibers as well as the non-coated PLGA fiber controls. As results, the PPy-PLGA fibers supported the attachment and differentiation of PC12 cells and embryonic hippocampal cells in comparison with the uncoated PLGA fibers, which may be attributed to biocompatibility of the individual components (PPy and PLGA)^{20,21,22}.

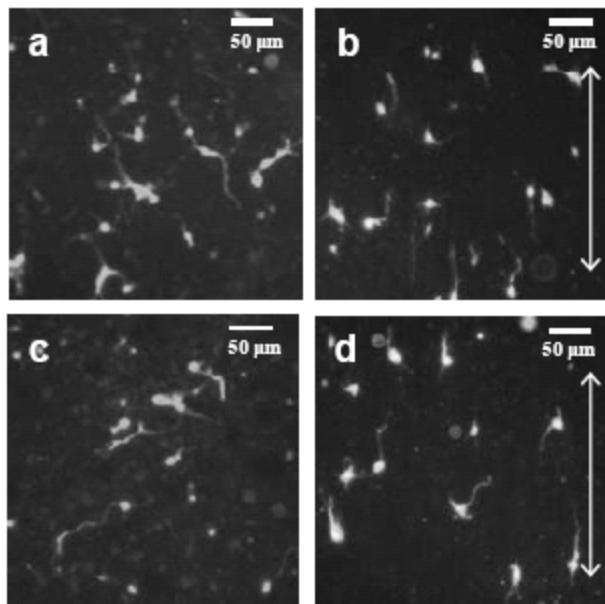


Fig. B.7. Fluorescence images of hippocampal neurons cultured on (a) RF, (b) AF, (c) PPy-RF, and (d) PPy-AF. Immunostaining for tau-1 (axonal marker) was employed to stain hippocampal cells and axons after 1 day in culture. Arrows indicate major directions of the aligned fibers of (b) and (d) in the images. Scale bars are 50 μm .

Electrical stimulation of neurons on electroconducting scaffolds, as our ultimate goal, was studied in the present article. We attempted to demonstrate the use of PPy-PLGA meshes as the potential nerve tissue engineering scaffolds delivering electrical cues through nanofibers. To do this, we examined PPy-PLGA meshes assess the effect of stimulation compared to non-stimulation. We electrically stimulated PC12 cells on PPy-RF and PPy-AF fibers at the potentials of 10 mV/cm and 100 mV/cm according to previously described protocols^{6,23}. Statistically significant longer neurites were observed on the stimulated cells compared to unstimulated controls ($p < 0.01$). PC12 cells stimulated at the potential of 10 mV/cm significantly extended longer neurites than cells with 100 mV/cm (**Figure B.8**). On random PPy-PLGA fibers, median lengths of neurites were 12.7, 18.9, and 15.6 μm for unstimulated cells, stimulated cells at 10 mV/cm, and at 100 mV/cm, respectively. In addition, electrical stimulation of the cells on aligned PPy-PLGA fibers exhibited similar trends with neurite lengths of 14.9 (unstimulated), 21.1 (10 mV/cm), and 17.0 μm (100 mV/cm). Electrical stimulation using aligned fibers resulted in further promotion of neurite outgrowth compared to random fibers, which indicates that fiber alignment and electrical stimulation appeared to be synergistic for neurite extension of PC12 cells. The results indicate that level of electrical potential has an impact on degree of stimulation

and that lower potential may be more favorable for promoting neurite outgrowth of PC12 cells. Li et al. found a similar trend with PC12 cells at various electrical currents, in which PC12 cells formed the more neurites below 10 μA ; promotion of neurite formation diminished as currents increased above 10 μA ³⁸. The exact effects of electrical stimulation are not fully understood; however, some mechanisms are postulated as follows: redistribution of membrane proteins responding to electrical field/current³⁹, decrease in membrane potentials more likely to cause membrane depolarization of neurons⁴⁰, and preferential deposition of biomolecules such as fibronectin on electrodes²³. These biocompatible, electroconducting nanofibrous scaffolds are suitable for electrically stimulating neurons and potentially enhancing nerve tissue regeneration.

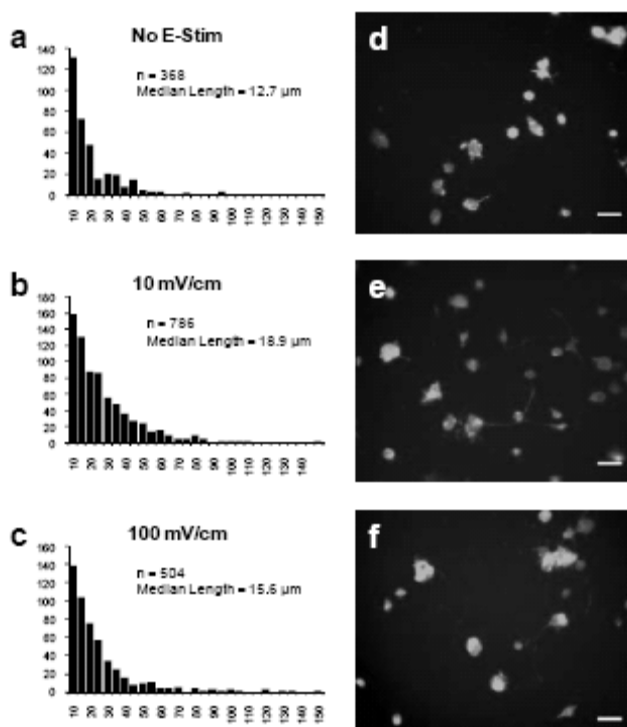


Fig. B.8. Electrical stimulation of PC12 cells through PPy-PLGA (PPy-RF and PPy-AF) fibers at 0 mV/cm and 10 mV/cm. Representative fluorescence images of electrically stimulated cells: (a) PPy-RF at 0 mV/cm (unstimulated); (b) PPy-RF at 10 mV/cm; (c) PPy-AF at 0 mV/cm; (d) PPy-AF at 10 mV/cm. Scale bars are 50 μm . (e) Median neurite lengths of unstimulated PC12 cells and electrically-stimulated PC12 cells (10 mV/cm) on random (PPy-RF) and aligned (PPy-AF) PPy-PLGA fibers.

B.4 Conclusion

Electrically conductive biomaterial scaffolds hold great promise in biomedical applications including neural tissue interfacing. We fabricated electroconducting nanoscaffolds using a simple method involving nano-thick deposition of PPy on biocompatible electrospun PLGA fibers. The PPy-PLGA displayed electrical activity and the nanofibrous features. The nano-scaled sizes and fiber orientation of the template fibers were retained with PPy coating so that the conducting nanofibers provide general advantages of conventional electrospun nanofibers, such as high surface area to volume ratio, interconnecting pores, and nanofibrous topographies. The PPy-deposited fibers were characterized using various techniques including XPS and surface conductance measurement. In vitro cell culture using PC12 cells and embryonic hippocampal neurons demonstrated that compatible cellular interactions on the fabricated PPy-PLGA meshes are appropriate for neuronal applications and present topographies for modulating cellular interactions comparable to the PLGA control nanofibers. Finally, electrical stimulation of PC12 cells on the conducting nanofiber scaffolds improved neurite outgrowth compared to non-stimulated cells; the lower electrical potential of 10 mV/cm encouraged more neurite outgrowth than the higher potential of 100 mV/cm. Additionally, further promotion in neurite outgrowth was observed with electrical stimulation on aligned conducting nanofibers. This work will aid to design neuronal tissue interfaces integrated with topographical and electrical cues for use in nerve tissue scaffolds and for neural interfacing.

B.5 Acknowledgment

This work was supported by NIH R01EB004429 (CES) and Institute for Critical Technologies and Sciences at Virginia Tech (ASG). The author would thank to Derek Ensign and Gregory Abraham for experimental assistance.

B.6 References

1. Gurunathan K, Murugan AV, Marimuthu R, Mulik UP, Amalnerkar DP. Electrochemically synthesized conducting polymeric materials for applications towards technology in electronics, optoelectronics and energy storage devices. *Mater Chem Phys* 1999;61:173–91.
2. Jager EWH, Smela E, Inganas O. Microfabricating Conjugated Polymer Actuators. *Science* 2000;290:1540–5.
3. Guimard NK, Gomez N and Schmidt CE. Conducting polymers in biomedical engineering. *Prog Polym Sci* 2007;32:876-921.
4. Ateh DD, Navsaria HA, Vadgama P. Polypyrrole-based conducting polymers and interactions with biological tissues. *J R Soc Interface* 2006;3:741-52.
5. Schmidt CE, Shastri VR, Vacanti JP, Langer R. Stimulation of neurite outgrowth using an electrically conducting polymer. *Proc Nat. Acad Sci USA* 1997;94:8948-53.
6. Gomez N, Schmidt CE. Nerve growth factor-immobilized polypyrrole: bioactive electrically conducting polymer for enhanced neurite extension. *J Biomed Mater Res* 2007;81:135-49.
7. Sanghvi AB, Miller KP, Belcher AM, Schmidt CE. Biomaterials functionalization using a novel peptide that selectively binds to a conducting polymer. *Nat Mater* 2005;4:496-502.
8. Song HK, Toste B, Ahmann K, Hoffman-Kim D, Palmore GT. Micropatterns of positive guidance cues anchored to polypyrrole doped with polyglutamic acid: a new platform for characterizing neurite extension in complex environments. *Biomaterials* 2006;27:473-84.
9. Gomez N, Lee JY, Nickels JD, Schmidt CE. Micropatterned Polypyrrole: Combination of Electrical and Topographical Characteristics for Stimulation of Cells. *Adv Func Mater* 2007;17:1645-53.
10. Li GN, Hoffman-Kim D. Tissue-Engineered Platforms of Axon Guidance. *Tissue Eng* 2008;14(1):33-50.
11. Pham QP, Sharma U, Mikos AG. Electrospinning of polymeric nanofibers for tissue engineering applications. *Tissue Eng* 2006;12:1197-1211.
12. Yang F, Murugan R, Wang S, Ramakrishna S. Electrospinning of nano/micro scale poly(L-lactic acid) aligned fibers and their potential in neural tissue engineering. *Biomaterials* 2005;26:2603-10.
13. Bashur CA, Dahlgren LA, Goldstein AS. Effect of fiber diameter and orientation on fibroblast morphology and proliferation on electrospun poly(D,L-lactic-co-glycolic acid) meshes. *Biomaterials* 2006;27:5681-8.
14. Li M, Guo Y, Wei Y, MacDiarmid AG, Lelkes PI. Electrospinning polyaniline-contained gelatin nanofibers for tissue engineering applications. *Biomaterials* 2006;27:2705-15.
15. Webster TJ, Waid MC, McKenzie JL, Price RL, Ejiogor JU. Nanobiotechnology: carbon nanofibres as improved neural and orthopaedic implants. *Nanotechnol* 2004;15:48-54.
16. Skotheim TA, Elsenauer RL, Reynolds JR, editor. *Handbook of Conducting Polymers*, Marcel Dekker, New York, 1998.
17. Nair S, Nataragan S, Kim SH. Fabrication of electrically conducting polypyrrole-poly(ethylene oxide) composite nanofibers. *Macromol Rapid Commun* 2005;26:1599-603.
18. Jakubiec B, Marois Y, Zhang Z, Roy R, Sigot-Luizard MF, Dugré FJ, King MW, Dao L, Laroche G, Guidoin R. In vitro cellular response to polypyrrole-coated woven polyester

- fabrics: Potential benefits of electrical conductivity. *J Biomed Mater Res* 1998;41:519-26.
19. Zhang Z, Roy R, Dugré FJ, Tessier D, Dao LH. In vitro biocompatibility study of electrically conductive polypyrrole-coated polyester fabrics. *J Biomed Mater Res* 2001;57: 63-71.
 20. Gilding DK. editor, *Biocompatibility of Clinical Implant Materials*, CRC Press, 1981.
 21. Wang X, Gu X, Yuan G, Chen S, Zhang P, Zhang T, Yao J, Chen F, Chen G. Evaluation of biocompatibility of polypyrrole in vitro and in vivo. *J Biomed Mater Res* 2004;68(3):411-22.
 22. Jiang XP, Marois Y, Traore A, *et al.* Tissue reaction to polypyrrole-coated polyester fabrics: An in vivo study in rats. *Tissue Eng* 2002;8(4):635-47.
 23. Kotwal A, Schmidt CE. Electrical stimulation alters protein adsorption and nerve cell interactions with electrically conducting biomaterials. *Biomaterials* 2001;22(10):1055-64.
 24. Jiang X, Tessier D, Dao H, Zhang Z. Biostability of electrically conductive polyester fabrics: An in vitro study. *J Biomed Mater Res* 2002;62:502-13.
 25. Dotti CG, Sullivan CA, Banker GA. The establishment of polarity by hippocampal neurons in culture. *J Neurosci* 1988;8(4):1454-68.
 26. Rostener B. *Fundamentals of Biostatistics* (6th Ed.), Thomson Brooks/Cole, 2006.
 27. Murugan R, Ramakrishna S. Nano-featured scaffolds for tissue engineering: a review of spinning methodologies. *Tissue Eng* 2006;12:435-47.
 28. Malinauskas A. Chemical deposition of conducting polymers. *Polymer* 2001;42:3957-72.
 29. De Giglio E, Guascito MR, Sabbatini L, Zambonin G. Electropolymerization of pyrrole on titanium substrates for the future development of new biocompatible surfaces. *Biomaterials* 2001;22:2609-16.
 30. Cairns DB, Armes SP. X-ray photoelectron spectroscopy characterization of submicrometer-sized polypyrrole-polystyrene composites. *Langmuir* 1999;15(23):8059-66.
 31. Tischler AS. Chromaffin cells as models of endocrine cells and neurons. *Ann NY Acad Sci* 2002;971:366-70.
 32. Burgess N, Miguire EA, O'Keefe J. The human hippocampus and spatial and episodic memory. *Neuron* 2002;35(4):625-41.
 33. Fukata Y, Kimura T and Kaibuchi K. Axon specification in hippocampal neurons. *Neurosci Res* 2002;43(4):305-15.
 34. McCaig CD, Rajniecek AM, Song B, Zhao M. Has electrical growth cone guidance found its potential? *Trends Neurosci* 2002;25(7):354-9.
 35. Sapelkin AV, Bayliss SC, Unal B, Charalambou A: Interaction of B50 rat hippocampal cells with stain-etched porous silicon. *Biomaterials* 2006;27:842-6.
 36. Corey JM, Lin DY, Mycek KB, Chen Q, Samuel S, Feldman EL, Martin DC. Aligned electrospun nanofibers specify the direction of dorsal root ganglia neurite growth. *J Biomed Mater Res A* 2007;83(3):636-45.
 37. Lee JY, Bashur CA, Gomez N, Goldstein AS, Schmidt CE. Enhanced polarization of embryonic hippocampal neurons on micron scale electrospun fibers. *J Biomed Mater Res A*. submitted.

38. Zhang Z, Rouabhia M, Wang Z, Roberge C, Shi G, Roche P, Li J, Dao LH Electrically conductive biodegradable polymer composite for nerve regeneration: electricity-stimulated neurite outgrowth and axon regeneration. *Artif Organs*. 2007;31(1):13-22.
39. Patel N, Poo MM. Orientation of neurite growth by extracellular electric fields. *J Neurosci*. 1982;2(4):483-496.
40. Patel N and Poo MM. Perturbation of the direction of neurite growth by pulsed and focal electric fields. *J Neurosci*. 1984;4(12):2939-2947.

Appendix C: Computational Predictions of the Tensile Properties of Electrospun Fibre Meshes: Effect of Fibre Diameter and Fibre Orientation

Triantafyllos Stylianopoulos¹, Chris A. Bashur², Aaron S. Goldstein², Scott A. Guelcher³, and Victor H. Barocas⁴

¹Department of Chemical Engineering and Materials Science, University of Minnesota, Minneapolis, MN 55455

²Department of Chemical Engineering, Virginia Polytechnic Institute and State University, Blacksburg, VA 24061

³Department of Chemical Engineering, Vanderbilt University, Nashville, TN 37235

⁴Department of Biomedical Engineering, University of Minnesota, Minneapolis, MN 55455

Abstract

The mechanical properties of biomaterial scaffolds are crucial for their efficacy in tissue engineering and regenerative medicine. At the microscopic scale, the scaffold must be sufficiently rigid to support cell adhesion, spreading, and normal extracellular matrix deposition. Concurrently, at the macroscopic scale the scaffold must have mechanical properties that closely match those of the target tissue. The achievement of both goals may be possible by careful control of the scaffold architecture. Recently, electrospinning has emerged as an attractive means to form fused fibre scaffolds for tissue engineering. The diameter and relative orientation of fibres affect cell behaviour, but their impact on the tensile properties of the scaffolds has not been rigorously characterized. To examine the structure property relationship, electrospun meshes were made from a polyurethane elastomer with different fibre diameters and orientations and mechanically tested to determine the dependence of the elastic modulus on the mesh architecture. Concurrently, a multiscale modelling strategy developed for type I collagen networks was employed to predict the mechanical behaviour of the polyurethane meshes. Experimentally, the measured elastic modulus of the meshes varied from 0.56 to 3.0 MPa depending on fibre diameter and the degree of fibre alignment. Model predictions for tensile loading parallel to fibre orientation agreed well with experimental measurements for a wide range of conditions when a fitted fibre modulus of 18 MPa was used. Although the model predictions were less accurate in transverse loading of anisotropic samples, these results indicate that computational modelling can assist in design of electrospun artificial tissue scaffolds.

C.1 Introduction

The goal of tissue engineering is to develop bioactive materials that, when implanted into tissue deficits, will integrate with the adjacent tissue, stimulate vascular infiltration and initiate normal tissue remodelling. Current strategies to achieve such clinically effective materials have frequently involved incorporating biological and pharmaceutical components into porous biomaterial scaffolds. Here, the selection of the biomaterial is based on biocompatibility, ease of processing into the desired three dimensional architecture and matching of the resultant mechanical properties with that of the target tissue.¹ Polymers that have been widely tested include natural polymers, such as collagen, agarose, silk and fibrin²⁻⁶ and synthetic polymers, such as poly(glycolic acid) (PGA), poly(lactic acid) (PLA), poly(ϵ -caprolactone) (PCL) and their copolymers⁷⁻¹⁰, and polyurethanes.¹¹⁻¹² Concurrently, design of the scaffold architecture remains a challenging task. To be effective, the scaffold must be capable of regulating morphology and function of adherent cells, without compromising tissue specific mechanical properties. In the case of anisotropic structural tissues (e.g. blood vessels, ligaments and heart valve leaflets) achievement of suitable mechanical properties remains a critical challenge.

Recently, electrospinning has emerged as a promising method for fabricating fibrous scaffolds for tissue engineering applications such as blood vessel,¹² anterior cruciate ligament (ACL)¹³ and cardiac tissue.¹⁴⁻¹⁸ Electrospinning involves the use of a high-voltage power supply to eject a polymer fibre from solution and deposit it onto a grounded target. Fibre diameter can be varied from 100 nm to more than 5 μm by controlling the electrospinning conditions, and orientation of the resultant network can be imparted by depositing this fibre onto a moving target.¹⁹ Importantly, the micro-scale architecture affects both the morphology of adherent cells,¹³ and the bulk mechanical properties of the scaffold.²⁰⁻²¹ Therefore, the architecture must be engineered to guide cell behaviour while remaining suitable for soft tissue engineering applications.²²⁻²³

The utility of electrospun fused fibre meshes, however, is limited by the absence of a theoretical framework with which to predict how the bulk mechanical properties depend on the properties of the individual fibres. Such a framework is inherently multiscale, with the scaffold dimension being on the *centimeter* length scale, while the underlying fibrillar architecture on the *micrometer* scale. The strong dependence of native tissue response on fibre orientation, diameter, and reorientation in response to strain²⁴ suggests that consideration of both length scales is

necessary, and thus, continuum constitutive models often cannot predict the tissue response under every loading condition.²⁵ The scale separation makes multiscale, structure based mathematical models an attractive option to describe the mechanical behaviour of engineered tissues.

In this study, fused fibre meshes were electrospun from a degradable poly(esterurethaneurea) (PEUUR) elastomer, and fibre diameter and orientation were systematically varied. Mechanical testing was performed to determine experimentally the dependence of the elastic modulus on the mesh architecture, while a multiscale, structural model previously developed for modelling reconstituted type I collagen gels²⁶⁻²⁷ was employed to predict the elastic properties of the polyurethane meshes. Finally, the model was extended to predict the mechanical properties of an electrospun tubular mesh that might serve as a scaffold for an engineered blood vessel.

C.2 Methods

C.2.1 Materials

All chemicals including the 1,6-diisocyanatohexane (HDI), poly(ϵ -caprolactone) diol (average molecular weight 1250 Daltons, PCL1250), 1,3-propanediol bis(4-aminobenzoate (PDAB), diethyl ether, dibutyltin dilaurate (DBTDL), 1,1,1,3,3,3-hexafluoro-2-propanol (HFIP), dimethyl formamide (DMF), and phosphate-buffered saline (PBS) were obtained from Sigma-Aldrich (St. Louis, MO) unless otherwise specified. Anhydrous (<50 ppm water) dimethyl sulfoxide (DMSO) was obtained from Acros Organics (Morris Plains, NJ). All chemical reagents were used as received except for PCL1250, which was dried for 24 h at 80°C under vacuum (10 mm Hg).

C.2.2 Polyurethane Synthesis

A segmented degradable PEUUR elastomer was synthesized using standard techniques in a three-neck, round-bottom flask equipped with argon inlet and outlet, condenser and stirrer.²⁸ Anhydrous DMSO was charged to a round-bottom flask fitted with a condenser. HDI was added to the flask, which was then immersed in an oil bath at 75°C, purged with argon, and stirred with a Teflon blade stirrer turned by an electric motor. A solution of dried PCL1250 was charged into

the reactor by means of an addition funnel. The NCO:OH equivalent ratio of the prepolymer was 2.0:1.0. The prepolymer content in the reactor was controlled at 14 wt%. DBTDL was added to the flask at 1000 ppm and the reaction was allowed to proceed for 3 h. A solution of chain extender in DMSO was prepared at 50°C and added to the resultant HDI.PCL1250.HDI prepolymer in the reaction vessel. The NCO:OH equivalent ratio of the polyurethane was controlled at 1.03:1.0 and the polymer concentration was 12 wt%. DBTDL was added to a concentration of 1000 ppm. The reaction was allowed to proceed at 80°C for 20 h. The polymer was then precipitated in diethyl ether and dried in a vacuum oven for 24 h at 80°C under 10 mmHg vacuum. The density of the resultant polymer was determined to be 1.13 g/cm³ using a pycnometer (AccuPyc 1330, Micromeritics, Norcross, GA).

C.2.3 Electrospinning

PEUUR was electrospun onto aluminum foil with controlled fibre diameters and degrees of orientation. To form isotropic meshes, aluminum foil was mounted on a stationary target and electrospun from a syringe equipped with a 22 gauge Teflon tipped needle using a 15 kV potential, a throw distance of 15 cm, and a syringe flow rate of 5 mL/h. PEUUR concentrations of 11.0 and 13.5 wt% in HFIP were used to produce meshes with different fibre diameters. To form meshes comprised of partially orientated fibres, aluminum foil was mounted on a 6.2 cm diameter wire mesh drum and a 13.5 wt% PEUUR solution was electrospun under the conditions described above. The drum was rotated at rates of 600 and 1300 rpm (corresponding to linear velocities of 2.0 and 4.4 m/s, respectively) to produce meshes with different degrees of fibre orientation. After electrospinning, the meshes were carefully peeled off of the aluminum foil for imaging and mechanical testing.

C.2.4 Scanning Electron Microscopy (SEM)

Fibre diameter and degree of orientation of fibre meshes were determined by analysis of SEM images. Briefly, electrospun meshes were mounted onto studs and sputtercoated with a 10 nm layer of palladium (Model 208HR, Cressington Scientific Instruments, Cranberry Township, PA). Images were acquired using a LEO 1550 Field Emission SEM (Carl Zeiss SMT, Thornwood, NY) operating at 5 kV with a 16 mm working distance. Resultant images were imported into ImagePro Plus software (ICube, Crofton, MD) for analysis of fibre diameter and

orientation. The degree of alignment was characterized by the angular standard deviation as described previously.¹³ Low angular standard deviations denote more strongly aligned meshes. The diameter and orientation of at least 150 fibres were analysed for each sample.

C.2.5 Mechanical Testing

The tensile modulus of the bulk PEUUR was determined from cast dogbones using ASTM D412-98a with modifications. Briefly, a 9 wt% solution of the PEUUR in DMF was prepared, and then heated in a 60°C water bath overnight. The solution was cast in Teflon dish, and allowed to dry in a vacuum oven for two days. A punch was used to create dogbones with a 10 mm gauge distance and 2.7 mm gauge width. Thicknesses, measured using digital calipers, were 0.2–0.4 mm. The samples were soaked in PBS overnight and tested at 37°C in PBS. The samples were pulled monotonically at a rate of 10 mm/min to 400% strain using a Tytron250 (MTS, Eden Prairie, MN). Modulus was measured from the linear range of the stress/strain curve. Results are presented as mean \pm standard deviation for $n = 3$ samples.

The tensile moduli of electrospun PEUUR meshes were determined using 15 \times 10 mm strips that had been soaked in PBS overnight before testing. The thickness of the meshes was on the order of 0.1 mm and therefore could not be accurately measured with calipers. Instead thickness was estimated from measurements of mesh mass, length, width and density (1.13 g/cm³) using an assumed porosity of 60% (based on published mercury intrusion porosimetry measurements¹⁴). Cyclic testing was performed with a gauge distance of 10 mm, a frequency of 0.5 Hz, and a maximum strain of 18%. The temperature was maintained at 37°C using a heated bath. Isotropic meshes were tested in one direction, and oriented meshes were tested both parallel and perpendicular to the direction of fibre alignment. A total of 220 cycles were performed, and the modulus was reported based on the last cycle. Modulus was calculated from the linear region of the stress strain curve (typically between 10 and 18% strain) using a cross-sectional area based on an assumed 60% mesh porosity. Results are presented as mean \pm standard deviation for $n = 3$ meshes.

C.2.6 Formulation of the Model

To accommodate the scale separation between the functional and structural scales of artificial tissues, a multiscale methodology was employed that incorporates the tissue microstructure directly. The scale-bridging method used in this study was the volume-averaging theory.²⁹⁻³⁰ A detailed description of the model can be found elsewhere^{26,31}; a summary is given here.

The model is developed in two scales: the microscopic scale, which provides a statistical representation of the microstructure and is called representative volume element (RVE); and the macroscopic scale, which represents the whole tissue. The RVE consists of a three-dimensional fibrillar network that is intended to replicate the fibre diameter, density and orientation of an electrospun mesh (**Figure C.1**). In the network, wherever two fibres intersect, they are connected by a crosslink that allows free rotation of the fibres and the mechanical response of the fibres is governed by a constitutive equation. The macroscopic scale is modelled with the finite element (FE) method. Separate RVEs are constructed around the Gauss points of the FE solution, and the macroscopic deformation field determines the deformation of the RVE boundary through the FE basis functions. The deformation of the RVE compels the fibres to deform, and the solution of the force balance among the fibres determines the local forces developed on the RVE. From the local RVE forces and using volume-averaging theory, the averaged Cauchy stress tensor is calculated for use at the macroscale (see Eq. (C.4)). The averaged Cauchy stress tensor is calculated at each Gauss point of the FE domain and then the macroscopic stress balance is solved. The mathematical formulation is nonlinear and requires iteration of the solution algorithm until convergence. The model accounts for the orientation of the network, the interaction among the fibres, and the realignment of the fibres during deformation. These phenomena play a key role in the mechanical response of the material and vary considerably from tissue to tissue.

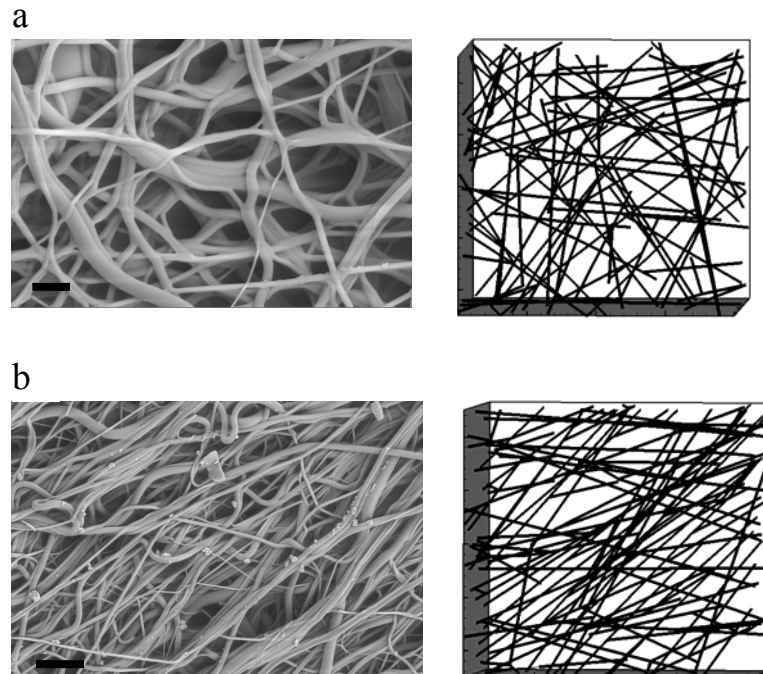


Fig. C.1. SEM images and model representations of electrospun meshes. (a) Unorientated mesh formed from an 11 wt% solution onto a stationary target. Angular standard deviation is 67.5° and scale bar is $1\ \mu\text{m}$. (b) Orientated mesh formed from a 13.5 wt% solution onto a target rotating at 2.0 m/s. Angular standard deviation is 41.2° and scale bar is $10\ \mu\text{m}$.

The RVEs were generated through a stochastic process³². Nucleation sites (seeds) were generated randomly inside a cubic space and gave birth to two segments that grew in opposite directions along a randomly chosen vector. The segments grew progressively by a unit length until they collided with the RVE boundary or with another segment. In the former case, a boundary crosslink was generated, and in the latter case, collision between two segments was defined when their distance was less than a prescribed fibre diameter, and an interior crosslink was generated at the point of collision. In both cases the crosslinked segment stopped growing. A fibre was defined as the line between two crosslinks associated with the same segment. Selecting the directional vectors from an anisotropic distribution allowed generation of networks with preferred alignments (**Figure C.1(b)**).

C.2.7 Governing Equations

The formulation described above requires a fibre constitutive equation for the microscopic scale, the equation that provides the averaged Cauchy stress, given by volume-averaging theory, and the stress balance for the macroscopic scale. Most polymers are incompressible and neo-Hookean³³, at least at moderate strains, and thus the polymer fibre constitutive equation used in this study is:

$$f = G_f A_f \left(\lambda^2 - \frac{1}{\lambda} \right) \quad (\text{C.1})$$

where f is the force on the fibre, G_f is the fibre shear modulus, A_f is the cross-sectional area of the fibre, and λ is the fibre stretch ratio. For an incompressible material the elastic modulus, E_f , is three times as much as the shear modulus. To account for the decrease in the fibre cross-section in response to stretching, A_f was computed as $A_f = A_o / \lambda$, where A_o is the cross-sectional area of the unstretched fibre.

The volume-averaged Cauchy stress tensor, S , was obtained from the microscopic stress tensor, s ³⁴:

$$S_{ij} \equiv \frac{1}{V} \int_V s_{ij} dV \quad (\text{C.2})$$

where V is the RVE volume and index notation is used throughout. Taking into account that $s_{ij} = s_{kj} \delta_{ik} = s_{kj} x_{i,k}$, where δ_{ik} is the Kronecker delta and x is the directional vector, the divergence theorem implies that

$$S_{ij} = \frac{1}{V} \int_{\partial V} x_i t_j dS \quad (\text{C.3})$$

where t is the traction exerted on the boundaries, ∂V , of the RVE. For a network of discrete fibres the integral of the traction is given by the forces on the boundary cross-links³⁵:

$$S_{ij} = \frac{1}{V} \sum_{\substack{\text{boundary} \\ \text{crosslinks}}} x_i f_j \quad (\text{C.4})$$

A detailed derivation of the macroscopic stress balance is given in Chandran and Barocas³¹. We assume microscopic equilibrium, $s_{ij,i} = 0$, and use Leibnitz's theorem, to express divergence of the macroscopic stress tensor as:

$$S_{ij,i} = \frac{1}{V} \oint_{\partial V} (s_{ij} - S_{ij}) u_{k,i} n_k dS \quad (\text{C.5})$$

where u is the displacement of the RVE boundary and n is the normal unit vector. The right hand side of Eq. C.5 is due to coupling between the non-uniform stress and the non-uniform deformation of the RVE boundary.

C.2.8 Comparison of the Model to Experimental Measurements

In order to compare model predictions of the elastic modulus to those measured experimentally for PEUUR meshes four model parameters had to be specified: fibre elastic modulus E_f , crosssectional area A_o , the fibre volume fraction, θ , and the network orientation. Fibre cross-sectional area and the network orientation were calculated from experimental measurements of fibre diameter and the angular standard deviation. The fibre volume fraction was set to 0.4 – to match the assumed volume fraction of the electrospun meshes – and the elastic modulus, E_f , was determined by fitting the model to the experimental stress–strain response for meshes electrospun from an 11.0 wt% solution. RVEs were generated, and their angular standard deviations were checked to match the experimental values. The simulations were repeated for four networks for each case studied, and the average value of the elastic modulus was taken. Uniaxial extension simulations were performed for rectangular slabs up to 18% strain to permit comparison with experimental samples.

C.2.9 Extension to Engineered Blood Vessels

The computational approach was employed to simulate inflation tests of an engineered blood vessel. The purpose was to demonstrate the utility of this computational framework for the design of a scaffold suitable for tissue engineering, and studies were undertaken to predict the effect of (1) fibre orientation and (2) mesh thickness on the mechanical response of the engineered vessel. Polymeric scaffolds have been used to construct small-diameter vascular grafts^{12, 36}, and their mechanical properties have been compared to these of normal arteries.^{11, 37} As a measure for the vessel stiffness, the stiffness parameter, β , proposed by Hayashi et al.³⁸ has been used according to the following equation:

$$\ln(P/P_s) = \beta(D/D_s - 1) \quad (C.6)$$

where P is the pressure, D is the diameter of the vessel, and P_s (=100 mmHg) and D_s are standard pressure and diameter, respectively. The stiffness parameter is calculated in the physiological pressures region (60–140 mmHg); a higher β value indicates a stiffer vessel.

Here, illustrative simulations of inflation tests were performed for vessel dimensions similar to those reported by Matsuda et al.¹². The simulated vessel had length 4 cm, thickness 250 μm , and inner diameter 3.0 mm. The model parameters were a fibre volume fraction, θ , of 0.4, a fibre diameter of 0.9 μm , and the elastic modulus, E_f , of 18 MPa. The vessel was inflated to 150 mmHg luminal pressure in 10 mmHg increments, and the expansion of the lumen was predicted. To study the effect of fibre orientation on the mechanical response of the vessel, three different fibre orientations were used: isotropic, axial and circumferential. The isotropic network was circumferentially aligned with an angular standard deviation of 64°, while orientated networks were either axially and circumferentially aligned with an angular standard deviation of 40°. The model predictions were compared to the response of a typical human intracranial artery.³⁸ The thickness of the simulated vessel was then varied to find the vessel thickness that exhibited the same mechanical behaviour as the human artery. The stiffness parameter, β , was also calculated and compared to published data for native and engineered arteries.

C.3 Results

C.3.1 Comparison of the Model to Experimental Measurements

Three cast dogbones of the PEUUR were tested to 400% uniaxial strain and the elastic ensile modulus was determined from the slope of the linear part of the stress–strain curves. The average value of the elastic modulus was 2.7 MPa.

The experimental results are summarized in **Tables C.1** and **C.2**. **Table C.1** shows the elastic modulus for isotropic meshes prepared from concentrations of 11.0 and 13.5 wt% in HFIP. The data suggest that the elastic modulus of the scaffolds is sensitive to the polymer solution concentration. **Table C.2** shows the experimental measurements for 13.5 wt% concentration with 0, 2.0, and 4.4 m/s drum velocities. The moduli parallel (\parallel) and perpendicular (\perp) to fibre alignment are also presented. Here, the modulus parallel to the fibre alignment increased systematically with decreasing angular standard deviation while the modulus perpendicular to the fibre alignment decreased with increasing alignment.

Table C.1. Measured fiber diameter, angular standard deviation and elastic modulus for PEUUR meshes electrospun from 11 and 13.5 wt% solutions onto a stationary target. Mean and standard deviations for fiber diameter and angle were calculated from $n \geq 150$ individual fibers. Mean and standard deviation for modulus were calculated for the 220th cycle for $n=3$ meshes.

Concentration in HFIP (wt%)	Fiber diameter (μm)	Angular standard deviation ($^\circ$)	Modulus (MPa)
11.0	0.53 ± 0.26	67.5	0.63 ± 0.27
13.5	0.90 ± 0.49	54.6	0.89 ± 0.44

Table C.2. Measured fiber diameter, angular standard deviation and elastic modulus for PEUUR meshes electrospun from 13.5 wt% solution at different rotation rates. Modulus was determined both parallel (\parallel) and perpendicular (\perp) to the direction of rotation. Mean and standard deviations for fiber diameter and angle were calculated from $n \geq 150$ individual fibers. Mean and standard deviation for modulus were calculated for the 220th cycle for $n=3$ meshes.

Speed (m/s)	Fiber diameter (μm)	Angular standard deviation ($^\circ$)	Modulus (MPa)
Stationary	0.90 ± 0.49	54.6	0.89 ± 0.44
2.0 \parallel	0.63 ± 0.30	41.2	1.41 ± 0.81
2.0 \perp	0.63 ± 0.30	41.2	0.57 ± 0.17
4.4 \parallel	0.57 ± 0.29	29.9	3.04 ± 1.87
4.4 \perp	0.57 ± 0.29	29.9	0.56 ± 0.16

The computational model was fit to the stress–strain curve for a PEUUR mesh electrospun from an 11.0 wt% solution (**Figure C.2**). The resultant best fit for the fibre Young’s modulus, E_f , was found to be 18 MPa (**Figure C.2**), which is more than six times greater than the measured modulus for the solution-cast polymer. The computed moduli are presented in **Figures C.3** and **C.4**. At the same figures the experimental moduli, as given in **Tables C.1** and **C.2**, are plotted in order to illustrate the comparison between theory and experiment. The predicted moduli for isotropic meshes were 0.64 MPa for a fibre diameter of 0.53 μm and 0.90 MPa for a fibre diameter of 0.9 μm . The predicted moduli for 41.2° angular standard deviation (2.0 m/s drum velocity) were 1.14 MPa (\parallel) and 0.37 MPa (\perp) and for 29.9° angular standard deviation (4.4 m/s drum velocity) were 2.60 MPa (\parallel) and 0.33 MPa (\perp). Here, the computed moduli of the meshes is lower than that of an individual fibre, E_f , because of volume fraction and network effects. From the comparison of the predicted and experimental moduli we conclude that the model predictions of the modulus were not significantly different from the experimental data for the isotropic meshes and the modulus parallel to the fibre direction for the orientated meshes ($p > 0.77$ in all cases). However, the model significantly underpredicted the tensile moduli perpendicular to the direction of stretching for the orientated meshes ($p < 0.01$).

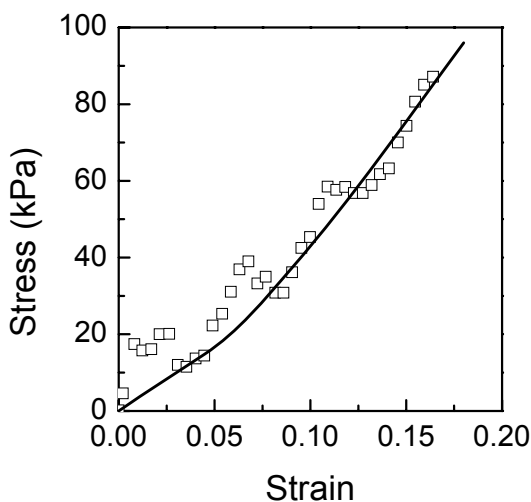


Fig. C.2. Experimental (squares) and computed (curve) stress–strain curve for PEUUR mesh electrospun from 11 wt% solution in HFIP.

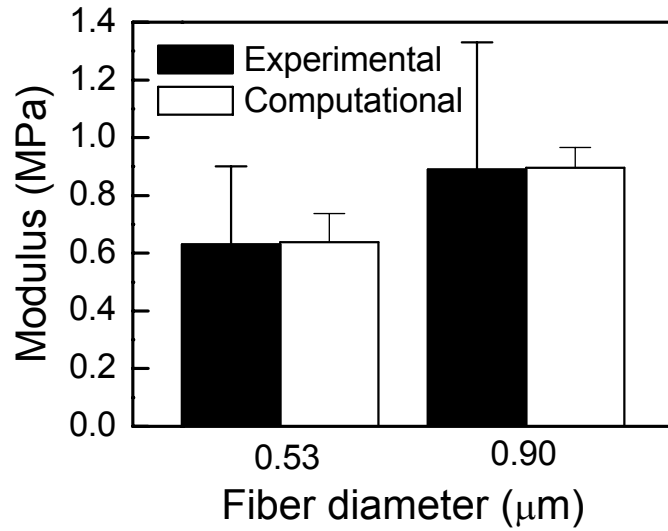


Fig. C.3 Experimental (black bar) and computed (white bar) moduli for PEUUR meshes electrospun from 11 (diameter 0.53 μm) and 13.5 wt% (diameter 0.90 μm) solutions at stationary drum. The standard deviations are also depicted.

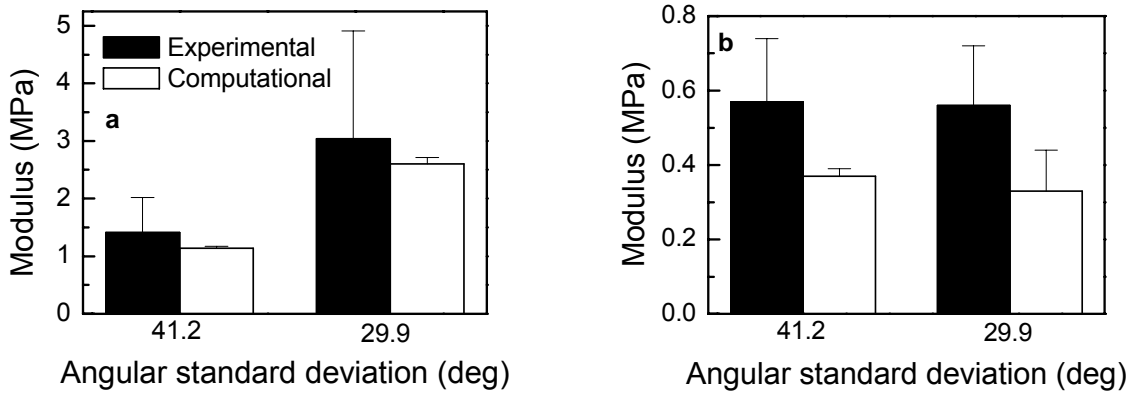


Fig. C.4. Experimental (black bar) and computed (white bar) moduli for PEUUR meshes electrospun from 13.5 wt% solution at rotation rates of 2.0 m/s (41.2°) and 4.4 m/s (29.9°) parallel (Fig. 9(a)) and perpendicular (Fig. 9(b)) to fibre alignment. The standard deviations are also depicted.

C.3.2 Extension to Engineered Blood Vessels

The predicted pressure–diameter response of the vessel for the three different orientations is shown in **Figure C.5**. In the same figure, the pressure–diameter response of a typical human intracranial artery is also shown³⁸. The shadowed area in the plot indicates the physiological pressure range. The model predicts that an axially orientated vessel is the most compliant, and the vessel stiffens with increasing circumferential orientation. The model predicts that PEUUR vessels would not follow the low-pressure response of normal arteries, which are very compliant because of the uncrimping and reorganization of the collagen fibres³⁹. At physiological pressures, however, the collagen fibres are under tension and the artery is stiffer than that predicted for a PEUUR vessel. Next, the wall thickness of the circumferentially orientated vessel was increased to 1000 μm to match the stiffness of the human intracranial artery (**Figure C.6**). The stiffness parameter (β), as calculated from the predicted pressure diameter curves of **Figure C.6** using Eq. (C.6), was 15.8 for 1000 μm wall thickness, as compared to 9.1 predicted for 250 μm thickness PEUUR vessel and 21.2 for a normal intracranial artery. For comparison, the thickness of the human intracranial artery is 100 μm ³⁸, which is thinner than either PEUUR vessel models.

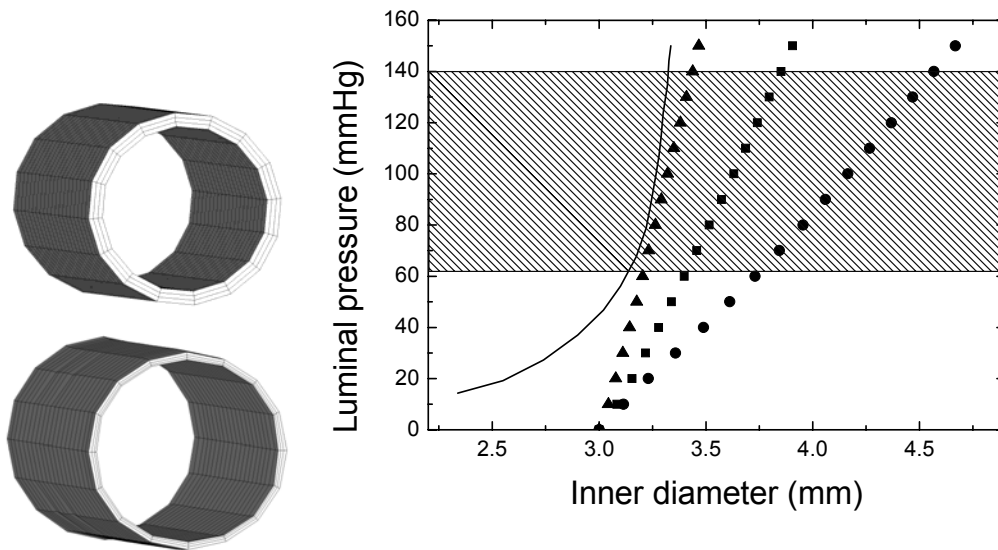


Fig. C.5. Initial and inflated at 150 mmHg luminal pressure configuration of the blood vessel (left). Pressure vs. inner diameter response of the vessel for random (squares), axially orientated (circles), and circumferentially orientated (triangles) meshes, and for a human intracranial artery³⁸ (solid).

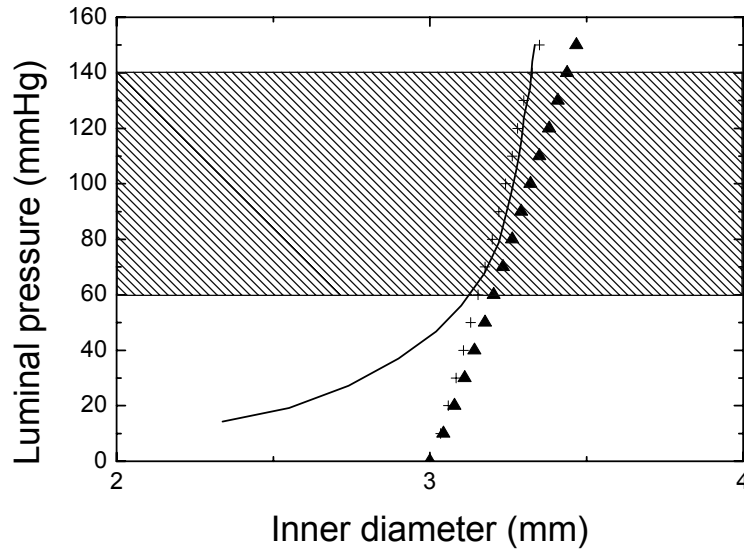


Fig. C.6. Pressure vs. inner diameter response for circumferentially orientated meshes for 250 μm (triangles) and 1000 μm (crosses) wall thickness, and for an intracranial artery³⁸ (solid).

C.4 Discussion

The tensile properties of electrospun polyurethanes were measured as a function of fibre diameter and orientation, and compared to those predicted using a mathematical model for fibrous networks. The experimental results revealed that the tensile properties of fibrous meshes are sensitive to the microstructural architecture. Aligned samples showed mechanical anisotropy consistent with their structural anisotropy. In particular, the moderately aligned samples (2.0 m/s drum velocity) exhibited a ratio of 2.5 between parallel and perpendicular modulus, while the more highly aligned samples (4.4 m/s drum velocity) exhibited a ratio of 5.4. Computational model predictions of the tensile properties were in good agreement with the experimental measurements for isotropic meshes and for anisotropic meshes in the direction parallel to fibre orientation. However, the model underpredicted the experimentally determined modulus for anisotropic meshes in the direction perpendicular to fibre orientation.

Simulated inflation tests of tubular meshes were performed to illustrate the utility of our computational approach to the design of engineered blood vessels. Here, our objective was to apply the model to predict the structure of the PEUR scaffold (vessel thickness and network

orientation) that would match the strength of normal tissue. The studies showed that a circumferentially-orientated network is stiffer than the other two network orientations tested, as was expected. In addition, the model predicted that a circumferentially-orientated PEUUR network would need to be 1000 μm thick to match the pressure–diameter response of a typical human intracranial artery. However, the model predicts that such a mesh would not possess the toe-in mechanical response intrinsic to blood vessels.

The stiffness parameter β of the simulated PEUUR vessels ranged from 9.1 to 15.8 depending on the wall thickness. **Table C.3** presents the β values predicted by the model along with experimental measurements for vessels made from polyurethane and for native arteries. The model predictions are within the range of β values reported in experimental studies for polyurethanes. Furthermore, comparison between the stiffness of native and simulated arteries suggests that polyurethane grafts can be designed with the mechanical properties of soft arteries. To achieve the properties of relatively stiff arteries, such as the intracranial artery considered in this study, the model suggests that the mesh thickness be increased and fibre orientation altered. However, additional options that could be tested readily using this model include increasing the fibre modulus – to simulate stiffer biomaterials (e.g. PLCL⁴⁰ or PTFE³⁷) – and decreasing mesh porosity.

Table 12. β -values predicted by the model and measured for different materials.

vessel type	polyurethane (model)	polyurethane ^{11,12}	carotid ¹¹	femoral ¹¹	intracranial ³⁸
β	9.1-15.8	8.4-29.5	5.25	19.84	21.2

The agreement of model predictions with experimentally determined mesh properties provides insights into the mechanics of electrospun networks under uniaxial strain, while discrepancies reveal limitations of the model framework. In particular, two discrepancies were identified. First, although a PEUUR modulus 2.7 MPa was measured for cast films, a fibre modulus, E_f , of 18 MPa was required in order to match the model prediction to the experimental data in **Figure C.2**. Second, although the model was able to accurately predict moduli parallel to fibre alignment, it underestimated moduli perpendicular to fibre alignment. Both of these

discrepancies may have resulted from assumptions that were built into the computational model as well as differences between the RVEs and real electrospun meshes structures.

Two intrinsic assumptions of this model – which was originally developed for collagen fibres (typically 50–200 nm in diameter) – are that bending forces are negligible and that fibres can rotate freely at crosslinks. These assumptions result in a model that considers only tensile strain, and therefore should generate predictions of mesh modulus that are independent of fibre diameter. Interestingly, the computational model predicts an increase in modulus with increasing fiber diameter (**Figure C.3**), but this increase likely reflects a decrease in the angular standard deviation (**Table C.1**). Because beam mechanics predicts that bending force scales as fibre thickness cubed, incorporation of fibre bending into our model should cause the mesh modulus to increase with increasing fibre diameter. Evidence of this trend has been observed previously^{20, 21} although contrary data have also been reported.⁴¹ A more detailed analysis of the mechanics of fibre networks, where fibre bending was incorporated, can be found in Wang et al.⁴² and Wang and Sastry⁴³. In those studies, Euler-Bernoulli beam theory was used for fibre length/diameter aspect ratios greater than five, while for lower aspect ratios Timoshenko beam theory was employed to account for deformation due to transverse shear. According to Head et al.⁴⁴ bending dominates in networks that possess a low fibre density or that consist of relatively short fibres. In contrast, networks with high fibre density or long fibre length are dominated by fibre stretching. Incorporation of bending into our model is expected to increase the stiffness of the scaffolds, and would likely result in a lower value for the fitted parameter E_f . In addition, because fibre bending is more pronounced when the meshes are stretched perpendicular to their direction of alignment, incorporation of bending into our model might increase predictions of modulus perpendicular to fibre alignment.

The properties of fibre crosslinks (e.g. geometry, restriction to fibre motion) also can affect the modulus of the mesh.⁴⁵ showed that the geometry of a crosslink and the angle that is formed between two connected fibres affect the network forces under loading. In addition, fixed crosslinks provide additional rigidity to fibre networks when fibre bending is not negligible.^{44,46} In our model we permitted free rotation at crosslinks. This likely diminished the predicted modulus of our meshes, especially in the case of strain applied perpendicularly to fibre orientation, where reorientation of the fibres is expected to be significant.

Finally, the model predictions can be affected by the equation used to describe the response of the fibre Eq. (C.1). In this study we treated the PEUUR fibres as a neo-Hookean material based on our experience on modelling polymer networks. Alternatively, phenomenological exponential expressions have been used^{26,32} that predict an almost zero force in compression to account for buckling of the fibres. The incorporation of fibre buckling into our model is not expected to affect significantly the tensile mechanical properties of the scaffolds, particularly for the properties parallel to the direction of strain as buckling is expected to occur primarily in the transverse direction.

In addition to limitations with the model assumptions, differences between model and experimental data may also have stemmed from our inability to determine accurately the properties of our electrospun mesh, including crosslink density, spatial homogeneity of mesh architecture and mesh porosity. From SEM images (**Figure C.1**) the diameter and orientation of individual fibres can be readily determined and used to generate RVEs. However, crosslinks between adjoining fibres cannot be unambiguously identified, and consequently their densities could not be incorporated into the design of RVEs. In addition, the RVEs were generated based on SEM images of the topmost fibres in a mesh. Microarchitecture (e.g. fibre diameter, orientation, angular standard deviation) was assumed to be uniform throughout the mesh thickness, but spatial homogeneity of mesh architecture was not verified. Finally, the fibre volume fractions of the PEUUR meshes were not determined. Instead, volume fraction was assumed to be 40% for all samples, based on the mercury intrusion porosimetry data of Kwon et al.¹⁴

Another limitation of this study is the small n value in the test data ($n = 3$). A larger sample size might have resulted in more accurate measurements for the mechanical properties of the meshes and would allow us to determine better the model accuracy.

The inclusion of a fitted parameter, E_f , in the model allowed us to compensate for limitations in the model assumptions as well as differences between the RVEs and real fibre meshes. In particular the high fitted value, $E_f = 18$ MPa, relative to the PEUUR modulus, $E = 2.7$ MPa, suggests that fibre bending and rigidity at fibre crosslinks may not be negligible. In addition, this discrepancy suggests that the volume fraction and crosslink density of the RVEs are underestimates of the true mesh properties. We must note, though, that the differences between the bulk modulus and E_f may have stemmed from differences in the processing

conditions used to produce solution cast films and electrospun meshes. Mechanical processing techniques, such as fibre spinning and film drawing are known to produce anisotropy in mechanical properties,⁴⁷ and electrospinning – in particular – has been shown to cause strain-induced hardening.⁴⁸

To conclude, the mechanisms that govern the macromechanical behaviour of tissues and tissue constructs is not yet well understood. In our work, we permitted nonaffine fibre deformations, based on research on network mechanics,⁴⁹ and the position of the fibres was determined by the solution of a force balance. Here, the accuracy of the model predictions depends largely on the micromechanics of the fibre network (e.g. fibre stretching, bending, buckling, crosslink bending). This approach differs from affine deformation models⁵⁰⁻⁵² in which fibres do not interact with each other but are treated as a collection of independent units embedded in the tissue matrix. In affine models, the fibres rotate and stretch homogeneously with the macroscopic deformation and the model predictions depend only on the fibre mechanical properties. Although nonaffine models are computationally more intensive, they should be more accurate because they account for microscopic network effects. Their accuracy, nevertheless, depends on the extent to which they capture the micromechanics of the network.

C.5 Acknowledgements

This work was supported by NIH grant 1 R01 EB005813-01 to VHB, and grants from the Charles E. Culpeper Foundation (03-130) and the Institute for Critical Technologies and Sciences at Virginia Tech to ASG. TS was also supported by a Doctoral Dissertation Fellowship from the University of Minnesota. Simulations were made possible by resources grants from the University of Minnesota Supercomputing Institute.

C.5 References

1. Butler, D.L., Goldstein, S.A., Guilak, F., 2000. Functional tissue engineering: the role of biomechanics. *Journal of Biomechanical Engineering* 122 (6), 570–575.
2. Enever, P.A., Shreiber, D.I., Tranquillo, R.T., 2002. A novel implantable collagen gel assay for fibroblast traction and proliferation during wound healing. *The Journal of Surgical Research* 105 (2), 160–172.
3. Grassl, E.D., Oegema, T.R., Tranquillo, R.T., 2002. Fibrin as an alternative biopolymer to type-I collagen for the fabrication of a media equivalent. *Journal of Biomedical Materials Research* 60 (4), 607–612.
4. Grassl, E.D., Oegema, T.R., Tranquillo, R.T., 2003. A fibrin-based arterial media equivalent. *Journal of Biomedical Materials Research A* 66 (3), 550–561.
5. Li, C., Vepari, C., Jin, H.J., Kim, H.J., Kaplan, D.L., 2006. Electrospun silkBMP2 scaffolds for bone tissue engineering. *Biomaterials* 27 (16), 3115–3124.
6. White, J.A., Deen, W.M., 2002. Agarosedextran gels as synthetic analogs of glomerular basement membrane: Water permeability. *Biophysical Journal* 82 (4), 2081–2089.
7. Agrawal, C.M., Ray, R.B., 2001. Biodegradable polymeric scaffolds for musculoskeletal tissue engineering. *Journal of Biomedical Materials Research* 55 (2), 141–150.
8. Goldstein, A.S., Juarez, T.M., Helmke, C.D., Gustin, M.C., Mikos, A.G., 2001. Effect of convection on osteoblastic cell growth and function in biodegradable polymer foam scaffolds. *Biomaterials* 22 (11), 1279–1288.
9. Moran, J.M., Pazzano, D, Bonassar, L.J., 2003. Characterization of polylactic acid-polyglycolic acid composites for cartilage tissue engineering. *Tissue Engineering* 9 (1), 63–70.
10. Temenoff, J.S., Mikos, A.G., 2000. Review: Tissue engineering for regeneration of articular cartilage. *Biomaterials* 21 (5), 431–440.
11. Hayashi, K., Takamizawa, K., Saito, T., Kira, K., Hiramatsu, K., Kondo, K., 1989. Elastic properties and strength of a novel small-diameter, compliant polyurethane vascular graft. *Journal of Biomedical Materials Research* 23 (A2 Suppl), 229–244.
12. Matsuda, T., Ihara, M., Inoguchi, H., Kwon, I.K., Takamizawa, K., Kidoaki, S., 2005. Mechanoactive scaffold design of small-diameter artificial graft made of electrospun segmented polyurethane fabrics. *Journal of Biomedical Materials Research. Part A* 73 (1), 125–131.
13. Bashur, C.A., Dahlgren, L.A., Goldstein, A.S., 2006. Effect of fiber diameter and orientation on fibroblast morphology and proliferation on electrospun poly(D,L-lactic-co-glycolic acid) meshes. *Biomaterials* 27 (33), 5681–5688.
14. Kwon, I.K., Kidoaki, S., Matsuda, T., 2005. Electrospun nano-to microfiber fabrics made of biodegradable copolyesters: Structural characteristics, mechanical properties and cell adhesion potential. *Biomaterials* 26 (18), 3929–3939.
15. Yang, F., Murugan, R., Wang, S., Ramakrishna, S., 2005.
16. Electrospinning of nano/micro scale poly(L-lactic acid) aligned fibers and their potential in neural tissue engineering. *Biomaterials* 26 (15), 2603–2610.
17. Zong, X., Bien, H., Chung, C.Y., Yin, L., Fang, D., Hsiao, B.S., et al., 2005. Electrospun finetextured scaffolds for heart tissue constructs. *Biomaterials* 26 (26), 5330–5338.

18. Pham, Q.P., Sharma, U., Mikos, A.G., 2006. Electrospinning of polymeric nanofibers for tissue engineering applications: a review. *Tissue Engineering* 12 (5), 1197–1211.
19. Boland, E.D., Pawlowski, K.J., Barnes, C.P., Simpson, D.G., Wnek, G.E., Bowlin, G.L., 2006. Electrospinning of bioresorbable polymers for tissue engineering scaffolds. In: Reneker, D.H., Fong, H. (Eds.), *Polymeric Nanofibers*. American Chemical Society, pp. 188–204.
20. Boland, E.D., Coleman, B.D., Barnes, C.P., Simpson, D.G., Wnek, G.E., Bowlin, G.L., 2005. Electrospinning polydioxanone for biomedical applications. *Acta Biomaterialia* 1 (1), 115–123.
21. Boland, E.D., Wnek, G.E., Simpson, D.G., Pawlowski, K., Bowlin, G.L., 2001. Tailoring tissue engineering scaffolds using electrostatic processing techniques: A study of poly(glycolic acid) electrospinning. *Journal of Macromolecular Science* 38 (12), 1231–1243.
22. Gupta, P., Elkins, C., Long, T.E., Wilkes, G.L., 2005. Electrospinning of linear homopolymers of poly(methyl methacrylate): Exploring relationships between fiber formation, viscosity, molecular weight and concentration in a good solvent. *Polymer* 46, 4799–4810.
23. Nair, L.S., Bhattacharyya, S., Bender, J.D., Greish, Y.E., Brown, P.W., Allcock, H.R., et al., 2004. Fabrication and optimization of methylphenoxy substituted polyphosphazene nanofibers for biomedical applications. *Biomacromolecules* 5 (6), 2212–2220.
24. Billiar, K.L., Sacks, M.S., 2000b. Biaxial mechanical properties of the natural and glutaraldehyde treated aortic valve cusp — Part I: Experimental results. *Journal of Biomechanical Engineering* 122 (1), 23–30.
25. Humphrey, J.D., 2003. Continuum biomechanics of soft biological tissues. *Proceedings of the Royal Society of London Series A- Mathematical Physical and Engineering Sciences* 459 (2029), 3–46.
26. Stylianopoulos, T., Barocas, V.H., 2007a. Volume-averaging theory for the study of the mechanics of collagen networks. *Computer Methods in Applied Mechanics and Engineering* 196, 2981–2990.
27. Agoram, B., Barocas, V.H., 2001. Coupled macroscopic and microscopic scale modeling of fibrillar tissues and tissue equivalents. *Journal of Biomechanical Engineering* 123 (4), 362–369.
28. Guelcher, S.A., Gallagher, K.M., Didier, J.E., Klinedinst, D.B., Doctor, J.S., Goldstein, A.S., et al., 2005. Synthesis of biocompatible segmented polyurethanes from aliphatic diisocyanates and diurea diol chain extenders. *Acta Biomaterialia* 1 (4), 471–484.
29. Whitaker, S., 1986. Flow in porous media I: A theoretical derivation of Darcy’s law. *Transport in Porous Media* 1, 3–25.
30. Drew, D.A., 1971. Averaged field equations for twophase media. *Studies in Applied Mathematics* L 2, 133–166.
31. Chandran, P.L., Barocas, V.H., 2007. Deterministic materialbased averaging theory model of collagen gel mechanics. *Journal of Biomechanical Engineering* 129, 137–147.
32. Stylianopoulos, T., Barocas, V.H., 2007b. Multiscale, structurebased modeling for the elastic mechanical behavior of arterial walls. *Journal of Biomechanical Engineering* 129, 611–618.
33. Macosko, C.W., 1994. *Rheology: Principles, Measurements and Applications*, 1st ed. WileyVCH, New York.

34. NematNasser, S., Hori, M., 1999. *Micromechanics: Overall Properties of Heterogeneous Materials*. NorthHolland, Amsterdam.
35. Oda, M., Iwashita, A.A., 1999. *Mechanics of Granular Materials*. Brookfield, Rotterdam.
36. Vaz, C.M., van Tuijl, S., Bouten, C.V., Baaijens, F.P., 2005. Design of scaffolds for blood vessel tissue engineering using a multilayering electrospinning technique. *Acta Biomaterialia* 1 (5), 575–582.
37. Sonoda, H., Urayama, S., Takamizawa, K., Nakayama, Y., Uyama, C., Yasui, H., et al., 2002. Compliant design of artificial graft: Compliance determination by new digital X-ray imaging systembased method. *Journal of Biomedical Materials Research* 60 (1), 191–195.
38. Hayashi, K., Handa, H., Nagasawa, S., Okumura, A., Moritake, K., 1980. Stiffness and elastic behavior of human intracranial and extracranial arteries. *Journal of Biomechanics* 13 (2), 175–184.
39. Roach, M.R., Burton, A.C., 1957. The reason for the shape of the distensibility curves of arteries. *Canadian Journal of Biochemistry Physiology* 35, 681–690.
40. Inoguchi, H., Kwon, I.K., Inoue, E., Takamizawa, K., Maehara, Y., Matsuda, T., 2006. Mechanical responses of a compliant electrospun poly(L-lactide-co-epsilon-caprolactone) small-diameter vascular graft. *Biomaterials* 27 (8), 1470–1478.
41. Huang, Z.M., Zhang, Y.Z., Ramakrishna, S., Lim, C.T., 2004. Electrospinning and mechanical characterization of gelatin nanofibers. *Polymer* 45 (15), 5361–5368.
42. Wang, C.W., Berhan, L., Sastry, A.M., 2000. Structure, mechanics and failure of stochastic fibrous networks: Part I — Microscale considerations. *Journal of Engineering Materials and Technology* 122 (4), 450–459.
43. Wang, C.W., Sastry, A.M., 2000. Structure, mechanics and failure of stochastic fibrous networks: Part II—Network simulations and application. *Journal of Engineering Materials and Technology* 122 (4), 460–468.
44. Head, D.A., Levine, A.J., MacKintosh, F.C., 2003. Distinct regimes of elastic response and deformation modes of cross-linked cytoskeletal and semiflexible polymer networks. *Physical Review E, Statistical, Nonlinear, and Soft Matter Physics* 68 (6 Pt (1)), 061907.
45. Berhan, L., Sastry, A.M., 2003. On modeling bonds in fused, porous networks: 3D Simulations of fibrous/particulate joints. *Journal of Composite Materials* 37 (8), 715–740.
46. Wilhelm, J., Frey, E., 2003. Elasticity of stiff polymer networks. *Physical Review Letters* 91 (10), 108103(4).
47. Wilkes Jr., G.L., 2003. In: Brady, R.F. (Ed.), *Mechanical Properties*. In: *Comprehensive Desk Reference of Polymer Characterization and Analysis*, American Chemical Society, Oxford University Press, pp. 624–668.
48. Gu, S.Y., Wu, Q.L., Ren, J., Vancso, G.J., 2005. Mechanical properties of a single electrospun fiber and its structures. *Macromolecular Rapid Communications* 26, 716–720.
49. Chandran, P.L., Barocas, V.H., 2006. Affine versus nonaffine fibril kinematics in collagen networks: Theoretical studies of network behavior. *Journal of Biomechanical Engineering* 128 (2), 259–270.
50. Billiar, K.L., Sacks, M.S., 2000a. Biaxial Mechanical Properties of the Native and GlutaraldehydeTreated Aortic Valve Cusp: Part II — A Structural Constitutive Model. *Journal of Biomechanical Engineering* 122 (4), 327–335.

51. Driessen, N.J., Bouten, C.V., Baaijens, F.P., 2005. A structural constitutive model for collagenous cardiovascular tissues incorporating the angular fiber distribution. *Journal of Biomechanical Engineering* 127 (3), 494–503.
52. Zulliger, M.A., Fridez, P., Hayashi, K., Stergiopoulos, N., 2004. A strain energy function for arteries accounting for wall composition and structure. *Journal of Biomechanics* 37 (7), 989–1000.

Appendix D: Computer Macros

D.1 ImagePro Macro to Take Fluorescent Images

' Default Script
Option Explicit

'To systematically collect fluorescent images
'Modified from "CollectImages" by Michelle Kreke
'Last modified March, 25 2009 by Chris Bashur

Sub CollectImages_Chris

```
Dim Iname As String*255, XX As String*2, str1 As String*255
Dim Axis(4) As String, Phase(4) As String, cont As String, i As Integer
Dim j As Integer, k As Integer, pic As Integer
Dim num_filters As Integer, intens(4) As Integer, direction As Integer, dend As Integer
Dim XPos As Single, YPos As Single, ZPos As Single
```

```
ret = IpStageShow(1)
```

```
' The program has its own routine, click physical limits of the stage
```

```
cont = "yes"
```

```
Do While cont = "yes"
```

```
    'set file names
```

```
    ret = IpStGetName("Select Name and Destination", "C:\RESULTS", "*.TIF", Iname)
```

```
    Iname = Trim$(Replace(Iname, Chr$(0), " "))
```

```
    Axis(1)="R"
```

```
    Axis(2)="L"
```

```
    Axis(3)="L1_ "
```

```
    Axis(4)="R1_ "
```

```
    'Set the origin for the stage
```

```
    ret = IpMacroStop("Move stage to middle of mesh", MS_MODAL
```

```
    ipStgVal = STG_CURRENT
```

```
    ret = IpStageControl(SETORIGIN, ipStgVal)
```

```
    'Define settings for the coverslip
```

```
    ipLVal = 150
```

```
    ret = IpAcqControl(49, 0, ipLVal)
```

```
    ret=IpStGetInt("Enter the amount of pictures at each position",num_filters,2,1,4)
```

```
    For i=1 To num_filters Step 1
```

```
        ret=IpStGetInt("Enter the exposure time in ms",intens(i),15,5,10000)
```

```
    Next i
```

```
    'Set the type of picture file extensions every time
```

```
    pic = 5
```

```
    Phase(1)="_dapi_ "
```

```
    Phase(2)="_WG_ "
```

```
    Phase(3)="_WG_ "
```

```
    'determine picture taking directions
```

```

direction = 1           '=2 if images in all directions, =1 if just one direction (for slides)

If direction = 1 Then dend = 2
If direction = 2 Then dend = 4

For i=1 To dend Step 1
  XPos = 0
  YPos = 0
  ZPos = 0.0
  ret = IpStageXY(XPos, YPos)
  ret = IpStageZ(ZPos)
  For j=1 To pic Step 1

    If direction = 2 Then
      If i=1 Then XPos = j*12/pic 'old YPos 7.5
      If i=2 Then XPos = -j*12/pic 'old YPos -7.5
      If i=3 Then XPos = -j*12/pic 'old XPos 7.5
      If i=4 Then XPos = j*12/pic 'old Xpos -7.5
    End If

    If direction = 1 Then
      If i=1 Then XPos = j*12/pic 'And Axis(1)="L" 'XPos as 20
      If i=2 Then XPos = -j*12/pic 'And Axis(2)="R"
      'If i=1 Then YPos = j*3/pic 'And Axis(1)="U" 'XPos as 20
      'If i=2 Then YPos = -j*3/pic 'And Axis(2)="D"
    End If

    ret = IpStageXY(XPos, YPos)
    ret = IpAcqShow(ACQ_LIVE, 1)
    ret = IpMacroStop("Click when image is focused", MS_MODAL)
    ret = IpAcqShow(ACQ_LIVE, 0)
    For k=1 To num_filters Step 1
      ipLVal = intens(k)
      ret = IpAcqControl(49, 1, ipLVal)
      XX=CStr(j)
      If Len(Trim$(XX))=1 Then XX="0"+Trim$(XX)
      str1=Trim$(Iname)+Phase(k)+Axis(i)+XX+".tif"
      Debug.Print str1
      ret = IpAcqSnap(ACQ_CURRENT)
      ret = IpWsConvertImage(IMC_GRAY, CONV_SCALE, 0, 0, 0, 0)
      IpDocClose
      ret = IpWsSaveAs(str1, ".tif")
      If k <> num_filters Then IpMacroWait(45)
    Next k
  Next j
Next i
ret = IpMacroStop("Are there more wells?", MS_MODAL + MS_YESNO)
If ret = 0 Then cont = "no"
Loop
End Sub

```

D.2 ImagePro Macro to Overlay Fluorescent Images

Sub OverlayImages

```
Dim str1(4) As String* 255, XX As String*2
Dim Iname(3) As String*255, root(3) As String*255, num_filters As Integer, colorID(3) As Integer
Dim j As Integer, i As Integer, ImID(3) As Integer, numobj As Integer
Dim AxisStart As Single, AxisStop As Single, IndexStart As Single, IndexStop As Single
Dim stats(10) As Single, Inten(10) As Single, diff(2) As Single, index(2) As Single
Dim k As Integer, m As Integer, Columns As Integer

Dim Axis(4) As String
Axis(1)="R" 'U
Axis(2)="L" 'R
Axis(3)="L2_" 'D
Axis(4)="R2_" 'L
IpOutputShow(1)
IpOutputClear()
ret = IpLutShow(1)

'Get File Names
ret = IpTemplateMode(1)
ret=IpStGetInt("Enter the amount of pictures at each position",num_filters,3,1,3)

For j=1 To num_filters Step 1
    ret = IpStGetName("Select Phase Image Set (red,green,blue)","C:\RESULTS","*.TIF", Iname(j))
    root(j)=Replace(Iname(j),Chr$(0)," ")
    IpOutput(root(j)+Chr$(13)+Chr$(10))
    i=Len(Trim$(root(j)))
    root(j)=Left$(Trim$(root(j)), (i-7)) 'i-7
Next j

'allows for appropriate scale bar to be added
ret = IpSCalSelect("OcrA 10x bin 2") 'adjust if different calibration
ret = IpSCalShow(1)
ret = IpWsCreate(400, 400, 72, IMC_RGB)

Begin Dialog UserDialog 294,203 ' %GRID:10,10,1,0
    OKButton 38,162,90,19
    CancelButton 164,162,90,20
    Text 54,6,163,18,"Click when scale bar set"
    TextBox 164,35,90,20,.TextBox1
    Text 32,40,90,14,"Start Axis",.Text1
End Dialog
Dim dlg11 As UserDialog 'sets the default number of pictures in each direction
dlg11.TextBox1 = "1"
If Dialog(dlg11)=0 Then End

ret = IpDocClose()

ret = IpTemplateMode(0)
'Select Range of Images
Begin Dialog UserDialog 294,203 ' %GRID:10,10,1,0
    OKButton 38,162,90,19
    CancelButton 164,162,90,20
    Text 54,6,163,18,"Select Range of Images"
```

```

    TextBox 164,35,90,20,.TextBox1
    TextBox 164,65,90,20,.TextBox2
    TextBox 164,95,90,20,.TextBox3
    TextBox 164,125,90,20,.TextBox4
    Text 32,40,90,14,"Start Axis",.Text1
    Text 32,70,90,14,"Stop Axis",.Text2
    Text 32,100,90,14,"Start Position",.Text3
    Text 32,130,90,14,"Stop Position",.Text4
End Dialog
Dim dlg1 As UserDialog          'sets the default number of pictures in each direction
dlg1.TextBox1 = "1"
dlg1.TextBox2 = "4"
dlg1.TextBox3 = "1"
dlg1.TextBox4 = "5"
If Dialog(dlg1)=0 Then End
AxisStart = CSng(dlg1.TextBox1)
AxisStop = CSng(dlg1.TextBox2)
IndexStart = CSng(dlg1.TextBox3)
IndexStop = CSng(dlg1.TextBox4)

'Collect and combine images
For i=AxisStart To AxisStop Step 1
    For j=IndexStart To IndexStop Step 1
        IpOutput("Axis "+CStr(i)+", Index "+CStr(j))
        XX=CStr(j)
        If Len(Trim$(XX))=1 Then XX="0"+Trim$(XX)
        For k=1 To num_filters Step 1
            str1(k) = Trim$(root(k))+Axis(i)+XX+".tif"
            ImID(k) = IpWsLoad(str1(k), "TIF")
        Next k

        For k=1 To 3 Step 1
            colorID(k)=-1
        Next k
        For k=1 To num_filters Step 1
            colorID(k)=(j-1+(i-1)*IndexStop)*(num_filters+2)+(k-1)
        Next k

        ret = IpCmChannelMerge3(0, colorID(1),colorID(2),colorID(3), CM_RGB, 1)
            'colorID(1)->red colorID(3)->blue
        ret = IpWsConvertImage(IMC_RGB, CONV_SCALE, 0, 0, 0, 0)
        ret = IpScalSelect("OcrA 10x bin 2")
        ret = IpWsPaste(16, 468)
        'add scale bar
        str1(4) = Trim$(root(1))+ "overlay"+Axis(i)+XX+".tif"
        ret = IpWsSaveAs(str1(4), "tif")
        ret = IpDocMinimize()
        ret = IpAppSelectDoc(0)
        ret = IpDocClose()
        ret = IpAppSelectDoc(1)
        ret = IpDocClose()
        ret = IpAppSelectDoc(2)
        ret = IpDocClose()
        If num_filters = 3 Then

```

```

        ret = IpAppSelectDoc(3)
        ret = IpDocClose()
    End If

'Determine Next Image
Begin Dialog UserDialog 390,180 '%GRID:10,7,1,1
    GroupBox 20,14,140,112,"Select Image Pair",.GroupBox1
    OKButton 50,140,90,21
    PushButton 240,140,90,21,"QUIT",.PushButton1
    TextBox 250,42,90,21,.TextBox1
    TextBox 250,77,90,21,.TextBox2
    Text 200,49,40,14,"axis",.Text1
    Text 200,77,40,14,"index",.Text2
    Text 220,14,110,14,"Other Image Pair",.Text3
    OptionGroup .Group1
        OptionButton 50,42,70,14,"Next",.OptionButton1
        OptionButton 50,70,90,14,"Previous",.OptionButton2
        OptionButton 50,98,90,14,"Other",.OptionButton3
End Dialog

Dim dlg2 As UserDialog
dlg2.TextBox1="1"
dlg2.TextBox2="2"

If Dialog(dlg2)=1 Then
    i=AxisStop
    j=IndexStop
ElseIf dlg2.Group1=1 Then
    j=j-2
    If j=-1 Then
        j=IndexStop-1
        i=i-1
        If i=0 Then
            i=1
            j=0
        End If
    End If
ElseIf dlg2.Group1=2 Then
    i=CSng(dlg2.TextBox1)
    j=CSng(dlg2.TextBox2)-1
End If
    If j=IndexStop Then
        Columns=7*(i)+1
        ret = IpDde(DDE_SET, "col", Str$(Columns))
        ret = IpDde(DDE_SET, "row", "3")
    End If
Next j
Next i

End Sub

```

D.3 ImagePro Macro to Analyze Fluorescent Images

Sub AnalyzeCellMorphology

```
Dim str1 As String* 255, str2 As String*255, XX As String*2
Dim Iname1 As String*255, Iname2 As String*255, root1 As String*255, root2 As String*255
Dim j As Integer, i As Integer, ImID1 As Integer, ImID2 As Integer,
Dim ImID3 As Integer, ImID4 As Integer, numobj As Integer
Dim AxisStart As Single, AxisStop As Single, IndexStart As Single, IndexStop As Single
Dim stats(10) As Single, Inten(10) As Single, diff(2) As Single, index(2) As Single
Dim k As Integer, m As Integer, Columns As Integer, check As Integer
```

```
Dim Axis(4) As String
Axis(1)="R"
Axis(2)="L"
Axis(3)="L1_"
Axis(4)="R1_"
IpOutputShow(1)
IpOutputClear()
```

'Get File Names

```
ret = IpTemplateMode(1)
ret = IpStGetName("Select Phase Image Set","C:\RESULTS","*.TIF", Iname1)
root1=Replace(Iname1,Chr$(0)," ")
IpOutput(root1+Chr$(13)+Chr$(10))
ret = IpStGetName("Select Fluorescent Image Set","C:\RESULTS","*.TIF", Iname2)
root2=Replace(Iname2,Chr$(0)," ")
IpOutput(root2+Chr$(13)+Chr$(10))
ret = IpTemplateMode(0)
i=Len(Trim$(root1))
root1=Left$(Trim$(root1), (i-7)) 'i-7
i=Len(Trim$(root2))
root2=Left$(Trim$(root2), (i-7)) 'i-7
```

'Select Range of Images

```
Begin Dialog UserDialog 294,203 ' %GRID:10,10,1,0
  OKButton 38,162,90,19
  CancelButton 164,162,90,20
  Text 54,6,163,18,"Select Range of Images"
  TextBox 164,35,90,20,.TextBox1
  TextBox 164,65,90,20,.TextBox2
  TextBox 164,95,90,20,.TextBox3
  TextBox 164,125,90,20,.TextBox4
  Text 32,40,90,14,"Start Axis",.Text1
  Text 32,70,90,14,"Stop Axis",.Text2
  Text 32,100,90,14,"Start Position",.Text3
  Text 32,130,90,14,"Stop Position",.Text4
End Dialog
```

```
Dim dlg1 As UserDialog 'sets the default number of pictures in each direction
dlg1.TextBox1 = "1"
dlg1.TextBox2 = "4"
dlg1.TextBox3 = "1"
dlg1.TextBox4 = "5"
If Dialog(dlg1)=0 Then End
AxisStart = CSng(dlg1.TextBox1)
```

```

AxisStop = CSng(dlg1.TextBox2)
IndexStart = CSng(dlg1.TextBox3)
IndexStop = CSng(dlg1.TextBox4)

IpSCalShow(1)
ret = IpDde(DDE_SET, "row", "3")
ret = IpDde(DDE_SET, "col", "1")
ret = IpDde(DDE_SET, "append", "1")

'Collect and Process Images and export to excel
For i=AxisStart To AxisStop Step 1
    For j=IndexStart To IndexStop Step 1
        IpOutput("Axis "+CStr(i)+"", Index "+CStr(j))
        XX=CStr(j)
        If Len(Trim$(XX))=1 Then XX="0"+Trim$(XX)
        str1 = Trim$(root1)+Axis(i)+XX+".tif"
        ImID1 = IpWsLoad(str1, "TIF")
        ret = IpSCalSelect("Oera 10x bin 2") 'sets calibration (change before running macro)
        str2 = Trim$(root2)+Axis(i)+XX+".tif"
        ImID2 = IpWsLoad(str2, "TIF")

        ret = IpSCalSelect("Oera 10x bin 2") 'sets calibration (change before running macro)
        ret = IpLutShow(1)

        'set required contrast and brightness by the number of images
        ipICal(0) = 1200
        ipICal(1) = 4095
        ret = IpBlbMultiRanges(ipICal(0), 1)
        ret = IpBlbCount()

        ret = IpBlbEnableMeas(BLBM_DENSITY, 1)
        ret = IpBlbEnableMeas(BLBM_DENSDEV, 1)
        ret = IpBlbMultiRanges(ipICal(0), 1)
        ret = IpSegShow(0)

        ipICal(0) = 0
        ipICal(1) = 4095
        ret = IpBlbMultiRanges(ipICal(0), 1)

        index(1) = 50
        index(2) = 50
        'ret = IpLutSetAttr(LUT_GAMMA, 300)
        'ret = IpLutApply()
        ret = IpLutSetAttr(LUT_BRIGHTNESS, index(1))
        ret = IpLutSetAttr(LUT_CONTRAST, index(1))
        ret = IpLutApply()
        m=0
        diff(1)=50 '50
        diff(2)=50 '50
        check=0

        'make loop to adjust images
        Do While (Abs(diff(2)) + Abs(diff(1)) > 30)
            m=m+1
            k=0

```

```

diff(2)=50
diff(1)=50
check=0
Do While Abs(diff(2)) > 5 'Or check=1
    k=k+1
    ret = IpBlbCount()
    ret = IpBlbUpdate(0)
    ret = ipblbget(GETRANGESTATS, 1, BLBM_DENSDEV, stats(5))
    ret = ipblbget(GETRANGESTATS, 1, BLBM_DENSITY, Inten(5))

    diff(1) = 1600 - Inten(10) '1600
    diff(2) = 450 - stats(10) '450
    ret = IpWsUndo(0)
    index(2) = index(2)+diff(2)/130
    ret = IpLutSetAttr(LUT_CONTRAST, index(2))
    ret = IpLutSetAttr(LUT_BRIGHTNESS, index(1))
    ret = IpLutApply()
    If k>5 Then diff(2)=1
Loop
k=0
check=0
Do While Abs(diff(1)) > 15 'Or check=1
    k=k+1
    ret = IpBlbCount()
    ret = IpBlbUpdate(0)
    ret = ipblbget(GETRANGESTATS, 1, BLBM_DENSDEV, stats(5))
    ret = ipblbget(GETRANGESTATS, 1, BLBM_DENSITY, Inten(5))
    diff(1) = 1600 - Inten(10)
    diff(2) = 450 - stats(10) '450
    ret = IpWsUndo(0)
    index(1) = index(1)+diff(1)/250
    ret = IpLutSetAttr(LUT_BRIGHTNESS, index(1))
    ret = IpLutSetAttr(LUT_CONTRAST, index(2))
    ret = IpLutApply()
    If k>5 Then diff(1)=1
Loop
    If k>5 Then diff(1)=50
    Debug.Print " Pixel deviation"; stats(10)
    Debug.Print " Pixel density"; Inten(10)
    Debug.Print " number of loops"; m
If m>3 Then '10
    diff(2)=1
    diff(1)=1
End If
If diff(2)=450 Then
    diff(1)=1
    diff(2)=1
End If
Loop

'ret = IpWsDuplicate()
ret = IpSCalSelect("OcrA 10x bin 2") 'sets calibration (change before running macro)
ret = IpDocMove(249, 135)
ret = IpBlbShow(1)
ret = IpBlbEnableMeas(BLBM_ASPECT, 1)
ret = IpBlbEnableMeas(BLBM_DIRECTION, 1)

```

```

ret = IpBlbEnableMeas(BLBM_MAJORAX, 1)
ret = IpBlbEnableMeas(BLBM_DENSITY, 1)
ret = IpBlbEnableMeas(BLBM_DENSDEV, 1)
ret = IpBlbSetFilterRange(BLBM_AREA, 250, 500000)

```

```

'ret = IpFltSobel
'image processing cell count (apply sobel filter no iphstequalize, cutoff 300 to 4095), fill holes (1)
'ret = IpLutSetAttr(LUT_BRIGHTNESS, 73)
ipICal(0) = 1700
ipICal(1) = 4095
ret = IpBlbMultiRanges(ipICal(0), 1)
ret = IpSegShow(0)
ret = IpBlbSetAttr(BLOB_FILLHOLES, 1)
ret = IpBlbSetAttr(BLOB_SMOOTHING,3)
ret = IpBlbCount()
ret = IpBlbSplitObjects(3)
'stats(10)=0
'ret = ipblbget(GETRANGESTATS, 1, 0, stats(5))
'Debug.Print " Cell Area"; stats(10)
ret = IpBlbUpdate(0)
stats(10)=0

ret = IpBlbUpdate(4)
ret = IpDde(DDE_SET, "target", "C:\Microsoft Office\Office\EXCEL.EXE")
If j=1 Then ret = IpBlbSaveData("", S_HEADER) 'not working properly
ret = IpDde(DDE_SET, "append", "1")

```

'Determine Next Image

```

Begin Dialog UserDialog 390,180 ' %GRID:10,7,1,1
  GroupBox 20,14,140,112,"Select Image Pair",.GroupBox1
  OKButton 50,140,90,21
  PushButton 240,140,90,21,"QUIT",.PushButton1
  TextBox 250,42,90,21,.TextBox1
  TextBox 250,77,90,21,.TextBox2
  Text 200,49,40,14,"axis",.Text1
  Text 200,77,40,14,"index",.Text2
  Text 220,14,110,14,"Other Image Pair",.Text3
  OptionGroup .Group1
    OptionButton 50,42,70,14,"Next",.OptionButton1
    OptionButton 50,70,90,14,"Previous",.OptionButton2
    OptionButton 50,98,90,14,"Other",.OptionButton3

```

End Dialog

```

Dim dlg2 As UserDialog
dlg2.TextBox1="1"
dlg2.TextBox2="2"

```

```

If Dialog(dlg2)=1 Then
  i=AxisStop
  j=IndexStop
ElseIf dlg2.Group1=1 Then
  j=j-2
  If j=-1 Then
    j=IndexStop-1
    i=i-1
    If i=0 Then

```

```

                i=1
                j=0
            End If
        End If
    ElseIf dlg2.Group1=2 Then
        i=CSng(dlg2.TextBox1)
        j=CSng(dlg2.TextBox2)-1
    End If

        ret = IpBlbUpdate(4)
        ret = IpBlbUpdate(0)
        ret = IpBlbSaveData("", S_Y_AXIS+S_DDE)
        If j=IndexStop Then
            Columns=7*(i)+1
            ret = IpDde(DDE_SET, "col", Str$(Columns))
            ret = IpDde(DDE_SET, "row", "3")
        End If
        IpAppCloseAll
    Next j
Next i
End Sub

```

D.4 ImagePro Macro to Calculate Porosity

Sub Porosity

```

Dim j As Integer, i As Integer, numobj As Integer
Dim stats(10) As Single, Inten(10) As Single, diff(2) As Single, index(2) As Single
Dim k As Integer, m As Integer, check As Integer

```

'set required contrast and brightness by the number of images

```

ipICal(0) = 1200
ipICal(1) = 4095
ret = IpBlbMultiRanges(ipICal(0), 1)
ret = IpBlbCount()

```

```

ret = IpBlbEnableMeas(BLBM_DENSITY, 1)
ret = IpBlbEnableMeas(BLBM_DENSDEV, 1)
ret = IpBlbMultiRanges(ipICal(0), 1)
ret = IpSegShow(0)

```

```

ipICal(0) = 0
ipICal(1) = 4095
ret = IpBlbMultiRanges(ipICal(0), 1)

```

```

index(1) = 50
index(2) = 50
'ret = IpLutSetAttr(LUT_GAMMA, 300)
'ret = IpLutApply()
ret = IpLutSetAttr(LUT_BRIGHTNESS, index(1))
ret = IpLutSetAttr(LUT_CONTRAST, index(1))
ret = IpLutApply()
m=0

```

```

diff(1)=50
diff(2)=50
check=0

'make loop to adjust images
Do While (Abs(diff(2)) + Abs(diff(1)) > 30)
    m=m+1
    k=0
    diff(2)=50
    diff(1)=50
    check=0
    Do While Abs(diff(2)) > 2 'Or check=1)
        k=k+1
        ret = IpBlbCount()
        ret = IpBlbUpdate(0)
        ret = ipblbget(GETRANGESTATS, 1, BLBM_DENSDEV, stats(5))
        ret = ipblbget(GETRANGESTATS, 1, BLBM_DENSITY, Inten(5))

        diff(1) = 135 - Inten(10) '
        diff(2) = 55 - stats(10) '
        ret = IpWsUndo(0)
        index(2) = index(2)+diff(2)/125
        ret = IpLutSetAttr(LUT_CONTRAST, index(2))
        ret = IpLutSetAttr(LUT_BRIGHTNESS, index(1))
        ret = IpLutApply()
        If k>5 Then diff(2)=1
    Loop
    k=0
    check=0
    Do While Abs(diff(1)) > 2 'Or check=1
        k=k+1
        ret = IpBlbCount()
        ret = IpBlbUpdate(0)
        ret = ipblbget(GETRANGESTATS, 1, BLBM_DENSDEV, stats(5))
        ret = ipblbget(GETRANGESTATS, 1, BLBM_DENSITY, Inten(5))
        diff(1) = 135 - Inten(10)
        diff(2) = 55 - stats(10) '
        ret = IpWsUndo(0)
        index(1) = index(1)+diff(1)/150
        ret = IpLutSetAttr(LUT_BRIGHTNESS, index(1))
        ret = IpLutSetAttr(LUT_CONTRAST, index(2))
        ret = IpLutApply()
        If k>5 Then diff(1)=1
    Loop
    If k>5 Then diff(1)=50
    Debug.Print " Pixel deviation"; stats(10)
    Debug.Print " Pixel density"; Inten(10)
    Debug.Print " number of loops"; m
    If m>15 Then
        diff(2)=1
        diff(1)=1
    End If
    If diff(2)=450 Then
        diff(1)=1
        diff(2)=1
    End If
End If

```

Loop

End Sub